From UV to NIR Light, Photo-Triggered 1,3-Dipolar Cycloadditions as a Modern Ligation Method in Solution and on Surface

Zur Erlangung des akademischen Grades eines

DOKTORS DER NATURWISSENSCHAFTEN

(Dr. rer. nat.)

Fakultät für Chemie und Biowissenschaften

Karlsruhe Institut für Technologie (KIT)–Universitätsbereich

genehmigte

DISSERTATION

von

Dipl. Chem. Paul Lederhose

aus

N-Mitropolka

Dekan: Prof. Dr. Willem Klopper

Referent: Prof. Dr. Christopher Barner-Kowollik, Dr. James P. Blinco

Korreferent: Prof. Dr. Hans-Achim Wagenknecht

Tag der mündlichen Prüfung: 21.10.2016

für meine Familie

Die vorliegende Arbeit wurde im Zeitraum von März 2013 bis Oktober 2016 unter Anleitung von Prof. Dr. Christopher Barner-Kowollik und Dr. James P. Blinco am Karlsruhe Institut für Technologie (KIT), Deutschland und Queensland University of Technology, Australien angefertigt.

Ich erkläre hiermit, dass ich die vorliegende Arbeit im Rahmen der Betreuung durch Prof. Dr. Christopher Barner-Kowollik und Dr. James P. Blinco selbstständig verfasst und keine anderen als die angegebenen Quellen und Hilfsmittel verwendet habe. Wörtlich oder inhaltlich übernommene Stellen sind als solche kenntlich gemacht und die Satzung des Karlsruher Instituts für Technologie (KIT) zur Sicherung guter wissenschaftlicher Praxis wurde beachtet. Des Weiteren erkläre ich, dass ich mich derzeit in keinem laufenden Promotionsverfahren befinde und auch keine vorausgegangenen Promotionsversuche unternommen habe.

Karlsruhe, den 05.09.2015

Abstract

The presented thesis explores the nitrile imine-mediated tetrazole-ene cycloaddition (NITEC) as a versatile photoinduced conjugation technique in solution and on surface. The NITEC reaction was found to be an efficient methodology for the formation of profluorescent sensor molecules featuring a fluorophore and a nitroxide moiety, and applied for the detection of redox and radical processes. A range of nitroxide functionalized tetrazoles was synthesized and converted to their corresponding profluorescent pyrazoline derivatives through UV irradiation in the presence of a dipolarophile. The nitroxide species had no effect on the photoinduced formation of the nitrile imine dipole, an important intermediate in the NITEC reaction. The formed pyrazolines were investigated with regard to their sensor performance *via* fluorescence spectroscopy. It was found, that close proximity of the nitroxide and fluorophore moieties enhanced the sensor performance of the cycloadduct. Selected pyrazoline derivatives were subsequently exposed to model radical or reductive environments, revealing good stability under the given conditions, as well as excellent detection ability of minute concentrations of radicals or reductants. Furthermore, the NITEC concept was extended into the visible light range. A pyrene moiety was fused to the core structure of the diaryl tetrazole allowing conjugation reactions triggered at 410 - 420 nm. The resulting pyrene functional tetrazole was employed for small molecule ligation, polymer end group modification and formation of block copolymers. Thus, a variety of electron deficient olefin species were found to be suitable dipolarophiles for the addition reaction with the *in situ* formed nitrile imine moiety. Rapid and efficient formation of the desired cycloadduct under mild conditions was observed for all cycloadditions performed. The presented approach is the first example of a visible light induced, catalyst free, ligation technique suitable for advanced macromolecular design. Interestingly, all cycloadducts emit in the NIR range, allowing for potential future applications for *in vivo* labelling and

tracking. In addition, the trigger wavelength of the pyrene functionalized tetrazole was extended deep into the NIR range *via* the combination of the NITEC with upconversion nanoparticles (UCNPs). Assisted by the UCNPs, photoinduced ligation of both, small and macromolecules was obtained with irradiation at 974 nm. Full conversion and rapid formation of the desired pyrazoline cycloadducts were observed. In addition, a block copolymer featuring the biological relevant biotin moiety was prepared *via* NITEC at 974 nm, demonstrating the suitability of the approach for applications in the field of biology. Biotin was found to retain bioactivity after being exposed to the NITEC reaction conditions. The efficient penetration ability of the NIR irradiation applied was verified by 'through tissue' conjugation experiments. After the NITEC reaction was demonstrated to be a powerful ligation tool in solution, the concept was employed for the modification of surfaces in a λ-orthogonal approach. The selective ability of the pyrene tetrazole and an UV-active diaryl tetrazole to undergo independent NITEC reactions at 410 – 420 nm, and 320 nm respectively, was demonstrated in solution. Importantly, the UV-active tetrazole remains unreacted if exposed to visible light, even for prolonged irradiation times. Subsequently, a surface grafted with pyrene functional tetrazole and UV-active tetrazole was prepared and utilized for formation of advanced patterned surfaces. The resulting structures were investigated *via* ToF-SIMS, verifying excellent spatial resolution and high degree of functionalization on the surface. The presented approach is the first example a λ-orthogonal modification technique, where photoinduced linkage reactions can be triggered selectively, allowing for simple fabrication of advanced patterns without the requirement for elaborate shadow masks.

Zusammenfassung

Im Rahmen der vorliegenden Arbeit wurde die Nitrilimin vermittelte Tetrazol-Ene Cycloadditionen (NITEC) als eine vielseitige photoinduzierte Konjugationsmethode untersucht. Die effiziente Synthese von profluoreszierenden, Nitroxid- und Fluorophor-haltigen Sensormolekülen mittels der NITEC Reaktion wurde gezeigt. Die hergestellten Derivate wurden für die Detektion von Redox- und Radikalprozessen verwendet. Eine Auswahl von Nitroxid-funktionalisierten Tetrazolen wurde synthetisiert und in Gegenwart von Dipolarophilen mit Hilfe von Licht zu den entsprechenden profluoreszierenden Pyrazolin-Derivativen umgesetzt. Dabei hatte die Gegenwart der Nitroxid-Gruppe keine Auswirkung auf die photoinduzierte Entstehung des Nitrilimin Dipols, welcher eine wichtige Rolle im Verlauf der NITEC Reaktion einnimmt. Die Sensorleistung der hergestellten Pyrazoline wurde mittels Fluoreszenzspektroskopie untersucht. Eine Steigerung der Sensorleistungsfahigkeit bei den Cycloaddukten mit kurzer Entfernung zwischen der Nitroxid-Gruppe und dem Fluorophor wurde festgestellt. Ausgewählte Pyrazolin-Derivate wurden in eine Radikal- oder Redoxumgebung versetzt, wobei eine ausreichende Stabilität der Cycloaddukte und deren exzellente Nachweisfähigkeit für minimale Mengen an Radikalen oder Reduktanten festgestellt wurde. Desweiteren wurde sichtbares Licht als Auslöser für die NITEC Reaktion eingeführt, indem eine Pyrengruppe in die Grundstruktur eines Diaryltetrazol eingebaut wurde. Die Konjugationsreaktionen konnten anschließend bei 410 – 420 nm durchgeführt werden. Das hergestellte Pyren-funktionalisierte Tetrazol wurde für die Kopplung kleiner Moleküle, Polymer Endgruppen-Umwandlungen und für die Bildung von Blockcopolymeren verwendet. Eine Reihe von elektronenarmen Olefinen zeigten sich für die Additionsreaktion mit dem *in situ* entstehenden Nitrilimin geeignet. Sowohl eine schnelle, als auch effiziente Formation des gewünschten Cycloaddukts unter milden Reaktionsbedinnungen wurde für

alle durchgeführten Cycloadditionen beobachtet. Die vorgestellte Methode ist das erste bekannte Beispiel für sichtbares Licht induzierte, katalysatorfreie Kopplungstechnik, welche für makromolekulares Design geeignet ist. Alle Cycloaddukte emittieren im nahen Infrarotbereich, was einen potenziellen Einsatz der Pyrazoline für *in vivo* Experimente als Fluoreszenzmarker und deren Verfolgung ermöglicht. Die Kombination des NITEC Konzeptes mit Photonen aufkonvertierenden Nanopartikeln (UCNPs) erlaubte eine deutliche Verschiebung der Anregungswellenlänge in den nahen Infrarotbereich. In Gegenwart von UCNPs wurden photoinduzierte Kopplungen der kleinen Moleküle oder Polymerketten bei 984 nm durchgeführt. Zusätzlich wurde ein Biotin funktionalisierter Blockcopolymer mittels der NITEC Reaktion bei 984 nm synthetisiert. Das im Bereich der Biologie relevante Biotin wurde durch die NITEC Reaktion nicht beeinflusst. Die funktionelle Gruppe blieb nach der lichtinduzierten Kopplungsreaktion weiterhin bioaktiv. Die Cycloadditionen wurden im Rahmen von Gewebepenetrationsexperimenten durchgeführt, um die Durchdringungsfähigkeit des nahen Infrarotlichtes zu demonstrieren. Nachdem die NITEC Reaktion als eine leistungsstrarke Kopplungsmethode in Lösung etabliert wurde, konnte das Konzept für die λ-orthogonale Modifizierung von Oberflächen angewendet werden. Zunächst wurde die selektive Anregung des Pyrentetrazols (410 – 420 nm) und eines UV-aktiven Tetrazols (320 nm) im Rahmen einer NITEC Reaktion in Lösung demonstriert. Das UV-aktive Tetrazol blieb dabei auch nach ausgedehnter Belichtung mit sichtbaren Licht intakt. Die hergestellten Oberflächenstrukturen wurden mittels ToF-SIMS analysiert, wobei eine exzellente räumliche Auflösung und hohe Funktionalisierungsgrade der Oberfläche festgestellt wurden. Das vorgestellte Konzept ist das erste Beispiel einer λ-orthogonale Modifizierungstechnik für Oberflächen, bei der selektive Anregung der photoinduzierten Reaktionen möglich ist. Diese Technik erlaubt die einfache Anfertigung von Oberflächen mit komplexen Mustern ohne den Einsatz von aufwendigen Schattenmasken.

Publications Arising From the Thesis

(3_b) Near infrared photoinduced coupling reactions assisted by upconversion nanoparticles

Paul Lederhose, Zhijun Chen, Rouven Müller, James P. Blinco, Si Wu, Christopher Barner-Kowollik, *Angewandte Chemie International Edition* 2016, DOI: 10.1002/anie.201606425.

(3_a) Lichtgesteuerte Kupplungsreaktionen im nahen Infrarot mittels Aufkonvertierungs-Nanopartikeln

Paul Lederhose, Zhijun Chen, Rouven Müller, James P. Blinco, Si Wu, Christopher Barner-Kowollik, *Angewandte Chemie* 2016, DOI: 10.1002/ange.201606425.

(2) Catalyst free visible light induced cycloaddition as an avenue for polymer ligation

Paul Lederhose, Kilian N. R. Wüst, Christopher Barner-Kowollik, James P. Blinco, *Chemical Communications* 2016, 52, 5928-5931.

(1) Design of redox/radical sensing molecules via nitrile imine-mediated tetrazole-ene cycloaddition (NITEC)

Paul Lederhose, Naomi L. Haworth, Komba Thomas, Steven E. Bottle, Michelle L. Coote, Christopher Barner-Kowollik, James P. Blinco, *Journal of Organic Chemistry* 2015, 80, 8009–8017.

Table of Contents

1 Introduction

Photochemistry is as old as the world and is involved into every aspect of life on our planet. The nature itself provides the most fascinating examples of the utilization of photochemical and photophysical processes such as photosynthesis[1] or the phenomenon of visualising the environment through one's eyes.[2,3] The versatility and efficiency of photochemical reactions demonstrated by the nature has ever inspired scientist to adapt this powerful technique to the demands of the fast growing and developing human civilization. Giacomo Luigi Ciamician (1857 – 1922) is considered to be the pioneer of photochemistry. He was a visionary, far ahead of his time with his suggestion, to utilize the sunlight as the ultimate renewable energy source.[4] He proposed utilization of solar energy in a suitable photochemical process as a possible route for the transition from fossil energy to renewable energy sources. This revolutionary idea to use sunlight for the triggering of a chemical processes continues to remain a highly intriguing challenge since its introduction by Giacomo Luigi Ciamician. In particular, the ever increasing energy consumption combined with the continually dwindling stocks of fossil fuel resources raises the question for alternative, environment friendly strategies to satisfy the energy demand.[5] Light driven reactions could be one potential solution.[6] However, the advantages of photoinduced reactions are not limited to the application on sunlight as a possible energy source. Other key features such as the spatial and temporal control, as well as the mild reaction conditions, make the light driven reactions to potent tools for mastering scientific challenges of today and tomorrow.[7-9] Energy storage and information transition, miniaturisation of the communication and information devices, as well as advanced medical

applications such as drug delivery are among the relevant research and application areas of photochemistry.[10]

Light induced ligation techniques are an important class of photochemical reactions employed for macromolecular design,[11] surface modification,[9] fabrication of 3D structures *via* direct laser writing[12], as well as *in vivo* labelling and tracking.[13-16] In particular, conjugation methods fulfilling the 'click chemistry' requirements[17] are highly sought, as they allow fast and efficient tethering of molecules in a spatially and temporally resolved manner. There exists a range of photo active moieties suitable for conjugation reactions, whereby a light triggered elimination, isomerisation reaction or electronic activation is involved into the coupling process.[18] The major part of these coupling techniques require UV light. The employment of such high energy irradiation can damage organic or inorganic moieties, as well as biological relevant compounds. Therefore, alternative photoligation strategies applying visible or NIR light are in high demand, as the employment of longer wavelengths is less harmful for the irradiated species.[19] An additional advantage of long wavelength irradiation is the increased penetration ability compared to the UV light. Therefore, visible or NIR light triggered reactions are valuable for *in vivo* deep tissue conjugation reactions. Tuning of the photophysical properties of light active moieties in order to achieve a bathochromic shift of their absorption spectrum is one possibility to overcome the application of UV light as a trigger. However, currently there are no photo active species suitable for additive free linkage reactions in the visible light regime. Photoredox catalysis and multiphoton processes such as upconversion or two photon absorption provide valuable alternatives for triggering of a light induced reaction in a longer wavelength region. All described strategies have strengths and limitations, which will be discussed further in Section 2.3.3., whereby the choice of the appropriate technique is driven by the requirements of the specific application. However, further development of visible light induced conjugation techniques is indispensable in order to satisfy the increasing

demands of progressing scientific research. The current thesis presents the nitrile imine-mediated tetrazole-ene cycloaddition (NITEC) of a tetrazole species and a suitable dipolarophile as a possible ligation technique for advanced (macro)molecular design on surfaces and in solution (refer to Figure 1). The concept was first demonstrated to be an efficient and robust conjugation tool for the formation of sensor molecules in presence of a nitroxide species, known to have potential impact on light induced processes. Subsequently, a bathochromic shift of the absorption spectrum was attempted by modifying the core structure of the tetrazole species. The resulting visible light active tetrazole was employed for additive free ligation of small molecules and macromolecular design such as formation of block copolymers. Further red shifting of the trigger wavelength into near infrared (NIR) region was achieved by combining of the NITEC concept with upconversion nanoparticles (UCNPs). Thus, 'through tissue' ligation experiments were performed, in order to demonstrate the penetration ability of the NIR irradiation applied. Finally, two tetrazoles with different activation wavelengths were employed in a λ-orthogonal approach for the preparation of advanced patterned surfaces. The concept was first evaluated in solution and then used for the modification of silica wafers.

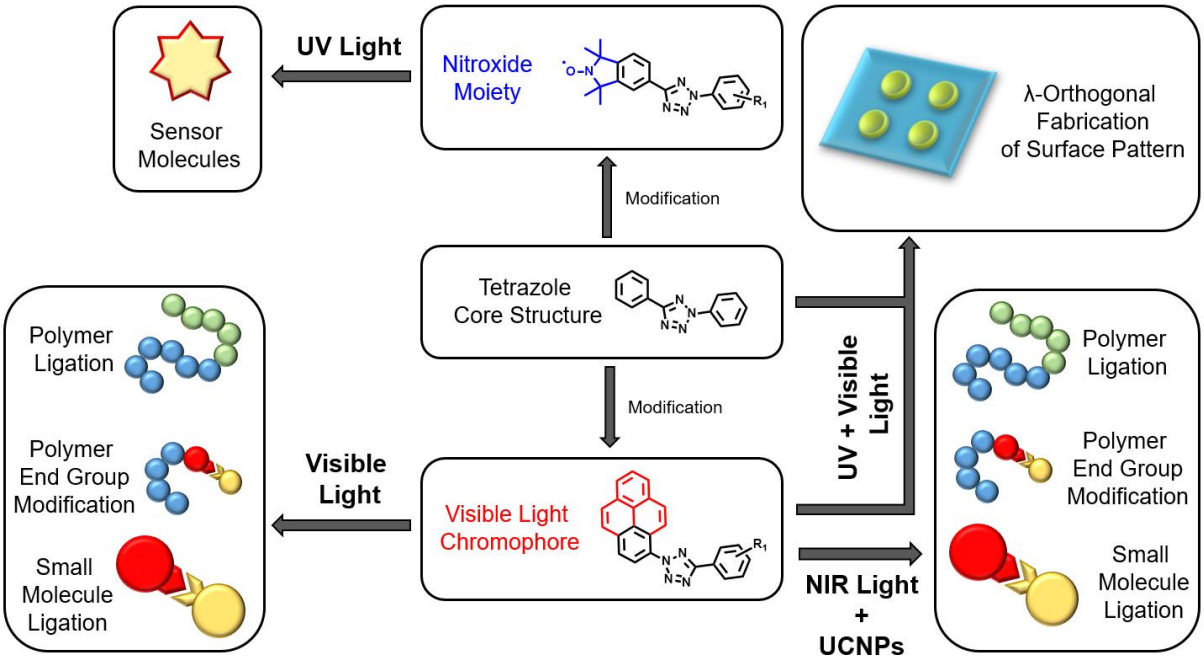

Figure 1 Overview of the projects described within the current thesis.

2 Theoretical Background and Literature Review

The current chapter provides a brief overview over the applied synthetic methods as well as selected topics related to the scientific work presented. A short summery of polymerization methods for the synthesis of well-defined, end group preserved polymers is given, with a focus on reversible deactivation radical polymerization methods. Subsequently, the concept of profluorescent nitroxides is presented, whereby the principle and synthesis are discussed. In addition, selected examples for applications of profluorescent nitroxides are given. The last section of the literature review is adressed to the photochemistry. Thus, the basics of photophysics and photochemistry are discussed. Furthermore, selected examples of efficient conjugation reactions are presented, whereby the basic mechanism, as well as current applications are provided. In the final section the state of the art techniques for triggering photoreactions *via* visible light or in NIR region are evaluetd. Modification of the photoactive species, photoredox chemistry, two photon absorbtion and upconverting nanoparticles are discussed. The basic mechanism, fields of applications, as well as advatages and disadvatages of each technique are described.

2.1 Techniques for the Synthesis of Well-Defined, End Group Preserved Polymers

Anionic polymerization was invented in 1956 by Michael Szwarc as a first example of a living polymerization technique.[20] This revolutionary approach enabled for the first time the synthesis of polymers with narrow molecular weight distributions featuring defined end group functionalities. Those functionalities were employed in an additional polymerization reaction for further modification of the obtained macromolecule. Thus, the end group capped polymer was used as a macroinitiator in order to form block copolymers. The pioneering work of Scwarc was continued in the following decades, whereby a variety of reversible deactivation radical polymerization (RDRP) techniques were introduced such as Reversible Addition-Fragmentation chain Transfer (RAFT) Polymerization, Atom Transfer Radical Polymerization (ATRP), and Nitroxide-Mediated Polymerization (NMP). Importantly, chain breaking events are suppressed and can still occur in the RDRP, while no such event is given in a living polymerization. In contrast to the living anionic polymerization, the RDRP techniques are less sensitive to water. In addition a wide variety of solvents and monomers are accessible. Although, the named techniques rely on different concepts, they all fulfil the following requirements: (*i*) narrow polydispersities, (*ii*) predictable molecular weight, (*iii*) high end group fidelity, (*iiii*) reuse of the formed polymer as a macroinitiator.[21] In the current section an overview over most common polymerization methodologies for the synthesis of well-defined polymers is provided, including RDRP and Ring Opening Polymerization (ROP). Thus, the general mechanism, the advantages and limitations of each technique will be addressed.

2.1.1 Ring Opening Polymerization (ROP)

Ring opening polymerization under controlled conditions continues to play a significant role in the modern synthesis of macroarchitectures.[22] The release of the ring strain of the employed monomer is the driving force of the polymerization process, allowing for the formation of the more stable linear structures. Therefore, the reactivity of the monomer is highly dependent on the ring size and conformation. Among established ROP monomers are lactide, lactone, cyclic ethers or siloxanes. A variety of strategies are available for the preparation of polymers from cyclic monomers including radical,[23] cationic[24] or anionic[25] ring opening reactions (refer to Scheme 1). In order to obtain efficient control over the radical ROP, a controlling species such as a RAFT agent should be added[23] (refer to Section 2.1.2.1 for detailed background on RAFT polymerization). In case of an anionic polymerization, the termination reaction by the recombination of two propagating macromolecular species is prevented by the repulsive interaction of their active centres. However, side reactions of the propagating chain such as transfer, or backbiting can occur, causing an increase of the polydispersity by formation of non-linear or shorter chains.[26] Therefore, the choice of the appropriate reactions condition is crucial. One of the key features is the reactivity of the initiating

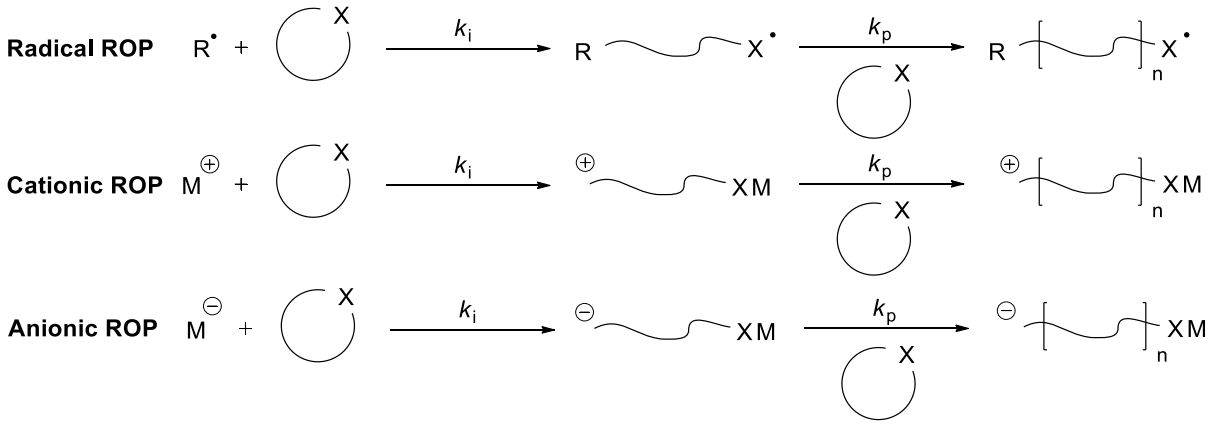

Scheme 1 Basic mechanisms of ring opening polymerization (ROP)

species, which is affected significantly by the solvent and the employed counter ion. More polar solvents solvate the ionic pairs and improve the initiation efficiency by increasing the distance between the cation and the anion.[27,28]

Coordinative ROP provides an alternative approach for the polymerization of cyclic monomers. Organic molecules,[29] metal complexes[30] or enzymes[31] can be applied to drive the polymerization to higher conversions and to retain the linear character of the synthesized chains. Although the propagation mechanism still follows the basics of ROP, additional steps are involved into the polymerization process. Metal complexes and organic molecules coordinate to the growing chain end and the monomer, ensuring close proximity of both species. In case of the enzymatic ROP, a monomer transformation into reactive linear derivatives by the enzyme occurs, followed by the subsequent introduction of the formed intermediate into the growing polymer chain. Although the catalytic systems provide rapid polymerization rates and prevent backbiting, several challenges ROP such as transfer reactions, the requirement of an elevated reaction set up or poor orthogonality towards functional groups must be addressed in the future scientific research.

2.1.2 Reversible Deactivation Radical Polymerization (RDRP)

Reversible deactivation radical polymerization methods combine the advantages of living polymerization with the versatility of free radical polymerization (FRP). A wide range of monomers and reaction conditions can be applied for the formation of well-defined polymers with high end group fidelity.[21] By suppressing termination reactions, occurring in the conventional FRP, the lifetime of the propagating chain radical can be extended from 1 s to ca 1 h or longer.[32] Two strategies were established in order to control the radical polymerization process, whereby an equilibrium between propagating radicals and a dormant species is the key feature. The first strategy is based on decreasing the radical concentration in the polymerization mixture by trapping the propagating radicals in a reversible deactivation process.[32] The second strategy utilizes a reversible addition fragmentation process to reduce the amount of irreversibly terminated chains. In contrast to the first approach, the radical concentration remains unaffected.[33] Importantly, the concentration of the mediating species must be decreased for all mentioned techniques, in order to obtain higher molecular weight polymers. However, a certain amount of the mediating species is required for controlling the polymerization. Consequently, there is a molecular weight limit for polymers synthesized *via* RDRP, defined by the classical Mayo equation.[34]

2.1.2.1 Reversible Addition-Fragmentation Chain Transfer (RAFT) Polymerization

In contrast to ATRP (refer to Section 2.1.2.2) and NMP (refer to Section 2.1.2.3) RAFT does not rely on decreasing the radical concentration by a reversible equilibrium between a dormant species and propagating chains. Under given conditions, the propagation rate and the overall radical

concentration of a RAFT polymerization and conventional FRP are similar.[35] The extended lifetime of a propagating chain is attributed to a reversible addition-fragmentation equilibrium with a controlling agent, also termed RAFT agent.[34,36] The control of the molecular weight is achieved by changing the initiator to RAFT agent ratio, whereby a liner correlation between the monomer conversion and the molecular weight is observed if the RAFT agent is chosen judiciously. The RAFT mechanism is displayed in Scheme 2. The initiation and termination reactions proceed in an identical manner as for a conventional FRP. In the initial phase of the polymerization, the growing chain ($P_n^{\bullet}$) forms a covalent bond with the RAFT agent **a** in a radical addition reaction. The formed radical intermediate **b** releases the R group in order to generate the radical species ($R^{\bullet}$). The resulting R group

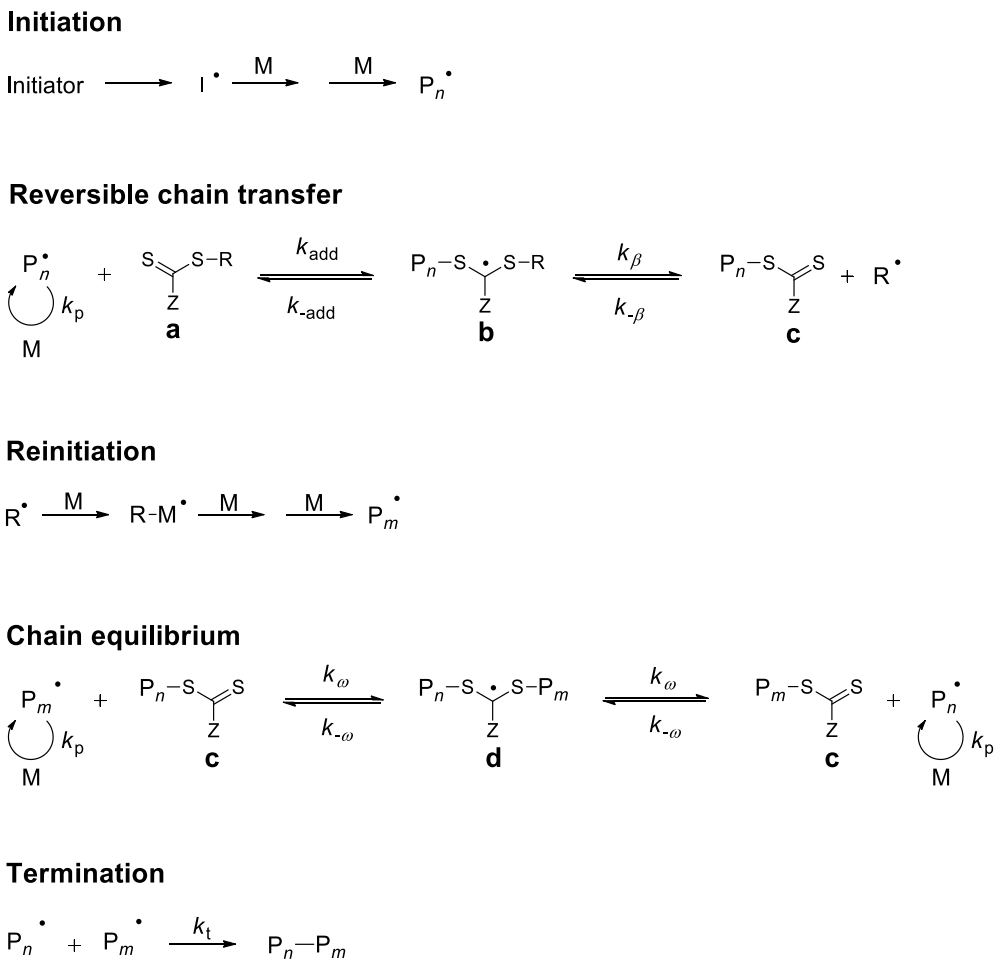

Scheme 2 Basic mechanism of the RAFT process, with RAFT agent **a** intermediates **b**, **d**, and macro-RAFT species **c**.[35]

radical initiates the propagating chain ($P_m^{\bullet}$). To ensure equal propagation probability for all chains combined with narrow polydispersities, high addition rates are required.[35]

RAFT agents should be carefully selected with respect to the monomer polymerized. Although there exists a variety of RAFT agents such as dithioesters,[37-39] trithiocarbonates,[40-42] xanthates[43-45] and dithiocarbamates,[46-48] they all feature a Z and R-groups. Both moieties play a key role in the RAFT polymerization. The Z-group coregulates the addition and the fragmentation reactions. In an efficient RAFT polymerization, the formation of intermediates **b** and **d** are favoured by the Z-group. However, the stabilisation by the Z-group should not prevent the intermediates from converting to species **c**, otherwise an inhibition of the polymerization can occur. The structure of R should facilitate the fragmentation of the radical species ($R^{\bullet}$) and allow monomer initiation by the formed carbon centered radical. In case of a poor initiation ability of ($R^{\bullet}$), inhibition or retardation of the polymerization can be observed.[35]

One of the distinct advantages of the RAFT polymerization is its versatility. A large variety of monomers and solvents can be employed, allowing for simple, fast and efficient preparation of desired polymers. The RAFT group can also participate in a post-polymerization modification approach. Several

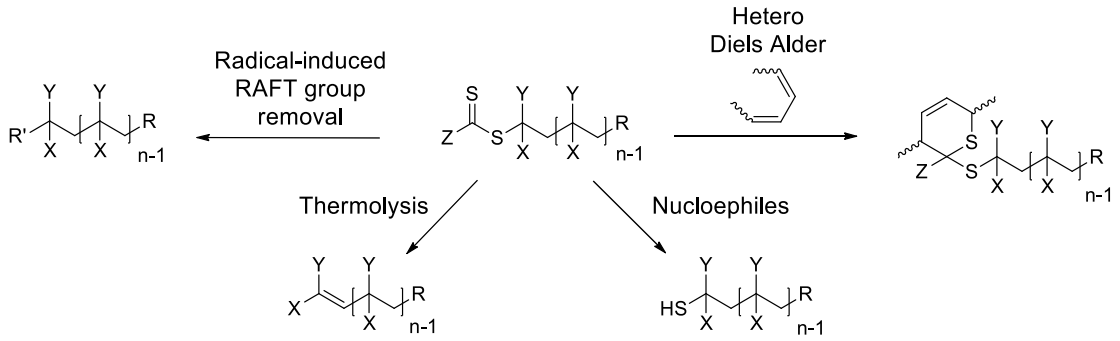

Scheme 3 Strategies for a post polymer modification of a RAFT end group.[49]

strategies to post-modify the RAFT group into different moieties have been established (refer to Scheme 3). The thiocarbonylthio moieties of the RAFT agent can be transformed to thiols in the presence of nucleophiles.[50,51] The resulting thiol species are available for a Micheal addition.[52] The thermolysis of the RAFT group yield alkene end capped chains.[53] Radical-induced RAFT group removal can be employed for the generation of hydrogen end capped polymers. Furthermore, functional *azo* initiators can be used for the introduction of a desired moiety to the chain end.[42] The C-S double bond is available for a Diels-Alder reactions with dienes if featuring an electron withdrawing substituents within the Z-group.[54] The presented transformation strategies provide a synthetic route to overcome the largest disadvantage of the RAFT: the colour and potential instability of the RAFT end groups incorporated into the polymer chains.[55-57] They also allow the preparation of advanced macromolecular architectures. However, suitable functionalities for post-polymerization macromolecular design can be incorporated into the polymer structure by their linkage to the R or Z group of the RAFT agent. Furthermore, the RAFT process can be utilized for synthesis of the desired macromolecular architecture.[58] A large range of polymer structures synthesized *via* RAFT approach is established, including block copolymers for micelle formation,[59-62] brush-,[63] comb-,[64] and star[65-67] polymers.

2.1.2.2 Atom Transfer Radical Polymerization (ATRP)

Atom transfer radical polymerization relies on a redox process involving a halogenated alkyl species and a transition metal (refer to Scheme 4). Thus, the halogenated alkyl species (P_n-X) is reduced in a radical process by the transition metal catalyst (Mt^n / L) in order to form the radical species ($P_n^{\bullet}$). The generated radical ($P_n^{\bullet}$) propagates in the presence of a monomer (M) to form a polymer chain. The reduction of the halide is reversible, whereby the activation and deactivation rate coefficients k_{act}, k_{deact} determine the

redox equilibrium. To ensure low radical concentration and consequently gain control of the polymerization, rather low equilibrium constant K_{eq} is required. The resulting high concentration of the dormant species (P_n-X) and a low concentration of the highly reactive radical species ($P_n^{\bullet}$) allow the suppression of the termination reaction.[68,69] The transition metal (Mt^n / L) is applied for the homolytic dissociation of the bond between the halogen and the alkyl moiety. The employed metal must possess the ability to expand the coordination sphere and change the oxidation number. A variety of metals have been found to be suitable for ATRP such as Mo,[70] Fe,[71] Ni,[72] and Cu.[73] The corresponding nitrogen containing ligands (L) are required in order to stabilize the low oxidation state of the metal complex. Furthermore, by changing the structure of the ligand, the kinetics of the polymerization can be affected. The linkage between the nitrogen atoms, the topology and the nature of the *N*-ligand can decrease or increase the value of k_{act} several orders of magnitude (refer to Figure 2).[74] Alternative ways to influence the activation rate is provided by substitution of the initiator species (primary < secondary < tertiary) or the corresponding halide leaving group (Cl < Br < I). Importantly the K_{eq} values of conventional monomers are less dependent on the steric effects as in the case for NMP or RAFT. The equilibrium constants for each monomer under given reaction conditions are a major factor, if block copolymers preparation *via* chain extending ATRP is targeted.[75,76] Generally, the monomer with the higher K_{eq} value should be polymerized first and chain

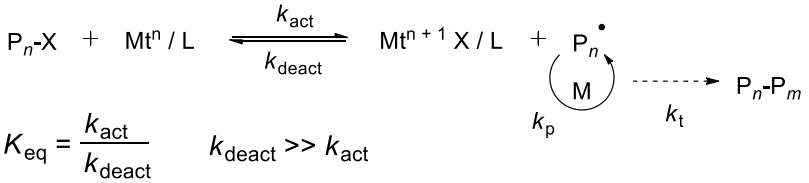

Scheme 4 Basic mechanism of ATRP. Redox equilibrium of the halogenated alkyl species (P_n-X) and reduced transition metal (Mt^n / L) vs. propagating chain $P_n^{\bullet}$ and oxidized transition metal (Mt^n X / L). K_{eq}, k_{act}, k_{deact} are the equilibrium constant, activation rate coefficient and the deactivation rate coefficient respectively. k_p is the propagating rate coefficient.[77]

extended with the monomer with lower K_{eq} value, e.g. poly(methyl methacrylate) should be applied as a macroinitiator for polymerization of poly(*n*-butyl acrylate). To overcome the 'order limitation', halogen exchange reactivity of the macroinitiator can be decreased by a halogen exchange reaction e.g. from Br to Cl.[78-80] Consequently, the order of monomers can be switched starting with *n*-BA and extending with MMA. The decreased K_{eq} value of the chloride end capped poly(*n*-butyl acrylate) macroinitiator leads to an increased initiator efficiency by slowing the reactivation process with respect to the propagation rate. Therefore, all chains start to grow nearly simultaneously, providing good control over the polymerization reaction and low polydispersities.[81]

Activators regenerated by electron transfer (ARGET) ATRP is an advanced methodology for controlling a radical polymerization. Compared to conventional ATRP, the process is more robust towards oxidation and thus requires significantly reduced amounts of the metal catalyst.[82,83] The key feature of the ARGET ATRP is an excess of a reducing agent such as hydrazine or Sn^{II}, allowing for the continuous reduction of Cu^{II} to Cu^{I} throughout the polymerization. Therefore, only minor amounts of Cu (in ppm range) are required for the polymerization of acrylates,[84]

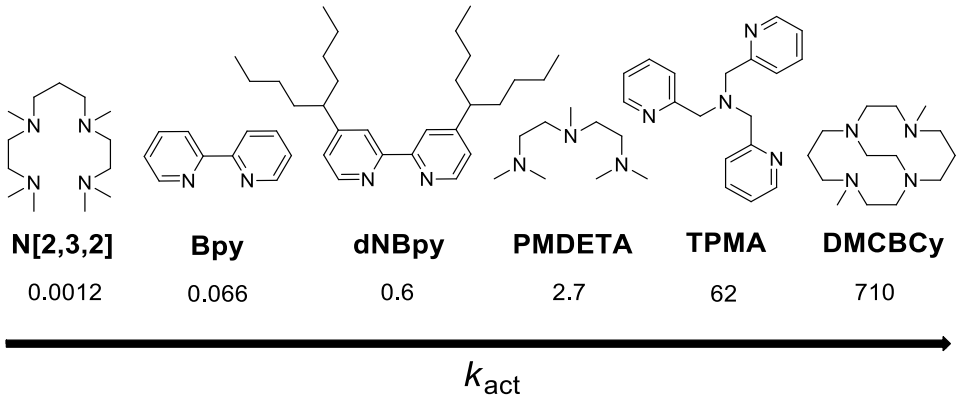

Figure 2 Activation rate coefficients in $M^{-1} \cdot s^{-1}$ for a range of *N*-ligands employed in a polymerization under ATRP conditions (initiator: ethyl-2-bromoisobutyrate, catalyst: $Cu^{I}Br$, solvent MeCN).[74]

methacrylates[85] and styrene[86] or formation of block copolymers.[87,88] Overall ATRP is a powerful technique for the synthesis of defined macromolecular architectures.[89] The advantages of the strategy are the commercial availability of the conventional reagents such as initiators, ligands and the metal catalysts. Although not as versatile as RAFT, ATRP can be applied for a wide range of monomers and solvents. Similar to RAFT, the Trommsdorf effect is not present and a variety of end groups can be introduced *via* functional ATRP initiators or through conversion of the halide species.[90] Polymer electrolysis was reported as an efficient methodology for Cu removal.[91] The novel strategy can potentially provide a long sought solution for a major disadvantage of the ATRP: contamination with metal catalyst such as Cu. Furthermore, ion exchange resins have been also applied for the copper removal.[92]

2.1.2.3 Nitroxide-Mediated Polymerization (NMP)

A reversible reaction between the propagating radical and a dormant species is the key feature of NMP. Thus, alkoxyamines are used as initiator / controlling agent, as they feature a labile C-O bond. Exposed to heat[93] or light[94] the homolysis of the single bond occurs. The resulting carbon centered radicals initiate macromolecular growth. The formed persistent nitroxide radical can then reform the dormant species by undergoing a reversible termination reaction with the propagating chains. In an alternative approach, a combination of a radical initiator and free electron containing TEMPO derivatives can be employed. The equilibrium constants for NMP are close to $1.5 \cdot 10^{-11}$ M (120 °C, styrene)[95] allowing the suppression of the termination reaction between the propagating chains by decreasing the overall radical concentration (refer to Scheme 5). In order to achieve good control over the polymerization process, the mediating species / initiation system needs to be chosen with respect to

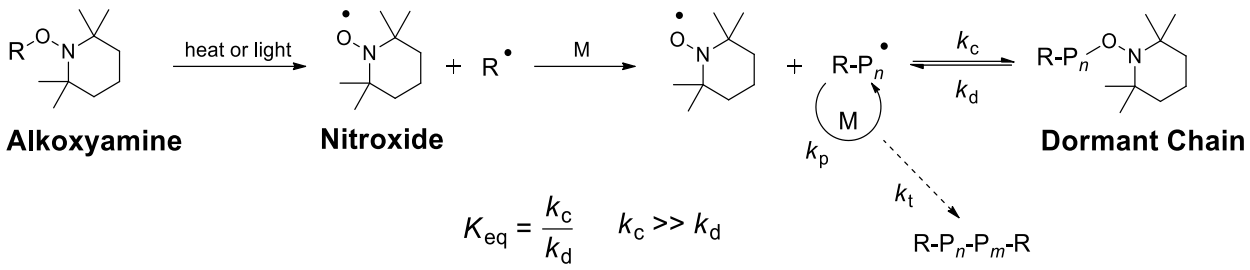

Scheme 5 Basic mechanism of the NMP. Light or heat induced homolysis of the alkoxyamine, in order to form a nitroxide and a carbon centered radical (R•). Polymerization process induced by the carbon centered radical (R•) with nitroxide as the mediating species. K_{eq}, k_c, k_d are the equilibrium constant, association rate coefficient and the dissociating rate coefficient respectively. k_p is the propagating rate coefficient.

the polymerized monomer. The relatively stable C-O bond of TEMPO provides lower equilibrium constants and is well suitable for synthesis of polystyrene. However, elevated temperatures are required for efficient polymerization control for more reactive monomers, as the stability of the C-O bond decreases when exposed to higher temperatures. To avoid higher polymerization temperatures often leading to side reactions, bulky substituents can be introduced into the TEMPO derivative. The resulting steric effects decrease the dissociation energy for the C-O bond cleavage, allowing the controlled polymerization of more reactive monomers such as butyl acrylate at temperatures lower than 70 °C.[96,97] One example of a sterically hindered TEMPO species is the *trans*-2,6-diethyl-2,6-bis(1-trimethylsilanoxyethyl)-1-(1-phenylethoxy)piperidine-N-oxyl (TEMPO-TMS) (refer to Scheme 6), whereby bulky TMS substituents are introduced into the core structure of the nitroxide in order to ease the homolysis of the C-O bond. However, the introduction of functional groups should be carried out with caution, as too bulky substituents can decrease the controlling performance of the TEMPO.[96]

In order to increase the labile nature of the C-O bond, nitroxides with H atom attached to the α-carbon such as DEPN or TIPNO have been synthesized.[98-100] Initially both derivatives were considered to be unstable under polymerization conditions, due to the potential abstraction of the H

atom, α to the nitroxide moiety. However, employed as mediating species DPN and TIPNO derivatives provide efficient control of the polymerization for styrene and other monomers at lower temperatures. It should be mentioned that other organic molecules containing a stable, free radical species can also be employed to gain control over a radical polymerization such as triazolinyl,[101] boronate,[102] and (arylazo)oxy[103] species. In addition, transition metals such as Mo[104] and Os[105] can be applied. The disadvantages of the NMP technique are the rather high temperatures required, difficulty to control the polymerization of disubstituted alkenes, and the high costs of the initiator species. However, NMP is suitable for a variety of monomers including those with acidic functional groups and allows for the synthesis of macro molecules employing organic compounds only.[32]

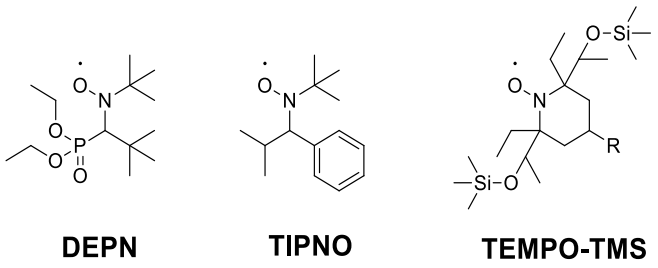

Scheme 6 Structures of DEPN, TIPNO and TEMPO-TMS.

2.2 Chemistry of Profluorescent Nitroxides

2.2.1 Concept

Due to their stable unpaired electron, nitroxides possess unique physical and chemical properties, and continue to find applications in the fields of biology, polymer and material science.[106] The first organic nitroxides were invented and studied by Piloty and Schwerin,[107] as well as by Wieland and Offenbacher[108] in the first two decades of 20th century. In 1959, Lebedev and Kazarnovsky introduced the 4-oxo-2,2,6,6-tertramethylpiperidine-*N*-oxyl radical, which was later converted to 2,2,6,6-Tetramethylpiperidin-1-yl)oxyl (TEMPO).[109,110] Their stability as a free radical species can be attributed to the delocalisation of the single electron between the oxygen and the nitrogen atoms (refer to Scheme 7), whereby steric hindrance can also have a contribution.[111] Although the nitroxide is an established reactive centre for a range of chemical reactions, it is not available for recombination with other nitroxide species. The stabilization of two free radical species *via* the delocalisation process (ca. 130 kJ · mol^{-1} x 2) is higher than the energy gained through recombination of two nitroxide species and formation of one O-O bond (140 kJ · mol^{-1}).[112-114] However, depending on the structure of the nitroxide, recombination of two nitroxides can occur *via* an alternative pathway. If a phenyl ring is attached in the α-position to the nitroxide, the delocalisation of the single electron by the aromatic system occurs, which should suggest an increase of the stability of the radical species. However, the resulting carbon centered radicals are highly reactive and can recombine with oxygen centered radicals, leading to the formation

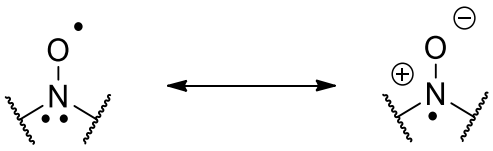

Scheme 7 Delocalisation of the single electron of the nitroxide.

of non-radical site products (refer to Scheme 8).[112] In addition, nitroxide species featuring hydrogen atoms in close proximity such as β-hydrogen are sensitive to disproportionation reactions. Through a hydrogen atom abstraction by an oxygen centered radical, a hydroxylamine and a nitrone can be formed (refer to Scheme 8).[112] Among other nitroxide species including derivatives featuring heteroatoms or unsaturated nitroxides, the 2,2,5,5-tetramethylpyrrolidine-1-yloxyl (PROXYL), the corresponding phenyl ring fused 1,1,3,3-tetramethylisoindoline-2-yloxyl (TMIO), and TEMPO possess remarkably robust structure.[115] Especially TMIO provides excellent stability towards ring opening reactions of the nitroxide moiety, e.g. the photoinduced radical cleavage of the N-C bond of the nitroxide (refer to Scheme 9).[116] The aromatic ring of the isoindoline core structure provides significant rigidity to the fused five membered ring, allowing efficient recyclisation reaction. The photostability of the nitroxides plays a key role for their application as profluorescent nitroxides (PFNs).

PFNs are hybrid species featuring a stable nitroxide covalently attached to a fluorophore.[117] Due to the fluorescence quenching ability of the nitroxide, the PFNs found various applications as sensor materials for monitoring

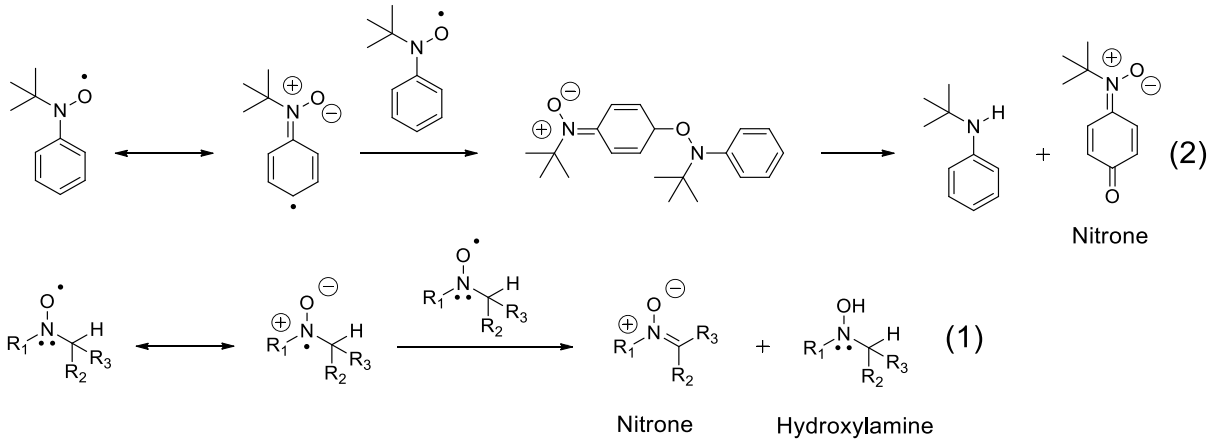

Scheme 8 Side reactions of the nitroxide species. (1) Recombination of nitroxide derivative featuring a phenyl ring in α-position. (2) Hydrogen abstraction reaction of nitroxide derivative featuring a hydrogen atom in β-position.

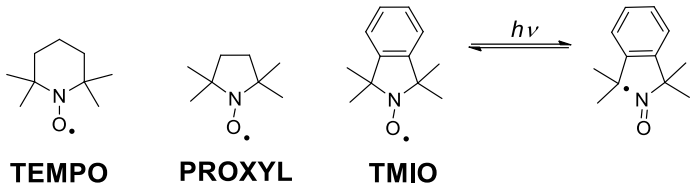

Scheme 9 Structures of TEMPO, PROXYL and TMIO. Photoinduced cleavage of the C-N bond and recyclisation of TMIO.

radical or redox processes.[118] First described by Stryer,[119] the pioneering work on PFNs was carried on by Bystryak[120] and Blough,[121-123] who both demonstrated the great potential of this unique compound class. The sensor mechanism of the PFNs relies on the fluorescence quenching ability of the nitroxide, caused by its paramagnetic nature. Located in close proximity to a fluorophore, the nitroxide moiety suppresses the emission of the chromophore.[117] However, through a conversion of the single electron in a chemical reaction such as reduction, oxidation or a radical termination, the nitroxide loses the quenching ability as it becomes diamagnetic. Consequently, the fluorescence becomes visible (refer to Figure 3).[118] The fluorescence quenching can occur intramoleculary and intermoleculary,[124-127] whereby the distance between the nitroxide and the emitting species is crucial for the quenching performance. Furthermore, the stability of the non-radical species formed should be considered, as some redox reactions of the nitroxide species are reversible. The resulting equilibrium between the nitroxide and the corresponding non-radical derivative can potentially negate the quenching performance. Generally, close proximity of the nitroxide and the fluorophore are required in order to achieve efficient fluorescence quenching. The electronical transitions in a fluorophore molecule are illustrated in the Figure 3. In a typical fluorescence process, an electron transfers from the singlet ground state of the fluorophore (S_0) to a vibrational level of an excited singlet state. Subsequent energy release

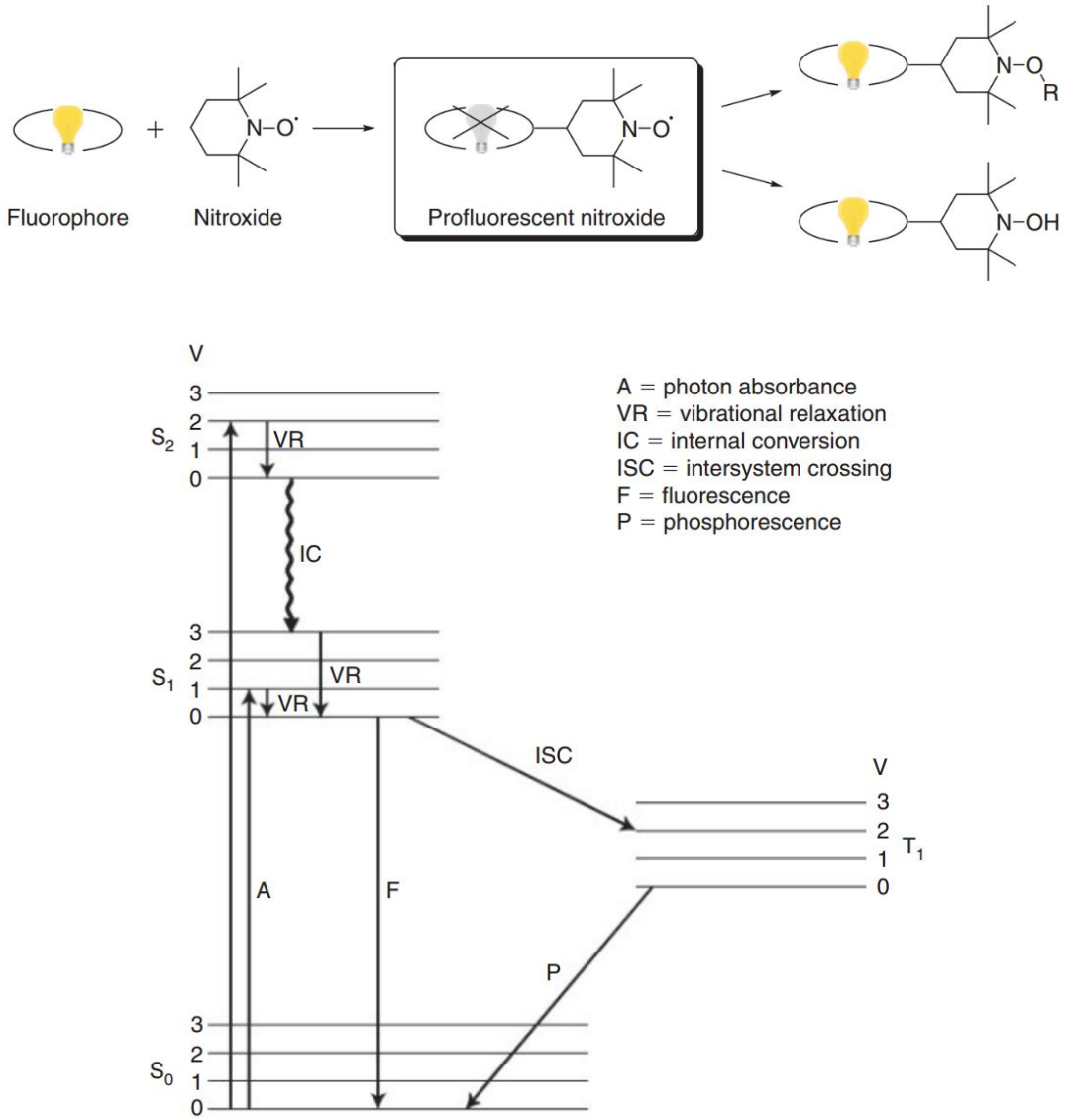

Figure 3 Schematic illustration of coupling of the nitroxide species (TEMPO) with a fluorophore, resulting in fluorescence quenching and the subsequent conversion of the nitroxide in a radical recombination or reduction reaction leading to recreation of the fluorescence (top). Jablonski diagram of photoinduced electronic transitions resulting in fluorescence or phosphorescence (bottom).[118] Reproduced from Blinco et al. (2011), with permission from CSIRO Publishing.

through vibrational relaxation and internal conversion allows the electron to reach the lowest excited singlet state (S_1). In case the energetic gap between the S_0 and S_1 states is small, the electron can return to the ground state by releasing the energy in an internal conversion process. However, in case of a fluorophore two other possible pathways for returning to the ground state exist. The first path involves fluorescence as an energy release

mechanism, whereby the excited electron reaches rapidly the ground state through the emission of light. The second pathway proceeds through an intersystem crossing process. Thus, the spin angular momentum of the electron changes, leading to the transition to a triplet state (T_1). The described transition is spin forbidden as only electronical transitions between states of the same spin multiplicity are allowed. However, depending on the structure of the excited molecule and the atoms involved, there is a finite probability of an intersystem crossing (ISC). In contrast to the S_1 state, the T_1 state has a significantly longer living time, as the transition to the S_0 is spin forbidden. Therefore, the energy release though the emission (phosphorescence) proceeds on a longer time scale compared to the fluorescence, enabling non-radiative release of the major part of the energy through an internal conversion process. Consequently, increased ISC ability of the fluorophore results in fluorescence quenching.[117] Nitroxides are able to increase the transition probability from S_1 to a T_1 state of the fluorophore. Given a close proximity of the unpaired electron of the nitroxide and the conjugated system of the fluorophore, an interaction between both moieties occurs, leading to

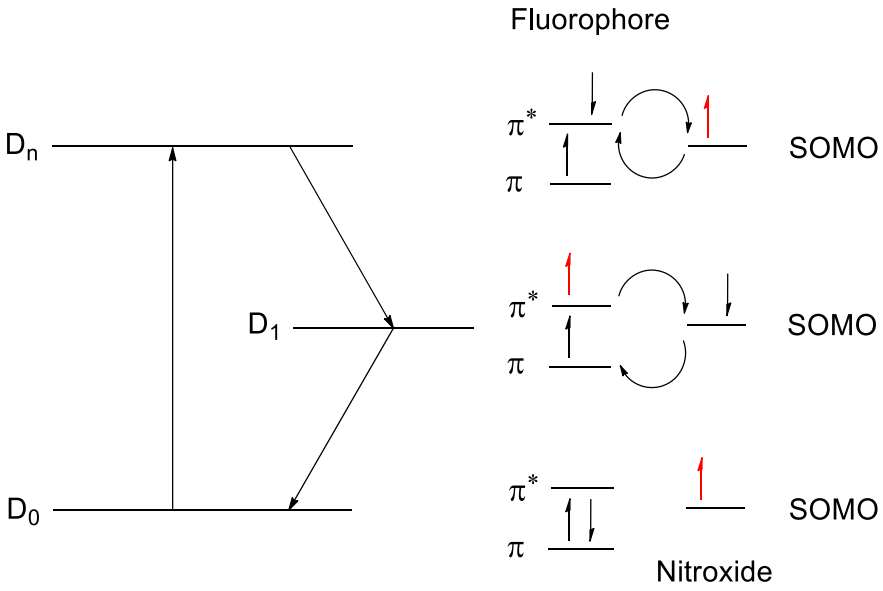

Figure 4 The mechanism of the electron exchange between D_n and D_1 and between D_1 and D_0.[118]

a change in the spin multiplicity. Consequently, the singlet ground state S_0 and the lowest single excited state S_1 become doublet states D_0 and D_n, respectively, due to the spin contribution of the single electron of the nitroxide (refer to Figure 4). The triplet state T_1 becomes D_1. In contrast to the singlet states, the transition between D_n and D_1 (S_1 and T_1 for the single states respectively) becomes a spin allowed transition, enabling efficient fluorescence quenching. Thus, electron exchange processes between the nitroxide and the fluorophore are suggested to be the major path for decreasing the fluorescence quantum yield.[117]

2.2.2 Synthesis

The design of the profluorescent nitroxides has been driven by two major factors. First to be considered is the distance between the nitroxide and the fluorophore, as close proximity of both species enables efficient fluorescence quenching. The second consideration applies to the stability of the PFN. The linkage unit between the nitroxide and the fluorophore is a key feature, ensuring short distance between the nitroxide and the fluorophore. The cleavage of the covalent connection between both moieties would negate the quenching performance.[128] Therefore, the connection of commercially available nitroxides and fluorophores *via* esterification,[122,123,129-134] amidation,[135-137] or sulfonamidation[138-140] employed in the early stages of the PFN research are less suitable for efficient PFNs (refer to Scheme 10). The resulting compounds contain long, hydrolysis sensitive linkages. Consequently the fluorescence quenching is rather low ranging between 2- to 30-fold. Furthermore, the potential cleavage of the linkage will negate the quenching performance even further, due to the resulting space separation between the nitroxide and the fluorophore.

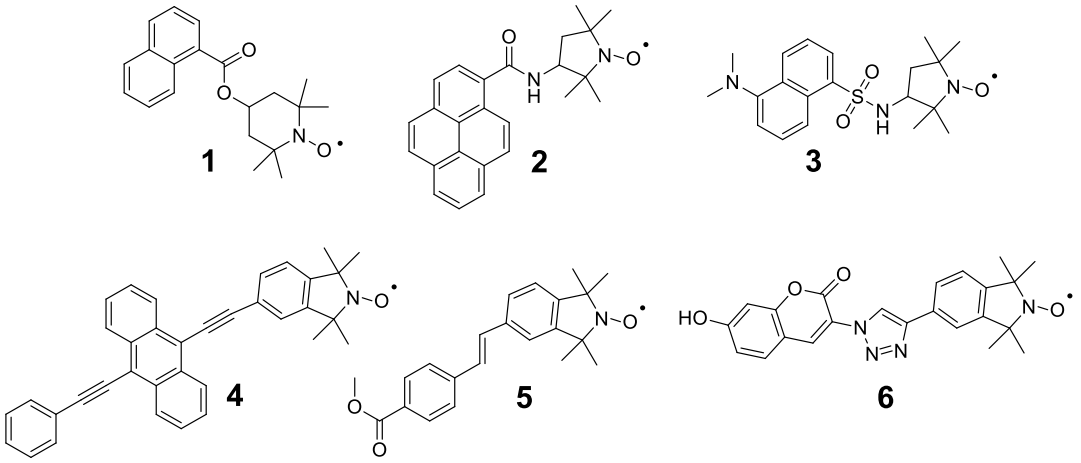

Scheme 10 Structures of hydrolysis sensitive PFNs **1**-**3**, synthesized *via* esterification (**1**), amidation (**2**), and sulfonamidation (**3**). Structures of robust PFNs **4**-**6** featuring carbon linkage between the nitroxide and the fluorophore.[118]

An alternative route for the synthesis of PFNs is provided by metal catalysed cross coupling reactions or cycloadditions. The strategy relies on halogenated or alkyne functionalized nitroxide derivatives coupled with commercially available fluorophores *via* Heck,[141,142] Songashira[142,143] and Suzuki[143-146] coupling, as well as copper mediated 1,3-dipolar cycloaddition[147] (refer to Scheme 10). The straight-forward coupling approach was applied for synthesis of a wide range of PFNs, whereby their photophysical properties and solubility could be tuned according to the requirements of the targeted application. It should be noted, that compound **6**, as well as the corresponding non radical derivatives, synthesized *via* copper mediated 1,3-dipolar cycloaddition, possess pH-dependent photophysical properties. Higher absorption and fluorescence emissions were observed in basic solutions, providing an additional sensor feature for the monitoring of pH values. However, the metal catalysed methodologies for the synthesis of PFNs are challenging due to the demanding synthetic routs applied.[147] Furthermore, the use of metals is a major drawback for *in vivo* applications.[148] Finally, all presented strategies do not allow *in situ* formation of the PFN, which could potentially facilitate their application in the field of biology and as a tool for surface modifications.

2.2.3 Applications

PFNs are efficient sensor materials for detection of redox/radical processes. Many of the limitations, present in the beginnings of the concept, have been overcome by novel synthetic routes for a variety of robust PFNs with efficient quenching performance and a broad range of absorption and fluorescence wavelengths (refer to Section 2.2.2). The advantages of the later generation of PFNs facilitated their utilization in various scientific fields. Due to their good compatibility with biological systems, PFNs have found application as *in vivo* redox process sensors. Blough and Simpson were among the pioneers to demonstrate the sensitivity of PFNs towards biologically relevant ascorbate.[123] By application of the methodology to several fruit juices, the quenching performance was found to be dependent on the concentration of the ascorbic acid.[149] Furthermore, the presence of

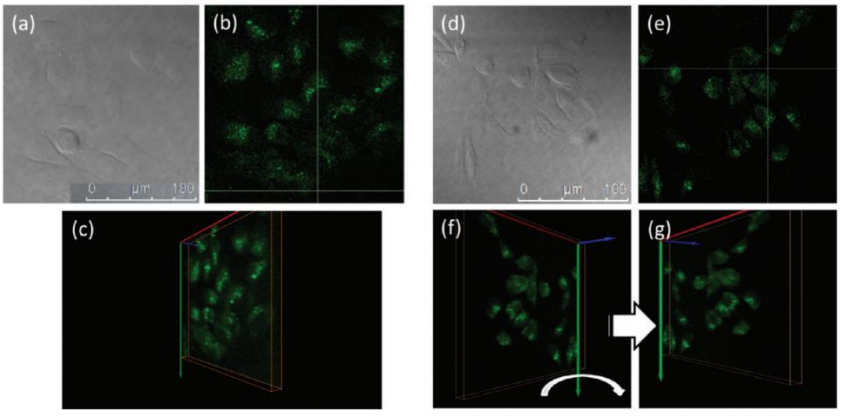

Figure 5 Two-photon fluorescence microscopy images from femtosecond excitation at 900 nm of Chinese hamster ovary CHO cells incubated with **4** and H_2O_2 of (a) differential interference contrast (DIC), (b) one 2PFM XY optical slice, (c) 2PFM 3D reconstructed image, and incubated with **7** and H_2O_2: (d) DIC, (e) one 2PFM XY optical slice, (f and g) 2PFM 3D reconstructed image.[150] This is an unofficial adaptation of an article that appeared in an ACS publication. ACS has not endorsed the content of this adaptation or the context of its use.

larger protein molecules was demonstrated to increase the reduction rate of the PFN.[151] More advanced systems such as whole-blood samples were investigated towards their antioxidant capacity by employing PFNs as the sensor species.[152] An elegant example of *in vivo* application of the profluorescent nitroxides is the work of Belfield and co-workers. Here, compounds **4** and **7** were applied for monitoring reactive oxygen species (ROS) damage in Chinese hamster ovary (CHO) cells. Both species were demonstrated to be non-toxic to the living system applied. In addition, two photon absorption was shown to be suitable for the PFN approach (refer to Figure 5).[150]

One of the most established application of the PFNs in material science is their use as radical sensors in polymer degradation studies. A variety of different approaches have been reported in solution and solid state, demonstrating the efficiency of the methodology.[153-156] Real time monitoring *via* fluorescence spectroscopy of a solid PMMA matrixes doped with PFN and a photo initiator were performed while exposing the polymer film to UV light in presence of a photo-mask. Spatial resolutions in a range of 10 µm were accomplished by this approach. Importantly, the photo-stability of the applied chromophore plays a major role for the effective

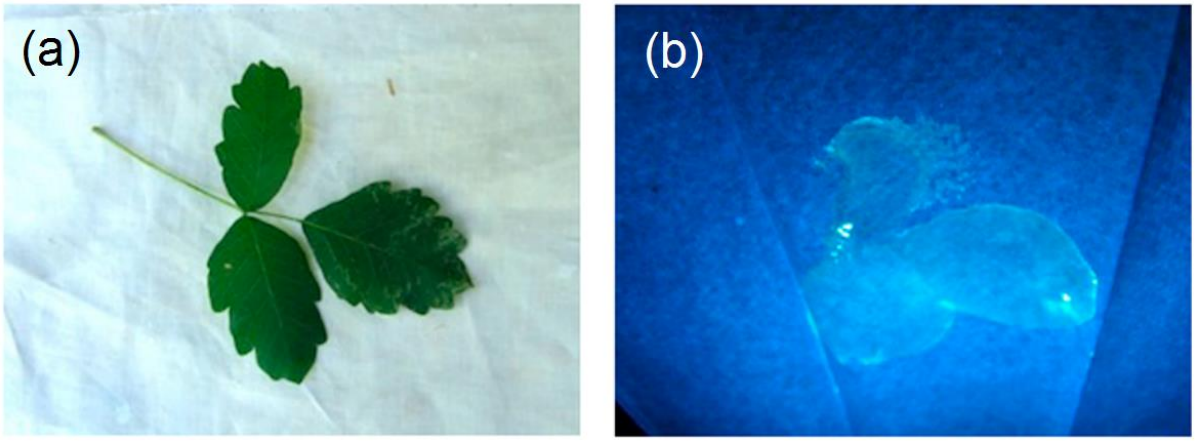

Figure 6 Poison oak leaves (a), fluorescense image of the same leaves after exposure to an acetone mixture of TEMPO functional PFN and *B*-*n*-butylboronic acid (λ_{ex} = 365 nm) (b). Reprinted with permission from [157]. Copyright 2016 American Chemical Society.

monitoring of light induced degradation processes.[158] Thermal polymer degradation has also been investigated extensively, including studies on initiator free,[128] as well as AIBN[159] and peroxide[144] doped polymer samples. Thereby, not only initial formation of radicals, but also the secondary radical damage was detected.[144]

An alternative application for the PFNs is the monitoring of ROS in particulate matter in order to quantify their toxicity. A variety of studies were undertaken including investigations of cigarette smoke[33] as well as diesel biodiesel particulate matter[160] and biomasses.[161] Thus, PFNs were demonstrated to be extremely sensitive detecting nmol amounts of radical species.[162] An interesting approach towards detection of minute amounts of toxic urushiol was reported by Braslau and co-workers.[157] The method allows rapid and efficient, radical induced detection of catechols in the presence *B*-*n*-butylboronic acid and a suitable PFN (refer to Figure 6).

2.3 Photochemistry

2.3.1 Theoretical Concept

All light induced transformations follow the basic principles of photophysics and photochemistry. The two essential rules in photochemistry concept are:[10]

1. Photochemical transformation (such as isomerisation or chemical reaction) of a molecule or an atom can only occur if light is absorbed.
2. One molecule can absorb only one photon at a time.

The second rule is applicable to a large part of the photoinduced processes. However, if high intensity irradiation sources are employed, multiphoton absorption is possible (refer to Section 2.3.3). To fulfil the basic requirement of photochemistry, namely the absorption of light, a suitable irradiation wavelength should be chosen. The ability of the molecule to absorb only defined amounts of energy can be explained by quantum mechanics. The energetic state of a molecule can be described by the Schrödinger equation. Assuming the nuclear motion is much slower than the electron motion, the Schrödinger equation can be simplified and solved, providing an infinite number of wavefunctions describing the energy states of the molecule. However, only some solutions are physically acceptable. Therefore, the energy of different molecular states is defined, or in other words quantized. The energy quantisation of molecular states is a key feature in photochemistry, as a excitation of a molecule can be achieved by applying appropriate irradiation wavelengths only. In addition, the selection rules for electronic transitions are to consider:[163]

1. Only transitions between states with the same spin multiplicity are allowed (spin selection rule).
2. Only transitions between states featuring a change in the parity are allowed (symmetry selection rule).

It should be noted, that both rules do not apply strictly. Parity forbidden transitions can occur due to the vibronic coupling, whereby the vibration of the molecule affects its symmetry. Spin forbidden transitions can be addressed to spin-orbit coupling occurring. However, the forbidden electronic transitions display much lower intensities compared to the allowed electronic transitions.[10] The macroscopic description of the light absorption is given by the Beer-Lambert Law (refer to Figure 7). A linear correlation between the absorbance and the concentration of the sample is expected for monochromatic light and a homogeneous sample. The absorbance strength of the molecule at a given wavelength is described by the molar extinction coefficient ε, being the joint between the quantum mechanical calculations and the macroscopic observations. Rather low ε values are observed for forbidden electronic transitions, while higher ε values can be expected for allowed electronic transitions.[163]

In case the appropriate wavelength is applied, the absorbed energy cause an electronic transition in the molecule, whereby an electron is promoted from a lower energy orbital to a higher energy orbital according to the

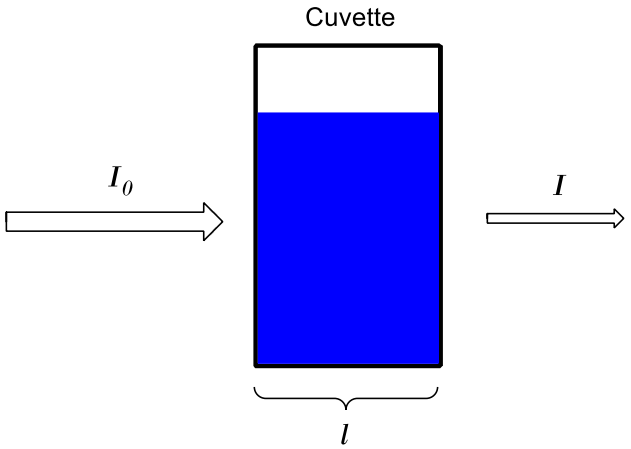

Figure 7 Schematic illustration of the Beer-Lambert Law. A is the absorbance; I_0 and I are the light intensities before and after the absorption; ε and c are the molar extinction coefficient and the concentration of the given species, respectively; l is the length of the absorption path.

transition rules. A variety of transitions are possible. A short overview over selected electronic transitions involving σ, π, anti-bonding σ^*, π^* and non-bonding n orbitals is presented below:[164]

$\sigma \rightarrow \sigma^*$ Mostly occur for saturated hydrocarbons and possesses rather lower excitation wavelengths (100 – 200 nm).

$n \rightarrow \pi^*$ Occur for unsaturated molecules featuring a free electron pair(s) located in the non-bonding orbital n of a heteroatom (e.g. N, O, S). Typically, the transition requires excitation above 270 nm. However, a red shift of the absorption can be achieved by extending the conjugated π system. Importantly, the transition is quantum mechanically 'forbidden', resulting in rather low molar extinction coefficients (ε < 20 L · mol^{-1} · cm^{-1}).

$\pi \rightarrow \pi^*$ Present in molecules with π electrons being involved into the conjugation system e.g. aromatic derivatives. With expansion of the conjugated system, a bathochromic shift of the absorbance can be achieved. Molar extinction coefficients are high, with values up to 10^5 L · mol^{-1} · cm^{-1}).

Typically, a variety of transitions can be observed in the absorbance spectrum of a molecule. The resulting spectrum shape can be explained by the Frank-Condon Principe (refer to Figure 8). The key feature of the concept is the approximation that electron motions appear on a much shorter time scale than the nuclear motions. Therefore, the electronic transitions can be considered to occur at fixed nuclear coordinates between the ground state and the excited state vertically above (illustrated by the vertical arrow). Importantly, the vibronic ground level is the most populated level in the ground state due to the Boltzmann distribution function. Consequently, it is the starting point for the electronic transition. The intensity of each transition can be referred to the integral overlap of

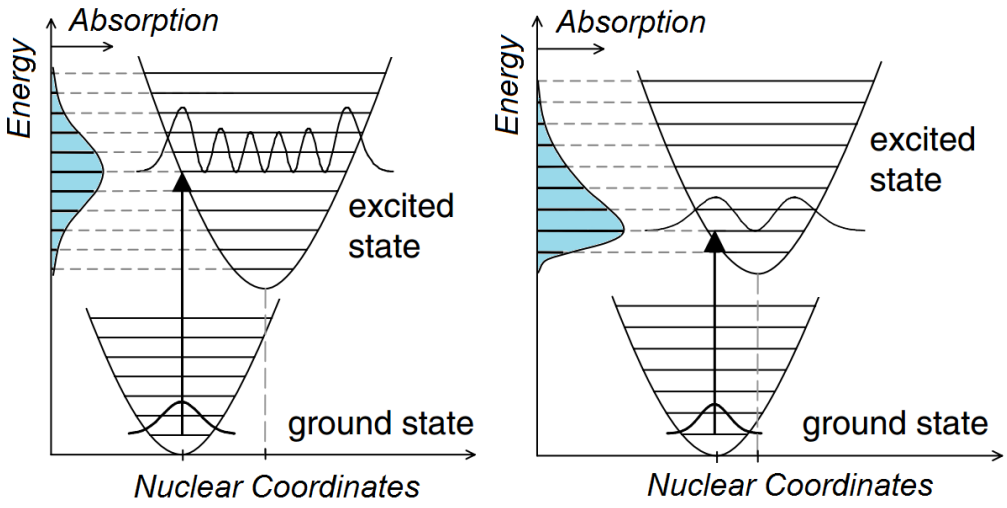

Figure 8 Illustration of the Frank-Condon principle. The arrow visualizes the transition from the ground state to an excited state, whereby the vibration sublevels with the corresponding wave functions are depicted in the potential curves. The resulting absorbance is illustrated in blue.[165] Reused with the permission by IOP.

both wave functions involved. Maximum overlap leads to the maximum absorption intensity, while a poor overlap results in a low absorption intensity. The transition occurs preferably from the most likely location of the electron in the energetic ground state to the most likely location of the electron in the excited state. [10]

Several deactivation mechanisms are available for the excited molecule in order to return to the ground state, including radiatiative and non-radiative deactivation. Radiative deactivation occurs *via* fluorescence or phosphorescence. In case of fluorescence, the excited molecule transits to the ground vibration level of the excited electronic state S_1 *via* vibrational relaxation. Subsequently, a spontaneous emission of the energy, known as fluorescence, occurs, resulting in returning of the electron to the ground state. Similar to the absorption, the fluorescence follows the Frank- Condon principle. The wavelength of the emission is higher than the wavelength of the excitation (Stokes shift), as a part of the absorbed energy is dissipated through the vibrational relaxation. An alternative deactivation process is

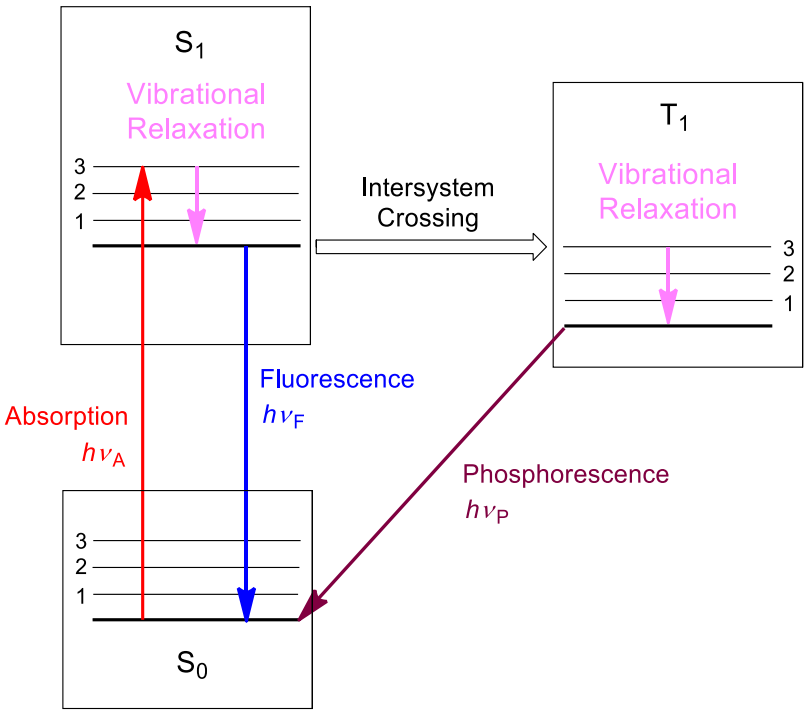

Figure 9 Radiative deactivation of an excited state illustrated by a Jablonski diagram. S_0, S_1 and T_1 represent the singlet ground state, excited singlet state and the triplet state respectively.

the phosphorescence, whereby the molecule in the excited singlet state S_1 undergoes an intersystem crossing to the triplet state (T_1). The transition from S_1 to T_1 is formally forbidden (spin electron rule), however, it occurs to a minor degree, if spin-orbital coupling is efficient. After vibrational relaxation to the lowest T_1 vibronic state, the radiative deactivation back to the singlet ground state, known as phosphorescence, can appear. In contrast to the fluorescence, which occurs on nanoseconds scale, the phosphorescence can have a life time up to seconds. This can be addressed to the fact, that the transition from the T_1 to the S_0 state is also spin forbidden.[10,164]

Apart from the radiative deactivation, non-radiative processes lead to the return to the ground single state, such as internal conversion. Furthermore, chemical processes involving the excited states can occur, resulting in relaxation of the molecule to the ground state with or without a change of its chemical structure. Importantly, the molecule in the excited state

possesses a different electronic structure compared to the ground state and should be considered as a new compound with its own specific reactivity. The photo induced chemical reactions often have low or no activation energy and proceed at high reaction rates, as they compete with over deactivation processes (refer to Figure 10).[10] An example of a mechanism of a photo induced chemical transformation is given in the next section.

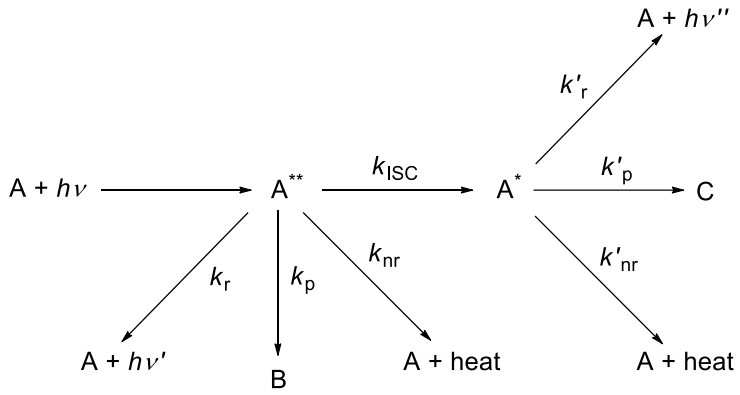

A	Molecule in the singlet ground state	k_{ISC}	Intersystem crossing rate coefficient
B, C	Molecules formed in a chemical reaction	k_p, k'_p	Chemical reaction rate coefficients
A^{**}	Molecule in the excited singlet state	k_r, k'_r	Radiative deactivation rate coefficients
A^{*}	Molecule in the triplet state	k_{nr}, k'_{nr}	Non-radiative deactivation rate coefficients

Figure 10 Schematic illustration of the deactivation processes of an excited molecule.[10] Reproduced with permission of WILEY-VCH Verlag.

2.3.2 Modern Photoinduced Conjugation Reactions

2.3.2.1 Photoenolisation of *o*-Methylphenylcarbonyl Compounds

Tchir and Porter were among the pioneers in the field of photoenol chemistry. Based on laser flash photolysis experiments of 2,4-dimethyl benzophenone, they suggested a mechanism for the photo induced Diels-Alder reaction.[166] Importantly, the term photo induced refers to the formation of the reactive *o*-quinodimethanes (photoenol), as 'photo-Diels-Alder' reactions are forbidden due to the Woodward–Hoffmann rules. UV irradiation of an *o*-methylphenyl ketone or aldehyde **a** leads to an electronic n-π^* transition and subsequent ISC to form excited species **b** (refer to Scheme 11). The short lived species **b** undergoes an H-abstraction to afford the radical intermediate **c** (τ = 67 ns). Two stereoisomers (**c**, **f**) are generated, due to intramolecular rotation of the formed species. Both derivatives undergo a rapid rearrangement to afford the corresponding *o*-quinodimethanes (**d**, **g**). While derivative **g** rearranges to the reagent **a**, the relatively long living species **d** (τ = 250 s) takes part in a Diels-Alder reaction in the presence of a dienophile to the cycloadduct **e**. The photoenol

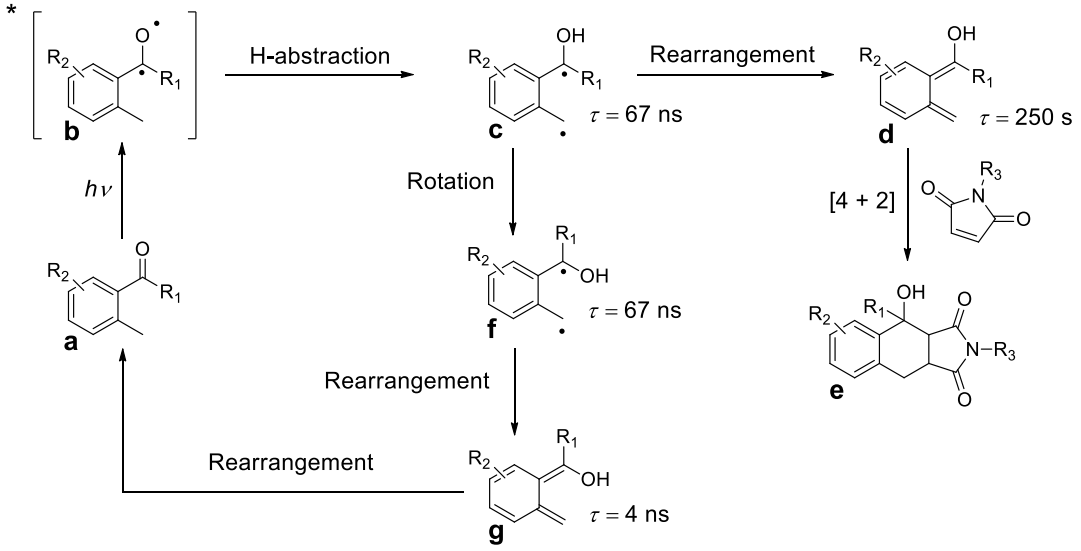

Scheme 11 Basic mechanism of the photoinduced formation of the photoenol (*o*-quinodimethanes) and the subsequent conversion of the formed intermediate in a Diels-Alder reaction.[167]

ligation strategy provides an efficient, rapid and catalyst free method for the design of macromolecular structures and the modification of surfaces.[18,168-171] In contrast to the majority of Diels-Alder reactions, the photoenol cycloaddition is irreversible. Depending on the structure of the *o*-methylphenyl carbonyl species, dienophiles with different electron densities can be employed. While highly electron deficient alkene derivatives such as maleimides are required for an efficient conjugation with *o*-methyl benzophenone derivatives,[166] *o*-methyl benzaldehyde can be accessed with acrylates,[172,173] acrylonitrile[174] and C-S double bonds.[175] The difference in the reactivity was recently utilised by Barner-Kowollik and co-workers to form ABC-triblock copolymers.[172] An α,ω-functional polymer block (B), end capped with an acrylate and *o*-methyl benzaldehyde moiety respectively, was converted in two subsequent steps with a maleimide functional polymer block (A) and an *o*-methyl benzophenone functional polymer block (B). An alternative approach employing a photo active acyclic imine derivative allows cycloadduct formation with the electron rich furan double bond. Furthermore, the reported method allows for the preparation of the photo reactive precursor in two steps, compared

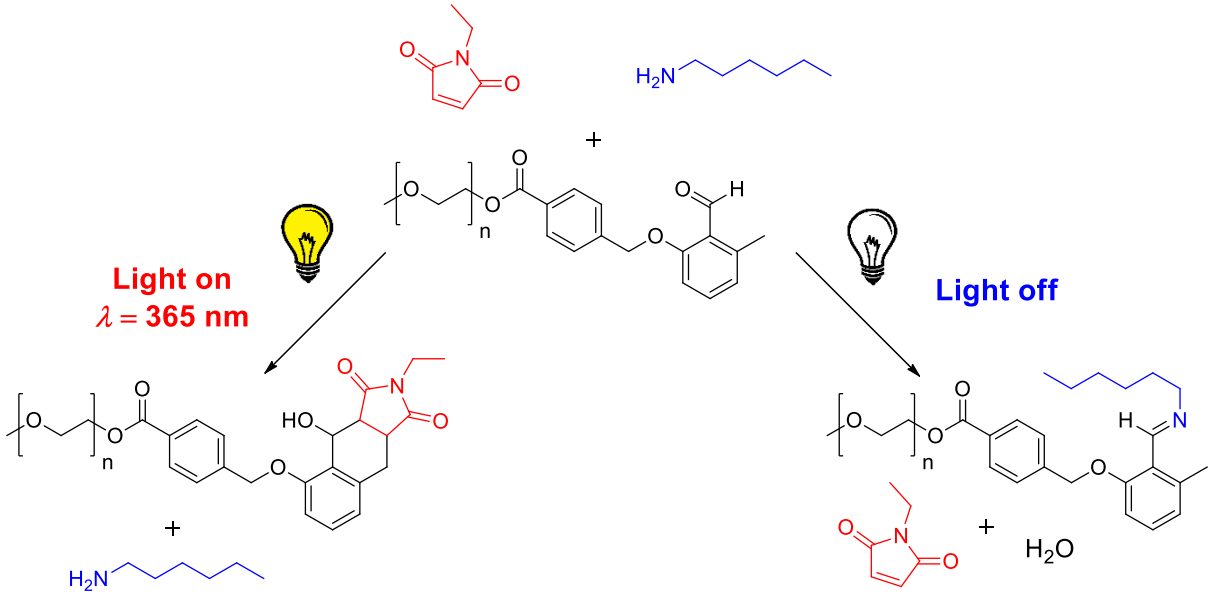

Scheme 12 Basic mechanism of the reaction channel control.[176]

to the four step linear synthesis required for the preparation of *o*-methyl benzaldehyde derivatives.[177] The photo induced reaction of the *o*-methyl benzaldehyde towards an alkene species can be suppressed, if an amine species is provided (refer to Scheme 12). Starting from a one pot system including the photo active species, a maleimide and an alkylamine, the cycloaddition can be triggered by light, while the imine formation takes places in the dark. The preference of a reaction channel is controlled by the amount of the ene compound.[176]

Photoenol chemistry provides an efficient and rapid coupling method. However, the preparation of the *o*-methyl benzaldehyde derivatives is challenging and requires four linear steps of synthesis. In addition, the cycloaddition reaction can be triggered by UV light only, as long a single photon excitation is applied.

2.3.2.2 Nitrile Imine-Mediated Tetrazole-Ene Cycloaddition (NITEC)

First discovered by Huisgen and co-workers forty years ago,[178] the NITEC reaction has recently been applied to a number of fields e.g. as a linker molecule in polymer science,[179-181] as a fluorescence marker for biological applications,[13,14,182] as well as for surface modifications.[183-186] NITEC is a two-step process. A photoinduced release of N_2 from the diaryl tetrazole occurs in the first step. Subsequent cycloaddition of the formed 1,3 dipole intermediate with a suitable dipolarophile takes place in the second step. The resulting cycloadduct displays strong fluorescence in a specific wavelength ranges, depending on the substituents of the diaryl tetrazole species.[187] The reaction is irreversible and occurs without the need of a

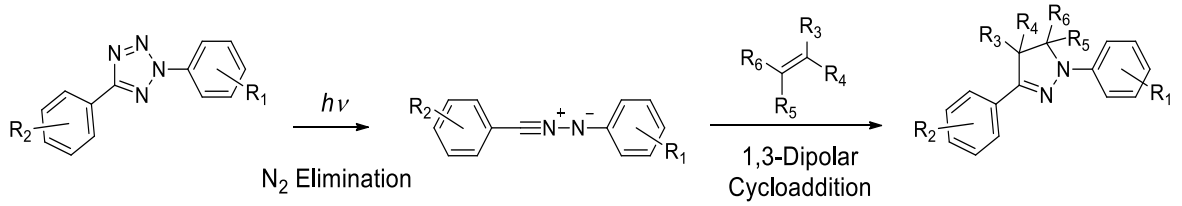

Scheme 13 Basic mechanism of the nitrile imine-mediated tetrazole-ene cycloaddition.[187]

catalyst. Full conversion of the reagents, rapid and exclusive formation of the desired cycloadduct can be achieved. One key factor for the success of the cycloaddition are the energy levels of the molecular orbitals involved. In Figure 11, the energy levels of the molecular orbitals of a nitrile imine and an olefin and their HOMO-LUMO interaction are displayed. Three reaction types should be considered. In the first reaction type, an interaction between the HOMO (highest occupied molecular orbital) of the nitrile imine and the LUMO (lowest unoccupied molecular orbital) of the dipolarophile (olefine) occurs. The resulting stabilisation ΔE_1 is significantly higher than the stabilisation ΔE_2. In the second reaction type an interaction between the LUMO of the nitrile imine and the HOMO of the dipolarophile (olefin) occurs. The resulting stabilisation ΔE_2 is significantly higher than the stabilisation ΔE_1. Both interactions are relevant for the third type of the reaction, where the stabilisation energies ΔE_1 and ΔE_2 are similar. Similar energies of the HOMO of the dipolarophile and LUMO of the ene species or *vice versa* are required to achieve an effective molecular orbitals interaction, leading to high ΔE and high reaction rates.[188] A large number of reactions of the *in situ* formed nitrile imine have been reported (refer to Scheme 14). Among the most prominent examples are the cycloadditions with alkenes, including electron deficient,[187] non-activated[14,179,189] and electron rich double bonds.[182] Furthermore, reactions with the triple bond of MeCN[181] and organic acids have been reported, whereby a 1,4-acyl shift

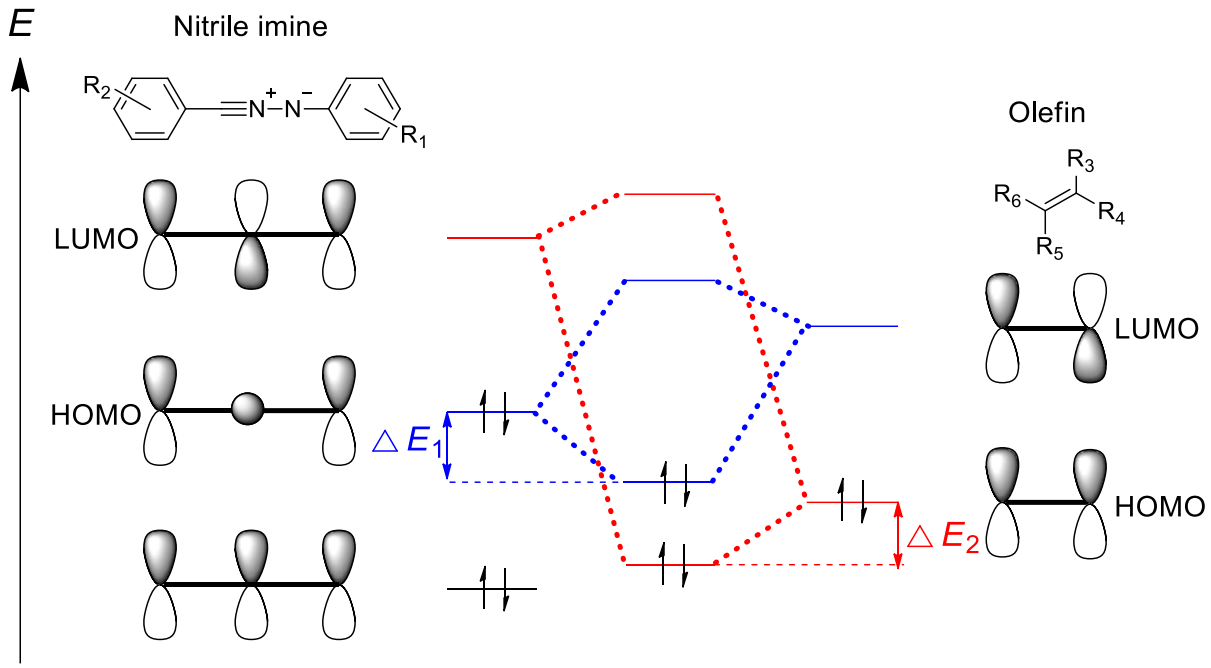

Figure 11 Energy levels of the molecular orbitals of nitrile imine and the olefine and their HOMO-LUMO interaction in a 1,3-dipolar cycloaddition, resulting in stabilization energies Δ E_1 and Δ E_2.[188]

occurs in case of the reaction with an acid.[190] Thiols,[191] imidazole[192] and water[193] are also known to undergo addition reactions with the nitrile imine species. Finally, the dimerization to a tetrazine has also been established as a method for single chain nanoparticle formation.[194] Due to such a variety of possible reaction channels for the nitrile imine intermediate, the question arises, if the NITEC reaction can fulfil the strict orthogonality criteria of a 'click reaction'.[17] To address this question, the significant impact of the substituents R_1 and R_2 on the reactivity of the nitrile imine formed must be considered (refer to Scheme 14). There exist over 30 published tetrazoles suitable for NITEC reactions. Each of the derivatives possesses unique reactivity properties towards nucleophiles or dipolarophile species. The reactivity of the diaryl tetrazole towards olefine species can be taken as an example to demonstrate the influence of the substituents. When equipped with an ester moiety in the no reaction of the

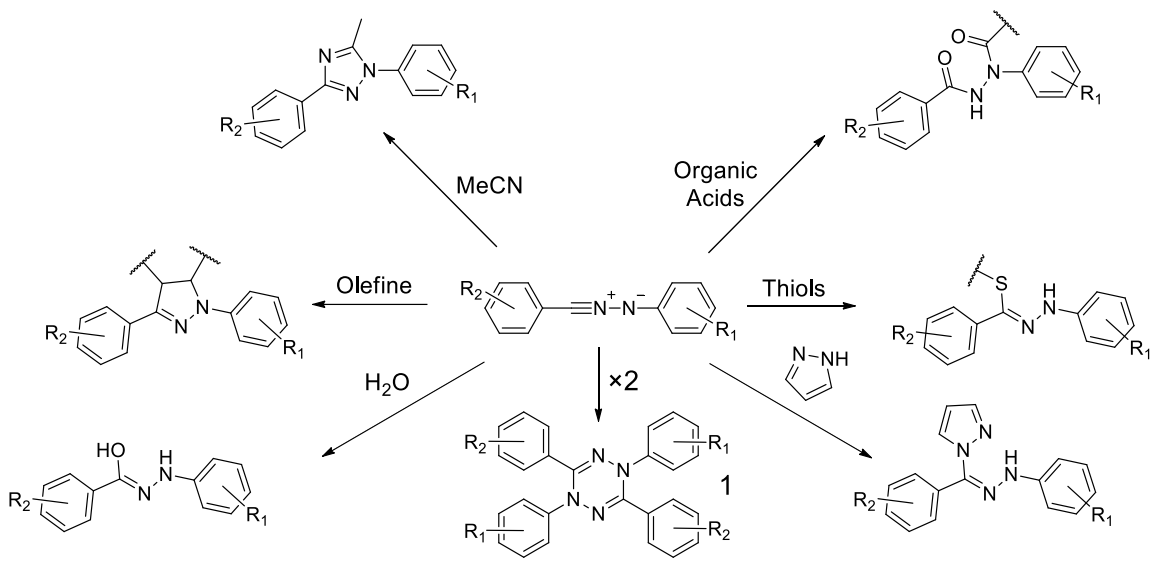

Scheme 14 Reaction pathways of nitrile imine, formed through a light induced decomposition of a diaryl tetrazole.

para R_2 position tetrazole [181] species towards electron rich and non-activated olefins is observed. Through the attachment of an additional methoxy or an dimethyl amine group, in the *para* R_1 position, the photoactive species becomes more reactive and suitable for addition reactions with non-activated and electron rich alkene species.[182,189] Furthermore, the ability of a tetrazole to undergo reactions with a variety of species is not necessarily a disqualifier for an orthogonality of the reaction. If the desired reaction channel is dominating, the target cycloadduct can be obtained almost exclusively, as illustrated for the photoenol in the previous section. Although reactions with water,[193] imidazoles, and MeCN,[181] as well as dimerization[187] are possible, their formation occurs mostly due to the lack of a suitable dipolarophile species. Therefore, NITEC can be a promising candidate for orthogonal conjugation approaches, if an appropriate dipolarophile is employed. To date, only a minority of the tetrazoles have been investigated with regard to their scope to perform conjugation reactions with a variety of coupling reagents. Further reactivity studies on tetrazole derivatives are needed in order to establish orthogonality of the NITEC reaction for a given application.

Apart from the orthogonality towards different moieties, the λ-orthogonality of the NITEC reaction towards other photo induced conjugation methods is an intriguing synthetic approach. Although several attempts to achieve λ-orthogonality of light triggered reactions have been undertaken,[195-197] it was Barner-Kowollik and co-workers, who introduced an efficient λ-orthogonality methodology for the conjugation of macromolecules (refer to Scheme 15).[9] Here, different irradiation wavelengths were applied, enabling independent coupling reactions of the photoenole (λ = 310 - 350 nm) and tetrazole (λ = 270 - 310 nm). The concept was demonstrated to be suitable for biological applications *via* the synthesis of protein end capped block copolymers. In an additional study the methodology was extended to form star polymers.[198]

In summary, NITEC provides a versatile and powerful conjugation technique. The required tetrazole species are easily accessible and provide

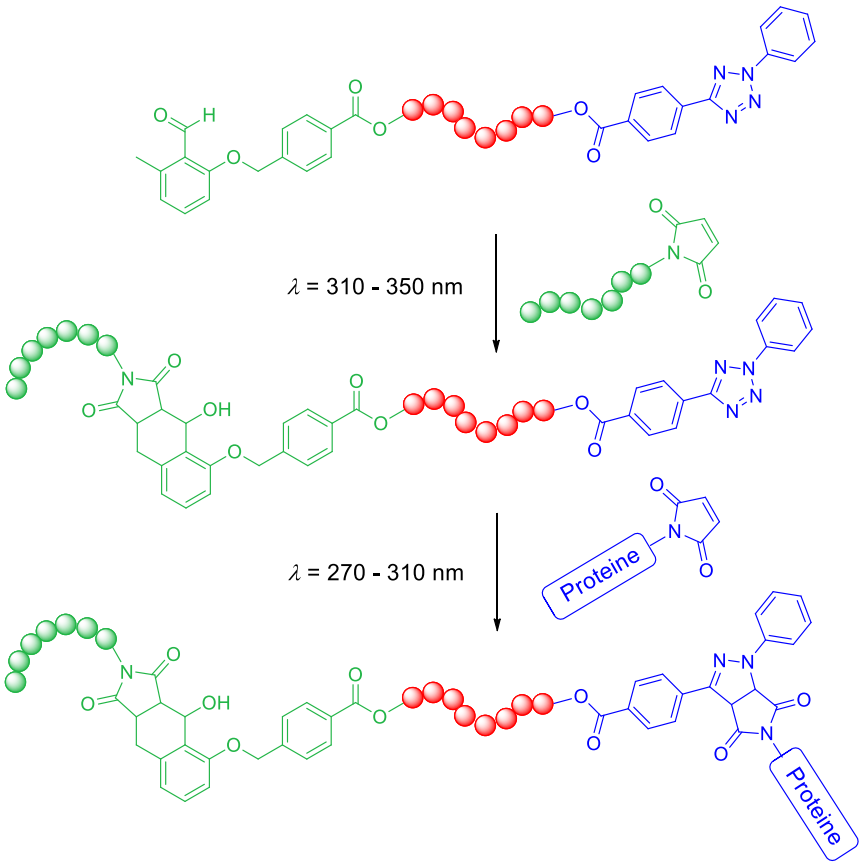

Scheme 15 λ-Orthogonal approach for macromolecular design.[9]

a wide range of reactivities as well as trigger wavelengths. However, shifting of the tetrazole absorption spectra into the visible light range remains an unfulfilled challenge and will be addressed further in Section 2.3.3.1.

2.3.2.3 Azirine Photoligation

The photoinduced 1,3-dipolar cycloaddition of an azirine is an alternative conjugation approach to the NITEC reaction. Starting from the *2H*-azirine, a nitrile ylide dipole is generated in a photoinduced ring opening reaction.[199] The photoinduced step is remarkably efficient, providing almost monophotonic yields.[200] The formed intermediate undergoes a rapid cycloaddition with an electron deficient multibond derivative (refer to Scheme 16).[201] The substituents of the three membered azirine ring have substantial impact on the reactivity of the formed dipole. Both, alkyl and aryl azirines substituted in the R_2 position are reported in the literature. Electron withdrawing groups in the R_2 position increase the reactivity for the diphenyl azirines. Thus, delocalisation of the negative charge located on the carbon of the nitrile ylide species is suggested to contribute to the stabilization of the dipole.[202] Furthermore, diphenyl azirines are reported to be reactive towards alcohols, allowing the formation of alkoxyimines. High electron density of the dipole and rather acetic alcohols are required for an effective addition reaction.[200] When functionalized with alkyl groups in the

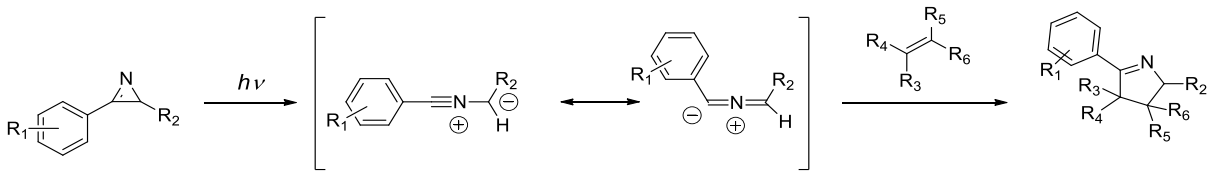

Scheme 16 1,3-Dipolar cycloaddition of an nitrile ylide, formed in a photoinduced ring opening reaction of a *2H*-azirine species.

R_2 position, the azirine derivatives reveal high reactivity towards CO_2 and CS_2 double bonds. In general, the nitrile ylides are suggested to be more reactive than nitriles imine formed in a NITEC reaction.[202] Although the photoinduced azirine reactions fulfil the requirements of a coupling method for the design of macromolecular structures, only Lin and co-workers have utilised this strategy for polymer-protein conjugation (refer to Scheme 17).[202] After establishing the conjugation reaction for the ligation of small molecules, the concept was applied for the linkage of an biologically relevant protein lysozyme with water soluble PEGs. The azirine functional protein was irradiated in the presence of fumaryl functional PEG for 2 min to yield the desired cycloadduct. Importantly, no Michael addition adducts were observed, verifying the efficiency of the rapid cycloaddition.

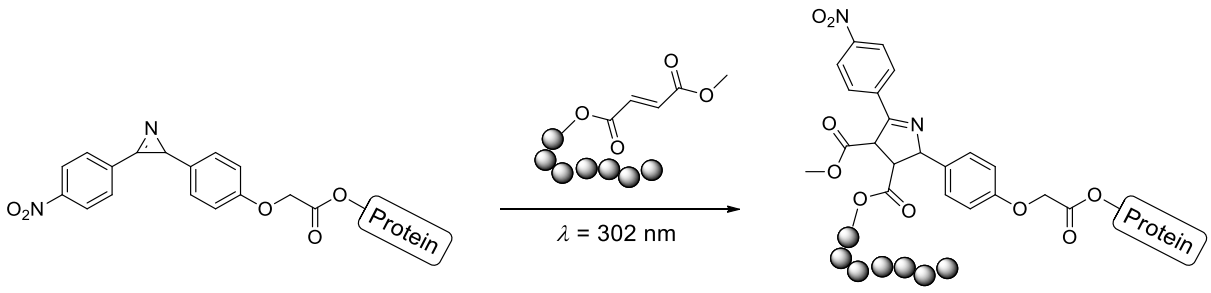

Scheme 17 Polymer-protein conjugation *via* light induced 1,3-dipolar cycloaddition of *2H*-azirine.[202]

2.3.3 Visible Light Chemistry: Strategies for Bathochromic Shift of the Irradiation Wavelength

Light induced reactions continue to gain strong attention from researches of all fields of chemistry. One of the main research areas of the photo triggered processes is the development of efficient conjugation reactions for macromolecular modifications, surface and interface functionalisation, as well as applications in the field of biology. Thus, reactions are often desired, which fulfil the 'click chemistry' criteria.[17] However, most of the photo active species employed, require UV light in order to perform efficiently. The application of such a high energy irradiation is a major disadvantage of the coupling reactions as a large part of organic and inorganic compounds, as well as biological systems are labile towards UV light.[203] Consequently, photo degradation can occur. To overcome the limitations of UV light induced reactions, a variety of strategies for triggering of the photoreactions with visible light or in the NIR range has been established. The current section provides an overview over the available strategies, explaining the basic principle of the approach, presents application examples, as well as discusses the advantages and disadvantages of each technique.

2.3.3.1 Modification of Photoactive Species

Modification of photoactive species in order to shift the trigger wavelength of a photoactive molecule into the visible or NIR range is an intriguing scientific task. The resulting advantages are the avoiding of additives or advanced experimental setups, required for other visible light inducted conjugation techniques. The design of a novel 'red-shifted' photo active species should be driven by several general factors, as well as structural considerations related to the specific light sensitive molecule. Bathochromic shift of the absorption spectrum is the key requirement for a photosensitive species in order to operate in a higher wavelength regime. The 'red-shift' can be achieved by expanding the aromatic systems included into the core structure of the photo active moiety, as well as the introduction of further substituents.[182,204-207] However, the reactivity of the photo sensitive molecule towards desired moieties can potentially be affected by the resulting changes in the molecules' structure.[205,206] In addition, large absorption coefficients do not imply efficient photo activation.[208] The photophysical properties of the modified chromophore are decisive for the success of the photoreaction. High intersystem crossing quantum yields and the ability to perform as a photosensitiser are among the most important features of the chromophore. Both properties allow for an

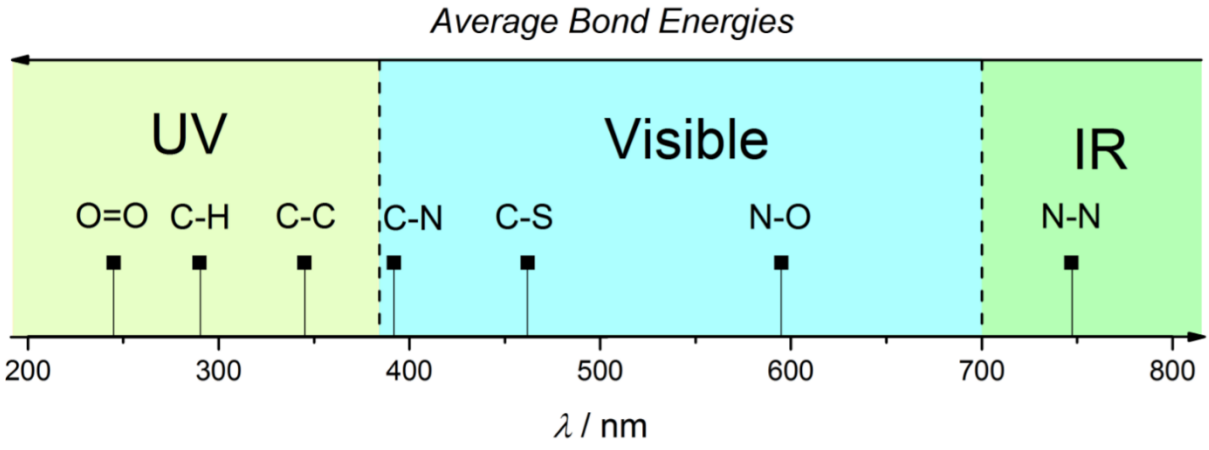

Figure 12 Plot of wavelengths matching the bond energies for various single bonds and O-O double bond. The arrow illustrates the increasing bond energies.[209]

efficient transition of the photoactive species into the reactive intermediate form. In addition, the irradiation wavelength should be adjusted to the desired photo induced structural change. Often, bond cleavage processes are involved into the mechanism of a photochemical induced reaction. Therefore, a trigger wavelength, possessing sufficient energy to break the photo labile bond, is required. In Figure 12, the average bond energies of various single bonds and O-O double bond in a range of 200 – 900 nm are illustrated. Cleavage of labile C-S and N-N single bonds can be achieved *via* visible light or IR irradiation. Harsh UV light is required for more stable O-O double bond. The reported energy values should be considered as benchmarks for a qualitative overview, as the bond stability can be influenced significantly by the chemical structure of the molecule. The effect of the solvent should be also considered. Importantly, the preparation and application of the compounds for visible light triggered reactions can be challenging due to their sensitivity to ambient light.

A prominent example of a photo induced conjugation approach is the NITEC

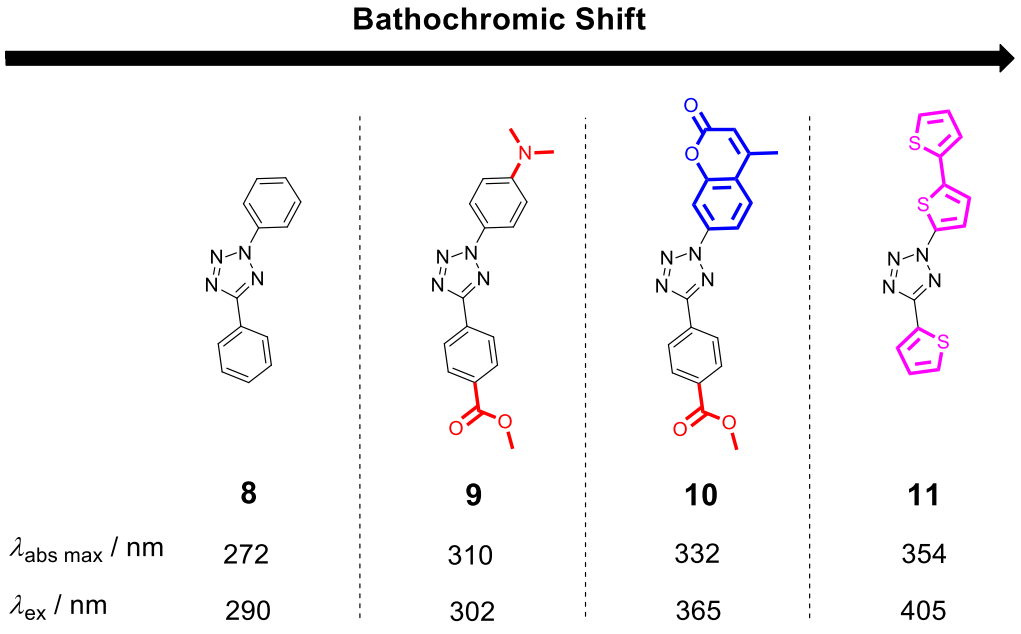

Figure 13 Structures, absorption maxima ($\lambda_{abs\ max}$) and excitation wavelength of the NITEC reaction (λ_{ex}) of the tetrazole species **8** – **11**. Bathochromic shift is illustrated by the arrow.[182,204-206,210]

reaction (refer to Section 2.3.2.2 for further details on NITEC). Several 'red shifted' tetrazoles have recently been reported. Thus, a bathochromic shift of the absorption was achieved *via* modification of the core structure of the tetrazole (refer to Figure 13).[159,184-186,190] While the non-functional diaryl tetrazole **8** absorbs at 272 nm, the tetrazole derivative **9**, substituted in both *para* positions, has an absorption maxima at 310 nm. Importantly, the introduction of the dimethylamine to the N^2 phenyl ring increases the reactivity of the tetrazole species towards non-activated alkene derivatives. By extending the aromatic system of the tetrazole, further red shifting of the absorption wave length was achieved, as demonstrated for the cumarin and the oligothiophene based tetrazole derivatives **10** and **11**. The trigger wavelengths of compounds **8**-**11** shift into the lower energy region with respect to the increasing absorption wavelength (λ_{ex} = 272 nm (**8**) to λ_{ex} = 405 nm (**11**)). It should be noted, that the presented data provides only a qualitative overview of the bathochromic shift of the tetrazole species. As stated before, irradiation at the $\lambda_{abs\ max}$ is not inherently linked to an efficient formation of the cycloadduct. The excitation wavelength, required for light triggering of the conjugation reaction, can potentially be associated with a subtle absorbance which is hidden within other absorbances from chromophores within the molecule that do not lead to triggering. Consequently, excitation wavelengths higher than the $\lambda_{abs\ max}$ are possible (refer to Figure 13, compound **10** and **11**). The provided irradiation wavelengths are based on the literature and do not necessarily represent the most efficient or the longest λ_{ex}. Interestingly, an extension

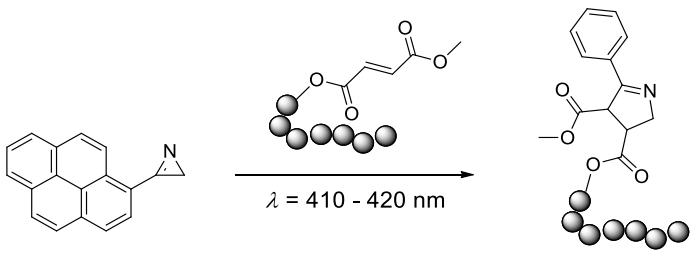

Scheme 18 Visible light induced 1,3-dipolar cycloaddition of a pyrene functionalized *2H*-azirine.[204]

of the aromatic system of the C^5 phenyl ring does not necessarily allow for an application of longer irradiation wavelengths.[190] Another recent example of the red-shifting of the photoactive species is the pyrene functional *2H*-azirine reported by Barner-Kowollik and co-workers. By extending the aromatic system of a phenyl azirine to a pyrenyl azirine derivative, a bathochromic shift of the absorption was achieved. Consequently, the corresponding photoinduced 1,3-dipolar cycloaddition of the pyrenyl functional *2H*-azirine species was performed at 410 - 420 nm. The approach was applied for small molecule ligation and polymer modification. It is the first example of a visible light triggered reaction allowing efficient small molecule and polymer conjugation.[204]

2.3.3.2 Photoredox Catalysis

MacMillan, Yoon and Stephenson are among the pioneers of visible light photoredox catalysis (VLPC).[211-213] Today, VLPC is a fast growing research area, attracting attention from scientists in various fields of chemistry. A large range of reactions including [2 + 2] cycloadditions,[214] dehalogenation reactions[215] and *β*-functionalization of carbonyl compounds[216] can be performed in the presence of photoredox catalysts by applying visible light only. Thus, irradiation sources > 500 nm can be employed, a unique feature not yet accessible by any additive free conjugation strategy.[217] The methodology allows efficient chemical transformations under mild conditions without additional heating. $[Ru^{II}(bpy)_3]^{2+}$ is a prominent and well understood example of a photoredox catalyst, which can be used to illustrate the basic mechanism of VLCP (refer to Figure 14). The transition metal complex possesses significant absorption at 452 nm, which can be assigned to the electron transition from d_{t2g} (HOMO, S_0) to π^* (LUMO, S_1) orbital in a metal to ligand charge transfer. The resulting excited state S_1 participates in an intersystem crossing process, in order to transform itself

quantitatively into the long living excited triple state T_1. Two reaction channels of T_1 are possible: a reduction or an oxidation (refer to Scheme 19). In a reduction process, the vacant electron position in the $t_{2g(M)}$ becomes occupied in an electron transfer from a single electron reduction agent. The oxidation occurs *via* photoinduced electron transfer

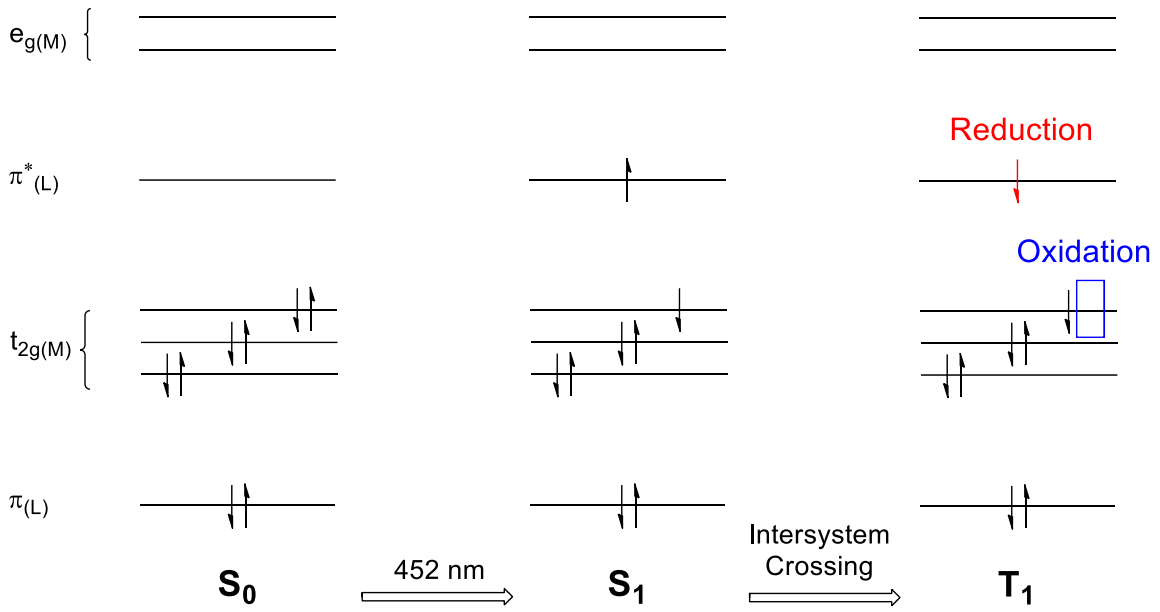

Figure 14 Schematic representation of orbital energy levels and photoinduced activation of $[Ru^{II}(bpy)_3]^{2+}$. S_0,S_1 and T_1 are the ground singlet state, the excited singlet state and the excited triplet state respectively. Reduction: high energy electron available for a reduction reaction. Oxidation: vacant electron position in the $t_{2g(M)}$ orbital available for a oxidation reaction.

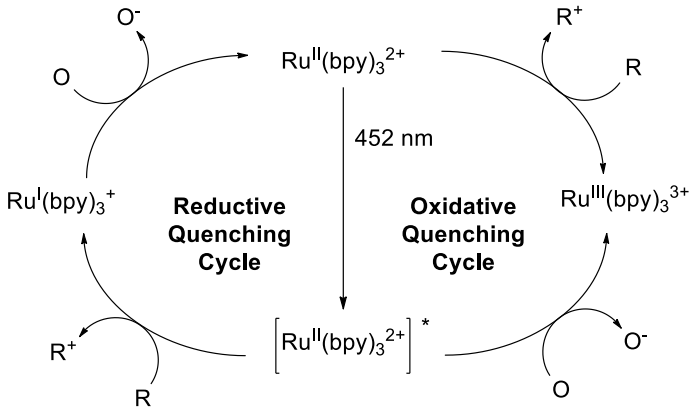

Scheme 19 Redox cycles of $[Ru^{II}(bpy)_3]^{2+}$. Reduction and oxidation agents are illustrated as (R) and (O) respectively.[218]

from the metal complex to a single electron oxidation agent. Both reactions are possible in case of the Ru photo catalyst, depending on the redox potentials of the reagents employed.[218] Organic photoredox catalysis allows for free conjugation or transformation of organic molecules and provides strategies for the synthesis of molecules not accessible *via* metal complex photo catalysis.[219] Xanthenes,[220] thiazines[221] and acridiniums[222] have been all established as visible light active photo catalysts.

A wide range of photo catalytic species has been reported, allowing tuning of the irradiation wavelength, as well as catalyst reactivity with respect to the specific reaction.[219,223] However, the application of a catalyst remains a major disadvantage for *in situ* reactions, where the additive can not be removed. Post reaction interaction of the catalytic species with moieties present in direct proximity is a possible disadvantage too. Furthermore, orthogonality of the photoinduced reaction towards existing functional groups must be assured, as alternative redox processes can potentially occur. Finally, the toxicity of the major part of current employed organic photo catalysts is unknown, limiting their application in the field of biology.

2.3.3.3 Simultaneous Two-Photon Absorption

Simultaneous two photon absorption (TPA) was predicted by Göppert-Mayer in 1929 as an alternative to one photon absorption.[224,225] Although the first evidence of such a process was given by Hughes and Grabner in 1950,[226] high intensity laser introduction in the 1960s allowed the experimental observation of TPA.[227,228] The basic mechanism of the absorption process is illustrated in Figure 15. In contrast to the one photon absorption (OPA), two photons are needed in TPA to reach the excited state. The electron in the ground state S_0 is transferred to the excited state S_1 by simultaneous absorption of two photons. Thus the molecule goes

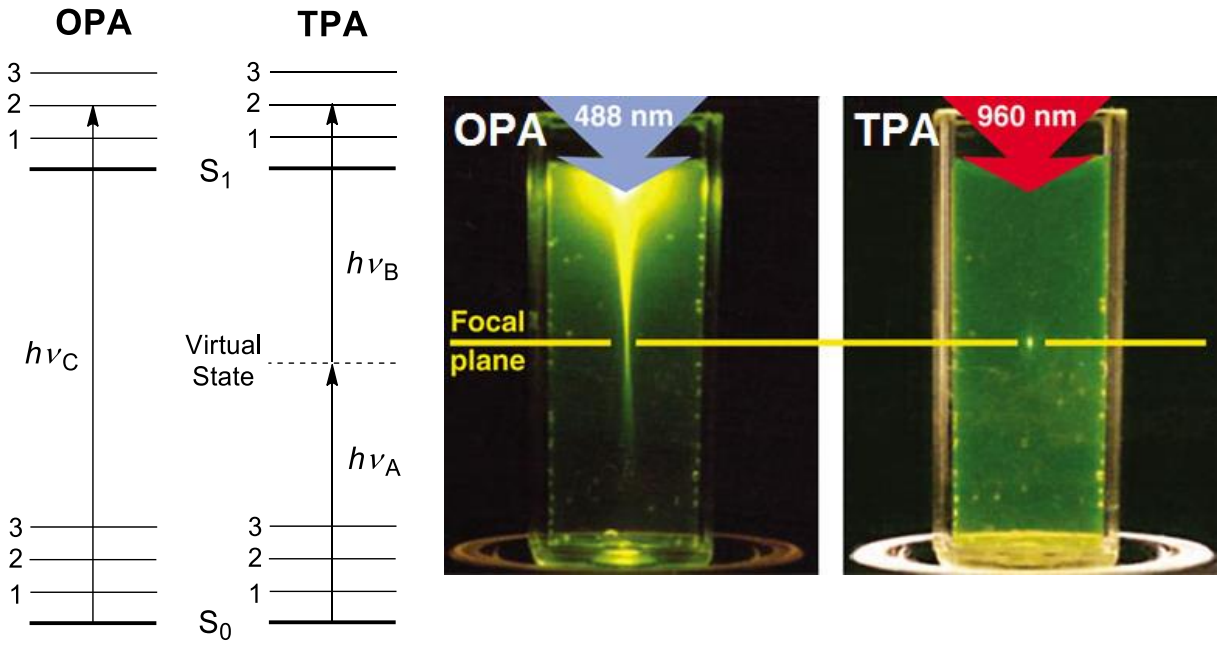

Figure 15 Left: Schematic illustration of the one photon absorption (OPA) and simultaneous two photon absorption (TPA). Right: TPA and OPA induced fluorescence of fluorescein solution (irradiation *via* laser).[229] Reprinted with permission from Nature Publishing Group.

through a virtual state with a short lifetime of several femtoseconds.[230,231] In contrast to the OPA, longer wavelengths are suitable for the TPA. Furthermore, as two photons are required to reach the excited state, the absorption increases with the square of the light intensity. Consequently, efficient excitation occurs at the laser focus only. In comparison, OPA depends linearly on the intensity, resulting in photo excitation along the irradiation beam (refer to Figure 15).[232] The ability to spatially confine the photoexcitation, along with the red shifting of the trigger wavelength, has been utilised in various application fields including fluorescence spectroscopy,[233] microscopy,[229] drug delivery,[234-236] as well as 3D lithography[237-239] and optical data storage.[240,241] Expanding the toolbox of the TPA induced chemical transformation reactions is a key feature for further development of the methodology. Several TPA induced reactions were established such as cycloadditions,[242,243] cycloreversion reactions,[244] isomerisations,[245-247] as well as polymerization techniques.[248] A recent

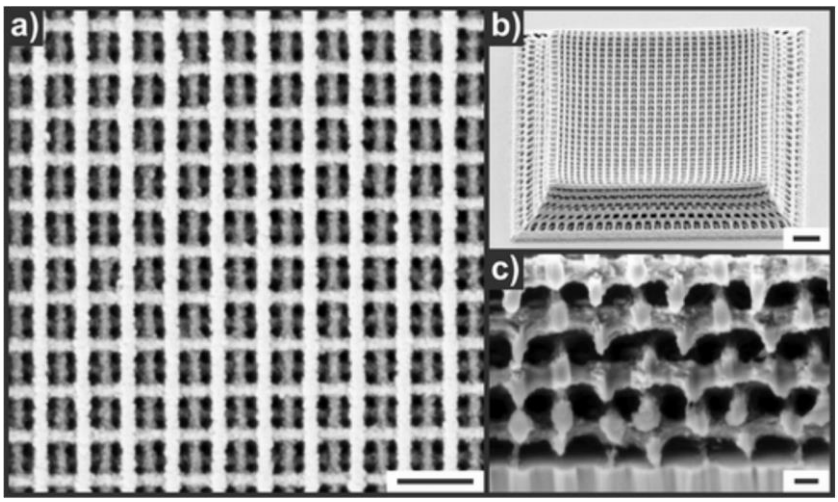

Figure 16 Scanning electron microscope (SEM) images of the woodpile photonic crystal. a) magnification of whereas b) image of the entire structure fabricated c) interior of the woodpile visualised *via* SEM after focused ion beam milling. Scale bares are 1 µm (a), 2 µm (b) and 200 nm (c)).[12] Reproduced with permission of WILEY-VCH Verlag.

example of 3D lithography *via* photoinduced photoenole chemistry was reported by Barner-Kowollik and co-workers.[12] A polymer species carrying dipolarophile moieties along the backbone was prepared and crosslinked *via* a multifunctional *o*-methyl benzaldehyde derivative at 700 nm. The applied strategy allowed the fabrication of woodpile photonic crystals with rod spacings down to 500 nm (refer to Figure 16). In addition, the suitability of the approach for post crosslinking surface modification was demonstrated.

TPA allows photo excitation in the visible light range in the absence of additives and without further modification of the light active moieties. However, an advanced experimental set up including a high intensity laser is required in order to perform TPA experiments. Furthermore, the rather long writing time limits the 3D microfabrications, as well as 3D optical data storage.[230] In addition, the TPA approach is less suitable in the field of the biology, as the laser can defocus while passing through the living tissue. The resulting intensity decrease of the trigger wavelength negates the efficiency of the photo excitation.

2.3.3.4 Upconverting Nanoparticles (UCNPs)

Lanthanide-doped UCNPs are one of the most recent examples of upconverting processes. First reported to assist photochemistry in 2009,[249] UCNP are an intriguing alternative to VLPC and TPA. The principle of UCNPs is based on the sequential multiphoton absorption by the long lived, metastable energy states of lanthanide species. Three different UC processes were reported: excited state absorption (ESA), energy transfer upconversion (ETU), and photon avalanche (PA).[250] However, ETU is the most common upconversion strategy, as it provides two orders of magnitude higher efficiency than ESA[251] and faster response to excitation than PA.[252] The basic mechanism of ETU is depicted in Figure 17. Both, sensitizer and emitter, absorb photons in order to populate the excited state E_1. A non-radiative energy transfer from the sensitizer to the emitter species allows the promotion to an upper emitting state E_2.

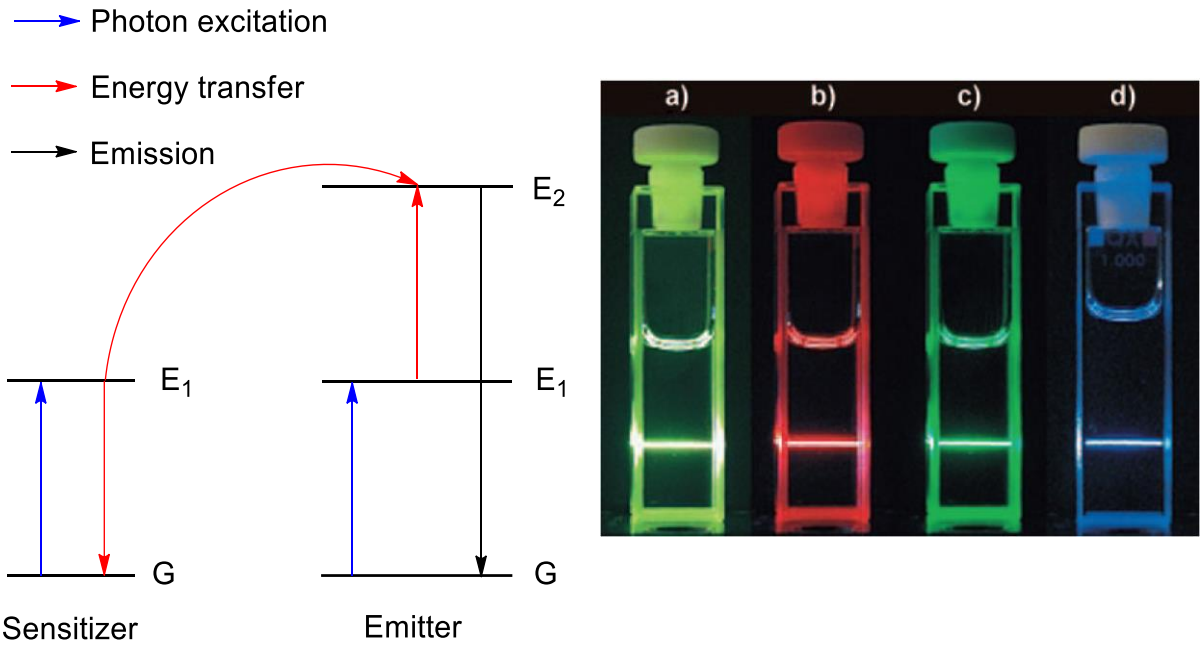

Figure 17 Left: basic mechanism of the energy transfer upconversion process. G and $E_{1,2}$ are the ground state and the excited states respectively. Right: upconversion luminescence images of 1 wt % colloidal solutions of UCNPs excited with 973 nm light. a) Total upconversion luminescence of the NaYF4 : 20 % Yb^{3+}, 2 % Er^{3+}. b) Upconversion luminescence (a) with red light filter applied. c) Upconversion luminescence (a) with green light filter applied. d) Total upconversion luminescence of the Yb^{3+}, Tm^{3+}- doped UCNPs.[252,253] Reproduced with permission of WILEY-VCH Verlag.

Thus, the sensitizer species returns to the ground state G, while the emitter returns to the ground state by releasing the photon in a luminescence process. The upconversion process is not limited to sequential absorption of two photons. Multiple photon absorption such as three and four photon absorption are well established in the literature, allowing the generation of various emission wavelengths (refer to Figure 17). In order to achieve high upconversion efficiency, long lived and highly populated excited states are required. Furthermore, a ladder like positioning of the energy levels of the emitter, featuring similar energy gaps between each level should be assured. Thus, the energy gaps between the G and E states should be similar for the emitter and the sensitizer.[252] By variating the structure and size of the nanoparticles, as well as the lanthanide applied, a range of emission and absorption wavelengths is accessible.[252,254,255]

A major part of UCNPs applications is based on three types of photoinduced reactions: photolysis, isomerisation and photo induced polymerization (refer to Scheme 20). Photolysis of *o*-nitrobenzyl[256-258] and coumarin[259] derivatives, as well as Ru complexes[260,261] are among the established

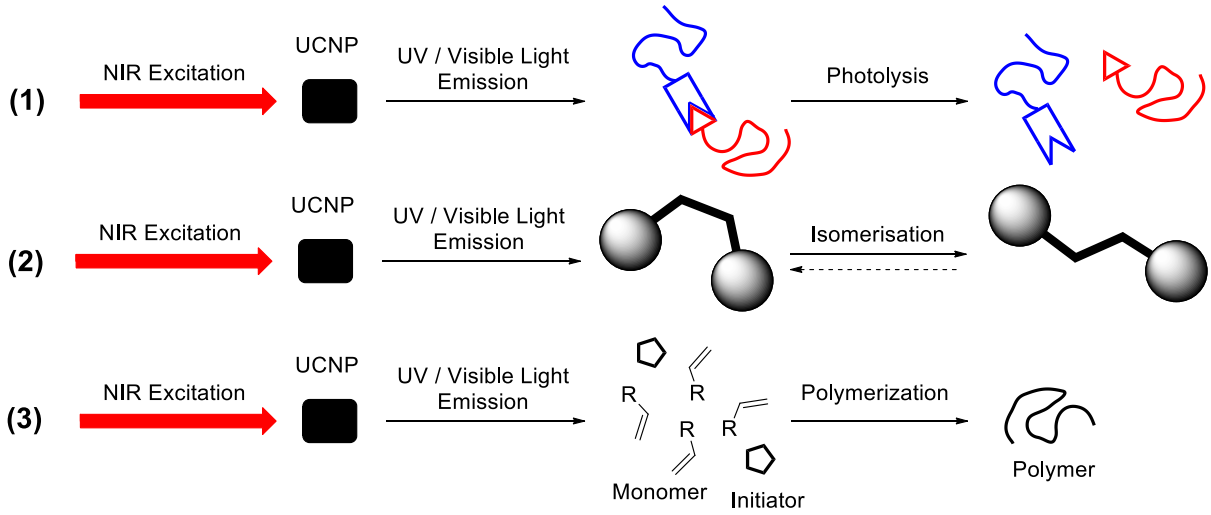

Scheme 20 Photoinduced reactions assisted by the UCNPs. (1) Photolysis. (2) Isomerisation. (3) Polymerization.[262]

methodologies. Since the UCNPs display low cytotoxicity,[263-266] they are well suited for *in vivo* applications featuring NIR reaction triggering. Several reports on spatially controlled *in vivo* drug delivery by photo induced bond cleavage were published, including attachment of the drug species to the upconverting nanoparticles,[258] as well as light triggered decomposition of drug loaded micelles.[267] UCNPs assisted polymerization techniques are applied for curing dental resins. Due to the long wavelength used, an improved penetration of the trigger irradiation was ensured, allowing the fabrication of the filling in a one step process. In comparison, layer by layer techniques are employed for the conventional UV induced hardening, often leading to shrinkage and re-infection.[262,268]

UCNPs operates at sufficiently lower intensities than TPA.[269-272] However, the irradiation intensities used can cause photodamage, due to the heat production of the laser beam. Furthermore, a combination of the UCNP concept with photoinduced 'click reactions' is not known yet. An efficient conjugation method triggered by NIR would be a major contribution to the UCNPs toolbox, allowing e.g. *in vivo* labelling or *in situ* attachment of drugs *via* the formation of a covalent bond

3 Design of Redox/Radical Sensing Molecules *via* NITEC

3.1 Introduction

Profluorescent Nitroxides (PFN) are an emerging class of molecular sensors for monitoring of redox and radical processes. However, the known synthetic pathways to yield PFNs are a major limiting factor for their future applications. Most strategies for the preparation of the PFNs are performed in the presence of a metal catalyst or include a hydrolytically sensitive linkage between the nitroxide and the fluorophore species. In addition, space resolved *in situ* preparation of PFNs, is vital in both the field of biology, as well as for preparation of patterned sensor surfaces, which to date, has not been possible. In the current chapter, the PFN concept has been combined with NITEC chemistry in order to introduce a novel, powerful approach for a catalyst free *in situ* preparation of profluorescent nitroxides (refer to Figure 18).[273] A variety of novel nitroxide functionalized diaryl tetrazole species was designed and converted, together with known tetrazole and maleimide species in a NITEC reaction. Rapid conversion of the reagents, as well as efficient formation of the desired cycloadduct occurred. The resulting pyrazoline compounds were investigated with regard to their fluorescence `switch on/off´ performance, which was dependent on the distance and orientation between the single

Parts of the current chapter are reproduced from Lederhose, P.; Haworth, N. L.; Thomas, K.; Bottle, S. E.; Coote, M. L.; Barner-Kowollik, C.; Blinco, J. P. *The Journal of Organic Chemistry* **2015**, *80*, 8009. Published by American Chemical Society 2015.

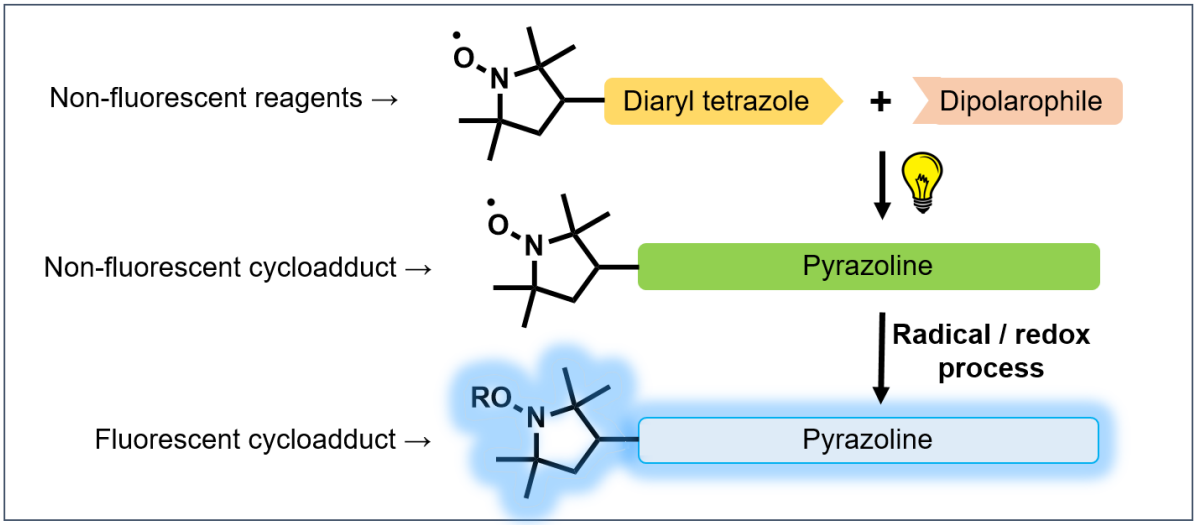

Figure 18 NITEC approach for the formation of profluorescent nitroxides.

electron of the nitroxide moity and the fluorophore. In addition, the sensor ability of selected pyrazoline cycloadducts towards redox and radical processes was demonstrated in model experiments.

3.2 Results and Discussion

Two major factors need to be considered when choosing the reagents for the preparation of PFN *via* NITEC reaction. The first point to be addressed is the distance between the nitroxide and the diaryl tetrazole. Electronical transitions to excited states are involved in the process of photo induced nitrile imine formation from the tetrazole species. As nitroxide species are well known to be excited state quenchers,[274-276] the efficiency of the nitrile imine formation was suggested to decrease, if the nitroxide moiety is placed in too close proximity to the tetrazole. The second point is the distance between fluorophore formed *via* NITEC and the nitroxide. The fluorescence quenching performance can potentially increase, if the distance between the free radical of the nitroxide and the fluorophore decreases.[118] Therefore, the position of the nitroxide in the initial diaryl tetrazole and the formed fluorescent cycloadduct plays a key role for both the NITEC reaction and the PFN sensor performance.

For the first generation of the pyrazoline containing PFNs, direct linkage between the nitroxide species and the tetrazole species was avoided in order to minimize the intramolecular quenching effects and to ensure efficient photoinduced formation of the nitrile imine. Equimolar amounts of diaryl tetrazole **1** and nitroxide functional maleimide **2** were dissolved in MeCN and irradiated at 254 nm (emission maximum of the lamp) for 15 min. Full conversion of both reagents and the formation of the desired radical-containing pyrazoline **3** was observed *via* thin-layer chromatography (TLC) as a compound with higher retention (refer to Scheme 21). The crude product mixture was purified *via* column chromatography and analysed by high-performance liquid chromatography (HPLC), high-resolution mass spectrometry (HRMS) and electron paramagnetic resonance spectroscopy (EPR). The HPLC elugrams of **3** are displayed in Figure 19. They indicate, that exclusive cycloadduct formation is observed with absence of any side products. Both emission and

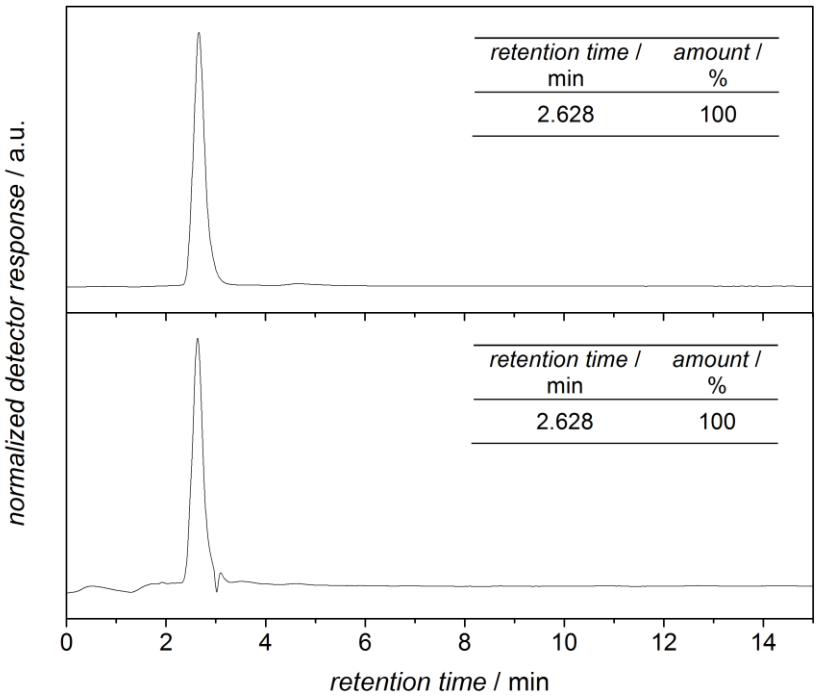

Figure 19 HPLC chromatogram of nitroxide pyrazoline **3** measured in THF / H_2O mixture (55:45, v / v); top: 430 nm emission detection by 350 nm excitation; bottom: 254 nm absorbance detection. Adapted with permission from [273]. Copyright 2016 American Chemical Society.

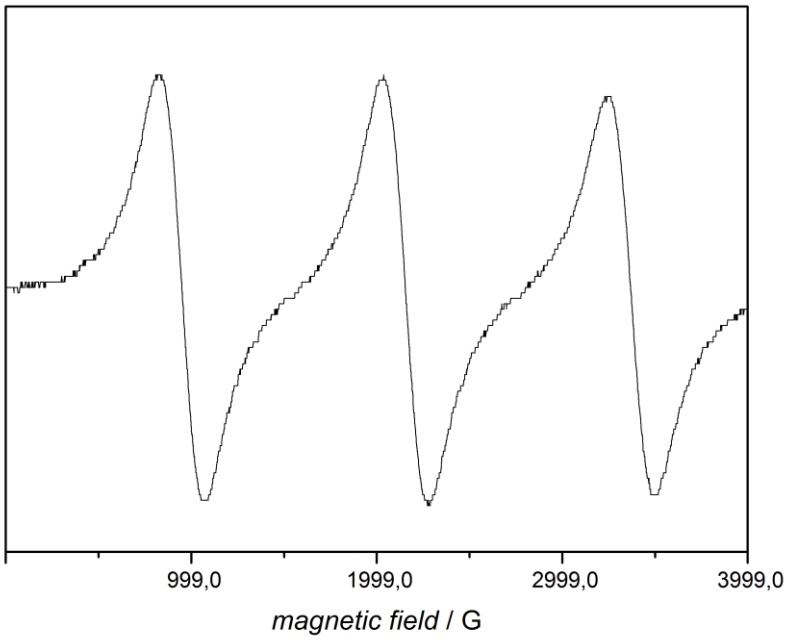

Figure 20 EPR spectrum of nitroxide pyrazoline **3** in THF. Adapted with permission from [273]. Copyright 2016 American Chemical Society.

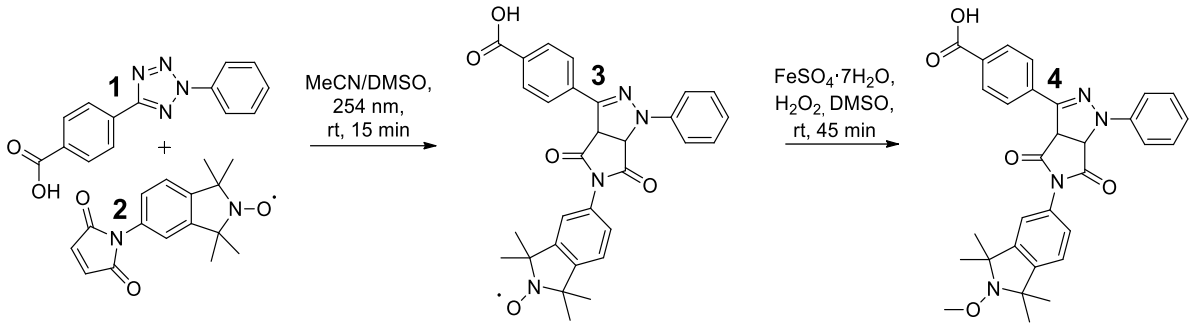

Scheme 21 NITEC of diaryl tetrazole **1** and maleimide **2** to form nitroxide pyrazoline **3**. Conversion of formed radical pyrazoline **3** to methoxyamine derivative **4**. Adapted with permission from [273]. Copyright 2016 American Chemical Society.

absorbance spectroscopy were employed, as the analysed pyrazoline derivative was expected to have potent fluorescence. Consequently, an absorption and emission signal appearing at identical retention times can be attributed to that of the cycloadduct. Although HPLC is a powerful method for quantification of the compound purity, it provides very little information about molecular structure of the analyte. Therefore, species **3** was analysed by EPR, confirming the presence of the single electron of the nitroxide by the three-line electron paramagnetic resonance (refer to Figure 20). HRMS provided an additional validification of the structure. Due to the paramagnetic properties of the nitroxide functional cycloadduct **3**, broad and featureless resonances in the NMR spectrum were observed. Thus, pyrazoline **3** was converted to a corresponding diamagnetic methoxyamine derivative **4** using Fenton chemistry (refer to Scheme 21).[277]

The photophysical properties of the paramagnetic nitroxide-containing pyrazoline **3** and its diamagnetic non-radical derivative **4** were compared in order to estimate the quenching efficiency of **3** as a PFN and subsequent fluorescence return after a radical-scavenging process. This was achieved using fluorescence spectroscopy. To ensure that equivalent concentrations of compounds were compared, the assumption was made that the nitroxide moiety has little influence on the molar absorptivity of the fluorophore and the UV-vis absorbance spectra of **3** and **4** were optically matched. The

quenching performance of the nitroxide species is demonstrated by comparison of fluorescence spectra **3** and **4** (refer to Figure 22). The peak intensity of radical containing species **3** is 32 % lower compared to its non-radical analogue **4**. Although the fluorescence quenching of compound **3** is substantial, it is much less pronounced than for other reported profluorescent species.[118] Poor orientation and relatively long distance between the free electron from the nitroxide and the pyrazoline containing fluorophore species are assumed to cause the poor quenching performance. The theory is supported by the theoretical calculations on the geometry of the formed cycloadducts (refer to Figure 21). Poor overlap between the π-system of the fluorophore and the radical centre is expected due to the relatively long distance of 9.3 Å and 58° tilting of the 2p orbital of the radical with respect to the fluorophore.

An improved quenching performance was aimed for the second generation of nitroxides. To afford this, a direct linkage of the diaryl tetrazole to the

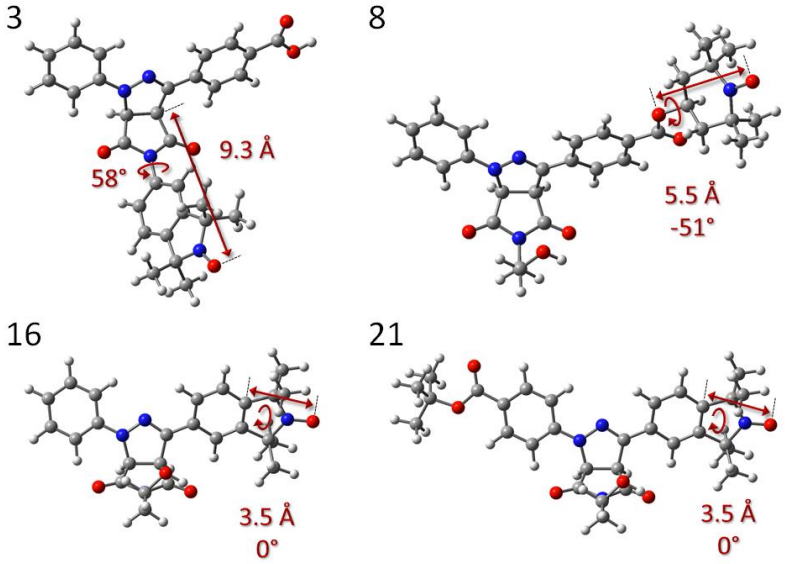

Figure 21 Optimized structures of compounds **3**, **8**, **16**, and **21** showing the distance of the fluorophore from the formal radical centre and its distortion from planarity, measured as the dihedral angle between the plane of the fluorophore and a plane perpendicular to the 2p orbital of the nitroxide. Adapted with permission from [273]. Copyright 2016 American Chemical Society.

nitroxide *via* formation of a new covalent bond was undertaken *via* an esterification reaction. TEMPO **5** and diaryl tetrazole **1** were coupled in presence of DCC and DMAP in THF to yield the nitroxide functional diaryl tetrazole **6** (refer to Scheme 22). The formed tetrazole species **6** was converted in presence of maleimide **7** to the cycloadduct **8** *via* NITEC reaction. Importantly, the nitroxide species covalently attached to the core structure of the tetrazole did not interfere with the process of the nitrile imine formation. Full conversion of both reagents applied in 1:1 ratio was observed after irradiation at 254 nm in MeCN for 15 min. The resulting reaction mixture was purified by column chromatography and analysed by HPLC, HRMS and EPR, confirming rapid and efficient formation of the target cycloadduct **8** (refer to Section 8.1.3, Figure 49 and Figure 50).

The quenching performance of the nitroxide is demonstrated by fluorescence spectra comparison of radical species **8** and the corresponding non-radical methoxyamine derivative **9** (refer to Figure 22). An improved fluorescence quenching for cycloadduct **8** was detected (ca. 3-fold

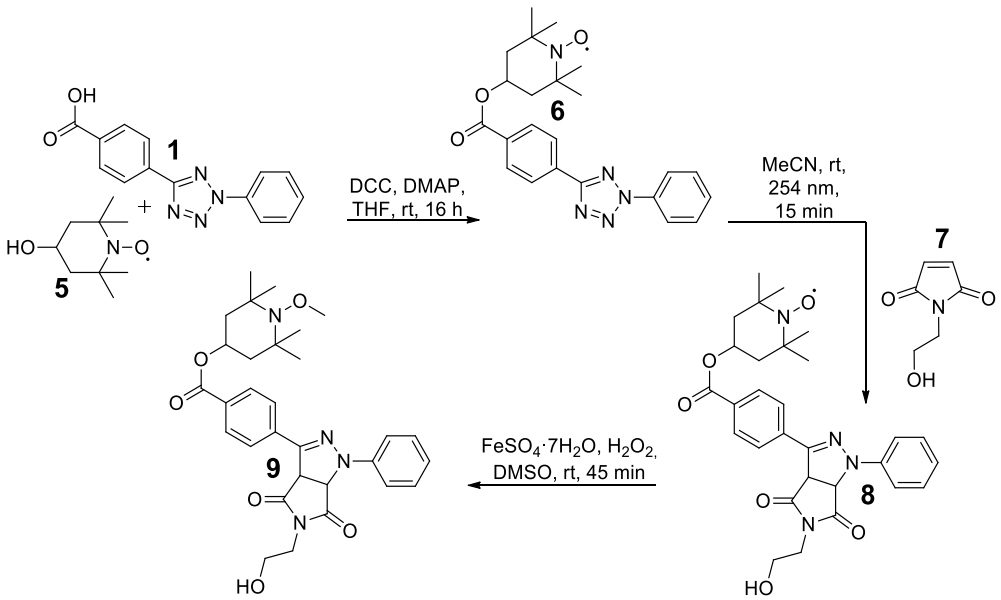

Scheme 22 Esterification of diaryl tetrazole **1** and hydroxyl functionalized nitroxide **5** to obtain radical diaryl tetrazole **6**. NITEC of the radical diaryl tetrazole **6** and maleimide **7** to form radical pyrazoline **8**. Conversion of the radical pyrazoline **8** to methoxyamine **9**. Adapted with permission from [273]. Copyright 2016 American Chemical Society.

fluorescence decrease with respect to the corresponding diamagnetic species **9**). The enhanced fluorescence quenching is associated with the shorter distance between the free electron spin and the pyrazoline containing fluorophore (9.3 Å for the first generation versus 5.5 Å for the second generation, refer to Figure 21). In addition, conjugative interaction between the free electron and the fluorophore potentially occurs, improving the fluorescence quenching in a through-bound process.

Although the quenching performance could be improved for the second generation, it was still below the state-of-art PFN sensor species providing up to 300-fold quenching.[145] Furthermore, employing an ester moiety as a linker between the nitroxide and the fluorophore leaves the pyrazoline containing PFN unstable towards hydrolysis. As the covalent attachment of the nitroxide to the diaryl tetrazole had little effect on the performance of the NITEC reaction, a direct carbon-carbon coupling between the nitroxide and the diaryl tetrazole was performed by fusing the nitroxide moiety into the core structure of the diaryl tetrazole. Consequently, an improved 'switch on/off' behaviour of the PFN was expected, due to the extreme close proximity between the single electron of the nitroxide and the pyrazoline

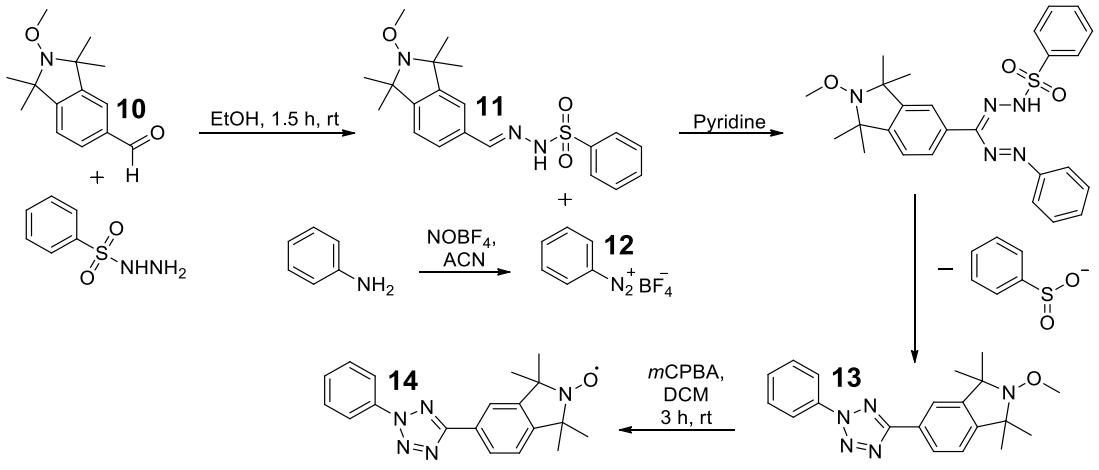

Scheme 23 Synthesis of nitroxide diaryl tetrazole **14**. Phenylsulfonylhydrazone **11** was formed from nitroxide **10** and benzenesulfonohydrazide. Arenediazonium salt **12** was formed from aniline. The methoxyamine **13** was oxidized to yield the radical diaryl tetrazole **14** using *m*CPBA. Adapted with permission from [273]. Copyright 2016 American Chemical Society.

containing fluorophore and their potential ability to interact through the conjugated bond system. In addition, the direct carbon-carbon linkage is less sensitive to hydrolysis, which is highly demanded for sensor application in the field of biology. Formyl functional nitroxide **10** and benzenesulfonohydrazide were reacted to yield intermediate **11** (refer to Scheme 23). Diazonium salt **12**, formed from aniline, was reacted with the *in situ* formed intermediate **11** to obtain methoxyamine **13**. The formed non-radical diaryl tetrazole **13** was deprotected by employing *m*CPBA as an oxidant. The synthetic route towards compound **14** from the aldehyde functional nitroxide did not succeed due to the potential reduction of the nitroxide moiety by the benzenesulfonohydrazide as a significant side reaction yielding a hydroxylamine species and then further intractable by-products. HRMS, HPLC and EPR were applied to confirm the structure and the purity of the compound **14**. Compound **13** was analysed by NMR and HRMS. Species **13** and **14** were then irradiated in the presence of maleimide **7** to conduct a NITEC reaction affording pyrazoline derivatives **15** and **16** (refer to Scheme 24). The ability of the diaryl tetrazoles to undergo a NITEC reaction, if an electron deficient alkene such as maleimide derivative is provided, is well known in the literature. Therefore, the observed efficient formation of the cycloadduct **15** after 15 min at 254 nm,

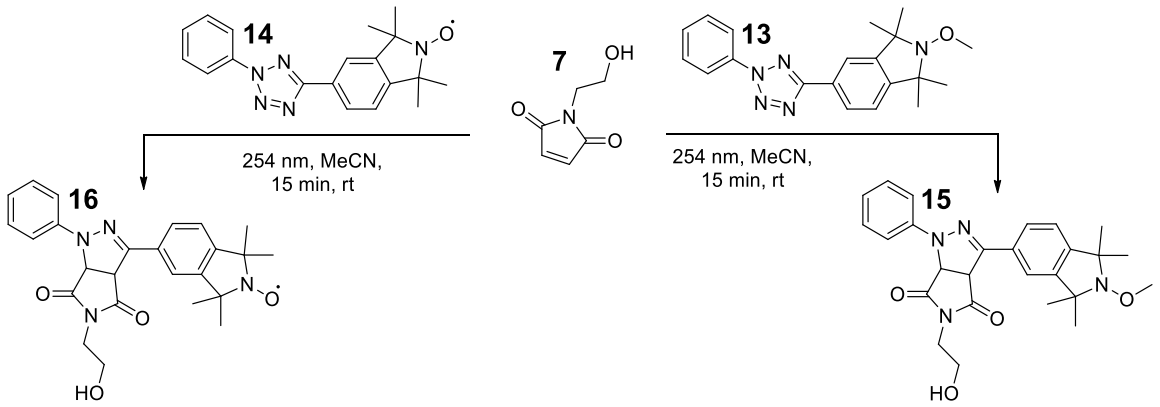

Scheme 24 NITEC of radical diaryl tetrazole **14** or methoxyamine **13** and maleimide **7** to form the radical pyrazoline **16** or methoxyamine **15**, respectively. Adapted with permission from [273]. Copyright 2016 American Chemical Society.

starting from the non-radical tetrazole **13** and maleimide **7** was expected. Interestingly, by applying identical reaction conditions to the nitroxide containing tetrazole **14**, full conversion of the reagents and the efficient formation of the desired cycloadduct was observed. Considering the fact that a variety of excited states are involved in the process of a nitrile imine formation from the tetrazole, the ability of nitroxide species to quench excited states should negate the photoreaction. In particular, if the nitroxide moiety is fused to the core structure of the diaryl tetrazole. However, no effect of the nitroxide on the NITEC reaction could be detected. The quenching performance of the nitroxide is demonstrated by fluorescence emission spectra comparison of the radical containing **16** to the corresponding non-radical methoxyamine derivative **15** (refer to Figure 22). A significantly improved fluorescence quenching was observed in comparison to the first- and second-generation compounds (ca. 31-fold fluorescence decrease with respect to the corresponding diamagnetic species **15**). The strong increase in the quenching efficiency arises due to the extremely close proximity of the single electron and the pyrazoline containing fluorophore compared to first- and second-generation species **3** and **8** (3.5 Å versus 9.3 and 5.5 Å for **3** and **8**, respectively) (refer to

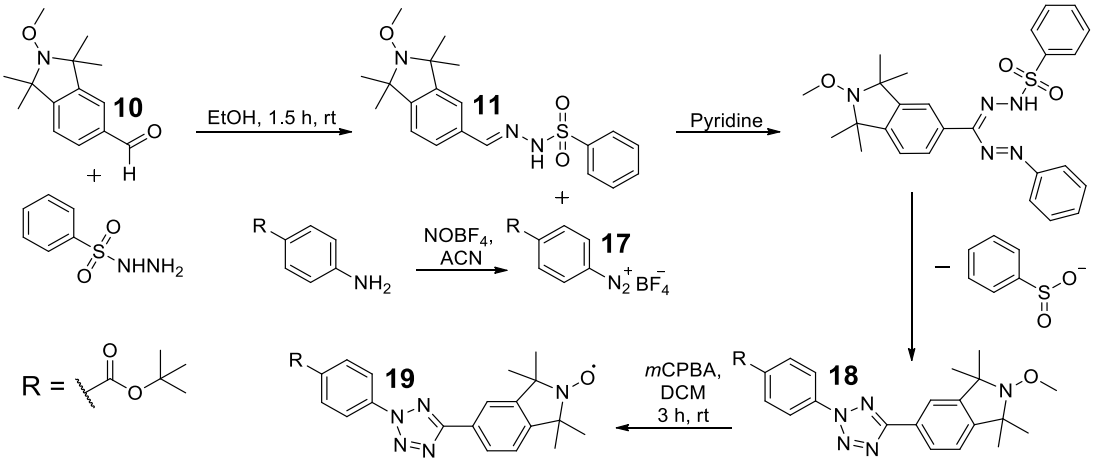

Scheme 25 Synthesis of radical diaryl tetrazole **17**. Phenylsulfonylhydrazone **11** was formed from methoxyamine **10** and benzenesulfonohydrazide. Arenediazonium salt **17** was formed from aniline. The methoxyamine **18** was oxidized to radical diaryl tetrazole **19**. Adapted with permission from [273]. Copyright 2016 American Chemical Society.

Figure 21). In addition better overlap of the 2p orbital of the nitroxide and the π-system of the fluorophore is assumed as both are located in the same plane (refer to Figure 21). The resulting fluorescence quenching performance of the compound **16** is similar to the performance of current employed PFNs.[118]

Although the third-generation of pyrazoline containing PFNs provides efficient 'switch on/off' behaviour, the corresponding diaryl tetrazole is lacking functional groups suitable for further modification such as attachment to biologically relevant species or surfaces. The possibility of simple and efficient functionalization with nitroxide capped diaryl tetrazole is a key factor for the most potential applications, especially in the field of the biology. Therefore, a *tert*-butyl ester functional diaryl tetrazole **18** was synthesized from the 1,1,3,3-tetramethylisoindoline-2-oxyl **10** and *tert*-butyl ester functionalized arenediazonium salt **17** (refer to Scheme 25). Again, the formed non-radical diaryl tetrazole **18** was deprotected employing *m*CPBA to yield corresponding free radical species **19**. The *tert*-butyl ester moieties of the species **18** and **19** is suitable for further modification of the tetrazole derivative. By a hydrolysis or a reduction of the ester moiety, an acid or an alcohol group can be introduced. Both

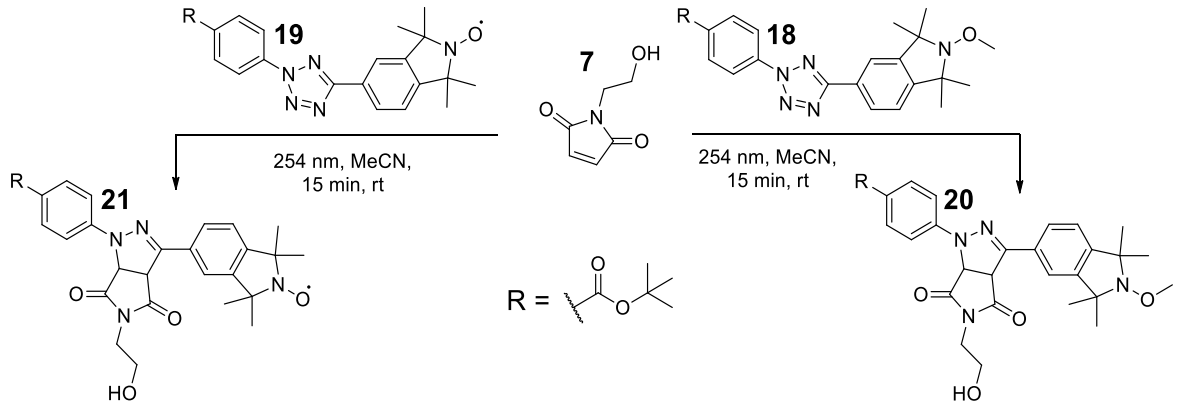

Scheme 26 NITEC of radical diaryl tetrazole **19** or methoxyamine **18** and maleimide **7** to form radical pyrazoline **21** or methoxyamine **20**, respectively. Adapted with permission from [273]. Copyright 2016 American Chemical Society.

functionalities enable a variety of ligation approaches. Diaryl tetrazoles **18** and **19** were both converted to cycloadducts **20** and **21**, respectively by exposing them to 254 nm irradiation for 15 min in presence of maleimide **7** (refer to Scheme 26). Again, no effect of the nitroxide on the NITEC reaction of the diaryl tetrazole **20** was observed. Interestingly, the introduction of the ester moiety to the N^2 phenyl ring had no significant effect on the cycloaddition reaction rate. Full conversion of the reagents and formation of the desired product was observed by employing similar reaction conditions as for PFN generations 1-3.

The quenching performance of the nitroxide is demonstrated by fluorescence spectra comparison of radical species **21** and the corresponding non-radical methoxyamine derivative **20** (refer to Figure 22). As the distance and the orientation between the fluorophore and the nitroxide are similar for the third and fourth generation of PFN, similar photophysical properties can be expected. The 'switch on/off' performance of **21** is comparable to the PFN of the third generation (21-fold fluorescence decrease for paramagnetic species **21** with respect to the corresponding diamagnetic species **20**). Red-shift of the emission spectra of **20** and **21** was the only photophysical change observed with respect to the third generation of the PFNs.

Quantum yields and corresponding extinction coefficients of the formed cycloadducts (refer to Figure 22) were determined in order to quantify the visual fluorescence quenching (refer to Table 1). As discussed above, short distance between the fluorophore and the nitroxide, as well as increased conjugation between both species enhances the quenching performance. The "switch on/off" performance of the first generation is rather poor, since the distance between the single electron of the nitroxide and the fluorescent pyrazoline is relatively long. Additionally, the non-conjugated character of linkage between the nitroxide and the pyrazoline decreases the quenching

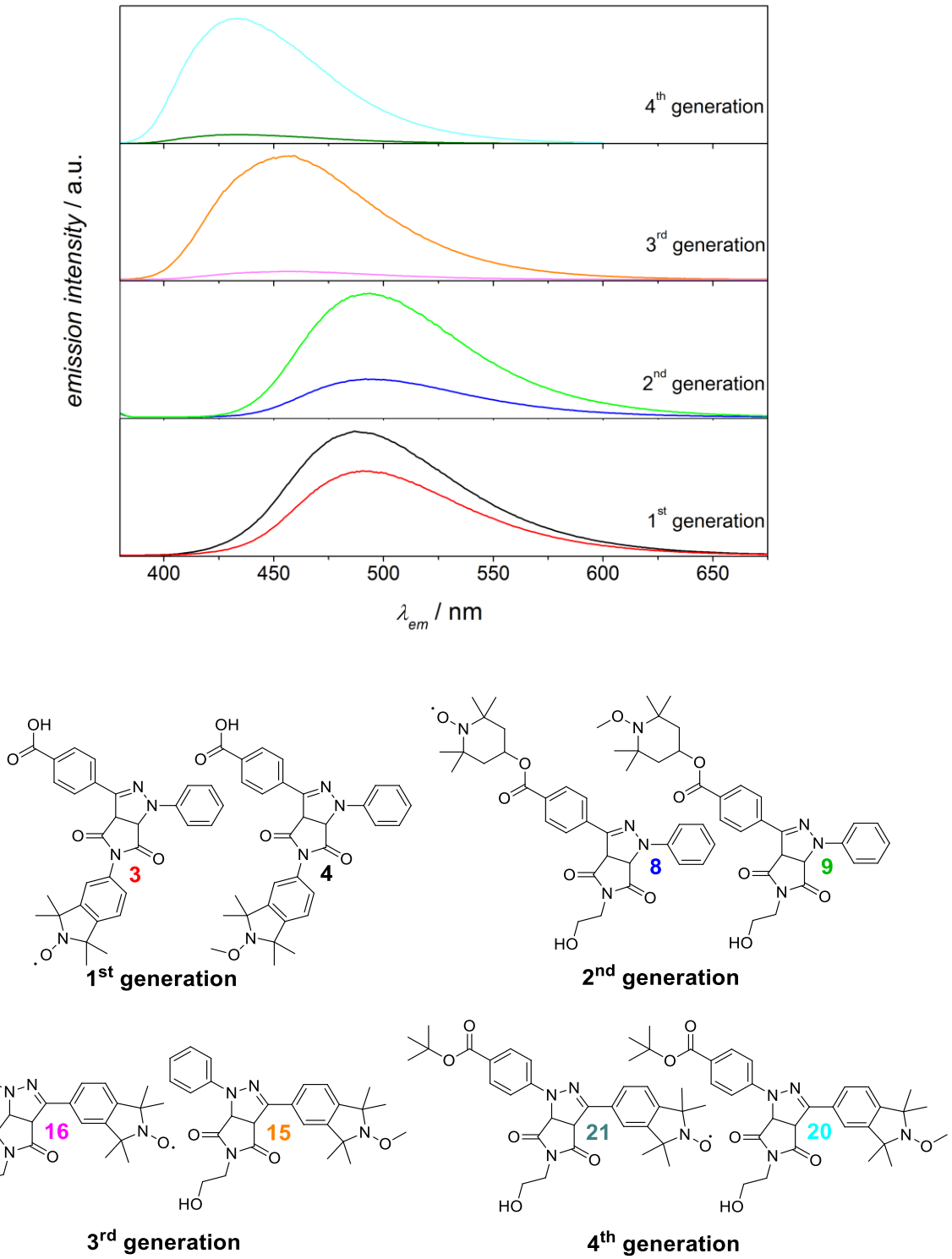

Figure 22 Normalized fluorescence emission spectra of radical pyrazolines **3**, **8**, **16**, and **21** and corresponding methoxyamines **4**, **9**, **15**, and **20** in MeCN, λ_{ex} = 377 nm (spectra of the radical pyrazoline and the corresponding methoxyamine were optically matched based on their UV absorbance at the excitation wavelength). Spectral lines have been color-coded with the structure numbers above for facile identification. Adapted with permission from [273]. Copyright 2016 American Chemical Society.

Table 1 Extinction coefficients and quantum yields of fluorescence for radical pyrazoline derivatives **3**, **8**, **16**, and **21** and corresponding methoxyamine analogues in MeCN (λ_{ex} = 365 nm). Adapted with permission from [273]. Copyright 2016 American Chemical Society.

cycloadduct	extinction coefficient / $M^{-1}\cdot cm^{-1}$	quantum yield (Φ_F)
3	14598	0.369
4	18144	0.436
8	17940	0.18
9	14884	0.58
15	12610	0.50
16	23791	0.016
20	25133	0.77
21	15936	0.036

efficiency due to the loss of the aromatic character of the tetrazole species at the joint position between the nitrile imine and the maleimide. An improved quenching performance was observed for the second generation of PFNs (3–fold) due to the shorter distance between the single electron of the nitroxide and the fluorescent pyrazoline moiety. Furthermore, the ester group, applied as a linker between the nitroxide and the pyrazole, can enhance the quenching due to improved conjugation between single electron of the nitroxide and the pyrazoline. For the third and fourth generation of the PFNs, almost complete fluorescence quenching was detected (31- and 21-fold quenching respectively). Such behaviour can be addressed to the extremely close proximity of the fluorophore and the nitroxide, as the nitroxide species was fused into the core structure of the tetrazole. The extinction coefficients, for the formed cycloadducts, range between 16000 and 25000 $M^{-1}\cdot cm^{-1}$, with the difference being attributed to the experimental error introduced by the small amounts of pyrazoline compound applied (< 1 mg). Moreover, subtle differences in the structures of the cycloadducts could also affect these values.

The comparison between the photo physical properties of the nitroxide containing pyrazoline and the corresponding non-radical pyrazoline simulates the 'ideal' quenching process. However, the 'switch on/off' performance of the formed PFNs was suggested to decrease for model sensing experiments. Full conversion of the nitroxide species to the corresponding non-radical derivative is challenging. Furthermore, side reactions affecting the fluorescence behaviour of the PFN can occur. Apart from the sensitivity and stability of the PFN, the time needed for the full switch on of the fluorescence under given conditions is vital. Only if the fluorescence peak intensity can be reached rapidly, the respective sensing data are reliable. In order to address the noted requirements, the ability of the profluorescent pyrazolines to perform as sensors for redox or radical systems was estimated by exposing the PFNs to a model redox processes or by placing them into a reactive radical containing environment. The redox conditions were simulated by dissolving the free radical containing pyrazolines **3**, **8**, **16** and sodium ascorbate (NaAsc) (ratio 20:1) in methanol. The resulting solution was monitored by fluorescence spectroscopy at 373 nm every 2 minutes for a period of 40 min (refer to Figure 23). NaAsc is an established nitroxide reducing agent, allowing mild reduction of the free radical containing species to the corresponding hydroxylamine occurs (refer to Scheme 27). In addition, the sodium ascorbate is suitable for *in vivo* applications, as it is soluble in water and non-toxic. Alternative reduction agents such as hydrazine derivatives are less suitable for the reduction experiments, as the species is often highly toxic and less selective. In presence of oxygen, the hydroxylamine formation is reversible, and a reoxidation of the hydroxylamine back to the

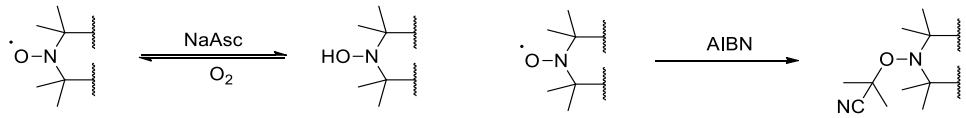

Scheme 27 General mechanism of the reduction of a nitroxide species in presence of NaAsc (left), radical scavenging reaction of a nitroxide species in presence of AIBN (right).

nitroxide can occur. As the model experiment was performed under atmospheric conditions, an excess of NaAsc was employed to suppress the reoxidation process and ensure the efficient formation of the fluorescent non-radical species. While no fluorescence increase was observed for compound **3**, a slight increase in the fluorescence intensity was detected for compound **8** (ca. 15 %) (refer to Figure 23). Cycloadduct **16** displayed the strongest fluorescence increase (ca. 7-fold) (refer to Figure 23), whereby a dramatic, exponential increase of the fluorescence intensity was observed over the first 35 min, indicating efficient formation of the fluorescent hydroxylamine. No induction period was detected. In the time period between 35 and 45 min, the fluorescence intensity reached a plateau due to the establishment of the equilibrium between the nitroxide and the hydroxylamine species. The redox sensitivity of the nitroxide functionalized

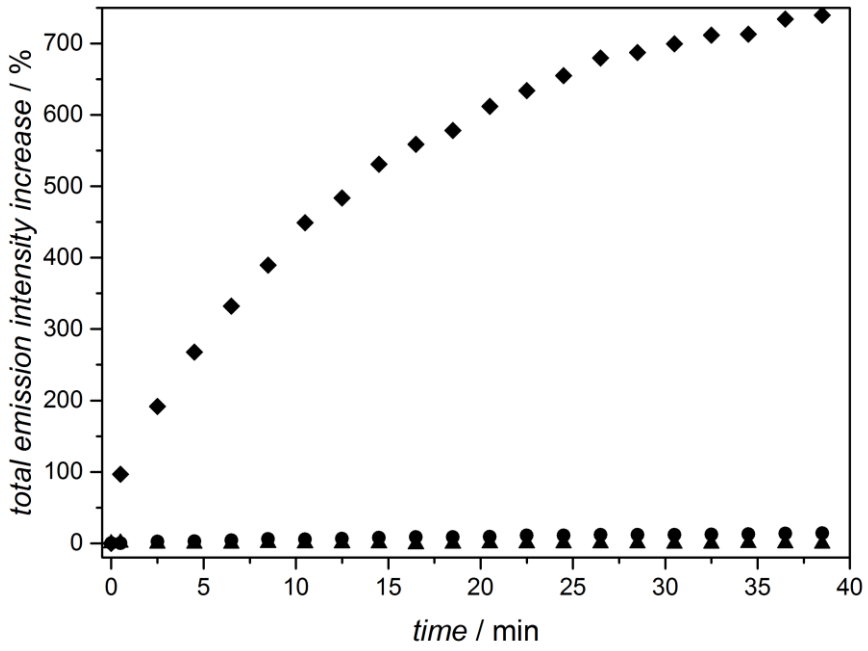

Figure 23 Evolution of the fluorescence emission intensity at 273 nm of the pyrazolines **3** (▲), **8** (●), **16** (♦) with time in the presence of sodium ascorbate (NaAsc) in methanol ($c_{pyrazoline}$ = $1.68 \cdot 10^{-5}$ mol·L^{-1}, ratio pyrazoline / NaAsc: 1 / 20). Adapted with permission from [273]. Copyright 2016 American Chemical Society.

pyrazoline ($c_{pyrazoline}$ = 17 µmol·L^{-1}, c_{NaAsc} = 340 µmol·L^{-1}, $t_{max\ fluorescence}$ = 35 min) toward sodium ascorbate is comparable to the literature known aromatic nitroxides ($c_{pyrazoline}$ = 3 µmol·L^{-1}, c_{NaAsc} = 5000 µmol·L^{-1}, $t_{max\ fluorescence}$ = 60 min).[123]

A reactive radical containing environment was simulated by placing nitroxide **16** in MeCN in presence of AIBN (ratio **16** / AIBN: 1:5). After purging with Ar for 30 min, the resulting mixture was heated to 60 °C. Fluorescence spectroscopy was applied for monitoring the PFNs 'switch on' performance at (λ_{ex} = 373 nm) every 2 minutes for a period of 70 min (refer to Figure 24). AIBN is a thermo-responsive initiator. Exposed to elevated temperatures, it decomposes and carbon centered radicals are released. The resulting isobutyronitrile radicals are available for a

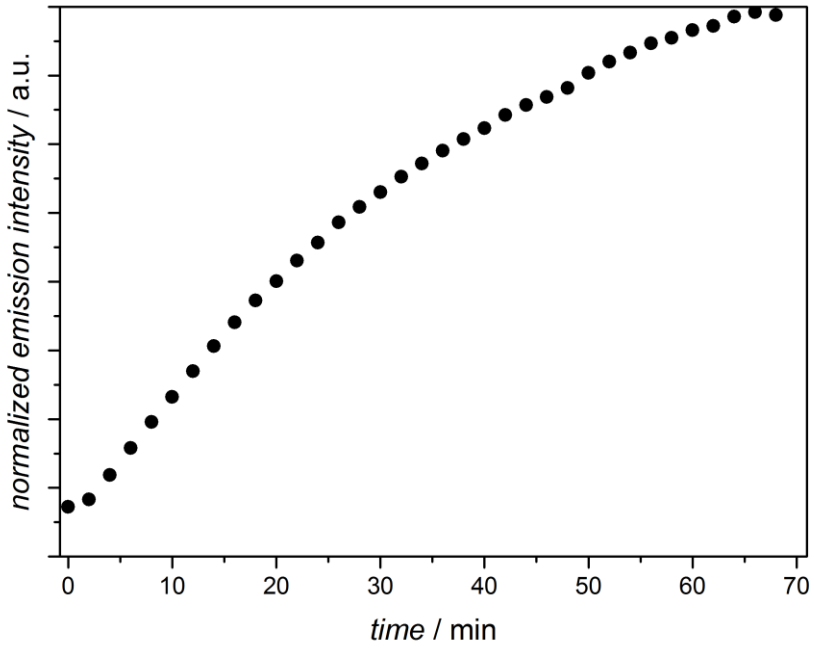

Figure 24 Evolution of the fluorescence emission peak intensity of the radical diaryl tetrazole **16** with time in the presence of AIBN in MeCN (c_{16} = 1.68·10^{-5} mol·L^{-1}, ratio **16** / AIBN: 1 / 5). The results for sensitivity of nitroxide containing pyrazolines towards radicals are in good agreement with the literature.[278] The developed system allows detection of carbon centered radicals at µM concentrations. Adapted with permission from [273]. Copyright 2016 American Chemical Society.

recombination reaction with the free single electron of the nitroxide moiety, leading to a 'switch on' of the fluorescence of the PFN (refer to Scheme 27). After a short induction time, a dramatic increase in the fluorescence of the monitored reaction mixture was observed. 70 min were needed to reach the peak fluorescence intensity. The emission of the PFN was observed to decrease after 70 min, indicating a radical driven formation of non-fluorescent side products or decomposition of the pyrazoline species. Compared to the reduction experiments, extended reaction times were needed to reach the maximum fluorescent intensity, which can be attributed to a smaller excess of AIBN applied. Also, competing termination reaction between isobutyronitrile radicals and incomplete decomposition of the AIBN after 70 min reduce the effective concentration of the radicals. However, PFN **16** displays excellent sensitivity towards carbon centered radicals, allowing detection of radicals at µM concentrations.

3.3 Conclusion

In summary, NITEC chemistry was employed to introduce a novel approach towards profluorescent nitroxides. A variety of nitroxide functionalized diaryl tetrazole species was designed and employed along known dipolarophile functional nitroxides, tetrazoles and maleimide derivatives for *in situ* formation of PFNs. Thus, different strategies for the covalent bond coupling between the fluorophore and the nitroxide were employed including linkage *via* NITEC reaction, or the direct attachment of the nitroxide moiety to the diaryl tetrazole. It was noted, that the presence of the nitroxide species had no influence on the process of the photoinduced cycloaddition. Efficient, rapid and clean formation of the desired cycloadduct under mild conditions was observed for all performed cycloadditions. Furthermore, the photo physical properties of the free radical containing cycloadducts and the respective non-radical hydroxylamine derivatives were compared, in order to estimate the quenching performance of the obtained PFNs. The quenching performance was demonstrated to be dependent on the distance and orientation between the unpaired spin of the nitroxide and the fluorophore. Shorter distances and planar orientation allowed for the best fluorescence quenching, while longer distances led to a poor 'switch on/off´ performance. To provide an attachment point for ligation reactions with the nitroxide functional tetrazoles a labile ester moiety was introduced. In addition, selected pyrazoline functional PFNs were investigated for their ability to detect redox/radical processes. Rapid 'switch on' times, good sensitivity and stability of the tested cycloadducts were confirmed in all examples.

Interestingly, the presence of the nitroxide in close proximity to the tetrazole species had no effect on the performance of the NITEC reaction when attached to the phenyl ring of the tetrazole in the C^5 position.

However, the introduction of the ester moiety to the phenyl ring in the N^2 position led to a shift of the fluorescence spectra to lower wavelengths for the corresponding pyrazoline derivative, while no effect on the fluorescence was detected for the attachment of the ester moiety to the phenyl ring in the C^5 position. The observation of such a dependency suggests that the position for the introduction of the substituents potentially plays a key role in modification of the photophysical properties of the diaryl tetrazole and the corresponding pyrazoline (e.g. for bathochromic shift of the NITEC trigger-wavelength).

4 Catalyst Free, Visible Light Induced Polymer Ligation

4.1 Introduction

In research to date, catalyst free, single electron induced coupling reactions have required almost exclusively the use of high energy UV light as a trigger. However, employing UV irradiation is a major limitation for the application of photo driven ligation methods for the design of (macro)molecules and their usage in the fields of biology or material science. This is due to a large majority of the organic, inorganic and biologically relevant moieties being UV sensitive. Therefore, exposure of those species to UV irradiation can facilitate unwanted side reactions or cause the formation of decomposition products. There are only limited examples of photo active compounds able to perform covalent linkage reactions induced by lower energy visible light. However, all known visible light coupling strategies are still in their infancy due to factors such as complex pathways for the synthesis of the photo active reagents and their lack of functionality, required for the further attachment to e.g. polymers or biologically relevant species. Herein, a novel visible light triggered, catalyst free ligation method *via* NITEC is introduced.[279] The presented approach enables efficient and exclusive linkage *via* formation of a new covalent bonds between a reactive nitrile imine, generated from a tetrazole, and an electron deficient double bond moiety under mild conditions. In

Parts of the current chapter are reproduced from Lederhose, P.; Wust, K. N. R.; Barner-Kowollik, C.; Blinco, J. P. *Chemical Communications* **2016**, *52*, 5928. Reproduced with permission of The Royal Society of Chemistry.

addition, it was possible to functionalize the tetrazole with a hydroxyl moiety, allowing for the simple attachment of the photo active group to other compounds *via* esterification. The methodology was applied for small molecule ligation, polymer end group modification and the design of block copolymers. A variety of dipolarophiles and polymer species were investigated, displaying the versatility and robustness of the presented strategy. In addition, the orthogonality of the coupling technique to a trithiocarbonate moiety, often used as a RAFT agent, was achieved, allowing the combination of the presented technique with RAFT process. Importantly, all of the synthesized cycloadducts are fluorescent in the NIR range, which can be a major feature for future bio-labelling applications.

4.2 Results and Discussion

Efficient formation of the nitrile imine in the visible light regime followed by a rapid and selective conversion of the *in situ* formed intermediate in a 1,3 dipolar cycloaddition are two key features that need to be fulfilled in a NITEC reaction. Both requirements were addressed through the introduction of functionalities to the core structure of the diaryl tetrazole, whereby modified synthetic paths from Chapter 3 were applied. Importantly, the photophysical properties of the chromophore employed, as well as its position in the tetrazole structure are crucial for a successful bathochromic shift of the NITEC reaction. In order to push the trigger wavelength of nitrile imine generation into the visible light region, the phenyl ring in the N^5 position of the tetrazole was extended from a phenyl to a pyrenyl ring system (refer to Scheme 28). This polycyclic aromatic species is known to absorb above 390 nm, if featured with appropriate substituents. Furthermore, the rather low fluorescence quantum yields of the pyrene moiety combined with good photosensitizing ability were expected to contribute to efficient photo-triggering of the tetrazole, in order to form the nitrile imine.[280] In contrast, chromophore species with high fluorescence yields and low photosensitizing performance were considered to be less suitable for the photo-triggering of a chemical reaction. The reason being that, due to the strong emission, the major part of the absorbed photo energy was suggested to be not available for chemical transformation of the molecule structure. The choice of the N^2 position as the attachment point for the pyrene moiety was driven by the results from the previous chapter, as well as careful studies of the tetrazole structures presented in the literature. As described in the Section 3.2 the fusing of the nitroxide species to the phenyl ring of the tetrazole core structure in the C^5 position had no influence on the photo-physical properties of the resulting tetrazole. Therefore, the introduction of the pyrene in the N^2 position was aimed. The selected design was supported by the literature, whereby

successful

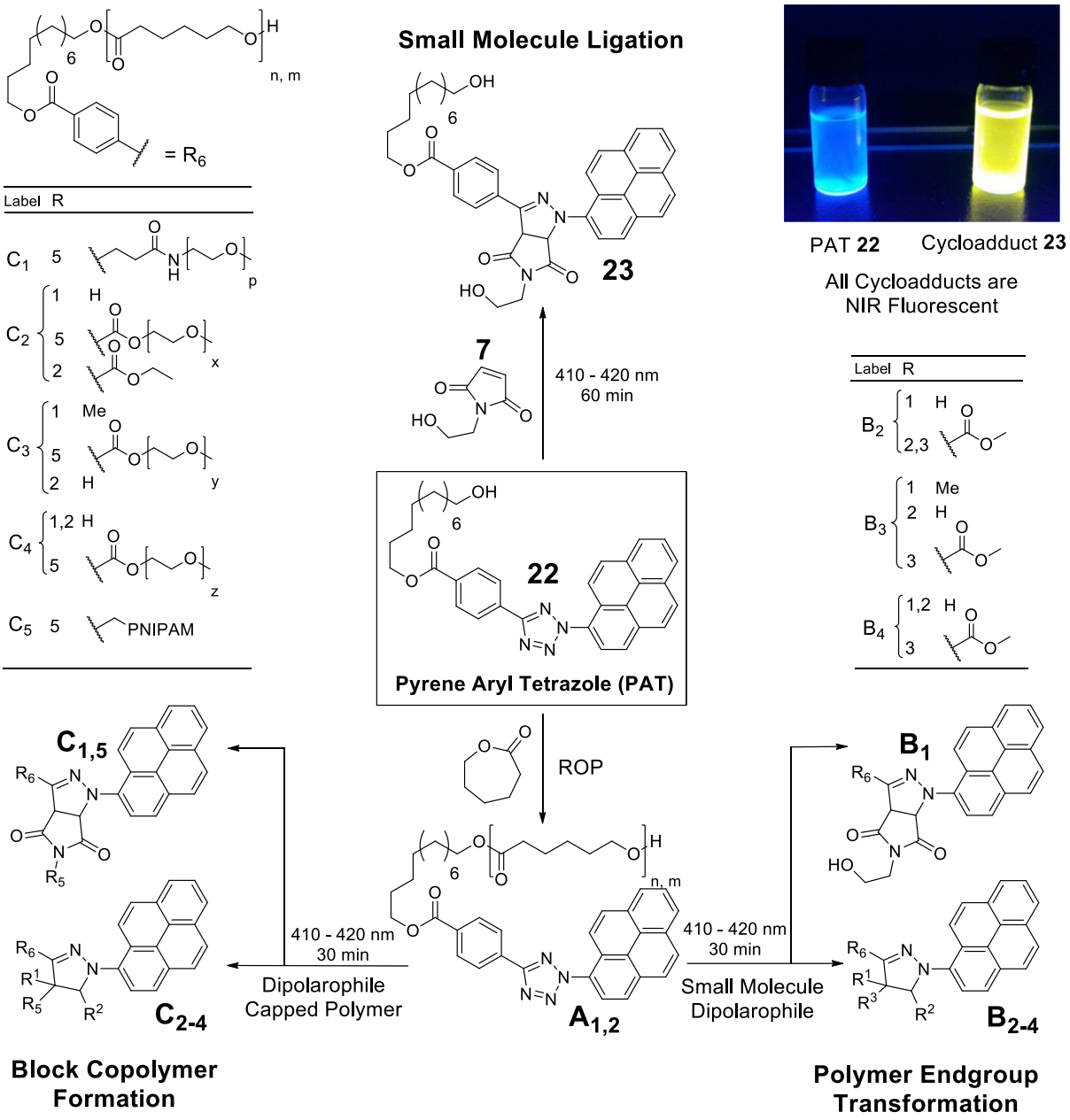

Scheme 28 Synthetic path for the visible light triggered formation of small molecule cycloadduct **23**, PCL formation **A1** (ratio PAT **22**: ε-caprolactone 1:24, 3 h, rt) and **A2** (ratio PAT **22**: ε-caprolactone 1:34, 7 h, rt) polymer end group modification and polymer-polymer ligation. For clarity only one regioisomere of **23**, **B3,4** and **C2-4** is displayed. Top left: NIR fluorescence of the cycloadduct **23**. Refer to Table 2 for reaction details of cycloadditions involving macromolecular species.[279] Reproduced with permission of The Royal Society of Chemistry.

Table 2 Reaction details for formation of macromolecular cycloadducts **B_{1-4}** and **C_{1-5}** (refer to Section 8.2.3 the structure of the employed dipolarophiles).[279] Reproduced with permission of The Royal Society of Chemistry.

Cyclo adduct	PAT end capped PCL	c_{PCL} / mmol·L^{-1}	$c_{dipolarophile}$ / mmol·L^{-1}	solvent	$Đ^{[a]}$	$M_n^{[a]}$ / kDa
B_1	A_1	0.18	2.7	MeCN	1.12	2.2
B_2	A_1	0.18	2.7	MeCN	1.11	2.1
B_3	A_1	0.18	2.7	THF	1.13	2.1
B_4	A_1	0.18	2.7	THF	1.14	2.1
C_1	A_2	0.12	0.18	MeCN	1.12	8.0
C_2	A_2	0.12	0.18	MeCN	1.15	8.4
C_3	A_2	0.12	0.18	THF	1.14	8.5
C_4	A_2	0.12	0.18	THF	1.15	8.7
C_5	A_2	0.12	0.14	MeCN	1.24	8.8

[a]M_n and $Đ$ of cycloadducts were determined by GPC using PMMA calibration standards.

bathochromic shift of the trigger wavelength for the NITEC reaction was reported, if expanded aromatic systems were introduced in the N^2 position.[205,207,242] To assure rapid and selective conversion of the nitrile imine formed, an ester moiety was attached to the phenyl ring of the tetrazole in the C^5 position (refer to Scheme 28). The introduction of an electron withdrawing group in the activated position allows more efficient cycloadduct formation with electron deficient dipolarophiles.[14] In contrast, diaryl tetrazole derivatives featuring electron donating moieties in the activated position of the C^5 phenyl ring are less selective and are reported to undergo rapid cycloaddition reactions without respect to electronical structure of the dipolarophile[189] as well as react with water or form dimers of nitrile imine species.[187] In addition, the diole extended ester group of PAT tetrazole provides an attachment point for further linkage reactions, making the PAT **22** suitable as a coupling reagent for biological applications, as well as for the design of macromolecular architectures. The PAT **22** was

prepared in a two-step synthesis affording 30 % overall yield. The analysis of the photophysical properties of the tetrazole species revealed an absorbance maximum at 345 nm with a tail reaching beyond 400 nm, allowing potential triggering of the NITEC reaction in visible light mode. Furthermore, fluorescence maximum at 598 nm with a quantum yield of 0.27 was observed, indicating that a major part of the absorbed light energy is converted in non-radiative processes, presumably involving ISC.

To verify the ability of the PAT to participate in a visible light induced generation of the nitrile imine species, as well as to prove the formed intermediate to undergo a cycloaddition reaction, a small molecule study was performed. The tetrazole species **22** (1 eq.) and the maleimide **7** (1.2 eq.) were both dissolved in MeCN and irradiated at 410 -420 nm at ambient temperature (refer to Scheme 28). Full conversion of the tetrazole species and formation of the target compound **23** was detected after 60 min. It should be noted that longer reaction times were needed if higher concentrations of the reagents were applied. The obtained reaction mixture were purified by column chromatography and characterized by NMR, ESI-MS, fluorescence spectroscopy, as well as UV-Vis spectroscopy. In addition, a control experiment employing the 'UV-active tetrazole' 4-(2-(4-methoxyphenyl)-2H-tetrazol-5-yl)benzoic acid was performed under identical conditions as applied for the PAT conversion. No conversion of the tetrazole species was detected, varying the PAT tetrazole to be the only known functionalized coupling species with a trigger wavelength of > 400 nm. The ^{1}H NMR data of the tetrazole **22** and the corresponding cycloadduct **23** are shown in Figure 25. A comparison of both spectra reveals several changes in the chemical structure of the tetrazole after the ligation trial has occurred. The new appearing multiplet (h) at 3.6 ppm can be assigned to the methylene moieties of the maleimide **7**, incorporated in the structure of the cycloadduct. The resonances (g) at 4.7 and (f) at 5.4 ppm can be assigned to the adjacent protons of the newly formed 5-membered ring.

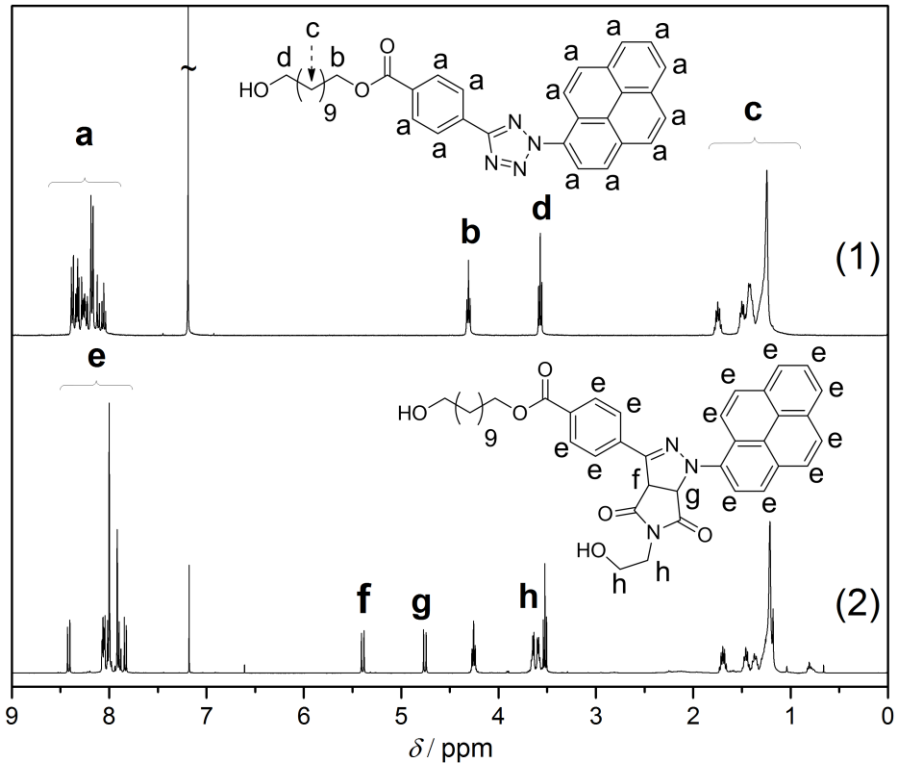

Figure 25 ^{1}H NMR spectra before and after the NITEC ligation with a small molecule maleimide. Refer to Scheme 28 for reaction conditions. (1) pyrene functional aryl tetrazole **22** before irradiation; (2) reaction mixture after irradiation (410 - 420 nm) and purification *via* column chromatography.[279] Reproduced with permission of The Royal Society of Chemistry.

The aromatic resonances of the PAT, located between 7.9 and 8.3 ppm change their position after the ligation reaction to become a broader multiplet with a new pattern between 7.8 and 8.4 ppm. As expected the positions of the signals (c), (d) and (b) remained unchanged.

The photophysical properties of the compounds applied for the small molecule study were investigated by fluorescence spectroscopy and UV-Vis spectroscopy in order to gain further knowledge about the reaction process of visible light NITEC (refer to Figure 26). By comparison of the UV-Vis absorbance spectra of tetrazole **22** and pyrazoline **23,** a strong overlap in the range 410 – 420 nm, employed for triggering of the NITEC reaction, was observed. As the absorbance of the **23** is significantly higher, compared to the absorbance of the PAT **22**, increasing inhibition of the

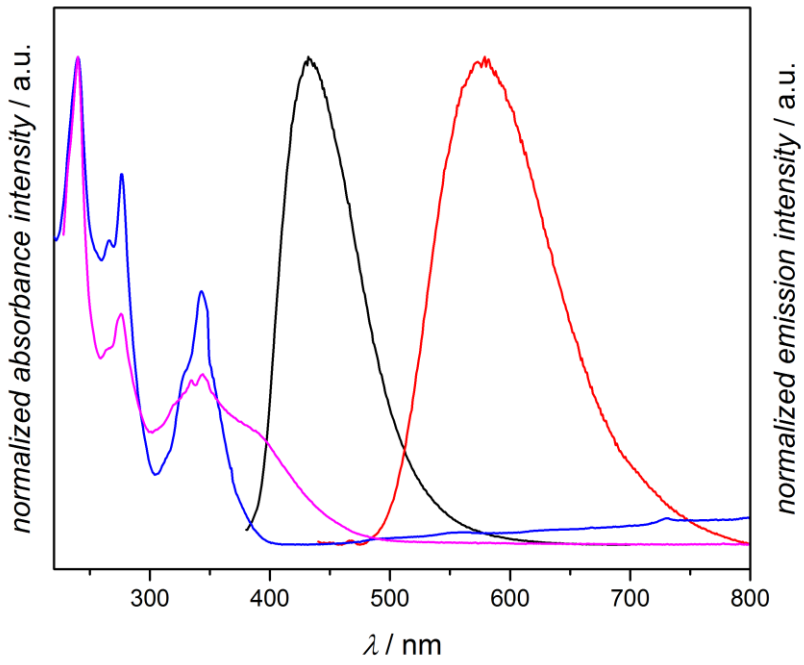

Figure 26 Absorption spectrum of the PAT **22** (blue line), cycloadduct **23** (pink line) and the emission spectrum of PAT **22** (black line, λ_{ex} = 365 nm), cycloadduct **23** (red line, λ_{ex} = 400 nm). All spectra were detected in MeCN.[279] Reproduced with permission of The Royal Society of Chemistry.

photoreaction with increasing cycloadduct formation can be assumed. The major part of the applied irradiation energy could potentially be converted by the **23**, leaving only a minor component of the photons available for the NITEC reaction. However, by applying a strong irradiation source and highly diluted reaction mixtures, the reaction was driven to quantitative conversion in only 60 min. The examination of the fluorescence spectra of the compounds **22** ($\lambda_{fl,\ max}$ = 441 nm) and **23** ($\lambda_{fl,\ max}$ = 441 nm) revealed a significant shift to higher wavelengths of the emission after the NITEC reaction. The detected fluorescence tail of the pyrazoline species **23**, reaching into NIR region, could potentially be applied in the future for *in vivo* labelling and tracking. The employment of near infrared regime provides a distinct advantage compared to visible light, as the emission of

the pyrazoline **23** does not overlap with the autofluorescence of the living tissue.[281-283]

After the visible light NITEC reaction was utilised successfully for the small molecule ligation, the extension of the concept as a tool for macromolecular design was attempted. The hydroxyl functional PAT was employed as an initiator in a ring opening polymerization (ROP) of ε-caprolactone in the presence of triazabicyclodecene in DCM, in order to form tetrazole end capped poly-*ε*-caprolactone (PLC). Two sizes of PCL (**$A_{1,2}$**) were obtained *via* variation of the initiator to monomer ratio and the application of different reaction times (refer to Scheme 28). Both polymers revealed excellent fidelity of the PAT end group and narrow polydispersity (refer to Section 8.2.3).

To verify that the visible light NITEC is suitable for design of macromolecular architectures, end group modification of the PAT end capped PCL **A_1** (M_n = 2.0 kDa (SEC), $Đ$ = 1.10) was performed. A variety of electron deficient alkene derivatives such as maleimide **7**, diethyl fumarate, MMA and MA were applied as dipolarophile, in order to demonstrate the versatility of the novel, visible light induced NITEC reaction. After dissolving the polymer species (1 eq.) in the presence of the corresponding dipolarophile (1.5 eq.) in an appropriate solvent, the resulting reaction mixture was irradiated at 410 - 420 nm for 30 min at ambient temperature (refer to Scheme 28). Full conversion of the tetrazole moiety and exclusive formation of the target cycloadducts **B_{1-4}** were observed for all performed reactions. The choice of solvent was driven by the reactivity of the dipolarophile. MeCN was applied as the solvent for the cycloadditions with maleimide **7** and diethyl fumarate, as both are very electron deficient alkene species, and MeCN would allow their rapid reaction with the nitrile imine intermediate. However, the MeCN was replaced with THF for the coupling reactions with MMA and MA dipolarophile, as both alkenes display a higher electron density of the double bond, which

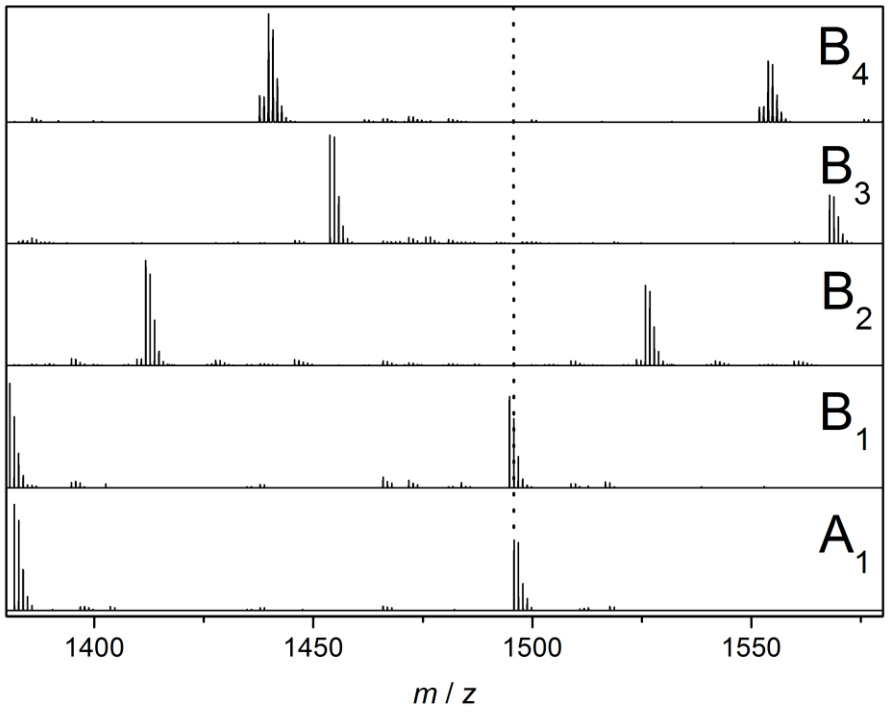

Figure 27 ESI-MS spectra of coupling reaction of PAT end capped PCL **A₁** and the corresponding dipolarophiles to form cycloadducts **B₁₋₄**. (Refer to Scheme 28 for structures of formed cycloadducts **B₁₋₄** and the reaction conditions); (Refer to Section 8.2.3, Table 6 for the exact masses and experimental values of the depicted polymer species **A₁** and **B₁₋₄**); location of the **A₁** signal is illustrated by a dotted line; rearomatisation of **B₄** was detected (Refer to Section 8.2.3 for further details).[279] Reproduced with permission of The Royal Society of Chemistry.

Table 3 Sum formula, the exact masses for experimental results, theoretical values and the deviation of both for PAT end capped PCL **A₁** and cycloadducts **B₁₋₄**.[279] Reproduced with permission of The Royal Society of Chemistry.

Label	Sum formula	m / z_{exp}	m / z_{theo}	$\Delta m / z$
A₁	$[C_{83}H_{116}N_4NaO_{19}]^+$	1495.815	1495.813	0.002
B₁	$[C_{83}H_{113}N_3NaO_{20}]^+$	1494.787	1494.782	0.005
B₂	$[C_{83}H_{114}N_2NaO_{21}]^+$	1525.818	1525.812	0.006
B₃	$[C_{82}H_{114}N_2NaO_{19}]^+$	1567.862	1567.859	0.003
B₄	$[C_{87}H_{122}N_2NaO_{21}]^+$	1553.831	1553.844	0.013

decreases the efficiency of their addition reaction with the nitrile imine species. If performed in MeCN, the nitrile imine acts also as a dipolarophile and can be partially converted in a cycloaddition with the C-N triple bond of the acetonitrile.

The short length of the PCL, and the low molecular weight of the dipolarophiles employed allows for the simplified purification and characterization of the cycloadducts. The ESI-MS spectra of PAT end capped **A_1** as well as the cycloadducts **B_{1-4}** is depicted in Figure 27. The corresponding theoretical and experimental m / z values are presented in Table 3. Full conversion of polymer **A_1** and almost exclusive formation of the target compounds **B_{1-4}** were detected. Good agreement between the predicted m / z values and the experimental results were observed for species **B_{1-3}**. In the mass spectrum of **B_4** a second product distribution with a shift of 2 Da compared to the distribution of the desired compound is present. This arises due to the rearomatisation reaction of **B_4**. The protons of the newly formed pyrazoline ring are less sterically hindered compared to the corresponding protons of species **B_{1-3}**. Therefore the thermodynamically favorited rearomatisation product is more likely to occur (refer to Scheme 29). A larger difference between the calculated m / z values and the experimental can be addressed to the overlap of the signals of **B_4** and **B_{4b}**, resulting in intensity changes in the isotopic pattern of the respective signals. It should be noted that minor amounts of undefined side products were also observed. However, the spectra of **B_{1-4}**

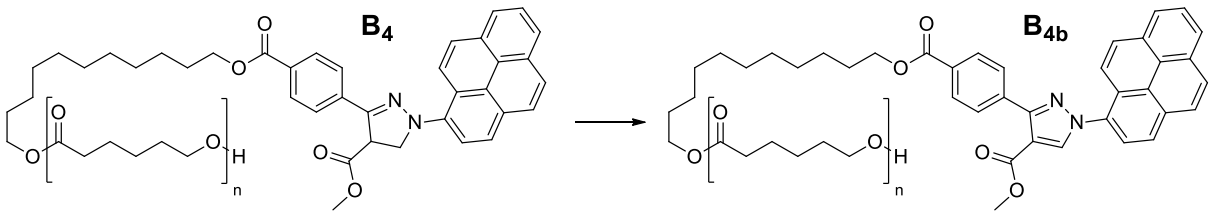

Scheme 29 Rearomatisation of the macromolecular species **B_4** under ESI-MS conditions.

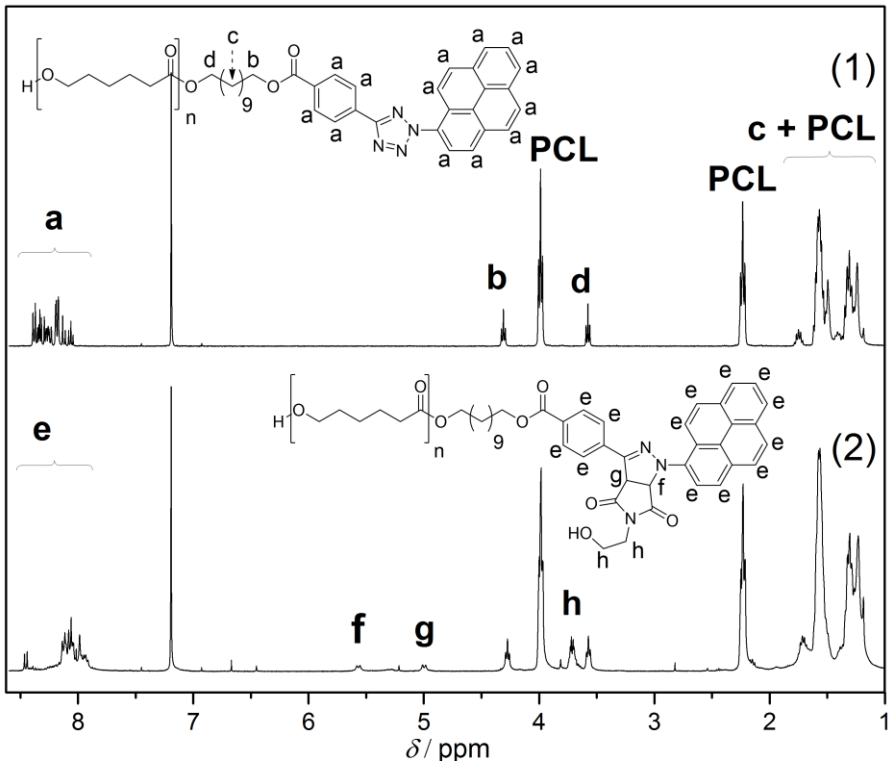

Figure 28 ^{1}H NMR spectra before and after photoinduced coupling of $\mathbf{A_1}$ with small molecule maleimide **7**. Refer to Scheme 28 for the reaction conditions. (1) PAT functional PCL $\mathbf{A_1}$ before irradiation; (2) reaction mixture after irradiation with visible light (410 – 420 nm) ($\mathbf{B_1}$).[279] Reproduced with permission of The Royal Society of Chemistry.

are remarkably clean considering the fact that the ESI-MS data was collected without further purification after the NITEC reaction. In addition, the rather poor ionisation properties of the pyrazoline compounds formed make the slight signals of impurities appear more distinct than in other characterization techniques (i.e. NMR). As such, the apparent yield is most likely underestimated by ESI-MS.

In order to provide a quantitative proof for the efficiency of the visible light induced end group modification *via* NITEC, ^{1}H NMR characterization of the cycloadducts $\mathbf{B_{1\text{-}4}}$ were performed. A comparison of the spectra of $\mathbf{A_1}$ and $\mathbf{B_1}$ was selected as a representative example of all end group conversions (refer to Figure 28). Full conversion and exclusive formation of the targeted cycloadduct was observed. No side products are visible, which is indicative for an efficient and clean end group modification. Compared to the

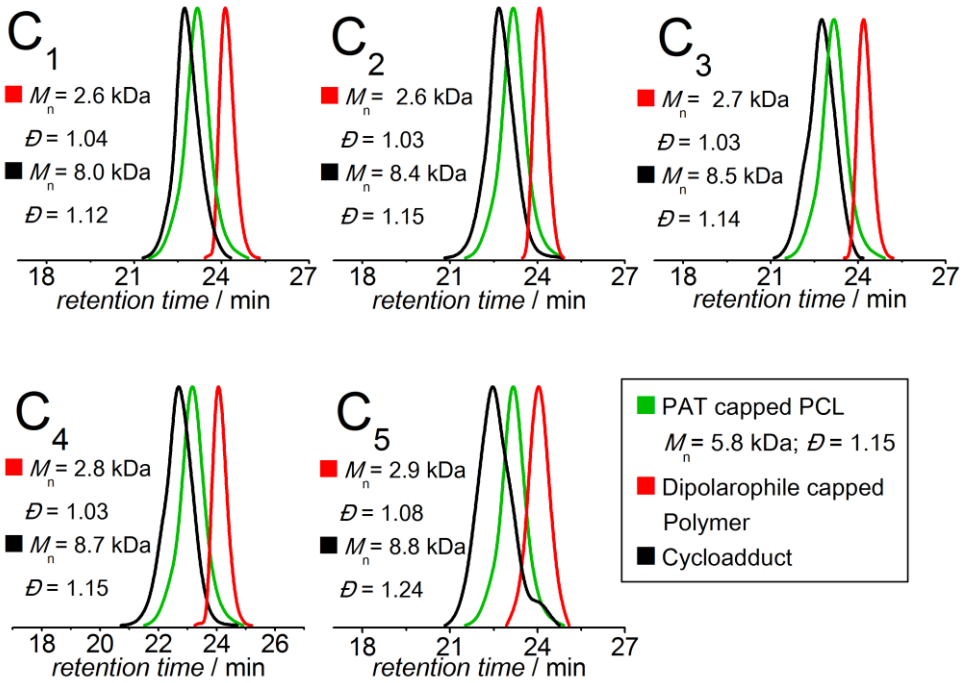

Figure 29 Normalized SEC traces of PAT functional PCL **A₂** (green line), corresponding dipolarophile functional PEG or PNIPAM (red line) and via NITEC formed block copolymers **C₁₋₅** (black line) respectively. M_n and $Đ$ were determined by GPC using PMMA calibration standards.[279] Reproduced with permission of The Royal Society of Chemistry.

spectrum of **A₁**, the NMR spectrum of **B₁** reveals several changes. A new resonance (h) between 3.6 and 3.7 ppm appears, which is assigned to the methylene protons of the introduced maleimide. Furthermore, the new signals (g) and (f) at 5.0 and 5.6 ppm respectively, were assigned to the adjacent protons of the newly formed 5-membered ring. The pattern of the resonances in the aromatic region (a) also changed the structure and appeared relocated at lower fields (e). As expected, the backbone resonances remained unchanged, and were not affected by the coupling reaction. Importantly, all synthesized pyrazoline containing cycloadducts show significant fluorescence in the NIR region.

After the visible light NITEC was verified to be an efficient methodology for polymer end group conversion, the concept was applied for the formation of block copolymers. PCL **A₂** (M_n = 5.8 kDa (SEC), $Đ$ = 1.15) was coupled with a range of dipolar functional PEG species. In addition, PNIPAM

prepared under RAFT conditions was coupled with PCL **A_2**, in order to demonstrate the orthogonality of the NITEC approach with RAFT agents. The PAT containing PCL (1 eq.) and corresponding dipolarophile (1.5 eq.) were dissolved in MeCN or THF and exposed to blue light (410 - 420 nm) for 30 min at ambient temperature (refer to Scheme 28). The water soluble polymer block (PEG or NIPAM) was applied in excess, as the unreacted residual can easily be removed by an aqueous work up. The resulting block copolymers were analysed *via* SEC (refer to Figure 29). For all cycloaddition reactions a new, monomodal molecular weight distribution at lower retention times was observed, while the traces of the starting polymers vanished. In addition, the *Đ* values of the cycloadducts **$C_{1\text{-}4}$** decreased, underpinning the success of the ligation (refer to Table 2). The small, low molecular shoulder observed for species **C_5** can be assigned as the residual PNIPAM **D_2**, as the compound was used in excess. The structures of all cycloadducts were confirmed by ^{1}H NMR (refer to Section 8.2.3). As with all pyrazolines arising from previous coupling reactions *via* the visible light NITEC, all the cycloadducts emit fluorescence in the NIR region.

4.3 Conclusion

The current chapter presents a novel approach for efficient, visible light induced, catalyst free, coupling chemistry. The design and application of a novel pyrene functional tetrazole species, able to participate in visible light induced NITEC reaction at 410 – 420 nm, is described. Rapid, clean and efficient formation of the target coupling products was observed for all performed cycloadditions. The concept was proven *via* ligation of low molecular weight dipolarophiles, whereby NMR, ESI-MS, fluorescence spectroscopy and UV-Vis spectroscopy were performed in order to optimize the reaction conditions and gain further knowledge of the reaction process. In addition, PAT end capped PCL was synthesized and employed for end group modification and block copolymer formation, demonstrating the potential of the novel introduced methodology as a tool for the synthesis of macromolecular architectures. A variety of dipolarophile species such as fumarate, maleimide and (meth)acrylates were utilised as dipolarophiles, in order to demonstrate the versatility of the coupling technique. Furthermore, the orthogonality of the NITEC reaction to trithiocarbonates was shown by coupling the PAT functional PCL with PNIPAM prepared under RAFT conditions. Importantly, all synthesized cycloadducts have significant emission in the NIR region. A significant bathochromic shift of the trigger wavelength for the NITEC reaction was achieved compared to the previous systems. However, tetrazole activation in the NIR region remains an intriguing challenge, as it would allow conjugation reactions in deep tissue.

5 Near Infrared Photoinduced Coupling Reactions Assisted by Upconversion Nanoparticles

5.1 Introduction

As described in the previous chapter, the trigger wavelength of a photoreaction can be shifted into the visible light region by merging an appropriate chromophore into the structure of the photo-active species. Although the achieved bathochromic shift enables the photo activation *via* blue light, coupling reactions induced by even lower energy, such as the near infrared light are highly sought. In the current chapter, a novel methodology for the formation of a covalent linkage *via* upconversion assisted, nitrile imine-mediated, tetrazole-ene cycloaddition (NITEC) triggered by NIR light, is introduced.[284] Herein, upconversion nanoparticles were excited at 974 nm. Through a photon upconversion process, an emission in the UV region was generated, suitable to trigger the photoreaction (refer to Figure 30). A tissue was optionally placed between the irradiation source and the reaction vessel, demonstrating the penetration ability of the NIR light. The strategy was applied for small molecule ligation, polymer end group modification and the coupling of polymer blocks in order to generate block copolymers. Rapid and exclusive formation of the desired product under full conversion of the

Lederhose, P.; Chen, Z.; Müller, R.; Blinco, J. P.; Wu, S.; Barner-Kowollik, C. *Angewandte Chemie International Edition* **2016**, DOI: 10.1002/anie.201606425. Reproduced with permission of WILEY-VCH Verlag.

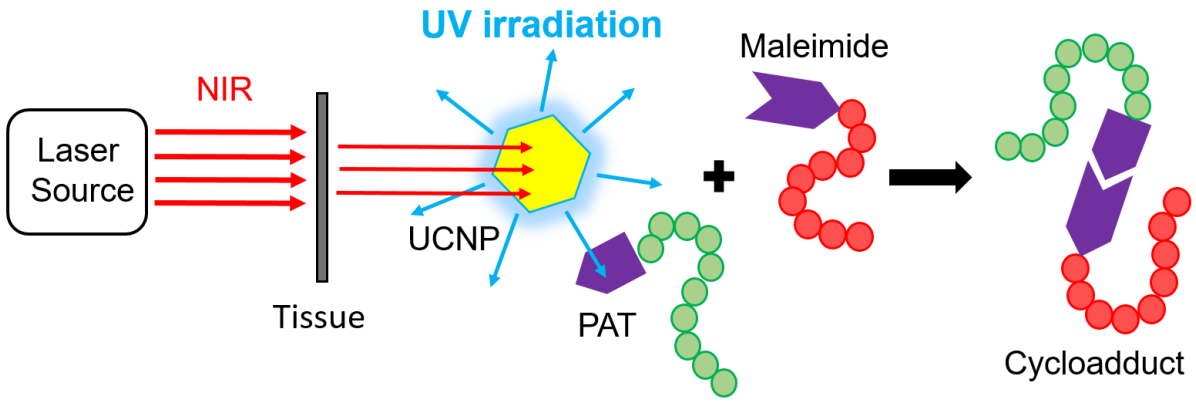

Figure 30 Schematic illustration of near infrared photoinduced coupling reactions assisted by upconversion nanoparticles. A tissue is optionally placed between the beam and the reaction vessel to demonstrate the penetration capability of the near infrared light.[284] Reproduced with permission of WILEY-VCH Verlag.

photo-active species was observed. The cycloaddition can be performed with low energy light and is insensitive to oxygen and moisture. Furthermore, upconversion nanoparticles (UCNPs) assisted photoinduced coupling chemistry was employed for polymer-polymer linkage in the presence of the bioactive and photosensitive species biotin, revealing the suitability of the strategy for biological applications. Interestingly, all formed cycloadducts emit in the NIR region. Therefore, *in vivo* tracking and labeling by NIR light is feasible, if the UCNPs are located in close proximity to the fluorescent cycloadduct.

5.2 Results and Discussion

To ensure an efficient formation of the nitrile imine intermediate, the excitation of the appropriate electronic transition of the tetrazole species by the UCNPs generated irradiation is highly important. Therefore, PAT **22** was applied as the photo-active species, as the fluorescence spectrum of the tetrazole overlaps significantly with the emission spectrum of the UCNPs in the wavelength region between 330 – 370 nm (Refer to Figure 31). Although the PAT was employed for blue light induced cycloadditions previously, the compound is also capable to participate in a NITEC reaction in the UV region. However, it should be mentioned, that the visible overlap of the emission spectrum of the irradiation source with the absorption spectrum of the light-sensitive compound is not always sufficient to trigger a photoreaction. Typically, an absorption spectrum represents a variety of possible electronic transitions of the photo-active molecule, whereby only selected transitions lead to the desired photoreaction. Importantly, no prediction about the effective excitation wavelength can not be made based on the absorption coefficients. High absorption intensity of a photo active species in a certain wavelength region does not necessarily imply a high photo-reactivity.[208]

The upconversion photoinduced coupling chemistry concept was first applied for small molecule ligation, in order to confirm the cycloadduct formation, optimize the reaction conditions, as well as to determine the efficiency of the ligation method compared to the established NITEC strategies. The use of small molecules has a distinct advantages compared to macromolecules such as polymers. A variety of analytical methods are available for monitoring the reaction process, as well as characterization of the final compound, e.g. NMR, ESI-MS, UV-Vis and fluorescence spectroscopy. Furthermore, purification methods such as column chromatography and recrystallization can be employed. For the upconversion photoinduced coupling experiments, a simple maleimide was

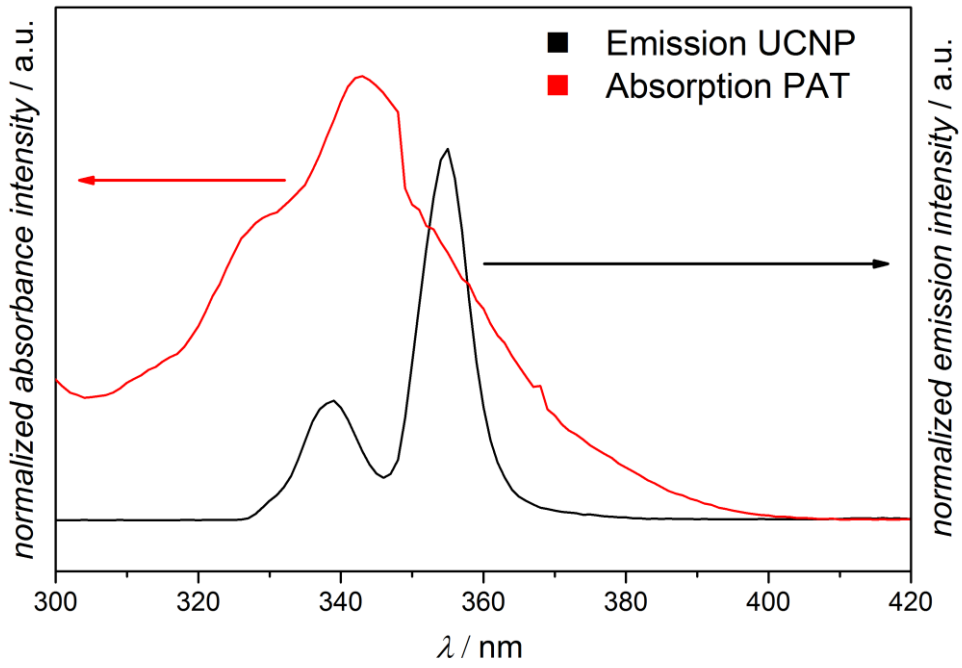

Figure 31 Magnification of the 300 - 420 nm region of the emission spectrum of UCNP (black line) and the absorption spectrum of PAT **22** (red line).[284] Reproduced with permission of WILEY-VCH Verlag.

applied as the dipolarophile, since it undergoes a rapid reaction with the *in situ* formed nitrile imine species, as alluded in the last chapter. PAT **22** (1.0 eq.) and hydroxy functional maleimide **7** (1.1 eq.) were both dissolved in acetonitrile. After addition of UCNPs, the resulting reaction mixture was exposed to NIR irradiation at 974 nm for 30 min at ambient temperature (refer to Scheme 30). As both, the PAT molecule and the pyrazoline containing cycloadduct are fluorescent, the kinetics of the NITEC reaction were monitored by measuring the emission spectrum of **22** (λ_{em} = 441 nm) and the product compound **23** (λ_{em} = 561 nm) (refer to Section 8.3.4). Full conversion of the tetrazole species after 30 min and formation of the respective cycloadduct were detected. HPLC was applied for analysis of the obtained reaction mixture as this characterization method is highly sensitive, quantitative and allows for the detection of minimal amounts of the product compound or any side products formed. In addition, control experiments in the absence of UCNPs were undertaken to ensure the photo

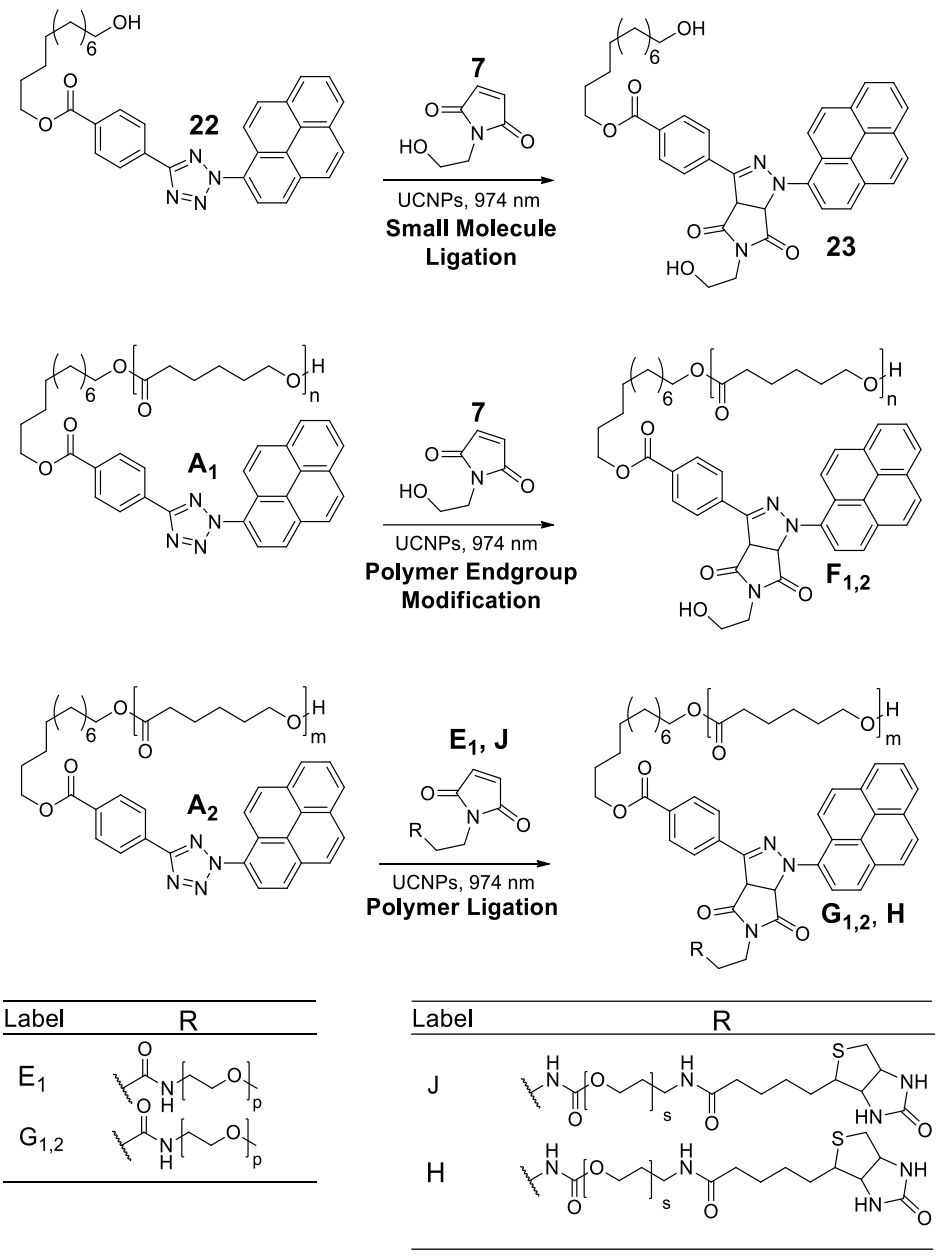

Scheme 30 Synthetic pathways for near infrared photoinduced coupling reactions to form the small molecule cycloadduct **23**, the end group modified PCL **F_1** (no tissue used) / **F_2** (tissue used), the block copolymers **G_1** (no tissue used) / **G_2** (tissue used) and the biotin functional block copolymer PCL-*b*-PEG **H**. Refer to Section 8.3.3 reaction details.[284] Reproduced with permission of WILEY-VCH Verlag.

activation *via* upconversion as the only pathway for the cycloadduct formation. Since no chemical information is given by the HPLC, a reference sample synthesized *via* blue light induced NITEC (refer to Section 8.2.3) was provided to ensure the formation of the cycloadduct **23**. The corresponding HPLC traces are depicted in the Figure 32. Full conversion of

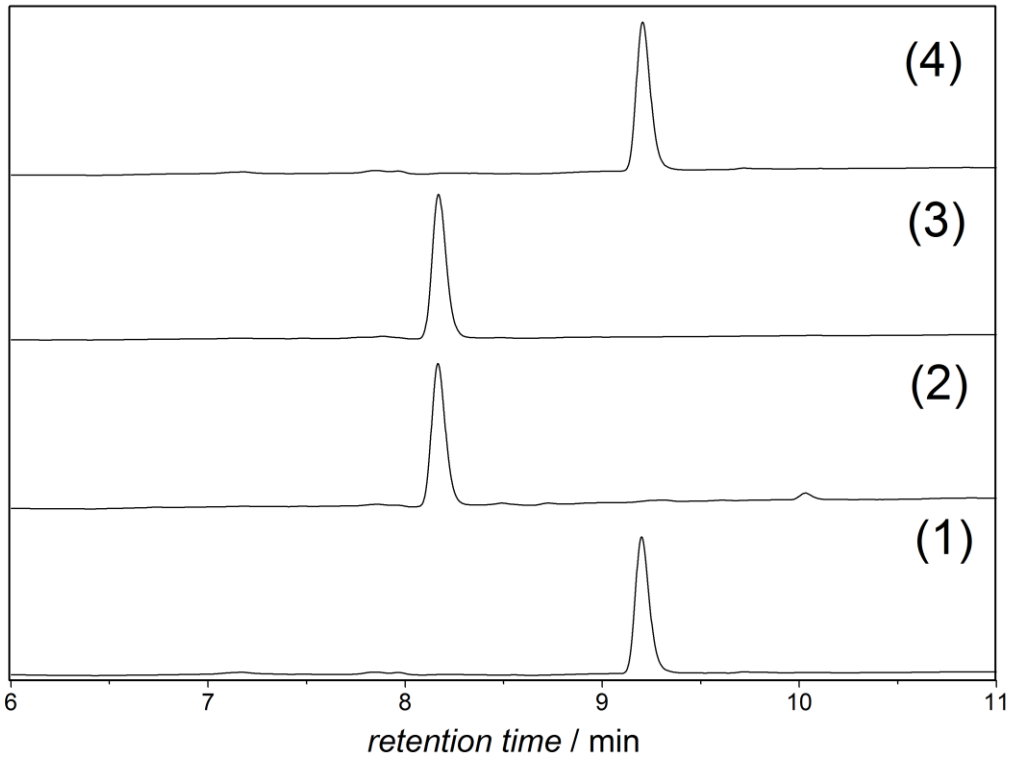

Figure 32 Normalized HPLC traces of PAT **22** (1), crude reaction mixture of PAT **22**, hydroxy functionalized maleimide **7** and UCNPs, irradiated at 974 nm in MeCN for 30 min (2) and reference sample of cycloadduct **23** synthesized according to literature in the absence of UCNPs (3), control experiment carried out in the absence of UCNPs under otherwise identical conditions as in the case of the small molecule ligation of PAT **22** and hydroxy functionalized maleimide **7** (refer to Scheme 30 for the reaction details); THF / MeCN / H_2O + 0.1 % trifluoroacetic acid was used as eluent and a 220 nm UV detector was employed.[284] Reproduced with permission of WILEY-VCH Verlag.

the tetrazole species and nearly exclusive formation of the desired cycloadduct were observed. Only minor amounts of side products were detected. Trace (1) represents the signal of the tetrazole before the irradiation eluting at 9.2 min. A shift to shorter retention time of 8.2 min was observed after the irradiation of the reaction mixture (analysed without further purification) (2). The signals of the reference sample (3) and the reaction mixture (2) correlate well, indicating the formation of an identical cycloadduct as in the case of the blue light induced NITEC reaction (refer to Chapter 2.3.3). Furthermore, no conversion was observed for the control experiment without UCNPs present (4), excluding alternative reaction pathways for the generation of the nitrile imine, such as thermal

decomposition of the tetrazole species. The structure of the formed pyrazoline **23** was confirmed by ESI-MS (refer to Section 8.3.3), providing additional evidence for the cycloadduct formed by the upconversion photoinduced coupling chemistry.

As the NIR triggered NITEC reaction was shown to be a powerful tool for the ligation of small molecules, the extension of the concept as a tool for macromolecular design was attempted. In comparison to the small molecule coupling, the modification or ligation of the polymer species is more demanding. Prolonged reaction times are required and a potential interference of the coupling reaction with the functional groups present in the polymer backbone or other end groups such as RAFT agents or ATRP initiators is possible. Furthermore, the analytical tools for the characterization of polymer species are limited, due to the large size and inhomogeneity of the molecules. Thus, rather low molecular weight polymers were employed to facilitate the characterization of the resulting macromolecular cycloadducts. In the first experimental sequence, the end group modification of a short, PAT functional poly(ε-caprolactone) PCL (M_n = 2.0 kDa (GPC), $Đ$ = 1.10) polymer was targeted (refer to Section 8.2.3 for synthesis and characterization). The tetrazole functional polymer $\mathbf{A_1}$ (1.0 eq.) and maleimide species **7** (1.5 eq.) were dissolved in MeCN. After addition of UCNPs to the solution, the resulting mixture was exposed to NIR light at 974 nm for 40 min at ambient temperature (refer to Scheme 30). Reactions, both with direct irradiation, $\mathbf{F_1}$, and with tissue-shielded irradiation source, $\mathbf{F_2}$, were performed, in order to estimate the penetration capability of the NIR light. The resulting product streams were analysed by ESI-MS (refer to Figure 33). Due to the short length and the ester moieties incorporated into the polymer backbone, the chosen PCL provides excellent ionisation properties in the ESI-MS. Full conversion of the polymer species $\mathbf{A_1}$ and formation of the desired cycloadducts $\mathbf{F_{1,2}}$ were detected. An extended reaction time (60 min) was required for the tissue-shielded

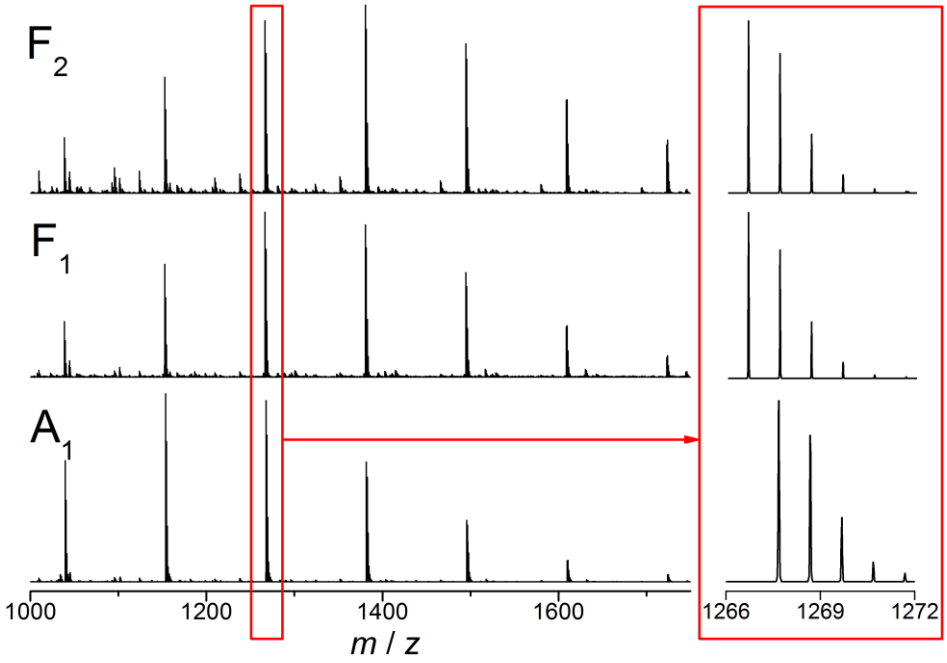

Figure 33 Magnified view in the region of 1000 - 1750 *m* / *z* of the high resolution ESI-MS spectrum of PAT end-capped poly(ε-caprolactone) (PCL) **A_1** and the cycloadducts **F_1** (no tissue used) and **F_2** (tissue used). Inset: magnified view of the isotopic patterns for **A_1** and **$F_{1,2}$** . Refer to Scheme 30 for the structures of formed cycloadducts **$F_{1,2}$** and the reaction conditions. Refer to Table 6 for the exact theoretical and experimental masses of the depicted polymer species **A_1** and **$F_{1,2}$**. Note that only a shift of approx. 1 Da results.[284] Reproduced with permission of WILEY-VCH Verlag.

experiment **F_2**, as the irradiation intensity was reduced by the tissue absorbance. However, no effect on the overall conversion or the products formed was observed by the presence of the tissue. For shorter polymers, the end group can potentially have a greater influence on the ionisation properties. Therefore, no quantitative statement can be made regarding the product distribution by ESI-MS, although the corresponding results suggest a high efficiency of the photoinduced coupling chemistry for end group modification. Quantitative analysis of the modified polymers **$F_{1,2}$** were achieved by ^{1}H NMR. As no visual difference was noted between the spectra of **F_1** and **F_2**, only data of **F_1** is discussed (refer to Figure 34). Full conversion and exclusive formation of the cycloadduct were observed. No additional species are visible, indicating efficient and clean end group modification. Compared to the spectrum of **A_1**, the NMR spectrum of **F_1** reveals several changes. A new resonance (h) between 3.6 and 3.7 ppm

appears, which is assigned to the methylene moieties of the introduced maleimide. Furthermore, the new signals (g) and (f) at 5.0 and 5.6 ppm respectively, were assigned to the adjacent protons of the newly formed 5-membered ring. The pattern of the resonances in the aromatic region (a) also changed the structure and shifted to lower fields (e). As expected, the backbone resonances remained unaffected by the coupling reaction. Interestingly, the fluorescence of the pyrazoline functional PCL, synthesized *via* NITEC, can potentially be triggered by NIR irradiation as long as the UCNPs are in close proximity. By combining the fluorescence properties of the pyrazoline revealing a tail into the NIR region with UCNPs, fluorophore excitation and the detection of the resulting fluorescence in NIR regime is possible.

In the second experimental sequence, a photoinduced block copolymer

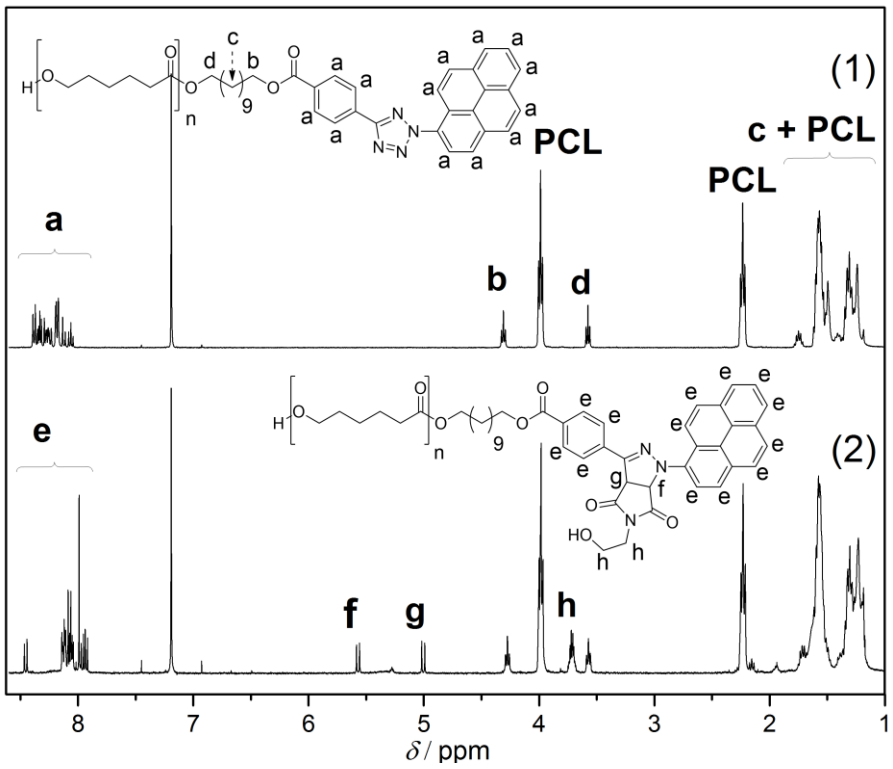

Figure 34 ^{1}H NMR spectra before and after the upconversion photoinduced coupling of $\mathbf{A_1}$ with small molecule maleimide **7**. Refer to Scheme 30 for the reaction conditions. (1) PAT functional PCL $\mathbf{A_1}$ before irradiation; (2) reaction mixture after irradiation with NIR in presence of UCNPs ($\mathbf{F_1}$).[284] Reproduced with permission of WILEY-VCH Verlag.

formation *via* UCNPs assisted NITEC was attempted. PCL and polyethylene glycol (PEG) blocks were employed for the linkage reactions as both species are suitable for biological applications due to their biocompatibility and non-toxicity.[285] The tetrazole functional polymer **A_2** (1.0 eq.) and the maleimide end capped PEG **E_1** (1.5 eq.) were dissolved in MeCN. After addition of UCNPs to the solution, the resulting mixture was exposed to NIR light at 974 nm for 60 min (refer to Scheme 30). An excess of the PEG polymer was employed to ensure full conversion of the tetrazole moiety. The residual maleimide functional PEG was removed by aqueous work up of the reaction mixture affording the desired block copolymer only. Again, both direct irradiation, **G_1**, and tissue-shielded irradiation, **G_2**, were carried out to simulate the differences between *in vitro* and *in vivo* environments. To quantify the efficiency of the coupling reaction, the resulting block copolymers were analysed by SEC (Figure 35). Similar to the end group

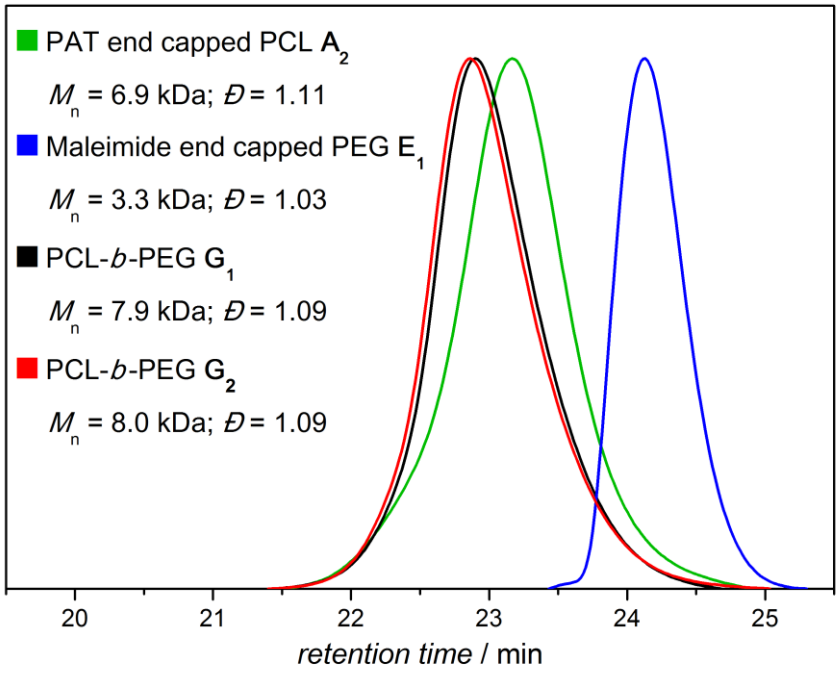

Figure 35 Normalized SEC traces of PAT functional PCL **A_2** (green line), maleimide functional PEG **E_1** (blue line) and block copolymers **G_1** (no tissue used, black line) and **G_2** (tissue used, red line) formed by upconversion photoinduced coupling reactions, respectively. M_n and $Đ$ were determined by SEC in THF using poly(styrene) calibration standards.[284] Reproduced with permission of WILEY-VCH Verlag.

modification experiments, full conversion of the PAT species and exclusive formation of the desired pyrazoline containing adduct was observed. Apart from the prolonged reactions time for **G_2**, no significant differences were noticed between the 'tissue free' and 'tissue-shielded' experiments. The SEC traces of **G_1** (black line) and **G_2** (red line) are both monomodal and reveal a significant shift to lower retention times compared to the tetrazole functional species **A_2** (green line). No residual reagent polymers are visible. In addition, the *Đ* values of the cycloadducts decreased after the coupling reaction, underpinning the efficiency of the ligation method. As the GPC provides no chemical information, the structures of **$G_{1,2}$** were verified by ^{1}H NMR (refer to Section 8.3.3, Figure 136, Figure 138).

In order to demonstrate the versatility of the upconversion photoinduced coupling chemistry for biological applications, a block copolymer carrying a photosensitive, bioactive biotin moiety was synthesized. The tetrazole functional polymer **A_2** (1.0 eq.) and the maleimide end capped PEG **J**

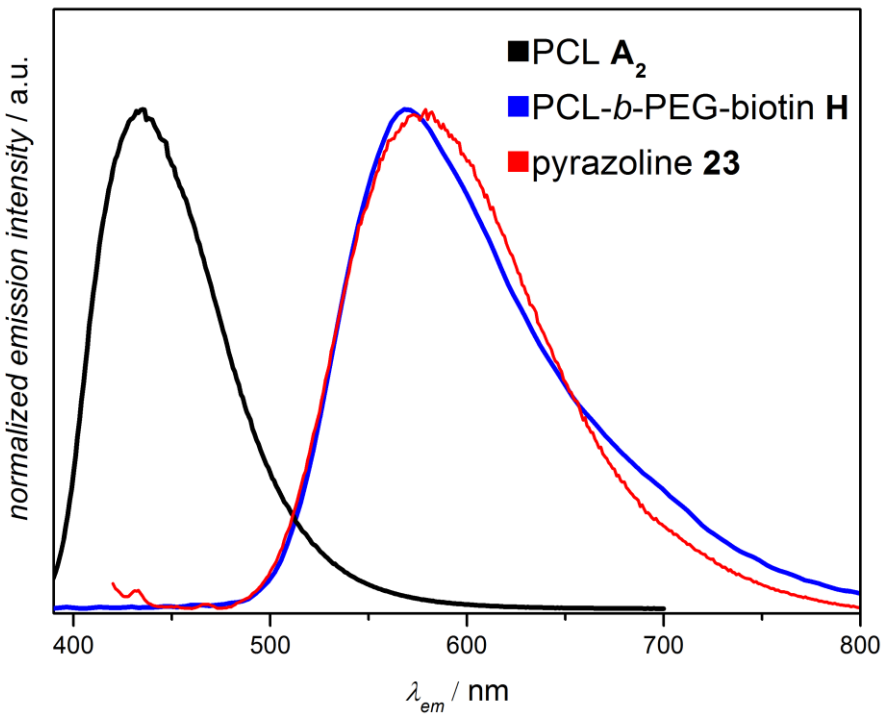

Figure 36 Normalized fluorescence spectra of PCL **A_1**, PCL-*b*-PEG-biotin **H** and pyrazoline **23**.[284] Reproduced with permission of WILEY-VCH Verlag.

(1.5 eq.) were placed into a reaction vessel in the presence of MeCN. After (adding the UCNPs to the solution, the resulting mixture was irradiated with NIR light at 974 nm for 60 min (refer to Scheme 30) to afford block copolymer **H**. A tissue was placed between the irradiation source and the reaction vessel to imitate *in vivo* environment conditions. After removing the UCNPs, the crude reaction mixture was analyzed by fluorescence spectroscopy, whereby full conversion of the tetrazole containing PCL $\mathbf{A_2}$ and formation of the bioactive PEG-*b*-PCL block copolymer was detected (refer to Figure 36). The fluorescence band of the starting material (black line, λ_{em} = 441 nm) vanishes, while a new, red shifted fluorescence band of the cycloadduct **H** arises (blue line, λ_{em} = 561 nm). The bioactivity of biotin functional species **H** was subsequently estimated by employing a biotin quantification kit. Thus, **H** was added to an aqueous solution of HABA (4'-hydroxyazobenzene-2- carboxylic acid) non-covalently attached

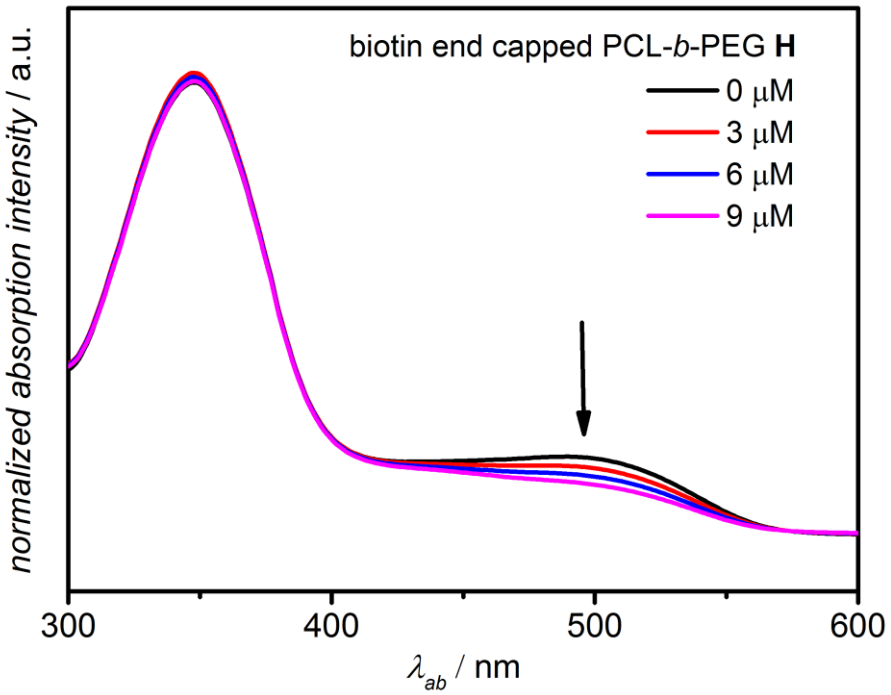

Figure 37 Absorption spectra of HABA / avidin mixtures before and after addition of a biotin containing solution **H** in the concentration range 0 – 9 µM. The arrow illustrates the absorption band used for the biotin activity calculations (refer to Section 8.3.4 for further details).[284] Reproduced with permission of WILEY-VCH Verlag.

to the avidin protein and displaying a strong absorption at 500 nm. As biotin has a high binding affinity towards avidin, it replaces HABA, whereby the absorption at 500 nm decreased proportionally. The formation of the new non-covalent complex of **H** and avidin was monitored by UV / Vis spectroscopy for a range of biotin concentrations (refer to Figure 37). 88 % of the species **H** was found to be bioactive by comparing the observed absorption decrease to a reference sample (refer to Section 8.3.4).

5.3 Conclusion

By combining the concepts of UCNPs with NITEC chemistry, a novel, powerful strategy for light induced photoligations is introduced. For the first time, the trigger wavelength of a photo-linkage reaction was extended into the near infrared region. The coupling methodology was applied for small molecule ligations as well as macromolecular design such as end group modification or the formation of block copolymers. Rapid formation of the desired cycloadduct under mild conditions at 974 nm was observed for all linkage reactions. No side product formation was detected. The structures of the target compounds were confirmed by HPLC, ^{1}H NMR, ESI-MS and SEC. The great potential of the upconversion assisted NITEC for *in vivo* applications was verified by 'through tissue' triggered coupling reactions in the presence of bioactive biotin. Importantly, the NIR induced linkage reaction had no influence on the bioactivity performance of the biotin species. All synthesized cycloadducts are fluorescent in the NIR region. Therefore, *in vivo* labelling and tracking *via* near infrared light only is a potential feature to be investigated further.

6 λ-Orthogonal Photoligations, Novel Avenue for Advanced Surface Patterning

6.1 Introduction

Control over the physical and chemical properties of a surface plays a key role for the advanced technological applications such as microfluidic lab-on-a-chip devices, sensors, antifouling coatings and platforms for biomolecule immobilization. Therefore new methodologies for easy and efficient functionalization of surfaces through formation of new covalent bonds are current research goals in many fields. Light induced reactions for tuning surface characteristics is one promising strategy due to the advantages of photo induced processes such as high reaction rates, high efficiency, orthogonality, mild reaction conditions and compatibility with the manufacturing environment. Furthermore, spatial and temporal control can be achieved, which allows the formation of patterned or gradient surfaces. In the current chapter, a combination of UV triggered NITEC and visible light triggered NITEC is presented as a novel λ-orthogonal ligation methodology in solution and on a surface. A strategy for λ-orthogonal photo-ligations in solution has been reported previously by the Barner-Kowollik team.[9] However, the current approach is the only example where two photo active compounds can be triggered, kinetically independent of one another, in solution or on a surface. This was achieved through careful choice of wavelength for the activation light source. The concept was first applied to small molecules in solution. In this case, a rapid, efficient and irradiation wavelength dependent formation of the desired cycloadduct was

observed. Subsequently, the λ-orthogonal photo-ligation concept was applied for spatially resolved and sequence controlled surface modification. A photo-active, wavelength selective pattern was introduced to the surface *via* λ-orthogonal photo-ligation. The space resolved structures were then modified using a grafting-from approach. This was achieved employing the visible light triggered NITEC and the UV triggered NITEC reacting independently of one another. The λ-orthogonal photo-ligation is first example of a fast, simple and efficient synthetic path for advance surface patterning without the use of elaborate mask.

6.2 Results and Discussion

For two photo ligations to operate λ-orthogonaly with one another, one reaction channel must be first triggered with a specific activation wavelength, while a different irradiation wavelength is necessary for the triggering of the second reaction channel. In the case of the pyrene aryl tetrazole (PAT) **22** and the "UV-tetrazole" moiety of species **30**, the absorption spectra of both photo-active groups were compared and the appropriate irradiation lamps were chosen to ensure the λ-orthogonality (refer to Figure 38). Although the PAT and 'UV-tetrazole' absorbance spectrum overlay partially, the PAT can be excited in visible light mode at 410 – 420 nm as reported previously, while the 'UV-tetrazole' was observed to be optically transparent in the region > 345 nm. Therefore a LED (410 – 420 nm, 9 W) was applied first to trigger the PAT followed by

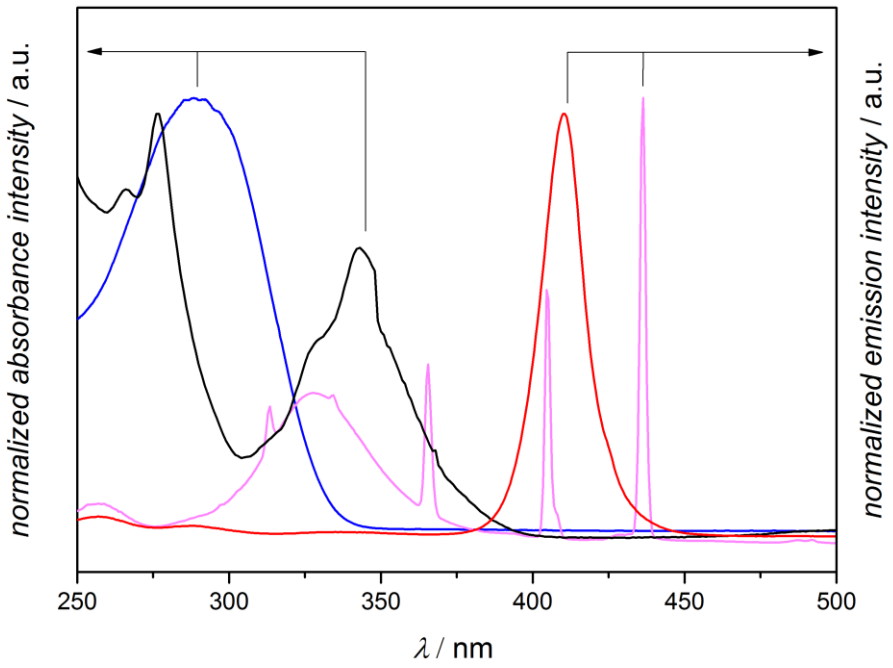

Figure 38 Normalized absorption spectra of UV-tetrazole derivative **30** (blue) and PAT **22** (black). Normalized emission spectra of visible light source (red) and UV irradiation source (pink).

the use of a UV lamp, with a broader irradiation spectra ($\lambda_{em,\ max}$ = 320 nm, 36 W), to activate the "UV-tetrazole" in the second step. However full conversion of the PAT species *via* NITEC is required, as any unreacted, visible light sensitive PAT will also be triggered by the UV light source applied.

In order to demonstrate the λ-orthogonality of visible light triggered NITEC and UV triggered NITEC, a small molecule ligation study was undertaken. A solution of PAT **22** (1.0 eq.) and monoethyl fumarate functional diearyl tetrazole **30** (1.0 eq.) in acetonitrile (MeCN) was irradiated at 410 – 420 nm for one hour at ambient temperature (refer to Scheme 31). The reaction mixture was monitored by TLC. While full conversion was observed for PAT **22** and the fumarate moiety of **30**, the UV tetrazole functionality remained unreacted. The formed cycloadduct **31** was purified by column chromatography and irradiated at 320 nm in MeCN for one hour (refer to Scheme 31). A magnification of the ^{1}H spectra between 4.5 and 9.0 ppm of the PAT **22** (1) the fumaryl functional UV tetrazole **30** (2) and the cycloadduct **31** (3) formed *via* visible light conjugation of **22** and **30** are shown in the Scheme 31. Full conversion of both reagents **22** and **30** as well as exclusive formation of the desired cycloadduct **31** were observed. Evidence to support this transformation was given by the observed shift for the aromatic protons of the pyrene moiety of **22** (located between 8.0 and 8.4 ppm, protons labelled (a)), when PAT was converted to cycloadduct **31** in presence of **30** *via* visible light NITEC reaction (protons labelled (d)). In addition, the two resonances (e) at 4.5 and 5.6 ppm can be assigned to the adjacent protons of newly formed 5 membered pyrazoline ring. Aromatic resonances (c) of **30** located at 7 ppm and between 8.0 and 8.3 ppm do not change their position in the spectra of **31**. This indicates the visible light stability of the diaryl tetrazole moiety. The resonances of monoethyl fumarate alkene moiety of **30** appearing at 7.2 ppm is not present in the spectrum of **31** due to its conversion in the visible light triggered NITEC

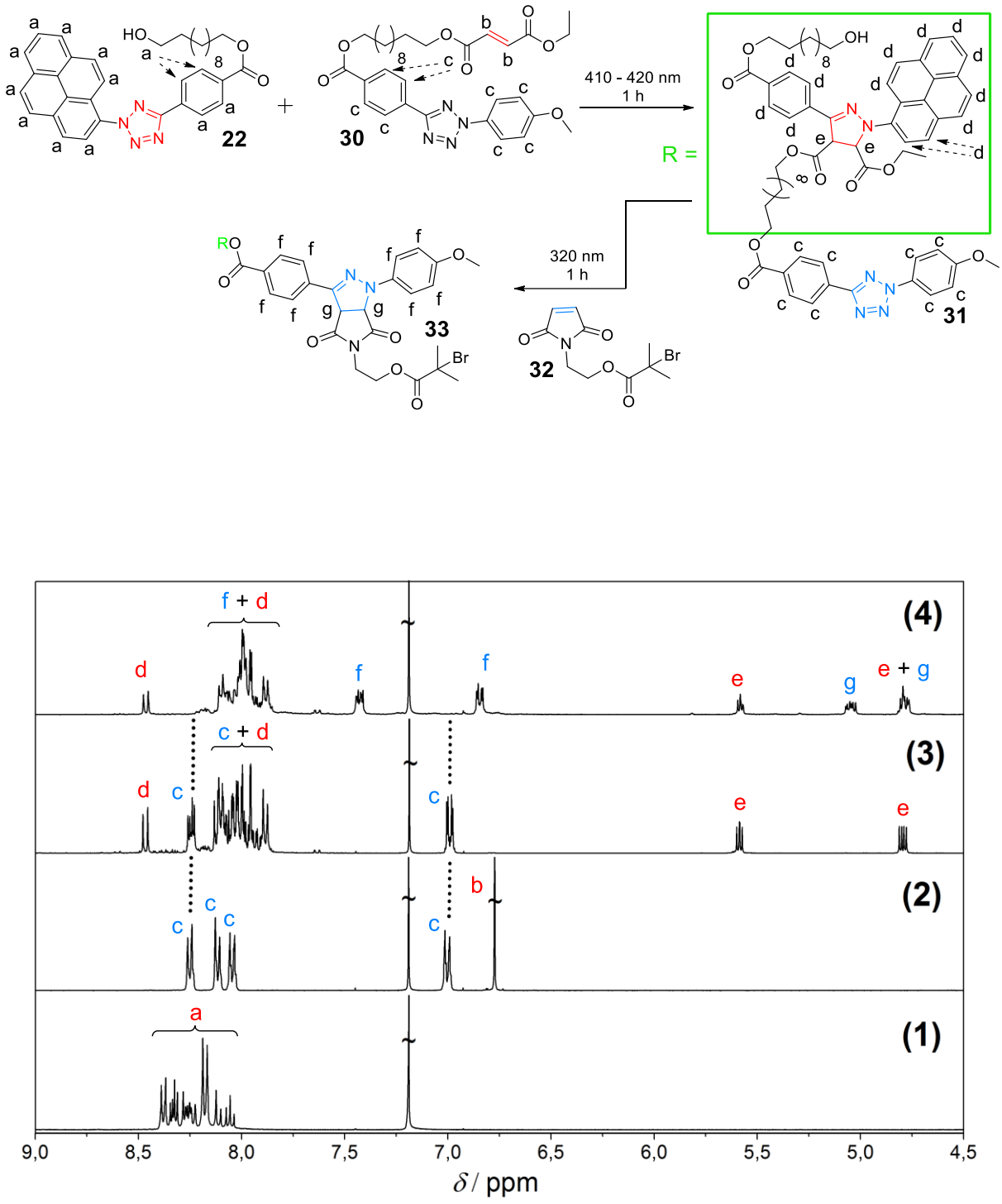

Scheme 31 λ-Orthogonal, photo-induced ligations, proof of concept in solution. Left side: photo-triggered ligation of PAT **22** with fumarate functional species **30** to form cycloadduct **31** bearing a "UV-tetrazole" (410-420 nm, 1 h, rt); photo-triggered conversion of "UV-tetrazole" containing species **31** in presence of maleimide **32** to form cycloadduct **33** (320 nm, 1 h, rt); for clarity only one regioisomere of **31**, **33** is displayed (refer to SI for further reactions details). Right side: ^{1}H NMR spectra of tetrazole species **22** (1), **30** (2) and formed cycloadducts **31** (3), **33** (4); Dotted lines illustrate the location of aromatic resonances from the monoethyl fumarate functional "UV-tetrazole" **31**, also observed in the spectra of cycloadduct **31**.

reaction. After irradiation of **31** (3) in presence of bromide end capped maleimide **32** at 320 nm, the desired cycloadduct **33** (4) was formed (refer to Scheme 31). Resonances (c), located in the aromatic region of **32** at 7 ppm and between 8.0 and 8.3 ppm, are replaced in the spectra of **33** by new multiplet between 6.7 and 8.4 ppm. In addition, two new resonances (g) at 4.6 and 5.1 ppm can be assigned to the adjacent protons of second formed 5 membered pyrazoline ring, partially overlaying with the resonances (e). Interestingly the length of the spacer, linking the monoethyl fumarate and the diaryl tetrazole species of **30**, has a significant influence on the visible light induced ligation reaction of PAT **22** and **30**. Reducing the alkyl spacer from eleven methylene units to two decreases the conversion of the monoethyl fumarate to < 5 % under identical reaction conditions, leading to a different reaction pathway, where unknown photodegradation of the PAT **22** molecule occurred. The observed decrease in the NITEC efficiency for molecules containing a shorter spacer unit was attributed to an increase in steric hindrance which makes the cycloaddition of the monoethyl fumarate and the nitrile imine difficult. Also an interaction between both tetrazole species can lead to the formation of side products or alternative quenching processes of the excited tetrazole species.

In addition to the wavelength selective triggering of NITEC reaction in solution, the utilization of the λ-orthogonal photo-ligations concept on surface was undertaken. Prior to this work there are no examples of λ-orthogonal surface photo-ligation in the literature. However, the extension of the λ-orthogonal photo-ligations concept as a tool for preparation of pattern surfaces is a demanding task and requires careful planning. The first challenge to be considered is the surface attachment of the photo active PAT molecule. To achieve this, PAT **22** was converted to an acid functional pyrene tetrazole **34**, which was subsequently amidated with 3-aminopropyltriethoxysilane (APTS) to yield compound **35** (refer to

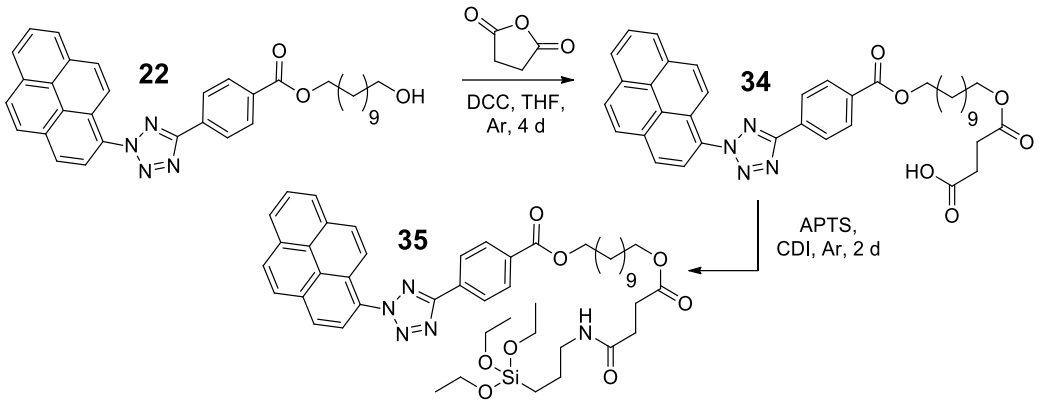

Scheme 32 Conversion of hydroxyl functional PAT **22** to an acid functional PAT **34** in presence of *N N'*-dicyclohexylcarbodiimide (DCC) and succinic anhydride. Amidation of acid functional PAT **34** in presence of 1,1'-carbonyldiimidazole (CDI) and APTS.

Scheme 32). Notably, the direct amidation of the aromatic acid of the tetrazole species could not be achieved under various conditions, including dicyclohexylcarbodiimide (DCC) and 1-ethyl-3-(3-dimethylaminopropyl)carbodiimide (EDC) couplings, as well as the acid activation using $SOCl_2$. The modest yield of 39 % is most likely due to the polymerization of the silane functional compound **35** onto the silica gel employed during the purification process *via* column chromatography. In addition, the compound was found to be unstable at elevated temperatures and spontaneously polymerized in the presence of moisture. Therefore, anhydrous solvents were required for preparing **35**. Additionally, ambient light needed to be avoided as the target compound absorbs in the visible light range. Due to the rather poor stability of the compound **35**, only an ^1H NMR spectrum was obtained for the verification of the purity and structure of the synthesized compound (refer to Figure 39). Several changes in the spectrum of **35** were observed compared to the spectrum of starting precursor **34**. While the signals (a), (b) and (c) remain unaffected by the transformation, the resonance (d) at 3.7 ppm shifts to lower fields at 4.1 ppm (g). The two new doublets, observed at 2.5 (k) and 2.7 (j) ppm, were assigned to the methylene moieties of the succinic anhydride incorporated in to the structure of PAT reaction.The multiplet (f)

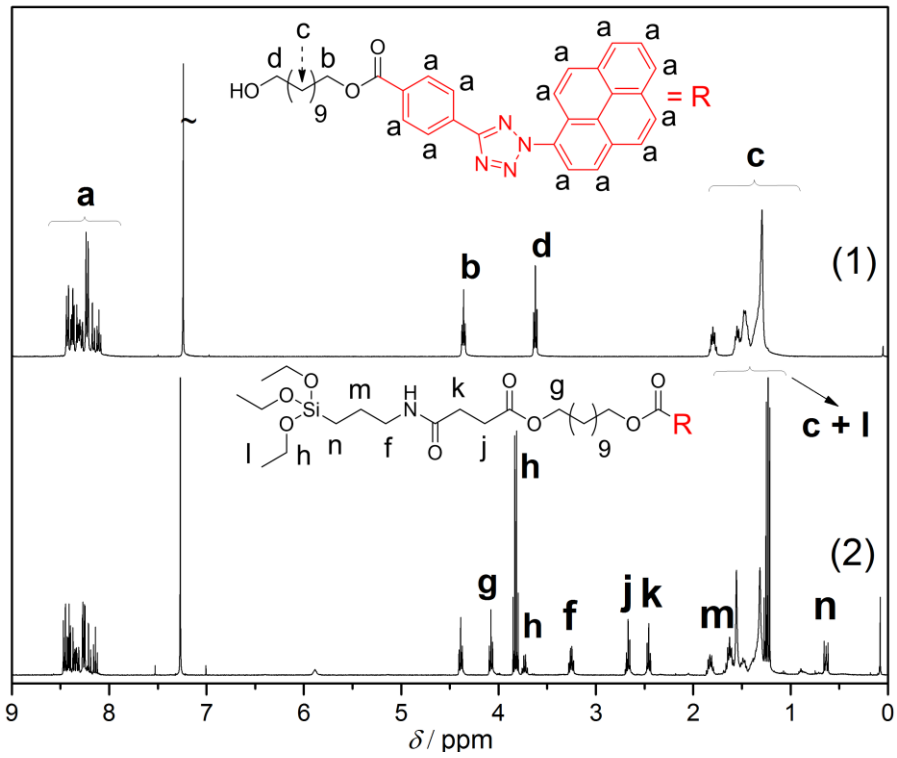

Figure 39 ^{1}H NMR spectra of PAT **22** (1), silane functional tetrazole species **35** formed starting from hydroxyl functional PAT **22** in a ring opening reaction with succinic anhydride and subsequent amidation of the formed intermediate **34** with APTES.

via ring opening between 3.2 and 3.3 ppm was assigned to the amide proton formed in the amidation reaction of species **34** with APTS. The resonances (m) and (n) at 1.8 and 0.7 ppm were assigned respectively to the methylene groups in the beta and alpha positions to the Si-heteroatom of the APTS. The multiplets (l) and (h), were attributed to the ethoxy moieties of the silane. The corresponding resonances at 3.9 and 1.2 ppm displayed the highest intensity in the spectrum as APTS contains three of ethoxy functional groups. In summary the ^{1}H NMR of **35** confirmed a clean and selective formation of the silane functional visible light active tetrazole derivative. ^{13}C NMR characterization of the species was attempted, but due to the prolonged experimental times required, the samples were observed to degrade/polymerise while the measurement was in progress (the silane functional tetrazole **35** was observed to self-polymerise in the NMR tube after ca 20 min). As self-polymerization was suggested under the analytical

conditions applied for ESI-MS measurements, no mass spectrometry of the target compound was performed.

The obtained PAT functional silane **35** was employed along with the fumarate functional 'UV-tetrazole' **30**, the halogenated maleimide **32** and **36** in a λ-orthogonal photo-ligation approach onto a silicon surface (refer to Figure 40). In the first step PAT functionalized silicon wafer **I** was prepared by covalent attachment of the silane containing species **34** to the surface. Tethering of the light sensitive species to the surface directly gives the maximum lateral resolution, since diffusion of the photo activated species can be avoided. The resulting wafer was characterised *via* ToF-SIMS, as the method is suitable for the investigation of patterned surfaces at higher resolutions. Importantly, in order for ToF-SIMS to be a viable characterization tool a unique fragment of the species attached must be identified, in order to confirm the structure of the compound on the surface. In the case of the PAT, the pyrene containing fragment $[C_{16}H_9O]^+$ was employed to verify high density PAT functionalisation of the surface (refer to Figure 40, PAT species was visualized by blue colour). The fragment being detected for the validation of the presence of PAT is found only when the tetrazole moiety is contained within the structure. When the nitrile imine intermediate or subsequent pyrazoline ring is formed, this fragment is no longer observed. Consequently, it confirms the successful patterning of PAT, as well as photo-reaction of tetrazole species in a NITEC reaction.

Since physio-adsorbed tetrazole can negate the spatial-resolution of the patterned surfaces, it is crucial for the λ-orthogonal methodology that only covalently tethered PAT is present on the wafer surface. Therefore control experiments were undertaken to exclude the possibility of non-covalent attached PAT (refer to Figure 41). PAT tetrazole **22** was reacted under identical conditions to those of silane **34**. After the work-up of the wafer, the absence of PAT on the surface was confirmed by ToF-SIMS. This confirmed, that the coating and purification methods applied led to no

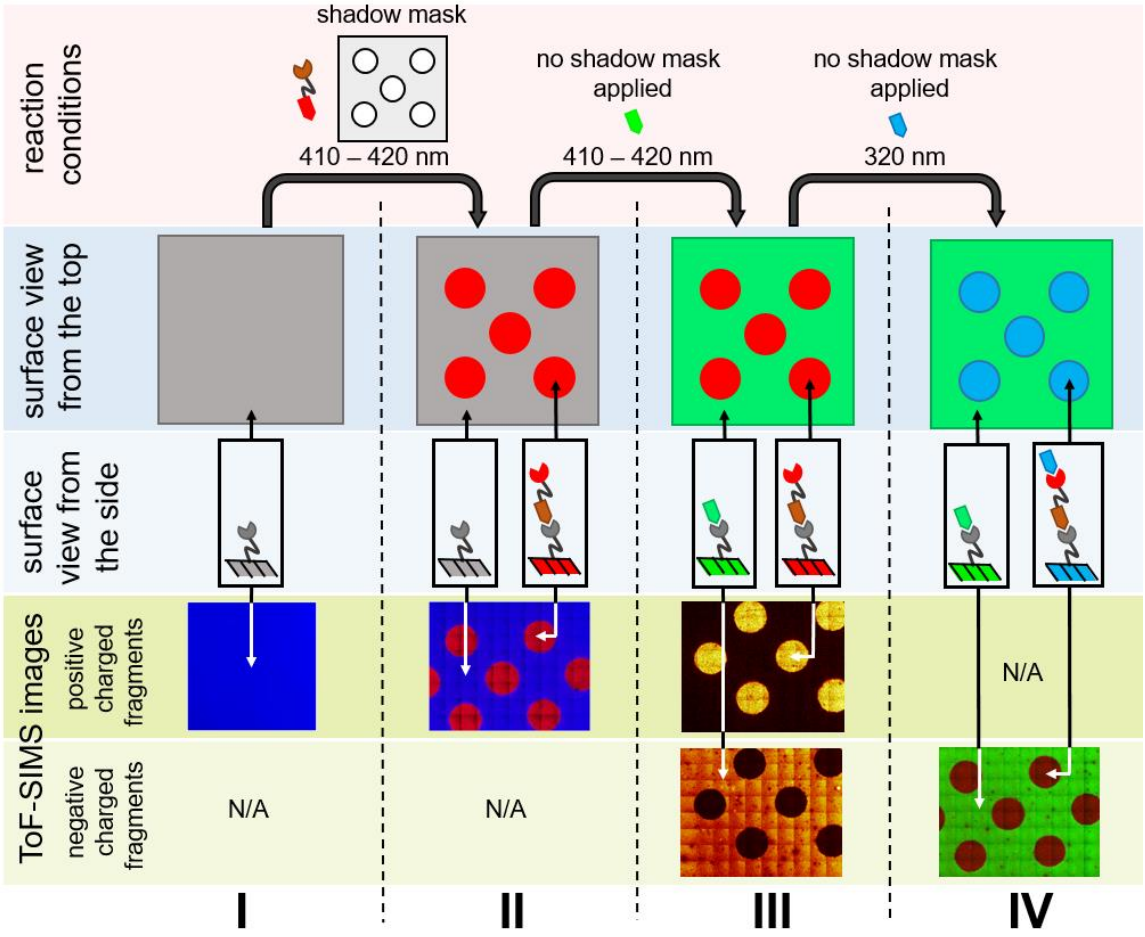

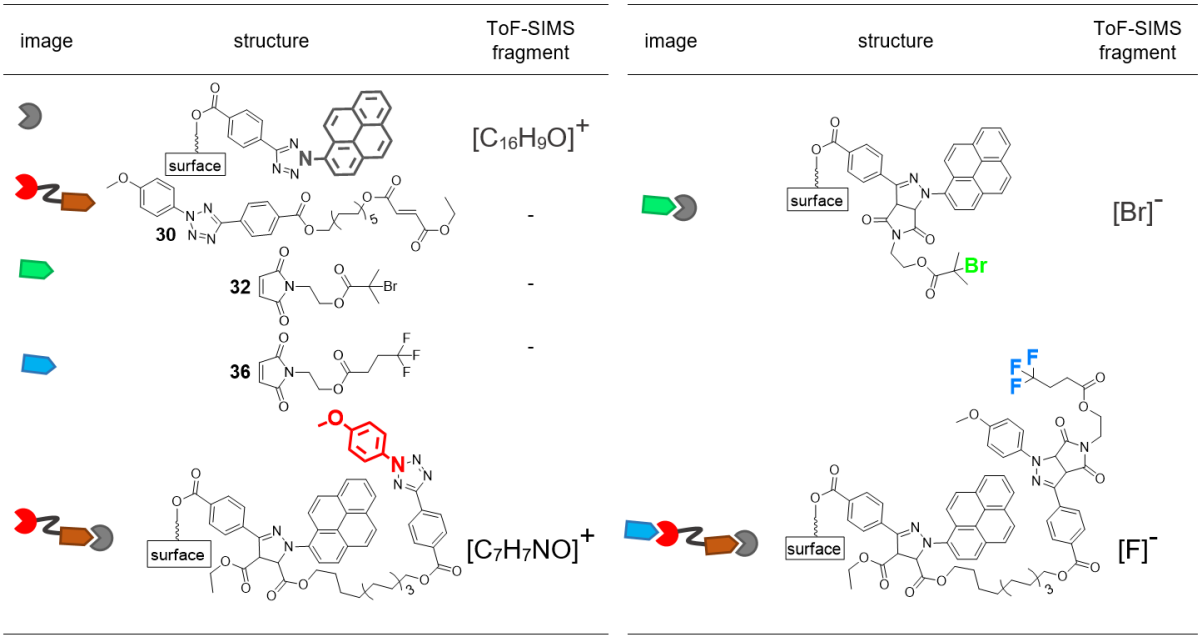

Figure 40 Overview over λ-orthogonal surface photo-patterning approach. Top: reagents and set ups employed for the formation of patterned surfaces **II** - **IV**. Centre: View of the surfaces **I** - **IV** from the top and from the side. Bottom: Space resolved ToF-SIMS images of surfaces **I** - **IV** recorded in positive and negative mode. Table: structures of reagents and cycloadducts; fragments used for ToF-SIMS imaging were highlighted in the structures using colours for the corresponding pattern.

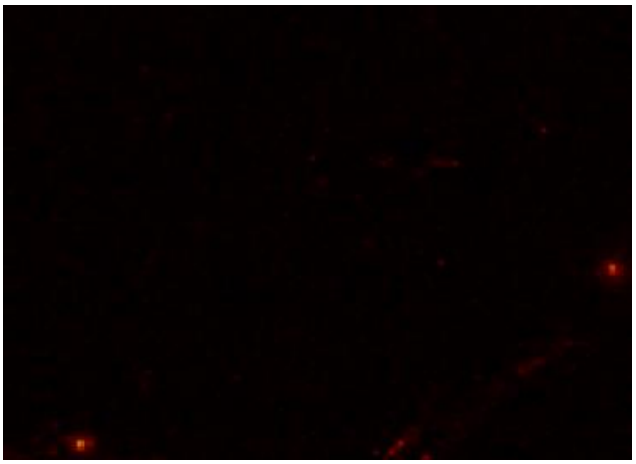

Figure 41 ToF SIMS image of the control experiment for preparation of the wafer **I**, PAT **22** was applied instead of silane **34**. Yellow colour illustrates the presence of the fragment $[C_{16}H_9O]^+$.

physio-adsorbed PAT being retained and reinforced the efficiency of the silanization approach.

After successful anchoring of the PAT to the silicon surface, patterning with the ene-containing 'UV-tetrazole' **30** was attempted. Wafer **I** was covered by a shadow mask and placed into argon purged solution of **30** in MeCN. The masked wafer was then irradiated at 410 – 420 nm under ambient conditions for 3 h, which yielded wafer **II**. This wafer had unreacted PAT located in the areas covered by the shadow mask, and UV tetrazole in the areas that underwent exposure to visible light (refer to Figure **40**). The characterization of wafer **II** was undertaken *via* ToF-SIMS analysis, revealing the formation of a patterned surface in a λ-orthogonal approach. The red circles indicate the surface regions covered by the 'UV-tetrazole' where $[C_7H_7NO]^+$ fragment was employed, verifying the presence of the photo active species. Similar to PAT, the $[C_7H_7NO]^+$ fragment is only visible as long the tetrazole is intact and provides a negative control in case of an successful NITEC reaction. Furthermore, no residual PAT was found in the regions exposed to the light. This allowed wavelength selective modification of the prepared wafer. In the blue area, the $[C_{16}H_9O]^+$ fragment of the PAT is observed as the visible light tetrazole remained

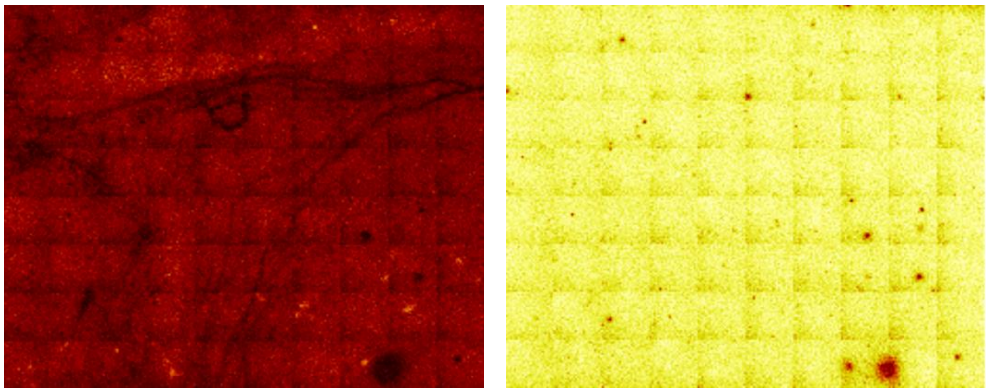

Figure 42 ToF SIMS image of the control experiment for photo triggered modification of the wafer **I**, in order to obtain pattern wafer **II**, functionalized with λ-orthogonal, photo active species PAT and 'UV-tetrazole'. Identical conditions were applied except keeping the reaction set up in the dark for the period of the experiment. Left: $[C_7H_7NO]^+$ fragment of the 'UV-tetrazole'. Right: $[C_{16}H_9O]^+$ fragment of the PAT. Yellow colour illustrates the presence of the respective fragment.

unreacted under the shadow mask. Since the resolution and contrast of the patterned surface can be negatively affected by the physio adsorbed 'UV-tetrazole', the covalent attachment of the 'UV-tetrazole' species is a key factor for the further success of the designed approach. Consequently, covalent linkage of the fumarate functional tetrazole derivative to the PAT species *via* NITEC was confirmed by a control experiment, in which no irradiation source was employed under identical conditions, as applied for preparation of wafer **II**. The corresponding sample was analysed *via* ToF-SIMS (refer to Figure 42). No absorption onto the silica surface was detected as the signal of the $[C_7H_7NO]^+$ fragment displayed poor intensity, while the $[C_{16}H_9O]^+$ fragment is still visible. The applied methodology provides a major advantage compared to the alternative strategy of sequential silanization of half a wafer with 'UV-tetrazole' silane and half a wafer with PAT silane. The photo patterning methodology allows simple preparation of high resolution patterns with great control of the borders of the λ-orthogonal regions. As stated in the Chapter 4, the PAT and the corresponding pyrazoline cycloadducts absorb in the visible light region. Therefore inhibition of the NITEC reaction by the formed cycloadduct takes place in solution as the absorbance of the pyrazoline is significantly higher

than the absorbance of the PAT. However due to the immobilisation of the visible light sensitive PAT on the surface, the absorption of the pyrazoline does not interfere with the absorption of the PAT, allowing more efficient NITEC reaction than in solution.

In the third step the wafer **II**, patterned with PAT and 'UV-tetrazole', was employed in a λ-orthogonal, visible NITEC reaction. Wafer **II** was placed into an argon purged solution of **32** in MeCN. A bromide end capped maleimide **32** was chosen as the dipolarophile for the NITEC reaction due to the sensitivity of the ToF-SIMS method towards halogenated species. The resulting reaction mixture was irradiated globally at 410 – 420 nm for 3 h, at ambient temperature. The obtained wafer **III** was found to have had the PAT converted to a bromide functional pyrazoline pattern, while 'UV tetrazole' located inside the circular pattern remained unreacted according to ToF-SIMS analysis (refer to Figure 40). Full conversion of the PAT molecule and efficient formation of the desired bromide end capped pyrazoline species was observed. The yellow coloured circle indicates the presence of the $[C_7H_7NO]^+$ fragment and the 'UV tetrazole' moiety respectively. $[Br]^-$ fragment was only detected surrounding the circular pattern, indicating the conversion of the PAT species in the visible light induced NITEC reaction. No $[Br]^-$ fragment was observed inside the circles. Therefore the physio absorbance of the bromine functional maleimide on the surface is rather unlikely. This result also confirmed the full conversion of the PAT species in the previous step of the surface modification sequence, as any residual PAT derivative remaining at this stage of the modification would have given bromide functional pyrazoline derivatives with the pattern and decrease the contrast in the ToF-SIMS measurement.

Finally, the 'UV-tetrazole' derivative was utilised in a UV light induced NITEC reaction. The wafer **III** was placed into argon purged solution of **36** dissolved in DCM. Fluoride end capped maleimide **36** was chosen as the dipolarophile for the NITEC reaction due to the sensitivity of ToF-SIMS method towards halogenated species. Additionally, the introduction of a

fluorinated species provides an excellent contrast to the bromide functional areas on the surface. The reaction mixture was then irradiated globally at 320 nm for 1 h, at ambient temperature. DCM was employed as the solvent as the CF_3 group functional maleimide was found to have poor solubility in MeCN. The obtained wafer **IV** was then analysed *via* ToF SIMS (refer to Figure 40). Full conversion of the 'UV-tetrazole' and the formation of the desired fluoride containing pyrazoline cycloadduct was observed. While the $[Br]^-$ fragment of the pyrazoline, formed in a visible light NITEC of PAT and **32**, is still present (visualized by the green colour), a novel $[F]^-$ fragment (visualized by the red colour) appeared. The presence of the $[F]^-$ fragment confirms the success of the NITEC reaction. The excellent contrast of the ToF-SIMS images of wafer **IV** visualised the high efficiency of this approach. As further confirmation, a control experiment was undertaken to ensure only covalent attachment of maleimide **36** under applied reaction conditions. The corresponding sample was analysed *via* ToF SIMS (refer to Figure 43). No irradiation source was employed in the control experiment. However, all other variables remained constant as applied for preparation of wafer **IV**. No physio adsorption of the species **36** was observed while the 'UV-tetrazole' moiety remained intact. In Figure 43 image (a) displays the $[C_7H_7NO]^+$ fragment of the 'UV-tetrazole. The circular pattern is fully functionalized with the UV-active tetrazole species. Image (b) shows the full reaction of the PAT, as the monitored $[C_{16}H_9O]^+$ fragment of the visible light tetrazole is negligible. Image (c) confirmed the presence of the $[Br]^-$ fragment on the surface surrounding the circular pattern, while image (d) provides negative control of the presence of a fluorinated species.

Initially, a chloride functional maleimide was employed to visualise the success of the UV triggered NITEC reaction *via* ToF-SIMS instead of species **36**. However the corresponding $[Cl]^-$ was distributed equally over the surface after the UV irradiation, with no pattern observed. The experimental result explained by a potential UV induced, radical cleavage of the halogenated species from the structures grafted to the surface or present

in the solution. The obtained radical species (surface based and in solution) can then undergo diffusion controlled recombination reaction, leading to a scrambling of the alkyl halides and loss of the spatial control of the reaction. Consequently, the UV stability of the species applied for the λ-orthogonal surface modification plays a major role for the success of the approach.

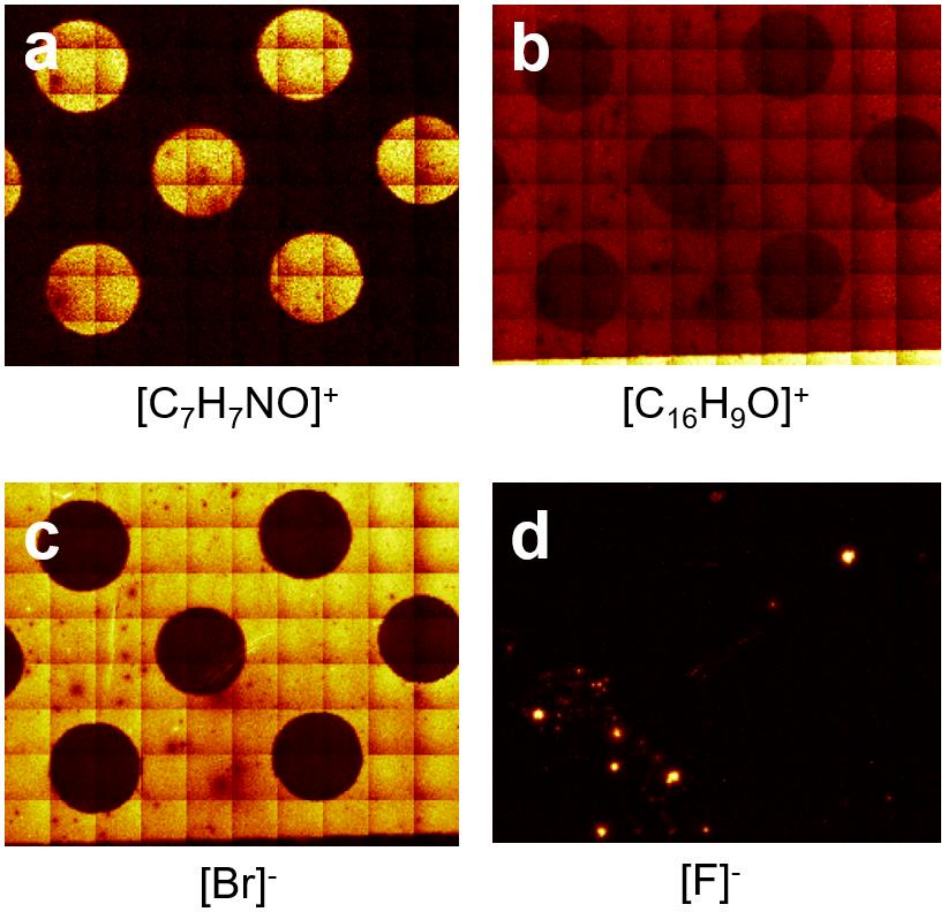

Figure 43 ToF SIMS image of the control experiment for photo triggered modification of the wafer **III**, in oder to obtain patterned wafer **IV**, functionalized with halogenated cycloadducts of PAT and 'UV-tetrazole'. Identical conditions were applied, except keeping the reaction set up in the dark for the period of the experiment. (a) $[C_7H_7NO]^+$ fragment of the 'UV-tetrazole'. (b) $[C_{16}H_9O]^+$ fragment of the PAT. (c) $[Br]^-$ fragment of bromide functional maleimide **32** grafted to the surface *via* NITEC. (d) $[F]^-$ fragment of fluoride functional maleimide **36** grafted to the surface *via* NITEC. Yellow colour illustrates the presence of the respective fragment.

6.3 Conclusion

In summary, a novel λ-orthogonal coupling approach is presented. NITEC reaction of UV light photo active tetrazole and the visible light active PAT were performed in different wavelength regimes allowing selective cycloadduct formation. The strategy features rapid, clean and equimolar conversion of the tetrazole moieties to the desired pyrazoline cycloadducts. The methodology was applied for small molecule ligation in solution, allowing for fast and simple λ-orthogonal coupling. The λ-orthogonality of the photo induced cycloadditions were confirmed *via* NMR studies. In addition, the approach was utilised for the preparation of tailored surface patterns. This was demonstrated using a silane functional PAT derivative grafted onto a silicon surface. The resulting photo active wafer was modified in three consecutive photo triggered reactions. In the first step a fumarate functional 'UV-tetrazole' was grafted to the surface *via* visible light induced NITEC in presence of a shadow mask. Importantly in this step, the UV active tetrazole moiety remained unaffected by the visible light irradiation. The resulting patterned wafer was subsequently employed for λ-orthogonal modification at 320 or 410 – 420 nm in the presence of halogenated maleimides. The corresponding wafers were analysed by ToF-SIMS. Excellent contrasts of the ToF-SIMS images for all performed photo triggered modifications of the wafers were observed, indicating full conversion of the tetrazole species and the efficient formation of the desired cycloadduct in each modification step. Furthermore, control experiments confirmed the absence of physically adsorbed species on the surface. The presented λ-orthogonal coupling concept is a powerful tool for the simple preparation of advanced structures in solution or on surfaces.

7 Summary and Outlook

Contemporary scientific research often requires methods for rapid and efficient molecular coupling methods *via* the formation of new chemical bonds. The concept of 'click chemistry' as a conjugation strategy was first introduced by Sharpless in 2001.[286] Since then, a range of novel techniques - some of them adhering to the strict requirements of the 'click chemistry' approach were established. Among others, light driven reactions are promising candidates for rapid, clean and efficient conjugation. In contrast to the classical thermal driven approaches, photoinduced reactions provide two distinctive advantages, namely: spatial and temporal control over the reaction process. Breakthrough advances have been made in the field of photochemistry, such as introduction of two photon absorption, upconversion and photoinduced redox catalysis concepts for assisting of chemical reactions. Furthermore, a wide range of photo active species for efficient linkage reactions, triggered by single photon absorption, in the absence of additives, have been established. However, the field of photochemistry is still full of challenges which need to be addressed, with perhaps the most highly sought after being the bathochromic shift of the trigger wavelength for photochemical reactions. The presented thesis demonstrates the benefits of the NITEC reaction as a conjugation method. During the course of this work the NITEC linkage technique was proven to be exceptionally robust, efficient and rapid under various reaction conditions. In the third chapter, the NITEC and PFN concepts were combined, allowing for the light triggered formation of profluorescent, pyrazoline containing nitroxides derivatives for sensing of redox/radical processes. It was found that the distance between the fluorescent pyrazoline and the nitroxide moiety is decisive for the sensor functionality.

Close proximity of both functionalities provides best sensor performance. The high sensitivity of the PFNs formed *via* NITEC towards carbon centered radicals and reductants was confirmed by fluorescence spectroscopy. Importantly, the nitroxide moiety, known to be an excited state quencher, had no effect on the photoinduced NITEC reaction, potentially involving photo-excited states. The synthetic tools established for the synthesis of various nitroxide functionalized tetrazoles are developed in chapter four. A bathochromic shift of the trigger wavelength for the NITEC reaction was achieved by extending the aromatic system of the tetrazole species. The resulting pyrene functional tetrazole was employed for additive free small molecule ligation, as well as macromolecular design *via* visible light trigger. Efficient and rapid formation of the desired cycloadduct was observed for all reactions. Interestingly, the pyrazoline species formed during the NITEC reaction, displayed NIR fluorescence, suitable for *in vivo* labelling and tracking. Although a significant bathochromic shift of the trigger wavelength could be achieved in chapter four, the application of visible light is still a limiting factor for biological approaches. Deep tissue, *in situ* triggering of conjugation reactions is only possible by NIR irradiation, due to its better penetration ability compared to the visible light. In order to induce the NITEC reaction by NIR, UCNPs were applied as an additive for the conjugation reaction of the pyrene functional tetrazole with maleimide species (chapter five). The combination of the UCNP and NITEC concepts allowed rapid and efficient conjugation of small molecules and polymers triggered by NIR light. In chapter six, the ability of the pyrene functional tetrazole to perform in a λ-orthogonal surface modification was demonstrated. Thus the selective triggering of NITEC reaction of the pyrene functional tetrazole in presence of a ‘conventional’ UV-sensitive tetrazole was performed. Subsequently, the UV-sensitive tetrazole was converted in the NITEC reaction. The performance of the two step ligation strategy was validated in solution, revealing the rapid and efficient formation of the desired cycloadduct. Furthermore, the technique was employed for the modification of surfaces. Thus, the ability of the light driven NITEC reaction

was utilized for simple, efficient, catalyst free formation of patterns under mild conditions. The excellent pattern contrast of the ToF-SIMS images of the modified structures underpins the significant potential of the presented approach.

Although the current thesis presents significant contributions to the 'toolbox' of light induced reactions, the challenges of photochemistry are still far from being complete. In particular, the presented projects provide several opportunities for further investigation. After the PFN formation was successfully established in solution, the application of the approach for creation of redox/radical sensitive surfaces such as cellulose is possible. Here, a combination of the profluorescent pyrazolines with the λ-orthogonal approach presented in chapter six is an intriguing challenge. By applying the pH-sensors to the maleimide segment, microstructured, multifunctional sensor materials for the determination of pH values, as well as detection of radical and redox species could be prepared. Furthermore, formation of PFNs *via* NITEC reaction in the visible light regime can be accomplished *via* the extension of the aromatic system of the nitroxide functional diaryl tetrazole derivative. The resulting photo active species is a promising candidate for *in vivo* labelling and tracking. Especially as the formed pyrazoline emits in the NIR range, facilitating the fluorescence detection. Apart from the combination with PFNs, the pyrene functional tetrazole can be applied in polymer chemistry. Here, preparation and application of a RAFT agent featuring the visible light active tetrazole species would be a key goal. In addition, the reactivity of the tetrazole species towards thiols and acids should be investigated. The UCNP assisted NITEC reaction is the first example of conjugation reaction triggered by NIR light. Although successful macromolecular design and conjugation of the biological relevant biotin moiety was demonstrated, the concept needs further exploration. *In vivo* labelling and tracking, as well as drug delivery applications are conceivable. Finally the λ-orthogonal surface modification approach provides a significant potential for the fabrication of lab on chip devices.

The potential differences in the reactivity of the pyrene functional tetrazole towards acids, thiols and maleimide moieties should be considered as a possible avenue for one pot coupling approaches. In addition, a combination of UV active tetrazole, photoenol and pyrene tetrazole could provide a 'three component' approach for λ-orthogonal surface pattering. Furthermore, the λ-orthogonal surface pattering approach could be accomplished using NIR light if combined with the UCNPs and TPA techniques.

8 Experimental Section

8.1 Design of Redox/Radical Sensing Molecules *via* NITEC

8.1.1 Materials

4-(2-Phenyl-*2H*-tetrazol-5- yl)benzoic acid **1** was synthesized according to the literature.[181] 5-Formyl-1,3-dihydro-1,1,3,3-tetramethyl-2H-isoindol-2-yloxy was synthesized.[287] All other reagents were purchased from commercial suppliers and used without further purification.

8.1.2 Methods and Analytical Instrumentation

Air-sensitive reactions were carried out under an atmosphere of ultrahigh purity argon.

^{1}H and ^{13}C NMR spectra were recorded on a 400 MHz spectrometer and referenced to the relevant solvent peak stated in the spectrum caption. The 4 methyl groups α to the protected nitroxide species from the methoxyamine derivatives are not visible in ^{13}C NMR.

ESI high-resolution mass spectra were obtained using a QTOF LC mass spectrometer which utilised ESI (recorded in the positive mode) with a methanol mobile phase.

Melting points were measured on a variable-temperature apparatus by the capillary method and are uncorrected.

Analytical HPLC was carried out on a HPLC system using a Prep-C18 scalar column (4.6 × 150 mm, 10 µm) with a flow rate of 1 mL / min.

All photoreactions were carried out in a photoreactor with 254 nm lamps (16 x 8 W).

General Procedure for Time-Resolved Fluorescence Measurements: Reduction with NaAsc: 500 μL stock solution of the desired pyrazoline in MeOH was added to 2.5 mL MeOH, and the fluorescence spectrum was recorded. After adding a stock solution of NaAsc in MeOH (ca. 30 μL) fluorescence measurements were taken every 2 min for 40 min in total. Radical scavenging: 500 μL stock solution of pyrazoline **16** in acetonitrile was added to 2.5 mL acetonitrile. The solution was purged with argon for 30 min, heated to 60 °C and the fluorescence spectrum was recorded. After adding argon purged stock solution of AIBN in acetonitrile (ca. 30 μL), fluorescence measurements were taken every 2 min for 70 min in total.

Computational Procedures: Geometries of all species were fully optimized using M06L/6-31 + G(d), a modern DFT functional chosen for its implicit consideration of dispersion.[288] Calculations were performed in the presence of acetonitrile solvent using the SMD solvent model. All conformations were fully searched at this level of theory to ensure global rather than merely local minima were found, and frequency calculations were performed to confirm the nature of all stationary points. All calculations were performed using the Gaussian 09 software suite.[289]

8.1.3 Synthesis

5-Maleimido-1,1,3,3-tetramethylisoindolin-2-yloxyl (2)

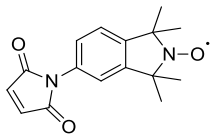

Maleic anhydride (48 mg, 0.49 mmol) was dissolved in 2 mL anhydrous Et_2O and added to a solution of 5-amino-1,1,3,3-tetramethylisoindolin-2-yloxyl (100 mg, 0.488 mmol) in 1 mL DCM. The reaction mixture was stirred for 3 h and the resulting yellow precipitate was recovered by filtration and washed with Et_2O. The isolated solid (116 mg, 0.38 mmol was then dissolved in 2.5 mL acetic anhydride to which sodium acetate (48 mg, 0.59 mmol) was added. The reaction mixture was stirred for 18 h. After removing the solvent under reduced pressure the crude product was purified *via* column chromatography on silica gel using hexane / ethyl acetate (3:2, v / v R_f 048.) as the eluent. After drying under high vacuum the title compound was obtained as yellow powder (67 mg, 71 %): HRMS (EI) m / z: calcd. for $[M + Na]^+$ $C_{16}H_{17}N_2NaO_3$ 308.1137 found 308.1138; EPR (THF) *g* 1.9944, a^N 1.4028.

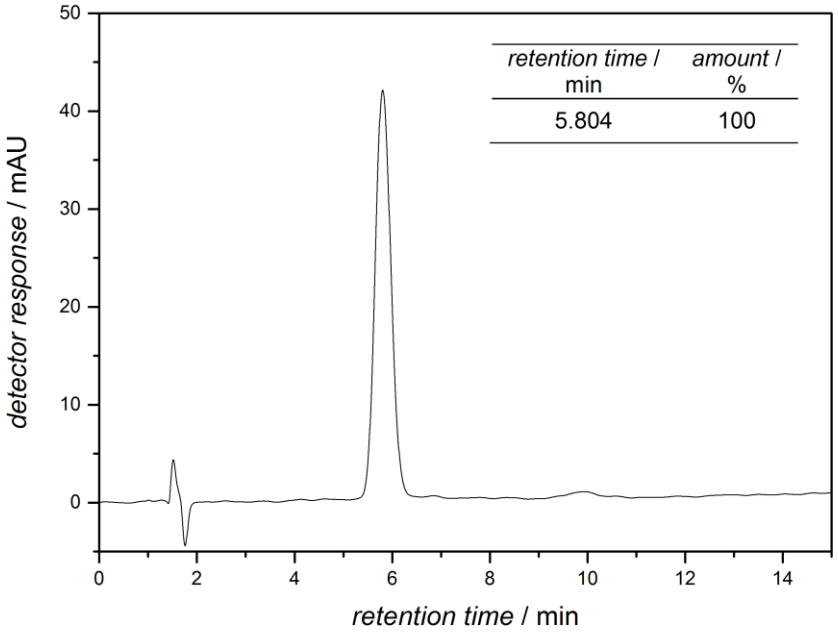

Figure 44 HPLC chromatogram of 5-maleimido-1,1,3,3-tetramethylisoindolin-2-yloxyl **2** measured in THF / H_2O mixture (35:65, v / v) and detected at 254 nm (absorbance).

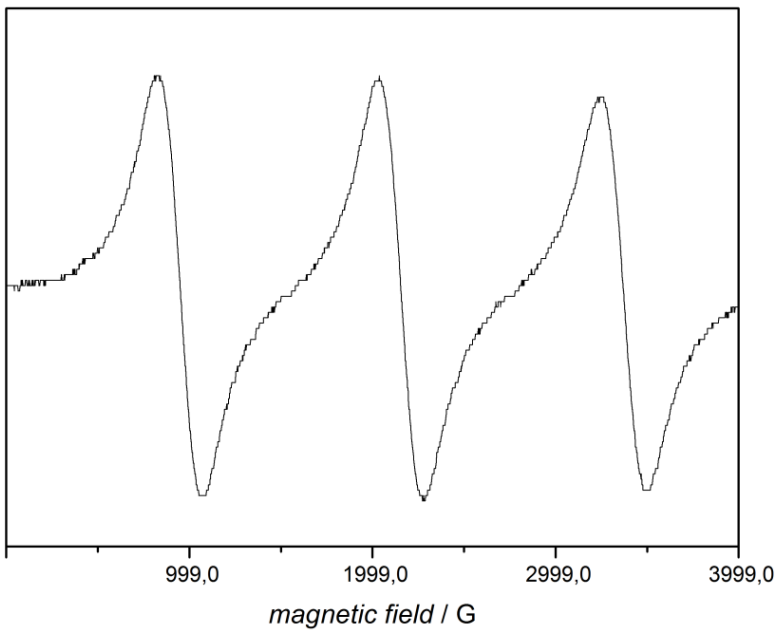

Figure 45 EPR spectrum of 5-maleimido-1,1,3,3-tetramethylisoindolin-2-yloxyl **2** in THF.

General Procedure for Synthesis of Cycloadducts

Diaryl tetrazole derivative was dissolved in acetonitrile. Maleimide derivative was added (Refer to Table 4 for further details). After irradiation with UV (254 nm) at ambient temperature for 15 min, solvent was removed under reduced pressure. The crude product was purified *via* column chromatography on silica gel using hexane / ethyl acetate as the eluent. ^{1}H NMR (400 MHz, $CDCl_3$): **15** δ = 7.92 (m, 1 H), 7.85 - 7.75 (m, 1 H), 7.63 - 7.51 (m, 2 H), 7.43 - 7.31 (m, 2 H), 7.22 - 7.10 (m, 1 H), 7.05 - 6.95 (m, 1 H), 5.20 (d, J = 11.0 Hz, 1 H), 4.93 (d, J = 10.9 Hz, 1 H), 3.80 (s, 3 H), 3.84 - 3.72 (m, 4 H), 2.03 - 1.91 (m, 1 H), 1.67 - 1.26 (m, 12 H); **20** δ = 8.02 - 7.91 (m, 3 H), 7.81 - 7.72 (m, 1 H), 7.59 - 7.50 (m, 2 H), 7.21 - 7.15 (m, 1 H), 5.32 - 5.27 (m, 1 H), 4.98 (d, J = 10.8 Hz, 1 H), 3.79 (s, 3 H), 3.85 - 3.73 (m, 4 H), 1.59 - 1.41 (m, 21 H); ^{13}C NMR (100 MHz, $CDCl_3$) **15** δ = 173.3, 172.3, 147.1, 145.8, 144.6, 142.9, 129.4, 129.2, 126.6, 121.7, 121.5, 120.2, 114.4, 67.1, 65.5, 65.5, 60.0, 53.6, 42.3; **20** δ = 172.7, 171.9, 165.8, 147.5, 147.1, 145.9, 144.2, 131.0, 129.0, 126.8, 124.4, 121.8, 120.4, 113.3, 80.5, 67.1, 65.5, 64.5, 59.7, 53.6, 42.3, 28.3. HRMS (EI) m / z: **3** calcd. for $[M + Na]^+$ $C_{30}H_{27}N_4NaO_5$ 546.1879 found 546.1867; **8** calcd. for $[M + 2H]^+$ $C_{29}H_{35}N_4O_6$ 535.2557 found 535.2528; **15** calcd. for $[M + H]^+$ $C_{26}H_{31}N_4O_4$ 463.2345 found 463.2315; **16** calcd. for $[M +Na]^+$ $C_{25}H_{27}N_4NaO_4$ 470.1930 found 470.1930; **20** calcd. for $[M + H]^+$ $C_{31}H_{39}N_4O_6$ 563.2870 found 563.2828; **21** calcd. for $[M + Na]^+$ $C_{30}H_{35}N_4NaO_6$ 570.2454 found 570.2373; EPR (THF) **3** *g* 1.9932, a^N 1.4394; **8** *g* 1.9918, a^N 1.5308; **16** *g* 1.9918, a^N 1.4061; **21** *g* 1.9920, a^N 1.4000.

Table 4 Overview over reaction conditions for the formation of the cycloadducts.

Cyclo adduct	Diaryl tetrazole	$c_{diaryl\ tetrazole}$ / mmol·L^{-1}	Malei mide	$c_{maleimide}$ / mmol·L^{-1}	V_{total} / mL	Eluent	R_f	*Yield* / %
3	1	5.8	2	5.8	6[a]	EE / H / AE, 1:1:0.02	0.60	65
8	6	6.2	7	9.3	6[b]	EE / H, 1:1	0.28	87
15	13	7.2	7	7.2	12[b]	EE / H, 1:2	0.32	74
16	14	7.2	7	7.2	12[b]	EE / H, 1:2	0.21	79
20	18	4.5	7	4.5	10[b]	EE / H, 1:1	0.34	84
21	19	5.4	7	5.4	15[b]	EE / H, 1:3	0.31	71

[a] MeCN / DMSO was used (100:1, v / v), [b] MeCN was used as solvent

4-(5-(2-Oxyl-1,1,3,3-tetramethylisoindolin-5-yl)-4,6-dioxo-1-phenyl-1,3a,4,5,6,6a-hexahydropyrrolo[3,4-c]pyrazol-3-yl)benzoic acid (3)*

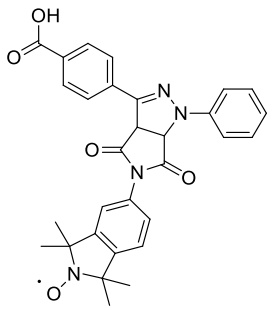

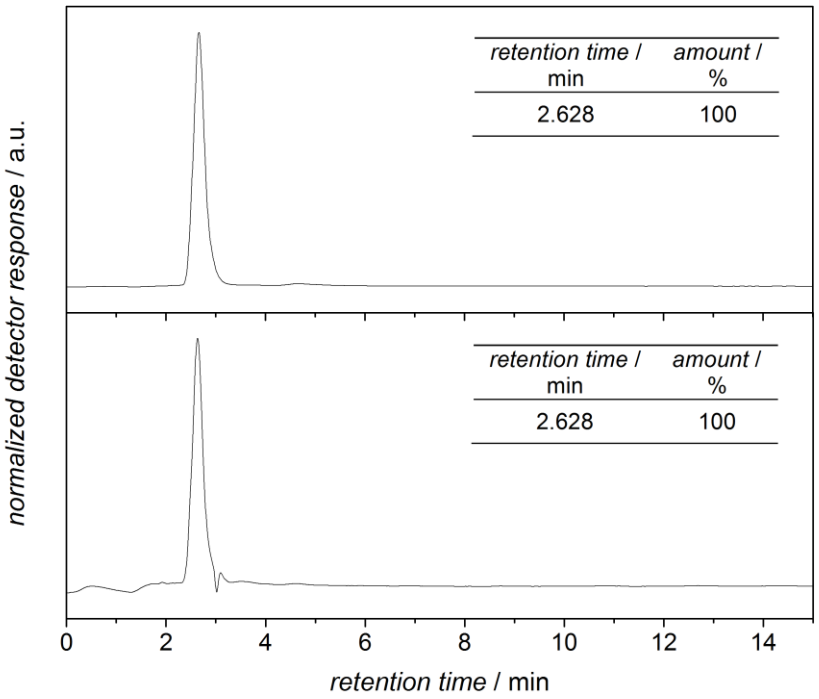

Figure 46 HPLC chromatogram of 4-(5-(2-oxyl-1,1,3,3-tetramethylisoindolin-5-yl)-4,6-dioxo-1-phenyl-1,3a,4,5,6,6a-hexahydropyrrolo[3,4-c]pyrazol-3-yl)benzoic acid **3** measured in THF / H_2O mixture (55:45, v / v); top: 430 nm emission detection at 350 nm excitation; bottom: 254 nm absorbance detection.

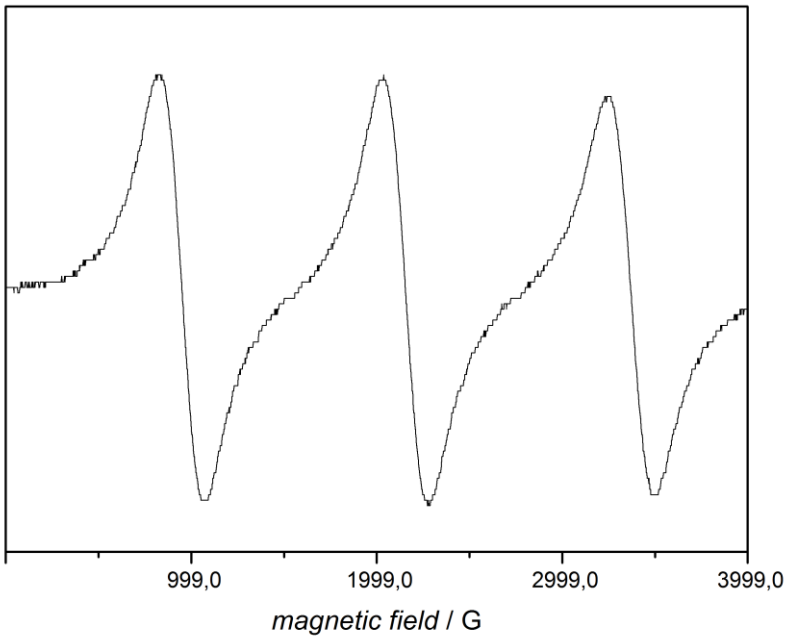

Figure 47 EPR spectrum of 4-(5-(2-oxyl-1,1,3,3-tetramethylisoindolin-5-yl)-4,6-dioxo-1-phenyl-1,3a,4,5,6,6a-hexahydropyrrolo[3,4-c]pyrazol-3-yl)benzoic acid **3** in THF.

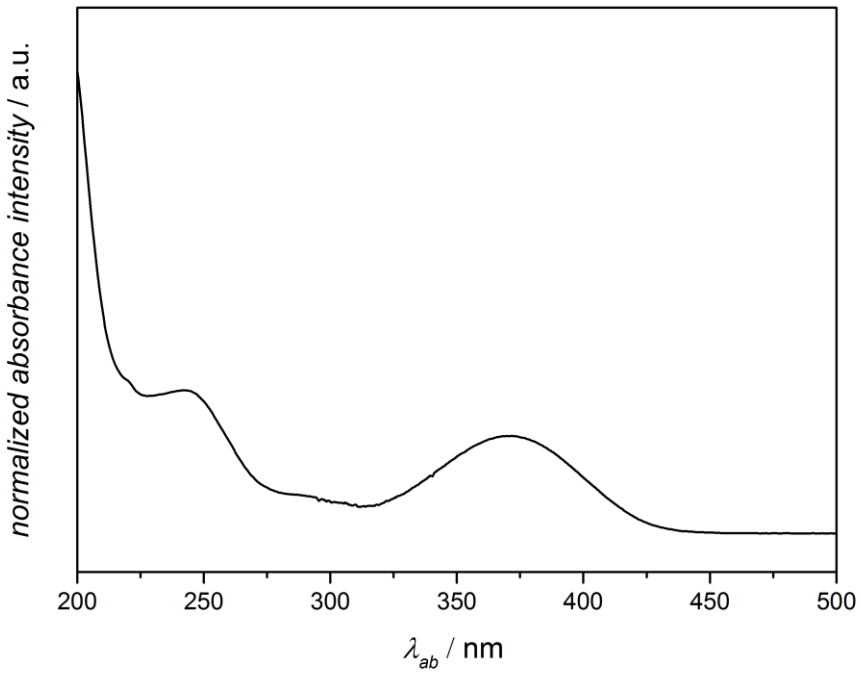

Figure 48 UV/VIS absorption spectra of 4-(5-(2-oxyl-1,1,3,3-tetramethylisoindolin-5-yl)-4,6-dioxo-1-phenyl-1,3a,4,5,6,6a-hexahydropyrrolo[3,4-c]pyrazol-3-yl)benzoic acid **3** in ACN.

*Compound degrades on the column and in sunlight and shows sensitivity to air. None of the degradation products show significant influence at the profluorescent behavior of the cycloadduct **3**.

1-Oxyl-2,2,6,6-tetramethylpiperidin-4-yl 4-(5-(2-hydroxyethyl)-4,6-dioxo-1-phenyl-1,3a,4,5,6,6a-hexahydropyrrolo[3,4-c]pyrazol-3-yl)benzoate (8)

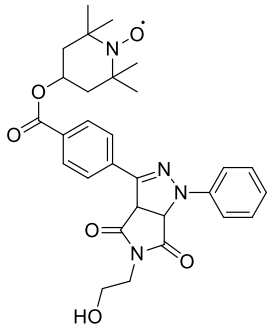

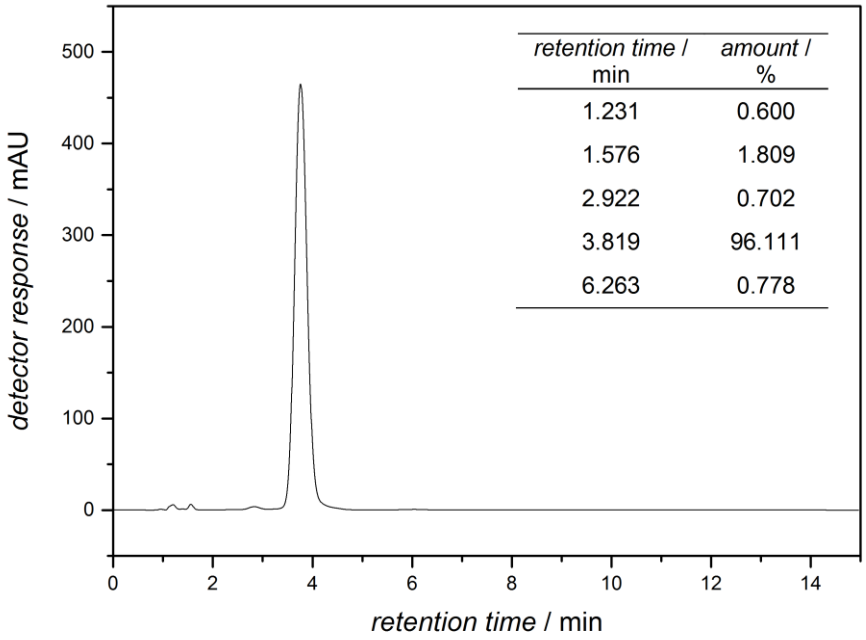

Figure 49 HPLC chromatogram of 1-oxyl-2,2,6,6-tetramethylpiperidin-4-yl 4-(5-(2-hydroxyethyl)-4,6-dioxo-1-phenyl-1,3a,4,5,6,6a-hexahydropyrrolo[3,4-c]pyrazol-3-yl)benzoate **8** measured in THF / H_2O mixture (35:65, v / v) and detected at 254 nm (absorbance).

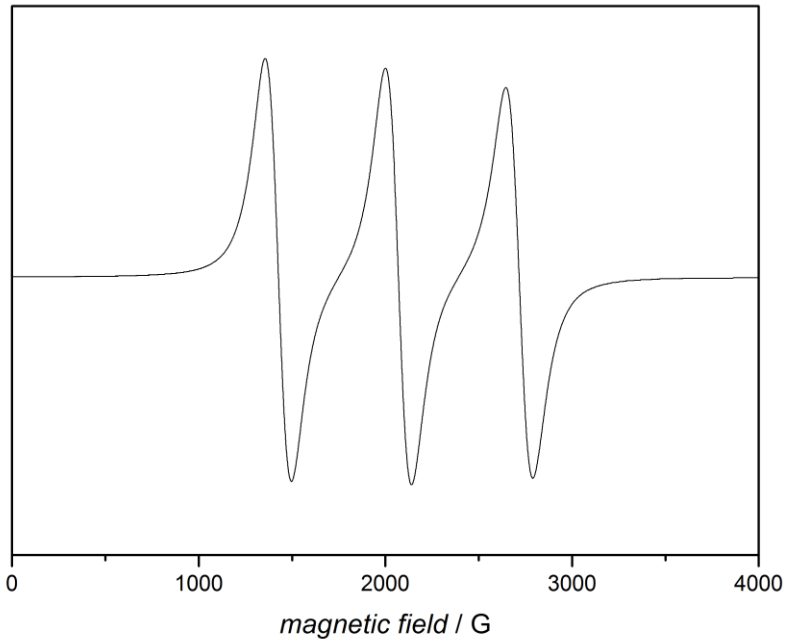

Figure 50 EPR spectrum of 1-oxyl-2,2,6,6-tetramethylpiperidin-4-yl 4-(5-(2-hydroxyethyl)-4,6-dioxo-1-phenyl-1,3a,4,5,6,6a-hexahydropyrrolo[3,4-c]pyrazol-3-yl)benzoate **8** in THF.

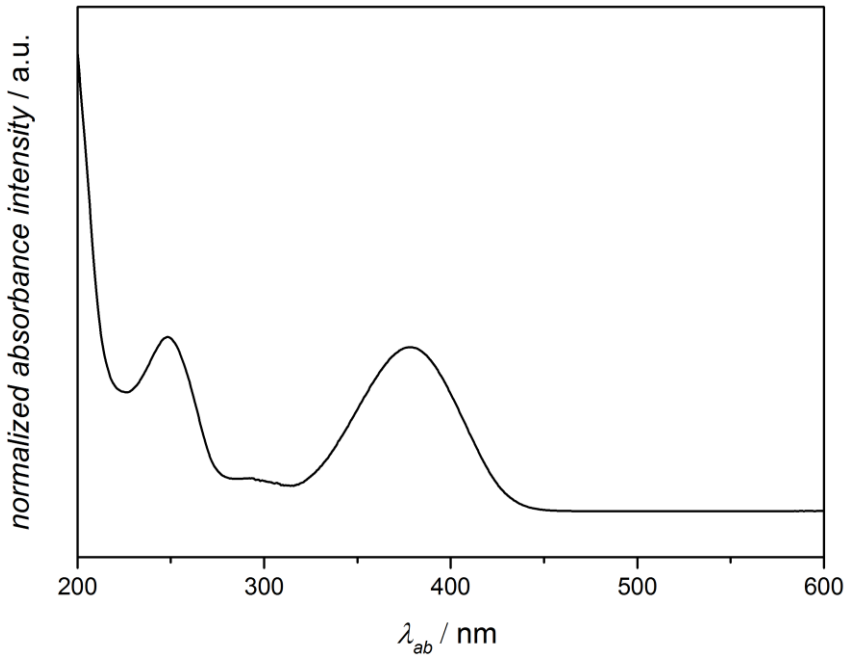

Figure 51 UV/VIS absorption spectrum of 1-oxyl-2,2,6,6-tetramethylpiperidin-4-yl 4-(5-(2-hydroxyethyl)-4,6-dioxo-1-phenyl-1,3a,4,5,6,6a-hexahydropyrrolo[3,4-c]pyrazol-3-yl)benzoate **8** in MeCN.

5-(2-Hydroxyethyl)-3-(2-methoxy-1,1,3,3-tetramethylisoindolin-5-yl)-1-phenyl-1,6a-dihydropyrrolo[3,4-c]pyrazole-4,6(3aH,5H)-dione (15)

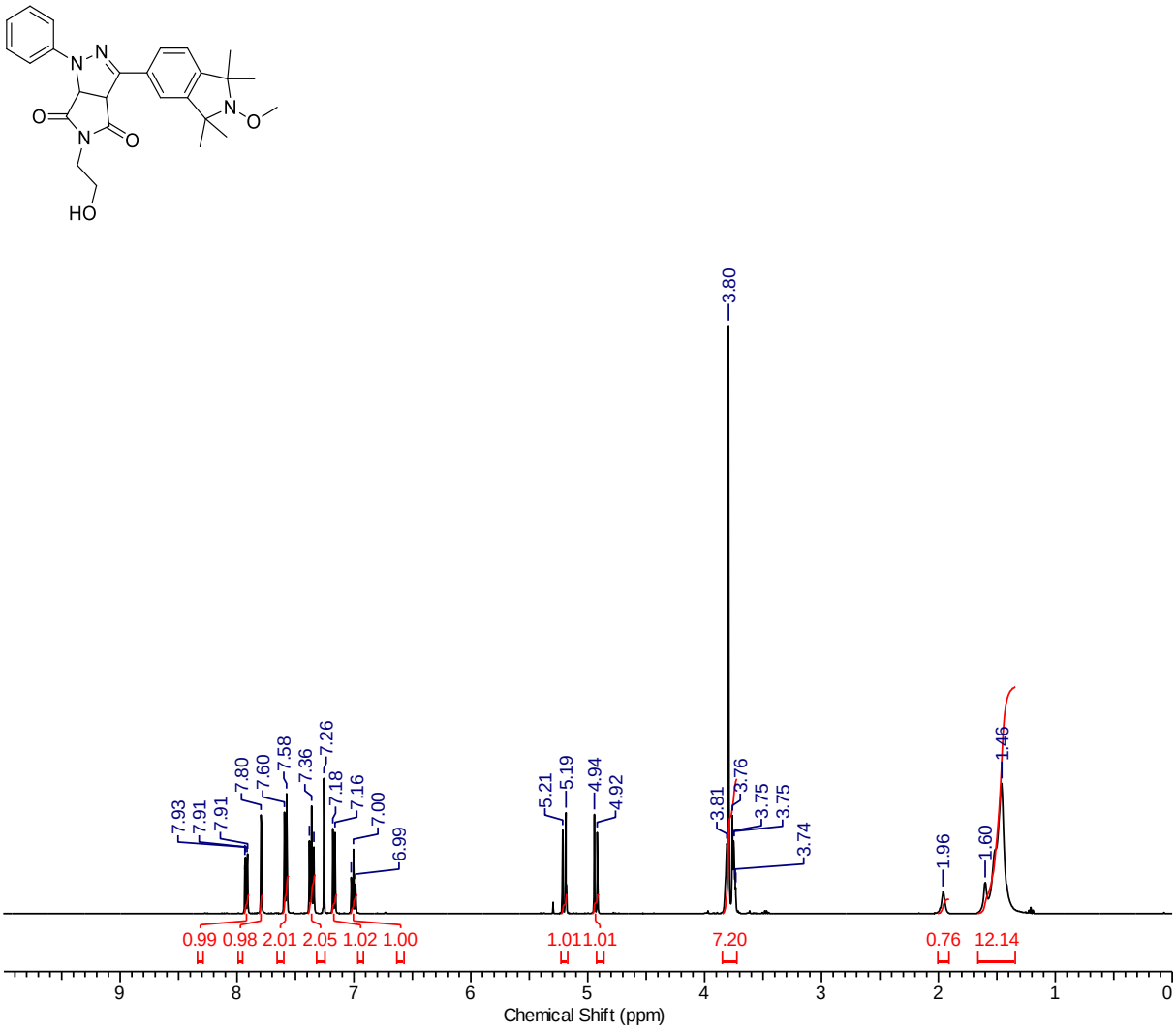

Figure 52 ^{1}H NMR (400 MHz, $CDCl_3$) spectrum of 5-(2-hydroxyethyl)-3-(2-methoxy-1,1,3,3-tetramethylisoindolin-5-yl)-1-phenyl-1,6a-dihydropyrrolo[3,4-c]pyrazole-4,6(3aH,5H)-dione **15**.

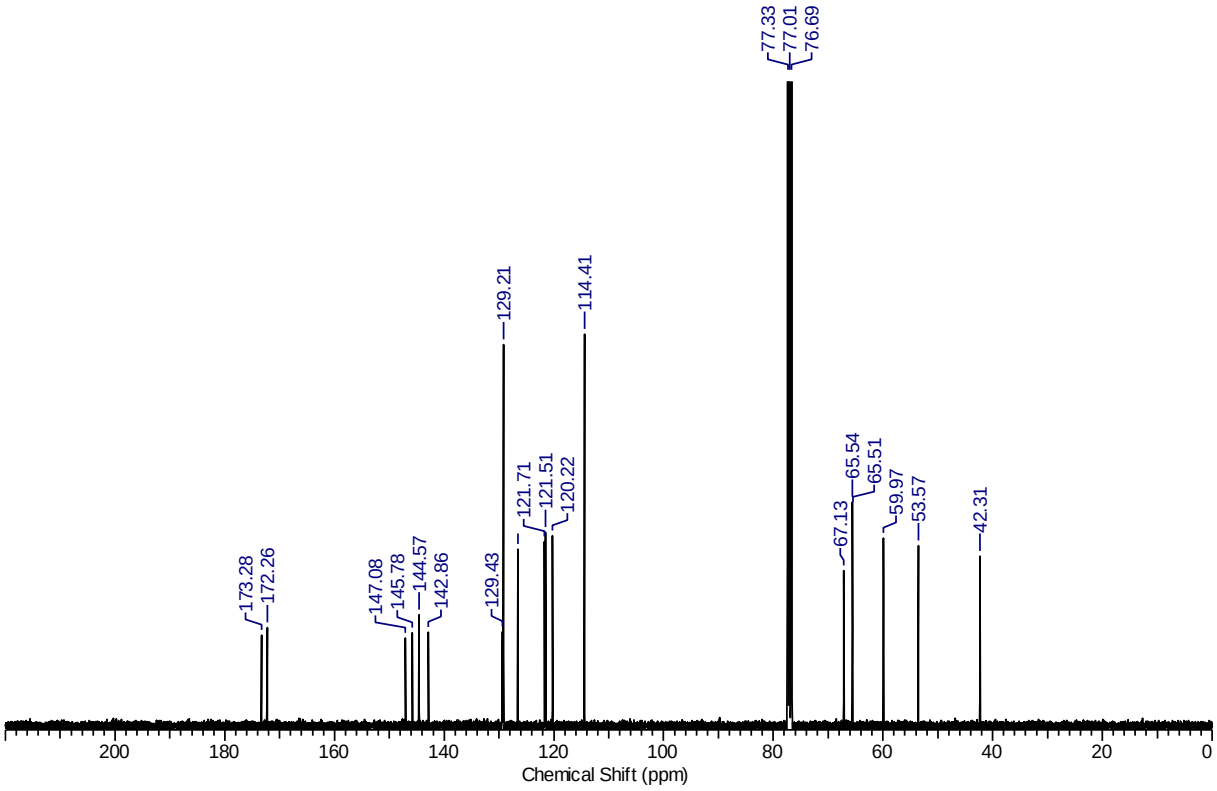

Figure 53 ^{13}C NMR (100 MHz, $CDCl_3$) spectrum of 5-(2-hydroxyethyl)-3-(2-methoxy-1,1,3,3-tetramethylisoindolin-5-yl)-1-phenyl-1,6a-dihydropyrrolo[3,4-c]pyrazole-4,6(3aH,5H)-dione **15**.

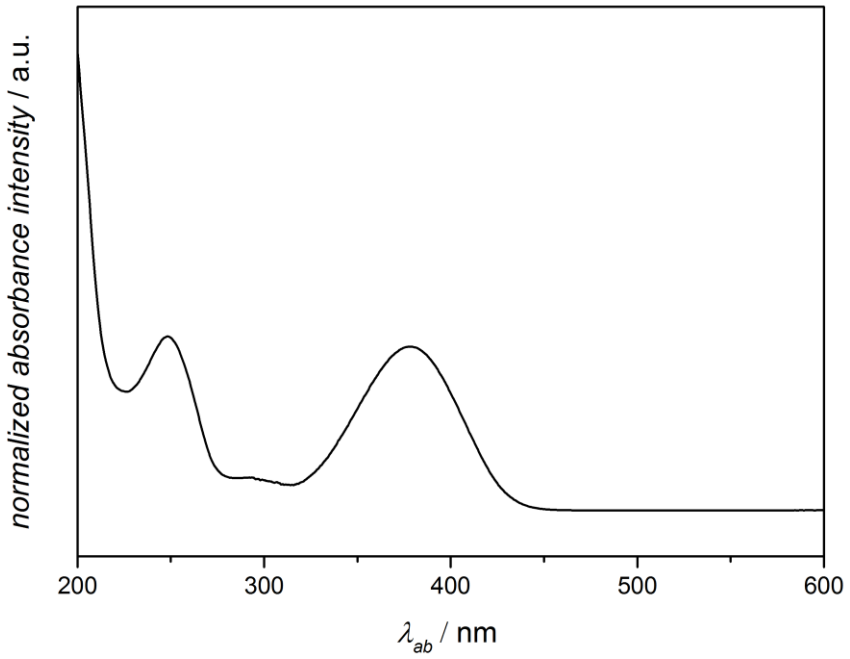

Figure 54 UV/VIS absorption spectrum of 2-oxyl-1,1,3,3-tetramethyl-5-(2-phenyl-2H-tetrazol-5-yl)isoindoline **15** in MeCN.

5-(2-Hydroxyethyl)-3-(2-oxyl-1,1,3,3-tetramethylisoindolin-5-yl)-1-phenyl-1,6a-dihydropyrrolo[3,4-c]pyrazole-4,6(3aH,5H)-dione (16)

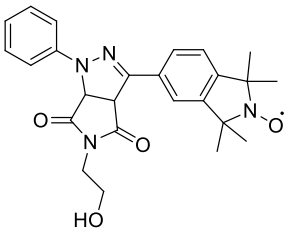

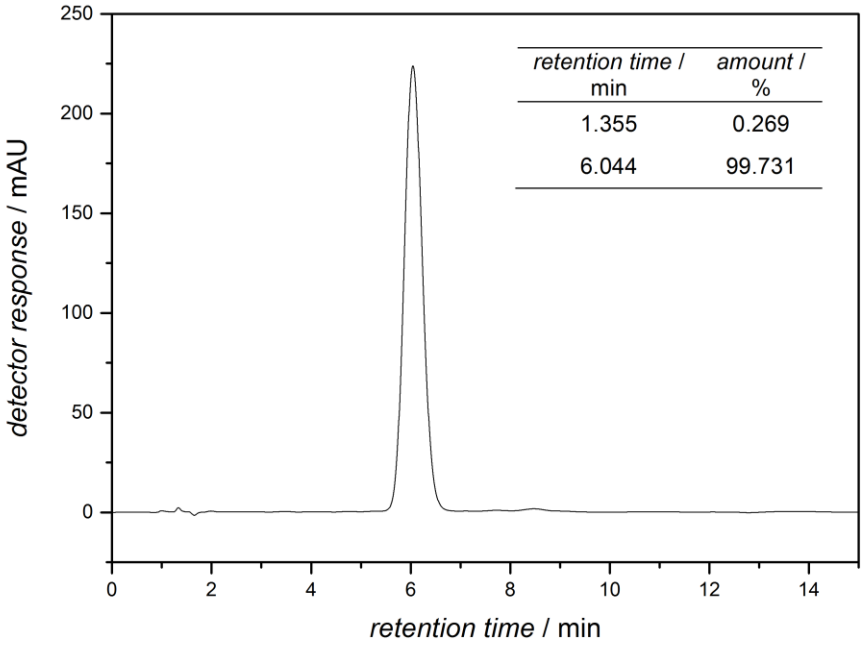

Figure 55 HPLC chromatogram of 5-(2-hydroxyethyl)-3-(2-oxyl-1,1,3,3-tetramethylisoindolin-5-yl)-1-phenyl-1,6a-dihydropyrrolo[3,4-c]pyrazole-4,6(3aH,5H)-dione **16** measured in THF / H_2O mixture (35:65, v / v) and detected at 254 nm (absorbance).

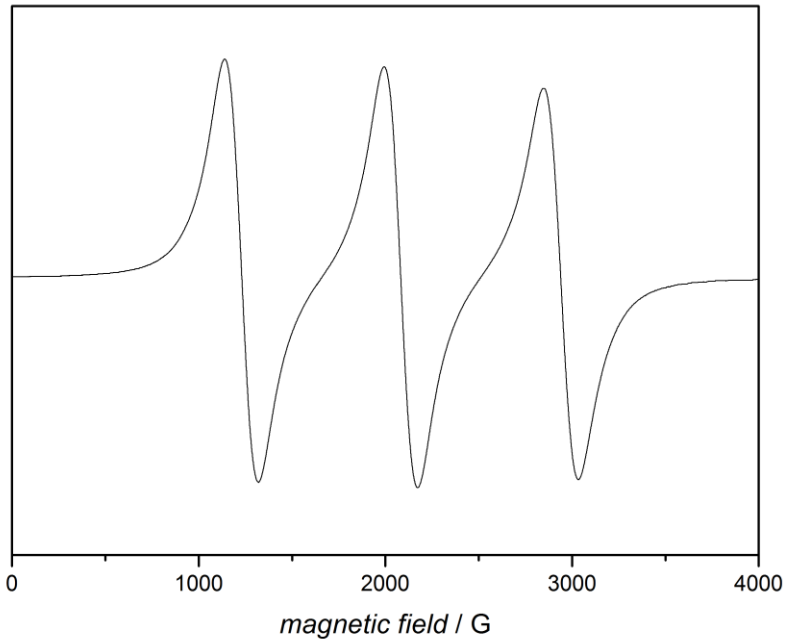

Figure 56 EPR spectrum of 5-(2-hydroxyethyl)-3-(2-oxyl-1,1,3,3-tetramethylisoindolin-5-yl)-1-phenyl-1,6a-dihydropyrrolo[3,4-c]pyrazole-4,6(3aH,5H)-dione **16** in THF.

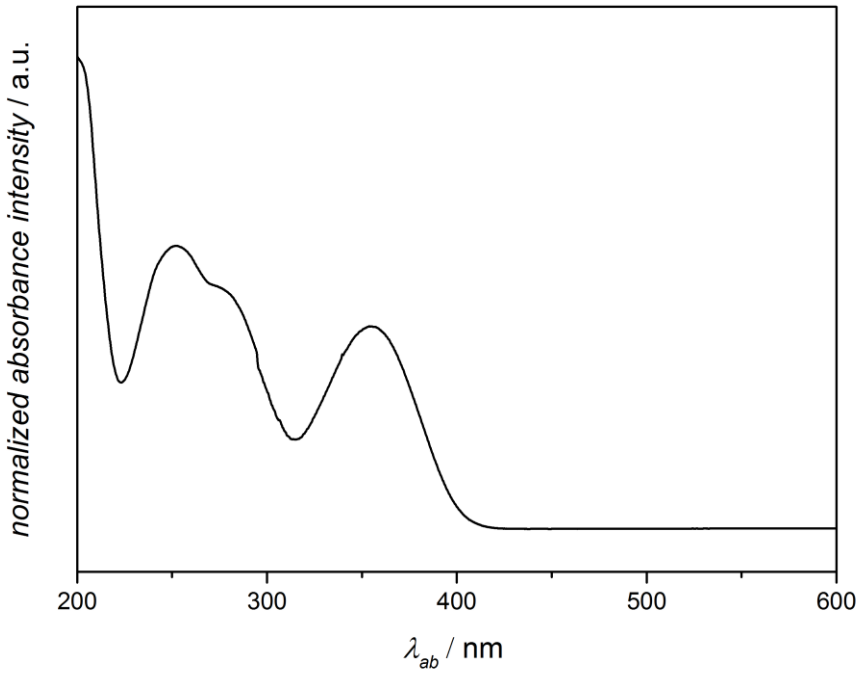

Figure 57 UV/VIS absorption spectrum of 2-oxyl-1,1,3,3-tetramethyl-5-(2-phenyl-2H-tetrazol-5-yl)isoindoline **16** in MeCN

tert-Butyl-4-(5-(2-hydroxyethyl)-3-(2-methoxy-1,1,3,3-tetramethylisoindolin-5-yl)-4,6-dioxo-4,5,6,6a-tetrahydropyrrolo[3,4-c]pyrazol-1(3aH)-yl)benzoate (20)

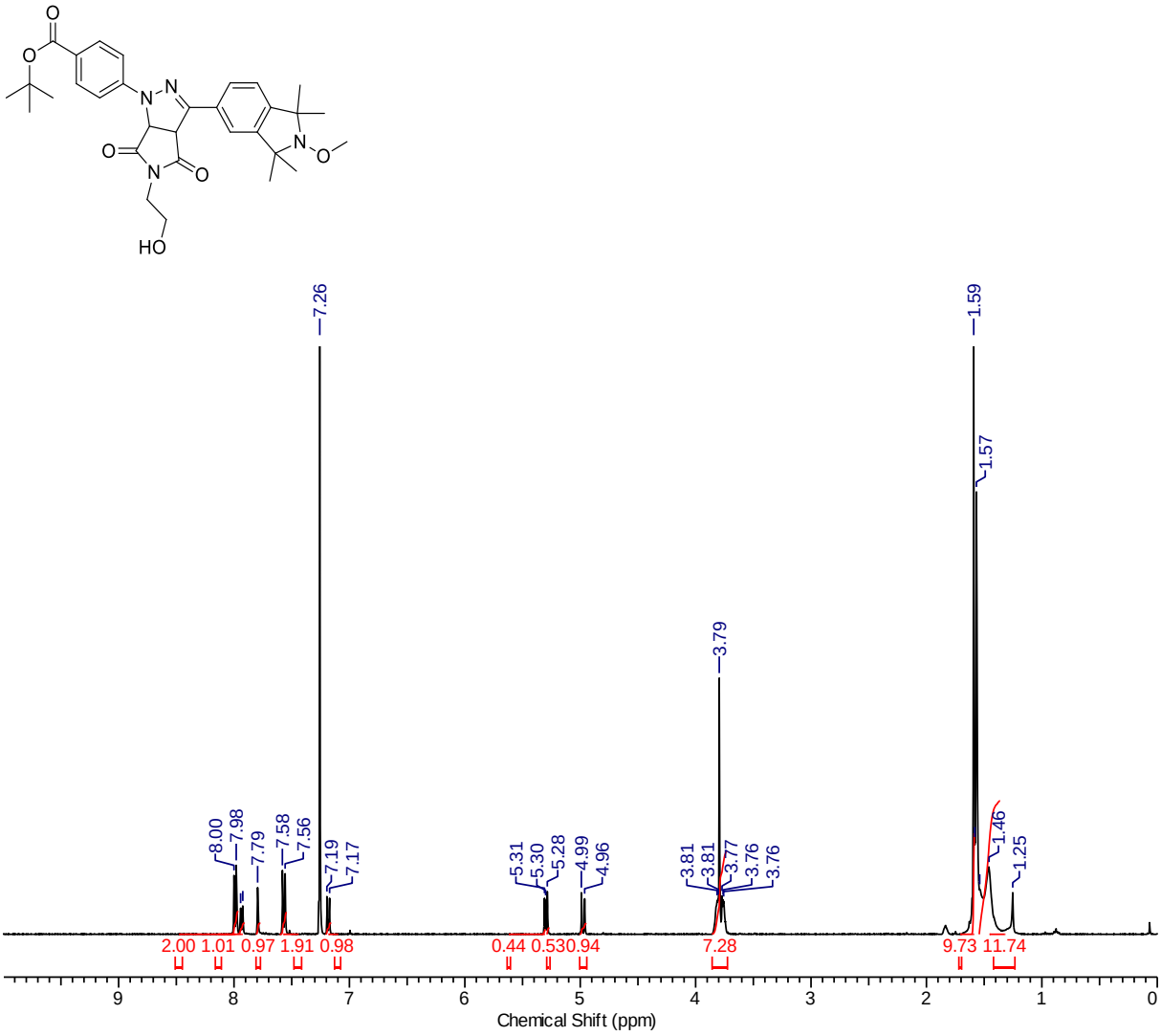

Figure 58 ^{1}H NMR (400 MHz, $CDCl_3$) spectrum of *tert*-butyl 4-(5-(2-hydroxyethyl)-3-(2-methoxy-1,1,3,3-tetramethylisoindolin-5-yl)-4,6-dioxo-4,5,6,6a-tetrahydropyrrolo-[3,4-c]pyrazol-1(3aH)-yl)benzoate **20**.

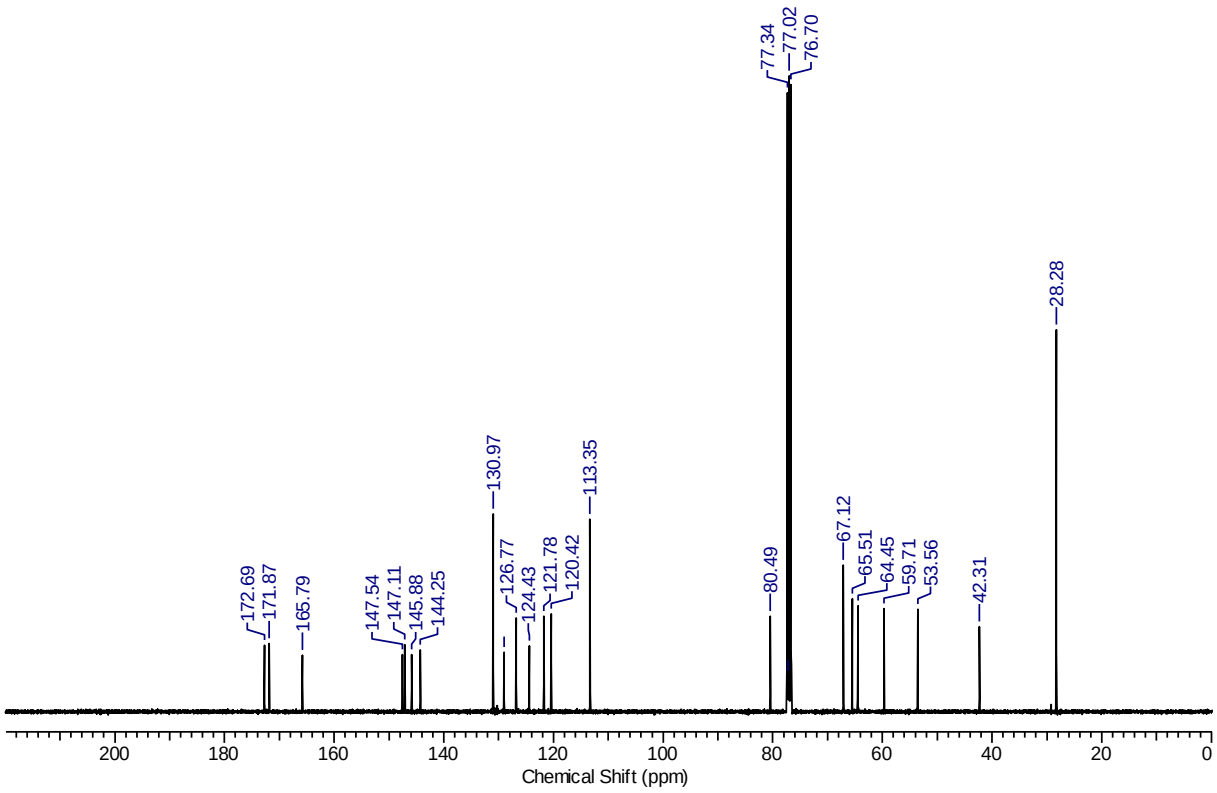

Figure 59 ^{13}C NMR (100 MHz, $CDCl_3$) spectrum of *tert*-butyl 4-(5-(2-hydroxyethyl)-3-(2-methoxy-1,1,3,3-tetramethylisoindolin-5-yl)-4,6-dioxo-4,5,6,6a-tetrahydropyrrolo-[3,4-c]pyrazol-1(3aH)-yl)benzoate **20**.

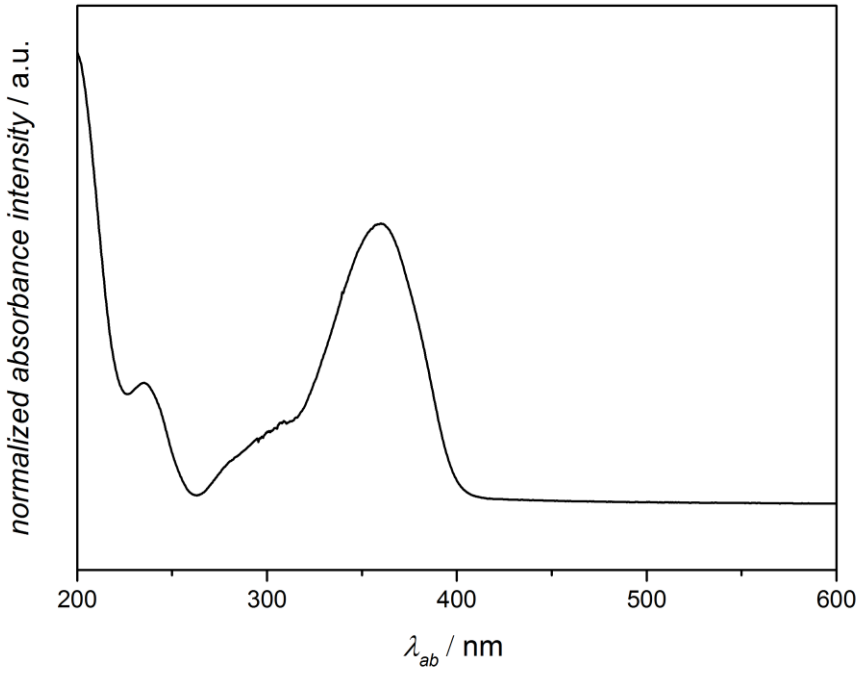

Figure 60 UV/VIS absorption spectrum *tert*-butyl 4-(5-(2-hydroxyethyl)-3-(2-methoxy-1,1,3,3-tetramethylisoindolin-5-yl)-4,6-dioxo-4,5,6,6a-tetrahydropyrrolo[3,4-c]pyrazol-1(3aH)-yl)benzoate **20** in MeCN.

tert-Butyl-4-(5-(2-hydroxyethyl)-3-(2-oxyl-1,1,3,3-tetramethyl-isoindolin-5-yl)-4,6-dioxo-4,5,6,6a-tetrahydropyrrolo[3,4-c]pyrazol-1(3aH)-yl)benzoate (21)

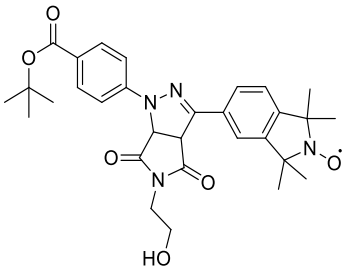

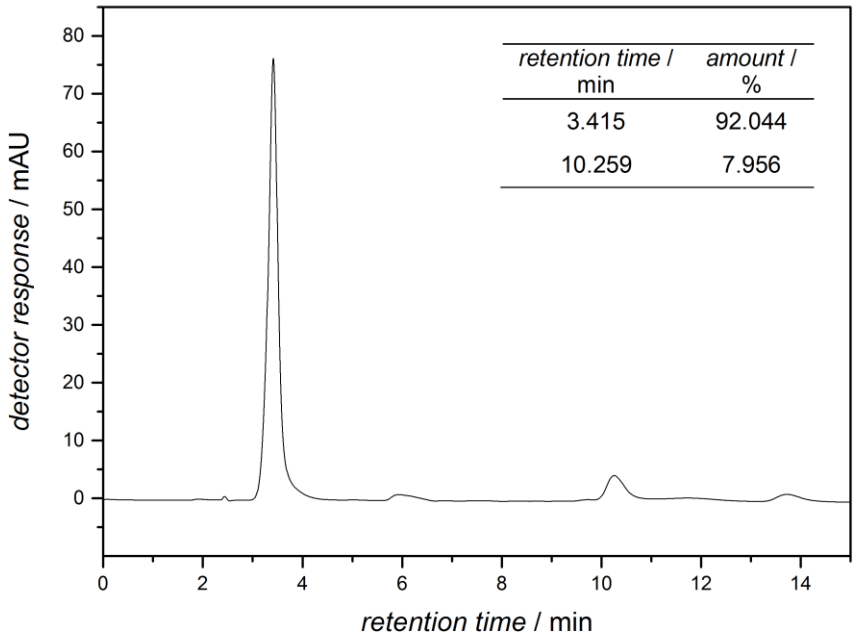

Figure 61 HPLC chromatogram of *tert*-butyl 4-(5-(2-hydroxyethyl)-3-(2-oxyl-1,1,3,3-tetramethylisoindolin-5-yl)-4,6-dioxo-4,5,6,6a-tetrahydropyrrolo[3,4-c]pyrazol-1(3aH)-yl)benzoate **21** measured in MeOH / H_2O mixture (70:35, v / v) and detected at 254 nm (absorbance).

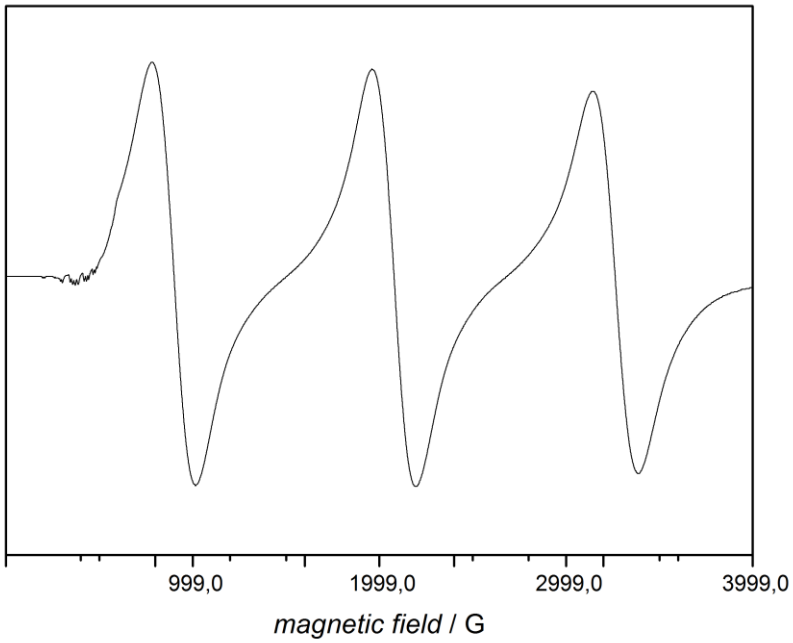

Figure 62 EPR spectrum of *tert*-butyl 4-(5-(2-hydroxyethyl)-3-(2-oxyl-1,1,3,3-tetramethylisoindolin-5-yl)-4,6-dioxo-4,5,6,6a-tetrahydropyrrolo[3,4-c]pyrazol-1(3aH)-yl)benzoate **21** in THF.

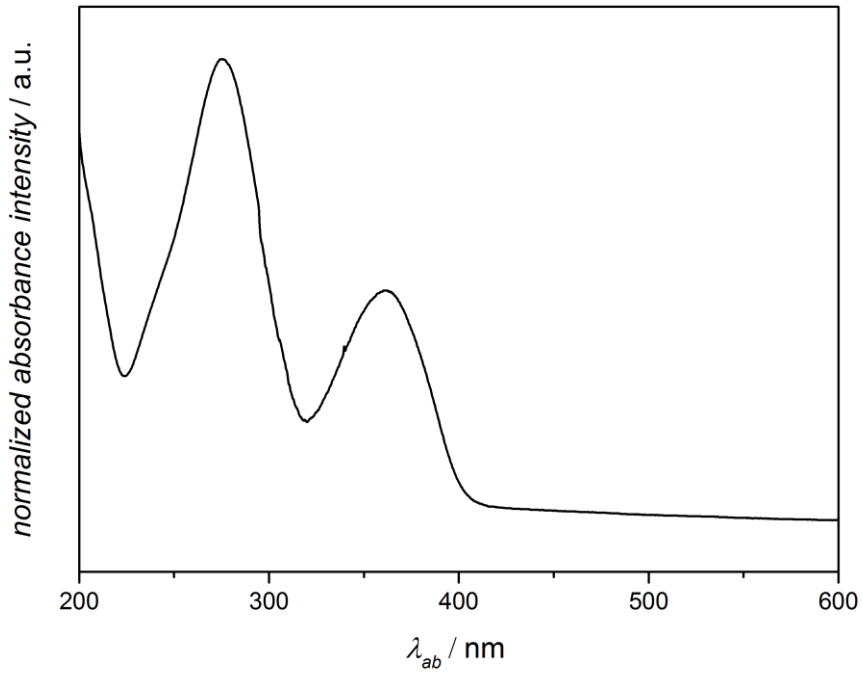

Figure 63 UV/VIS absorption spectrum of *tert*-butyl 4-(5-(2-hydroxyethyl)-3-(2-oxyl-1,1,3,3-tetramethylisoindolin-5-yl)-4,6-dioxo-4,5,6,6a-tetrahydropyrrolo[3,4-c]pyrazol-1(3aH)-yl)benzoate **21** in MeCN.

4-(5-(2-Methoxy-1,1,3,3-tetramethylisoindolin-5-yl)-4,6-dioxo-1-phenyl-1,3a,4,5,6,6a-hexahydropyrrolo[3,4-c]pyrazol-3-yl)benzoic acid (4)*

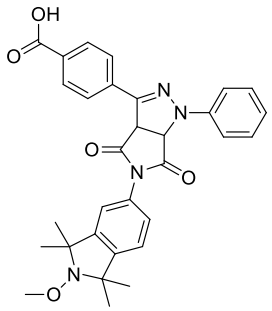

4-(5-(2-Oxyl-1,1,3,3-tetramethylisoindolin-5-yl)-4,6-dioxo-1-phenyl-1,3a,4,5,6,6a-hexahydropyrrolo[3,4-c]pyrazol-3-yl)benzoic acid **3** (20.1 mg, 0.04 mmol) and $FeSO_4 \cdot 7H_2O$ (27.8 mg, 0.1 mmol) was dissolved 0.5 mL DMSO. H_2O_2 (16 µL, 0.14 mmol) was added slowly at 0 °C. Reaction mixture was stirred for 45 min. 30 mL 2 M HCl was added. The aqueous phase was extracted with Et_2O (4×10 mL). The organic layer was dried over Na_2SO_4 and DCM removed under reduced pressure. The crude product was purified via column chromatography on silica gel using hexane / ethyl acetate / acetic acid (2:1:0.01, v / v / v R_f 0.65) as the eluent. After drying under high vacuum the title compound was obtained as yellow oil (15.2 mg, 73 %) ^{1}H NMR (400 MHz, $CDCl_3$): δ = 8.21 - 8.15 (m, 4 H), 7.68 - 7.66 (m, 2 H), 7.41 - 7.37 (m, 2 H), 7.17 - 7.09 (m, 2 H), 7.04 - 6.96 (m, 2 H), 5.41 - 5.36 (d, J=11.05 Hz, 1 H), 5.10 - 5.05 (d, J=11.06 Hz, 1 H), 1.47 - 1.35 (m, 12 H); 13C NMR (100 MHz, $CDCl_3$) δ = 173.03,172.21, 167.42, 146.03, 145.74, 144.44, 143.40, 135.09, 131.55, 131.21, 129.58, 129.88, 127.38, 126.82, 122.78, 121.53, 120.97, 114.52, 67.10, 66.34, 65.52, 54.24; HRMS (EI) m / z: calcd. for $[M + H]^+$ $C_{31}H_{31}N_4O_5$ 539.2294 found 539.2306.

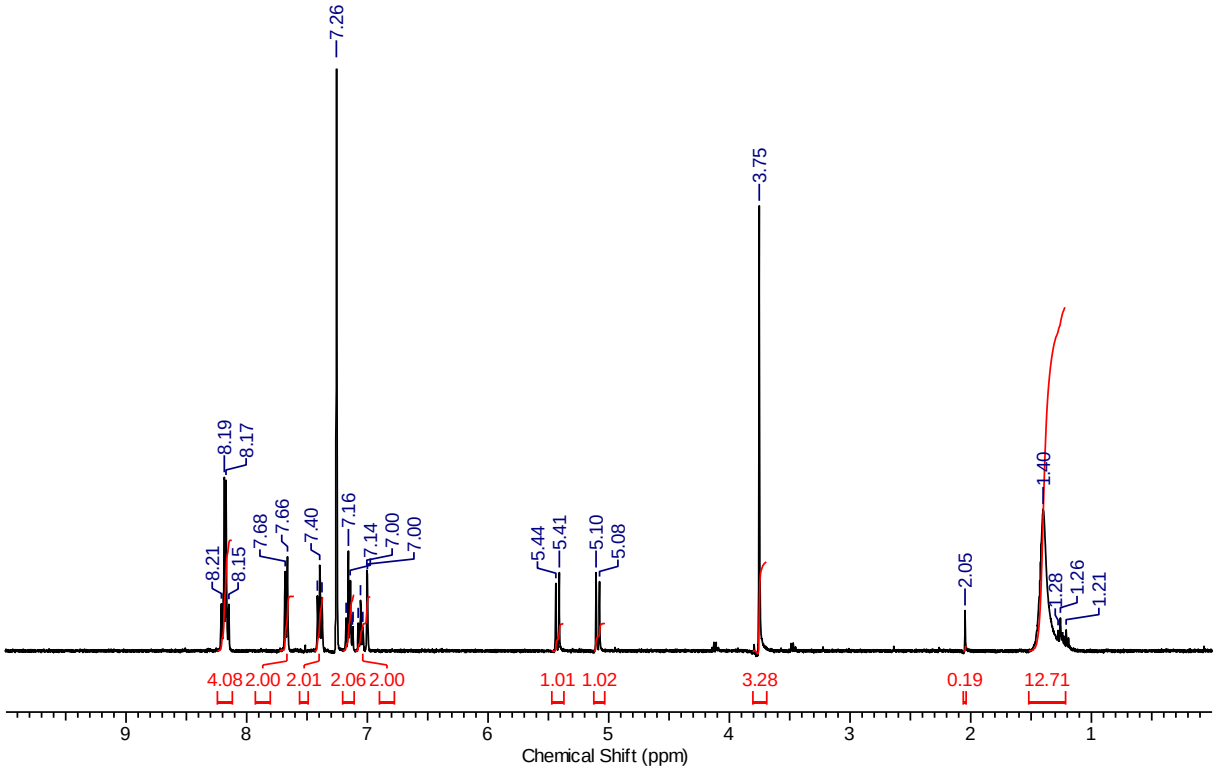

Figure 64 ^{1}H NMR (400 MHz, $CDCl_3$) spectrum of 4-(5-(2-methoxy-1,1,3,3-tetramethylisoindolin-5-yl)-4,6-dioxo-1-phenyl-1,3a,4,5,6,6a-hexahydropyrrolo[3,4-c]pyrazol-3-yl)benzoic acid **4**.

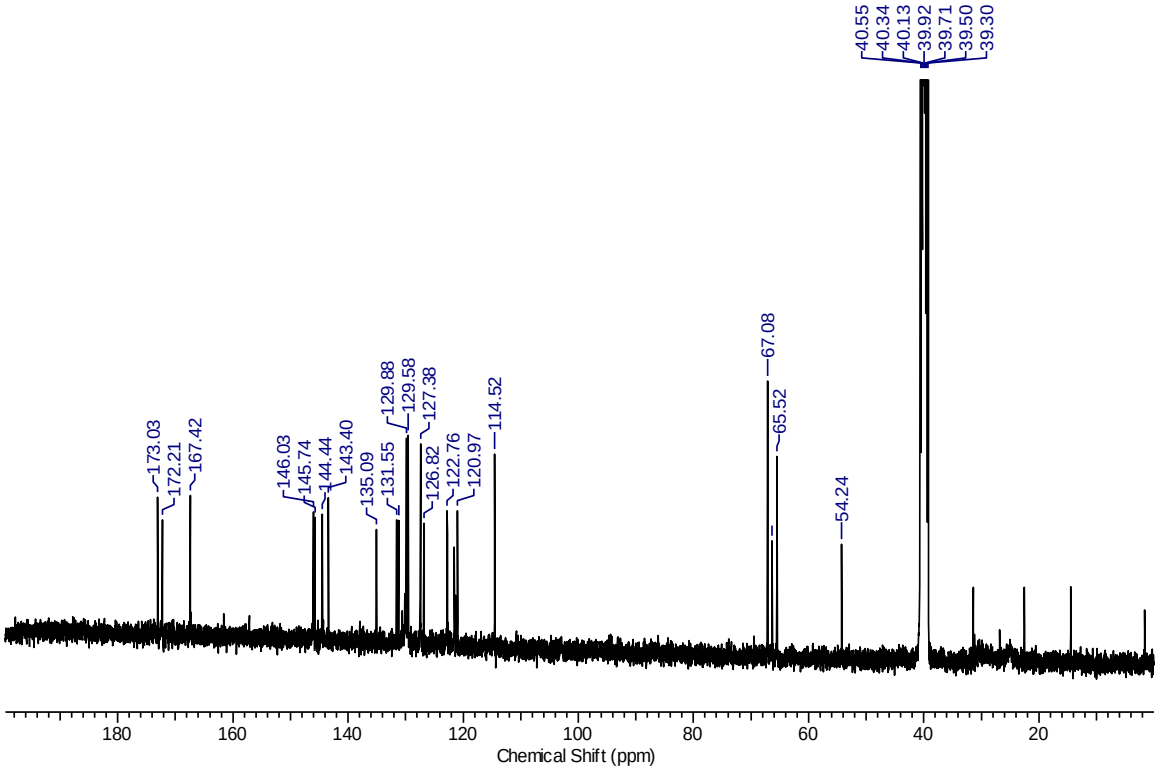

Figure 65 ^{13}C NMR (100 MHz, $CDCl_3$) spectrum of 4-(5-(2-methoxy-1,1,3,3-tetramethylisoindolin-5-yl)-4,6-dioxo-1-phenyl-1,3a,4,5,6,6a-hexahydropyrrolo[3,4-c]pyrazol-3-yl)benzoic acid **4**.

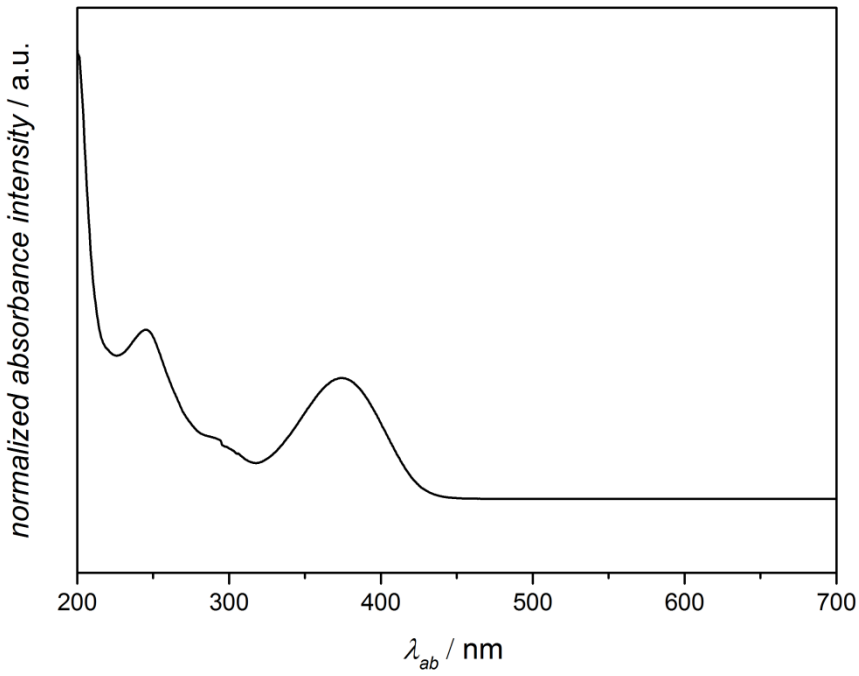

Figure 66 UV/Vis spectrum of 4-(5-(2-methoxy-1,1,3,3-tetramethylisoindolin-5-yl)-4,6-dioxo-1-phenyl-1,3a,4,5,6,6a-hexahydropyrrolo[3,4-c]pyrazol-3-yl)benzoic acid **4** in MeCN.

*Compound degrades on the column and shows degradation on air / in sunlight.

1-Oxly-2,2,6,6-tetramethylpiperidin-4-yl 4-(2-phenyl-2H-tetrazol-5-yl)benzoate (6)

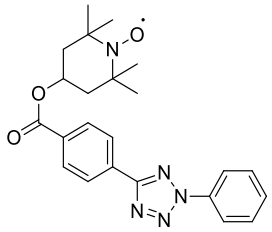

The hydroxyl functional TEMPO **5** (125.6 mg, 0.73 mmol), DMAP (10.0 mg, 0.08 mmol) and diaryl tetrazole **1** (200 mg, 0.76 mmol) were dissolved in 5 mL THF. After the solution was cooled to 0 °C, DCC (181.6 mg, 0.88 mmol) was added. The reaction mixture was stirred at ambient temperature for 16 h. After THF was removed in vacuum the obtained solid was dissolved in Et_2O extracted with 1 M hydrochloric acid (2 × 50 mL) and washed with a saturated $NaHCO_3$ solution (50 mL). The organic layer was dried over Na_2SO_4 and Et_2O removed under reduced pressure. The crude product was purified via recrystallization in EtOH (2 × 8 mL). The title compound was obtained as pink powder (101 mg, 33 %): HRMS (EI) m / z: calcd. for $[M + Na]^+$ $C_{23}H_{26}N_5NaO_3$ 443.1933 found 443.1925; EPR (THF) *g* 1.9914, a^N 1.5248.

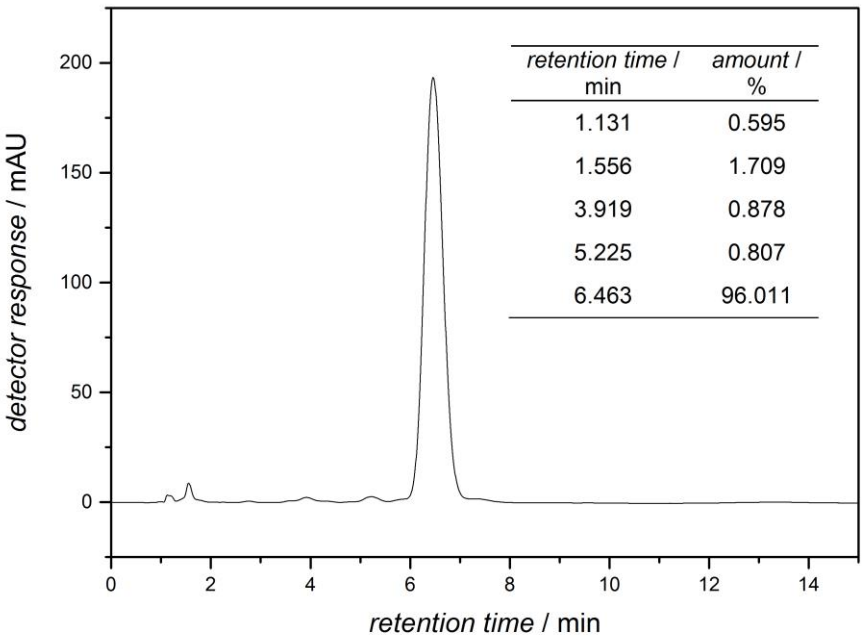

Figure 67 HPLC chromatogram of 1-oxly-2,2,6,6-tetramethylpiperidin-4-yl 4-(2-phenyl-2H-tetrazol-5-yl)benzoate **6** measured in THF / H_2O mixture (55:45, v / v) and detected at 254 nm (absorbance).

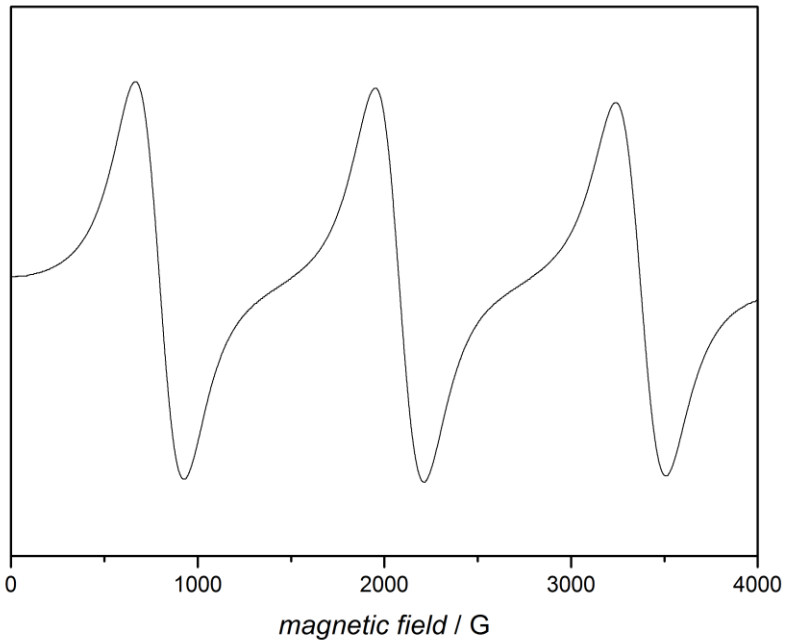

Figure 68 EPR spectrum of 1-oxly-2,2,6,6-tetramethylpiperidin-4-yl 4-(2-phenyl-2H-tetrazol-5-yl)benzoate **6** measured in THF.

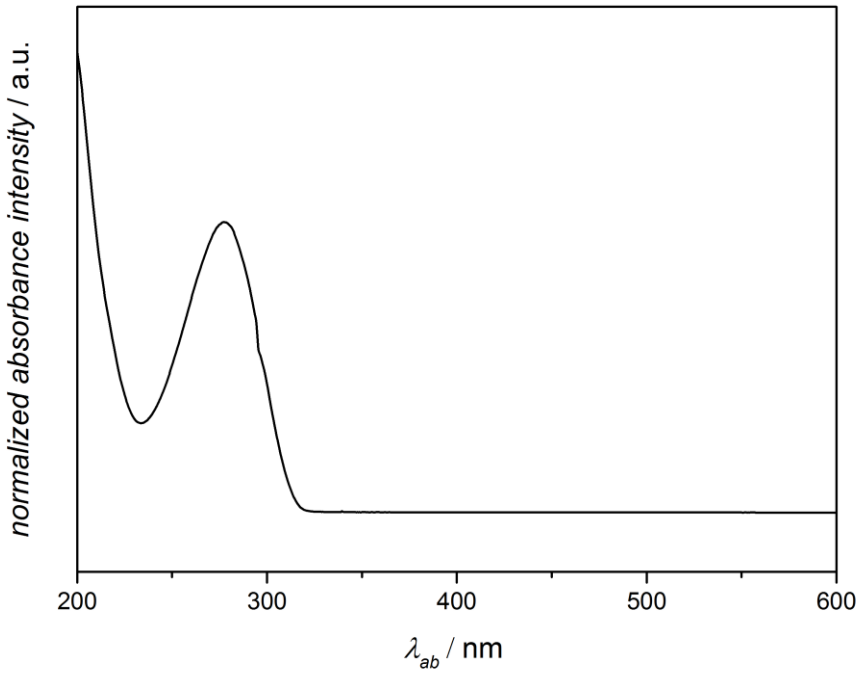

Figure 69 UV/VIS absorption spectrum of 1-oxly-2,2,6,6-tetramethylpiperidin-4-yl 4-(2-phenyl-2H-tetrazol-5-yl)benzoate **6** in MeCN.

1-Methoxy-2,2,6,6-tetramethylpiperidin-4-yl-4-(5-(2-hydroxy-ethyl)-4,6-dioxo-1-phenyl-1,3a,4,5,6,6a-hexahydropyrrolo[3,4-c]pyrazol-3-yl)benzoate (9)

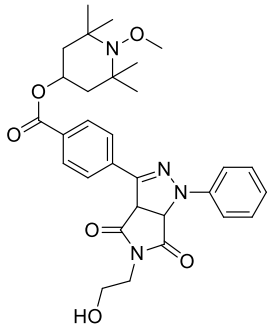

1-Oxyl-2,2,6,6-tetramethylpiperidin-4-yl-4-(5-(2-hydroxyethyl)-4,6-di-oxo-1-phenyl-1,3a,4,5,6,6a-hexahydropyrrolo[3,4-c]pyrazol-3-yl)benzo-ate **8** (7.0 mg, 0.01) and $FeSO_4 \cdot 7H_2O$ (9.3 mg, 0.03 mmol) was dissolved 0.17 mL DMSO. H_2O_2 (8.6 µL, 0.08 mmol) was added slowly at 0 °C. Reaction mixture was stirred for 45 min. 30 mL 2 M HCl was added. The aqueous phase was extracted with Et_2O (4 × 10 mL). The organic layer was dried over Na_2SO_4 and DCM removed under reduced pressure. The crude product was purified via column chromatography on silica gel using hexane / ethyl acetate (3:2, v / v R_f 0.28) as the eluent. After drying under high vacuum the title compound was obtained as yellow oil (5.1 mg, 70 %). 1H NMR (400 MHz, $CDCl_3$) δ = 8.14 - 8.02 (m, 4 H), 7.64 - 7.51 (m, 2 H), 7.43 - 7.30 (m, 2 H), 7.08 - 6.97 (m, 1 H), 5.33 - 5.21 (m, 3 H), 4.94 (d, J = 11.1 Hz, 1 H), 3.84 - 3.72 (m, 5 H), 3.64 (s, 3 H), 2.10 - 1.64 (m, 5 H), 1.32 - 1.20 (m, 12 H); 13C NMR (100 MHz, $CDCl_3$) δ = 172.8, 172.0, 165.6, 143.8, 141.4, 134.4, 130.8, 129.7, 129.3, 126.7, 122.0, 114.5, 67.6, 65.5, 60.0, 59.8, 53.3, 44.1, 42.4, 33.0, 20.8; HRMS (EI) m / z: calcd. for $[M + H]^+$ $C_{30}H_{37}N_4O_6$ 549.2713 found 549.2706.

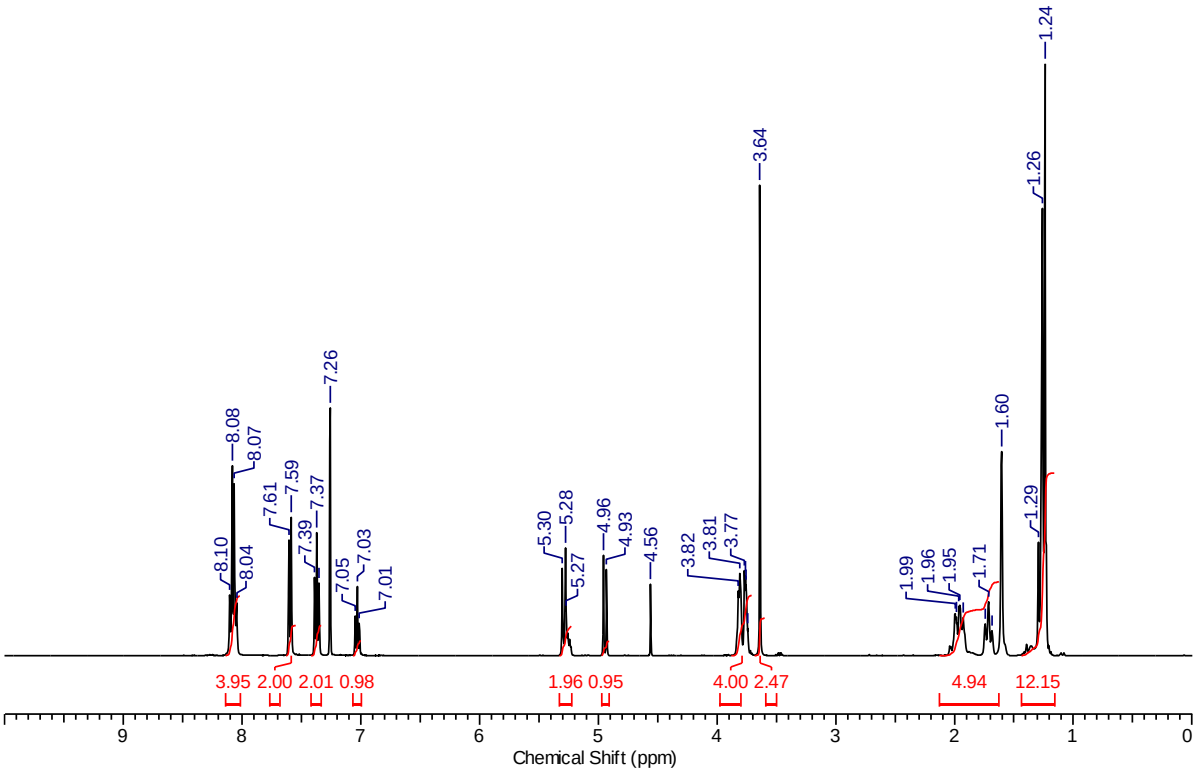

Figure 70 ^{1}H NMR (400 MHz, $CDCl_3$) spectrum of 1-methoxy-2,2,6,6-tetramethylpiperidin-4-yl 4-(5-(2-hydroxyethyl)-4,6-dioxo-1-phenyl-1,3a,4,5,6,6a-hexahydropyrrolo[3,4-c]pyrazol-3-yl)benzoate **9**.

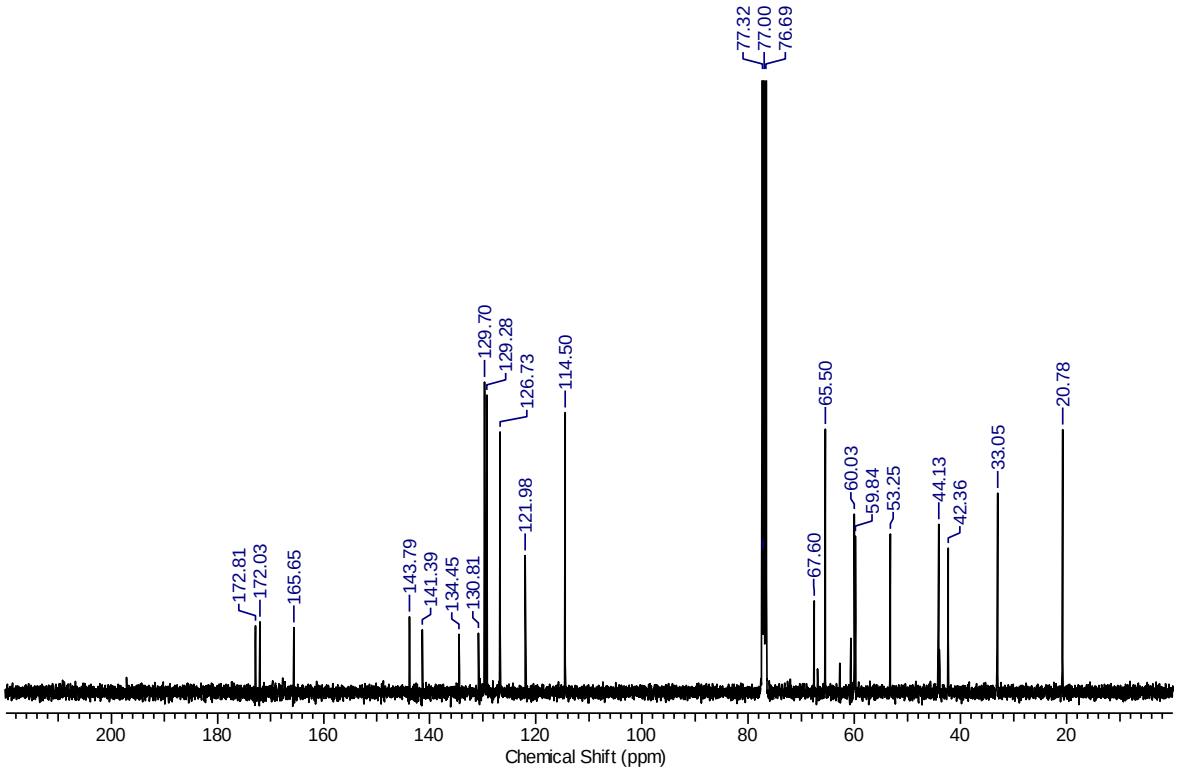

Figure 71 ^{13}C NMR (100 MHz, $CDCl_3$) spectrum of 1-methoxy-2,2,6,6-tetramethylpiperidin-4-yl 4-(5-(2-hydroxyethyl)-4,6-dioxo-1-phenyl-1,3a,4,5,6,6a-hexahydropyrrolo[3,4-c]pyrazol-3-yl)benzoate **9**.

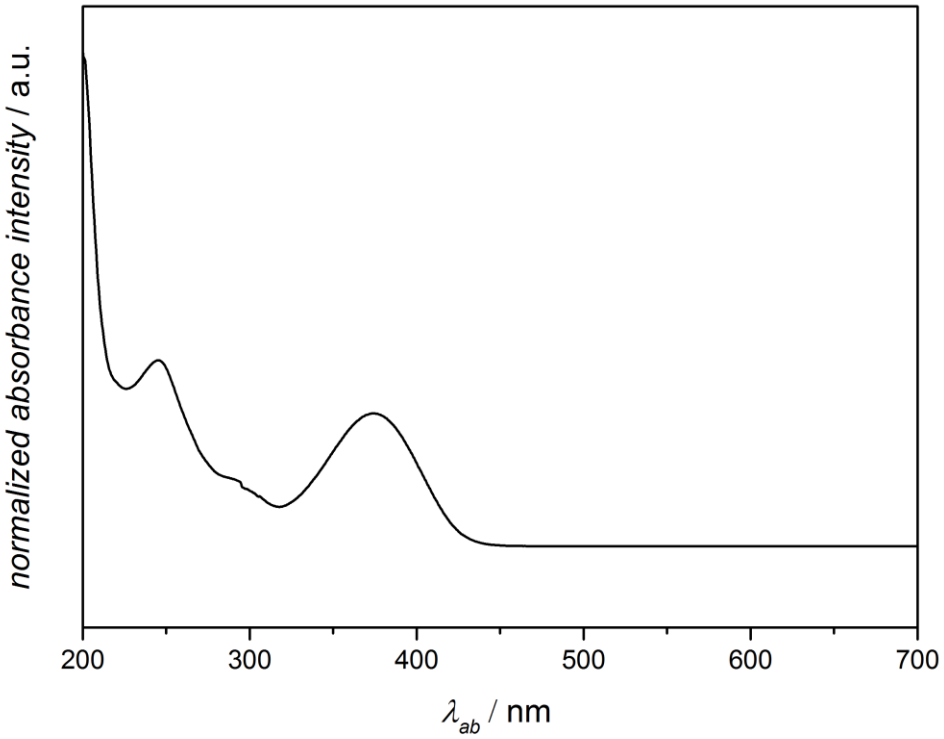

Figure 72 UV/VIS absorption spectrum of -methoxy-2,2,6,6-tetramethylpiperidin-4-yl 4-(5-(2-hydroxyethyl)-4,6-dioxo-1-phenyl-1,3a,4,5,6,6a-hexahydropyrrolo[3,4-c]pyrazol-3-yl)benzoate **9**.

2-Methoxy-1,1,3,3-tetramethyl-5-(2-phenyl-2H-tetrazol-5-yl)isoindoline (13)

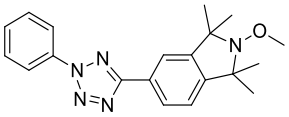

A mixture of 2-methoxy-1,1,3,3-tetramethylisoindoline-5-carbaldehyde **10** (114.0 mg, 0.49 mmol) and benzenesulfonohydrazide (84.3 mg 0.49 mmol) in 6.5 mL EtOH was stirred at ambient temperature for 1.5 h. A white precipitate formed after addition of 13 mL water was collected in a funnel. The solid was dissolved in 1.5 mL pyridine (solvent A). In parallel $NOBF_4$ (127.6 mg, 1.09 mmol) was dissolved in 1 mL ACN (dry) under argon. A solution of aniline (100 mg 1.07 mmol) in 3 mL ACN (dry) was added.at -30 °C. The reaction mixture was stirred for 20 min at -30 °C and additional 20 min at room temperature. A white precipitate formed after addition of 15 ml of cold Et_2O (dry) was collected in a funnel. The Arenediazonium salt (81 mg, 0.69 mmol) was dissolved in 1 ml ACN and added to solvent A at 0 °C. The reaction mixture was stirred for 3 h at room temperature, diluted in 30 mL ethyl acetate and extracted with 2 M hydrochloric acid (2 × 100 mL). Ethyl acetate was removed under reduced pressure. The crude product was purified via column chromatography on silica gel using hexane / Et_2O (5:1, v / v Rf 0.51) as the eluent. After drying under high vacuum the title compound 13 was obtained as yellowish oil (60.0 mg, 35 %). ^{1}H NMR (400MHz, $CDCl_3$) δ = 8.24 - 8.12 (m, 3 H), 8.05 - 7.97 (m, 1 H), 7.61 - 7.55 (m, 2 H), 7.53 - 7.47 (m, 1 H), 7.32 - 7.22 (m, 1 H), 3.81 (s, 3 H), 1.65 - 1.32 (m, 12 H); ^{13}C NMR (100 MHz, $CDCl_3$) δ = 165.3, 147.9, 146.1, 136.9, 129.6, 126.3, 126.2, 122.1, 120.3, 119.8, 67.1, 65.5; HRMS (EI) m / z: calcd. for $[M + H]^+$ $C_{20}H_{24}N_5O$ 350.1981 found 350.1944.

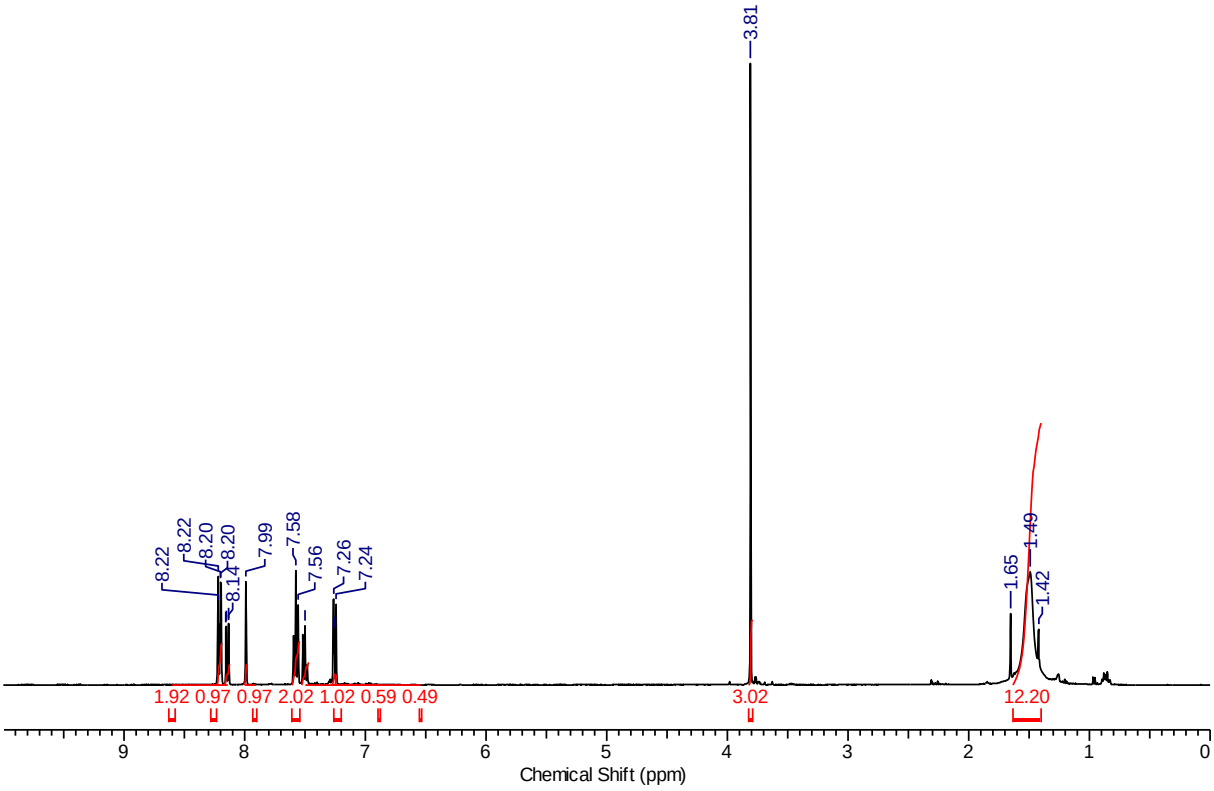

Figure 73 ^{1}H NMR (400 MHz, $CDCl_3$) spectrum of 2-methoxy-1,1,3,3-tetramethyl-5-(2-phenyl-2H-tetrazol-5-yl)isoindoline **13**.

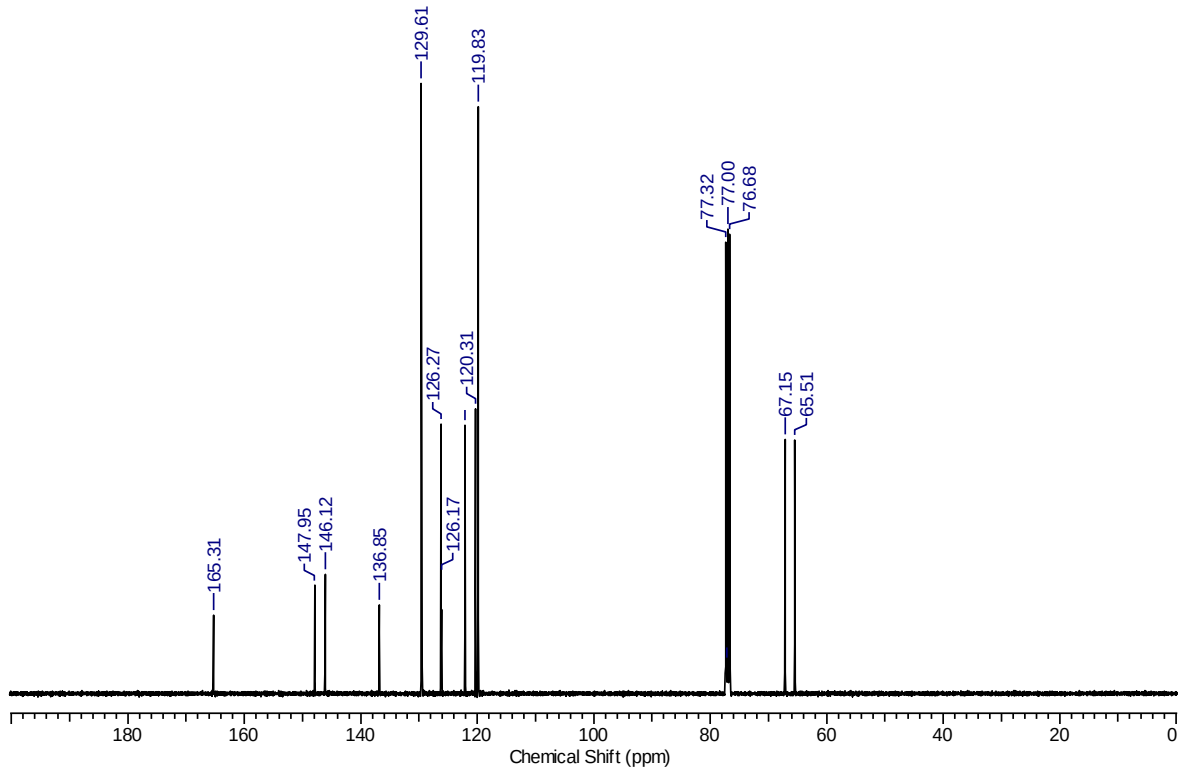

Figure 74 ^{13}C NMR (100 MHz, $CDCl_3$) spectrum of 2-methoxy-1,1,3,3-tetramethyl-5-(2-phenyl-2H-tetrazol-5-yl)isoindoline **13**.

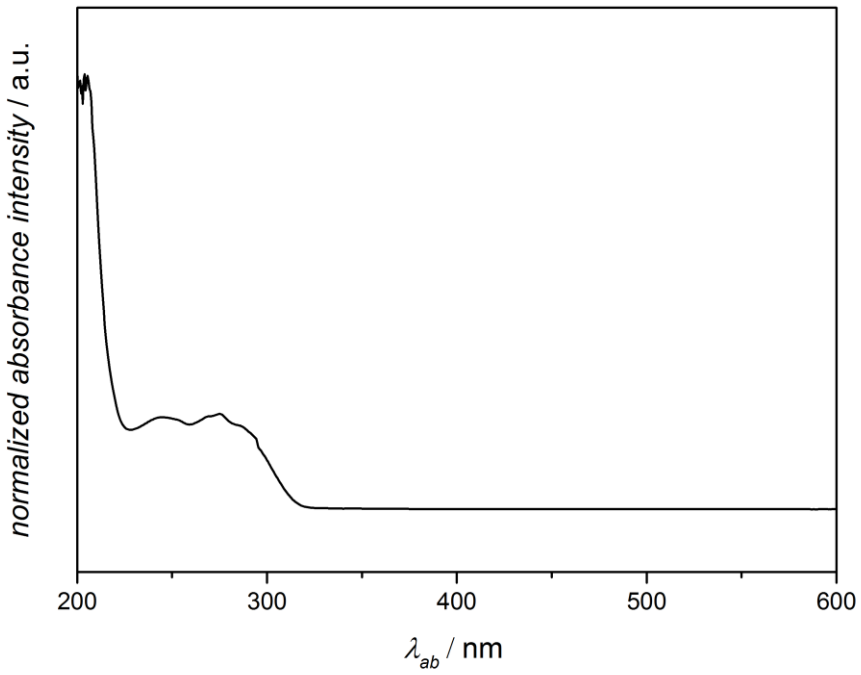

Figure 75 UV/VIS absorption spectrum of 2-methoxy-1,1,3,3-tetramethyl-5-(2-phenyl-2H-tetrazol-5-yl)isoindoline **13** in MeCN.

2-oxyl-1,1,3,3-tetramethyl-5-(2-phenyl-2H-tetrazol-5-yl)isoindoline (14)

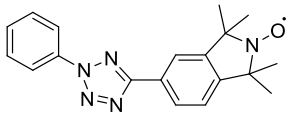

2-Methoxy-1,1,3,3-tetramethyl-5-(2-phenyl-2H-tetrazol-5-yl)isoindoline **13** (20 mg, 0.06) was dissolved in 1 mL DCM. *m*CPBA (33.7 mg, 0.15 mmol) was added at 0 °C. Reaction mixture was stirred for 3 h at room temperature. Reaction mixture was diluted with DCM and 2 M NaOH (2 × 50 mL). The organic layer was dried over Na_2SO_4 and DCM removed under reduced pressure. The crude product was purified via column chromatography on silica gel using hexane / ethyl acetate (4:1, v / v R_f 0.59) as the eluent. After drying under high vacuum the title compound was obtained as orange oil (15.8 mg, 82 %). HRMS (EI) m / z: calcd. for $[M + Na]^+$ $C_{19}H_{20}N_5NaO$ 357.1566 found 357.1527; EPR (THF) *g* 1.9924, a^N 1.375.

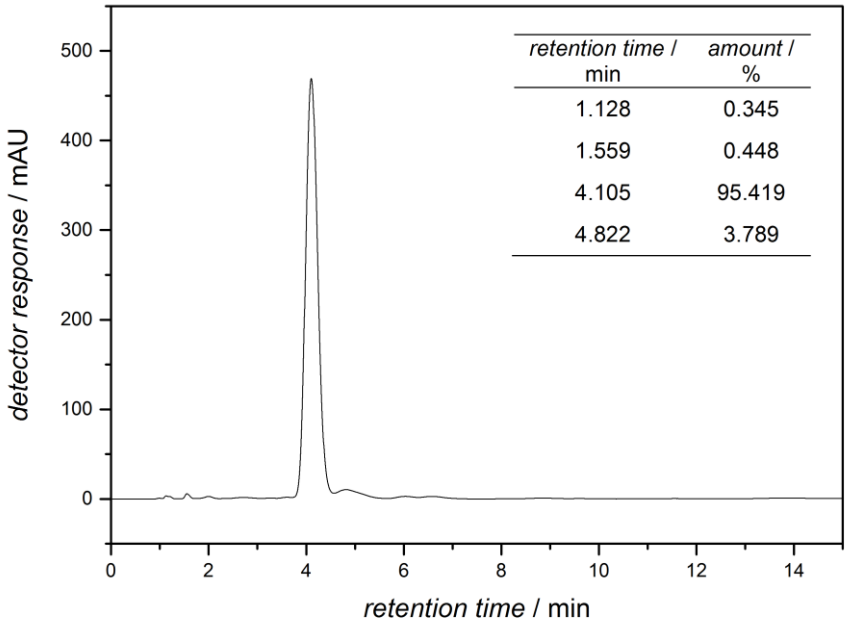

Figure 76 HPLC chromatogram of 2-oxyl-1,1,3,3-tetramethyl-5-(2-phenyl-2H-tetrazol-5-yl)isoindoline **14** measured in THF / H_2O mixture (55:45, v / v) and detected at 254 nm (absorbance).

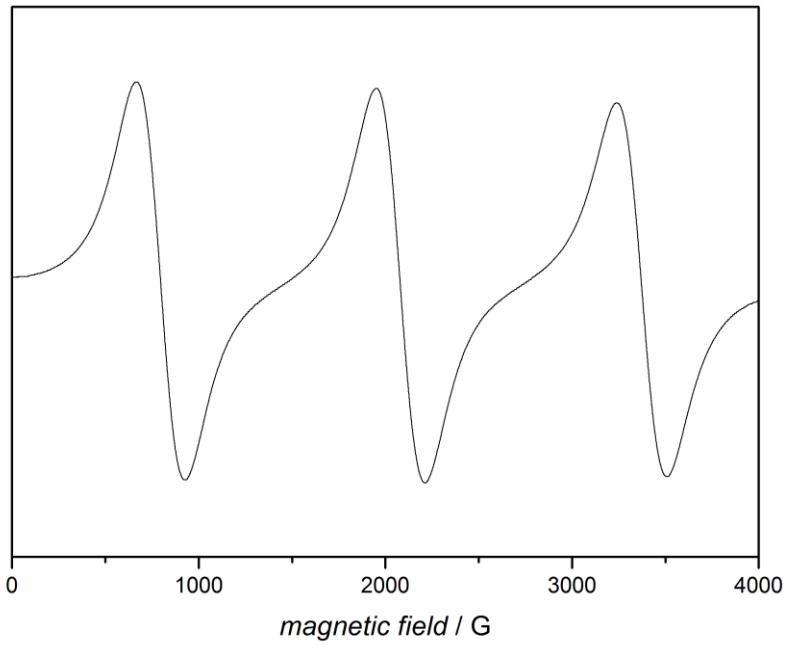

Figure 77 EPR spectrum of 2-oxyl-1,1,3,3-tetramethyl-5-(2-phenyl-2H-tetrazol-5-yl)isoindoline **14** measured in THF.

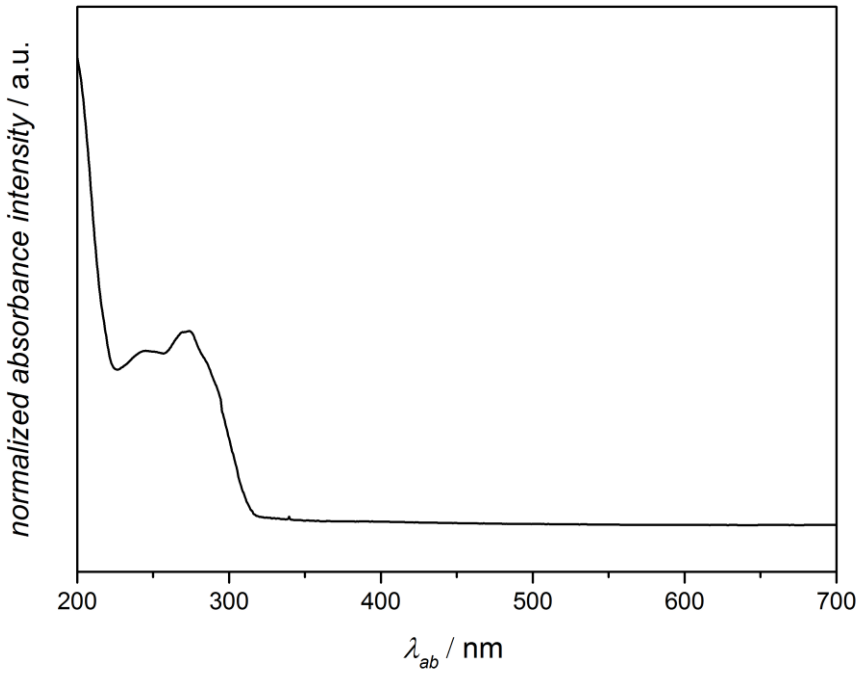

Figure 78 UV/VIS absorption spectrum of 2-oxyl-1,1,3,3-tetramethyl-5-(2-phenyl-2H-tetrazol-5-yl)isoindoline **14** in MeCN.

tert-Butyl-4-(5-(2-methoxy-1,1,3,3-tetramethylisoindolin-5-yl)-2H-tetrazol-2-yl)benzoate (18)

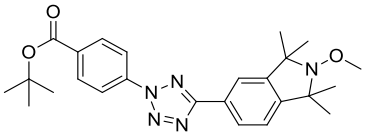

A mixture of 2-methoxy-1,1,3,3-tetramethylisoindoline-5-carbaldehyde **10** (1500.0 mg, 6.44 mmol) and benzenesulfonohydrazide (1120.0 mg 6.44 mmol) in 90 mL EtOH was stirred at ambient temperature for 1.5 h. A white precipitate formed after addition of 180 mL water was collected in a funnel. The solid was dissolved in 20 mL pyridine (solvent A). In parallel $NOBF_4$ (1810.0 mg, 15.47 mmol) was dissolved in 14 mL ACN (dry) under argon. A solution of *tert*-butyl 4-aminobenzoate (2900.0 mg 15.03 mmol) in 10 mL ACN (dry) was added.at -30 °C. The reaction mixture was stirred for 10 min at -30 °C and additional 10 min at room temperature. A white precipitate formed after addition of 50 ml of cold Et_2O (dry) was collected in a funnel (diazonium salt). The diazonium salt (1530.0 mg, 5.24 mmol) was dissolved in 5 ml ACN and added to solvent A at 0 °C. The reaction mixture was stirred for 3 h at room temperature, diluted in 100 mL ethyl acetate and extracted with 2 M hydrochloric acid (2 × 400 mL). Ethyl acetate was removed under reduced pressure. The crude product was purified *via* column chromatography on silica gel using hexane / ethyl acetate (9:1, v / v R_f 0.52) as the eluent. After drying under high vacuum the title compound was obtained as orange oil (630.0 mg, 22 %). ^{1}H NMR (400 MHz, $CDCl_3$) δ = 8.30 - 8.24 (m, 2 H), 8.22 - 8.12 (m, 3 H), 8.06 - 7.93 (m, 1 H), 7.27 - 7.14 (m, 1 H), 3.88 - 3.76 (m, 3 H), 1.87 - 1.26 (m, 21 H); ^{13}C NMR (100 MHz, $CDCl_3$) δ = 165.6, 164.5, 148.2, 146.2, 139.4, 132.9, 131.0, 126.4, 125.9, 122.2, 120.4, 119.4, 81.9, 67.2, 65.5, 28.2; HRMS (EI) m / z: calcd. for $[M + H]^+$ $C_{25}H_{32}N_5O_3$ 450.2505 found 450.2483.

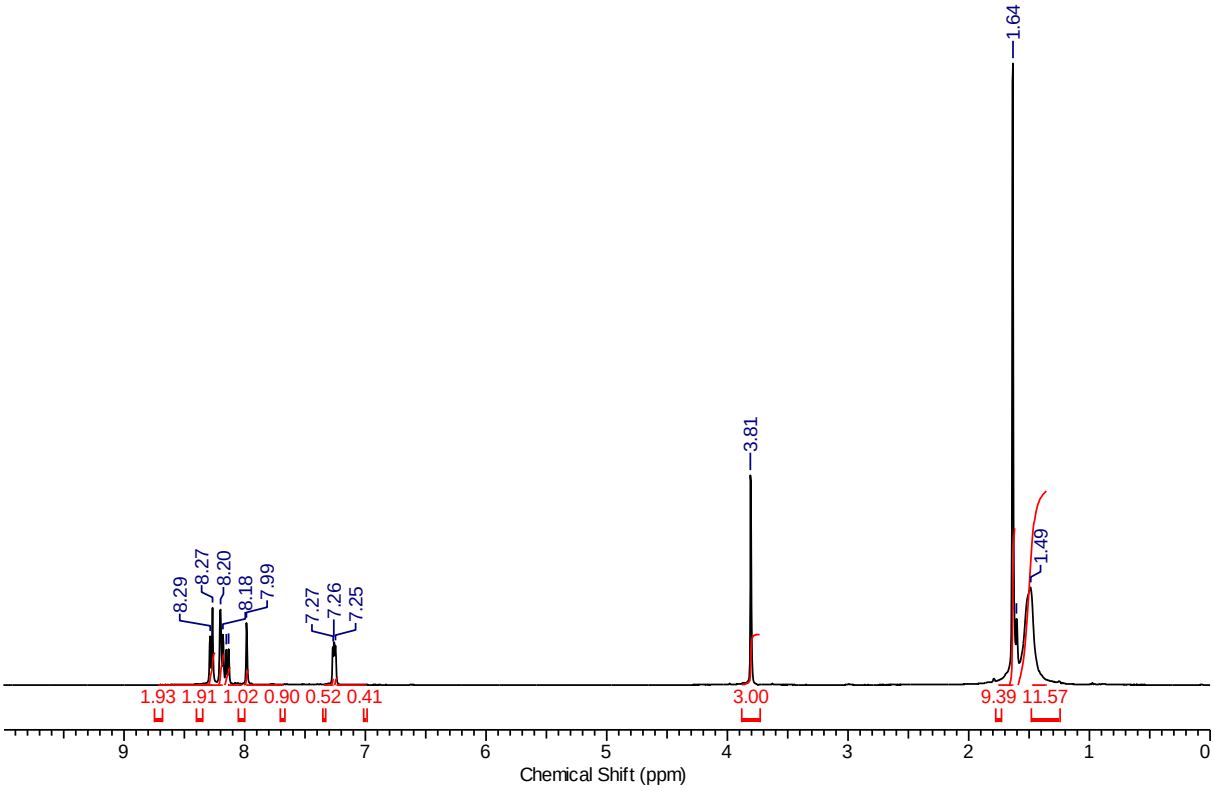

Figure 79 ^{1}H NMR (400 MHz, $CDCl_3$) spectrum of *tert*-butyl 4-(5-(2-methoxy-1,1,3,3-tetramethylisoindolin-5-yl)-2H-tetrazol-2-yl)benzoate **18**.

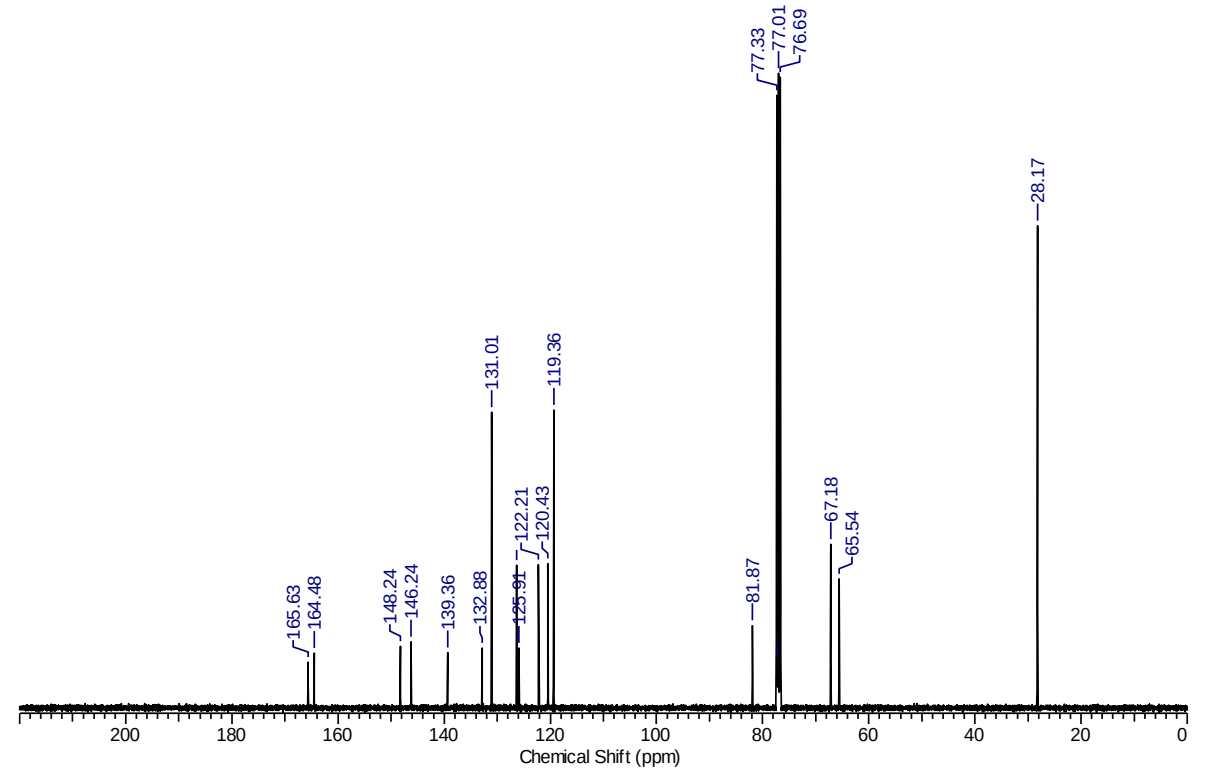

Figure 80 ^{13}C NMR (100 MHz, $CDCl_3$) spectrum of *tert*-butyl 4-(5-(2-methoxy-1,1,3,3-tetramethylisoindolin-5-yl)-2H-tetrazol-2-yl)benzoate **18**.

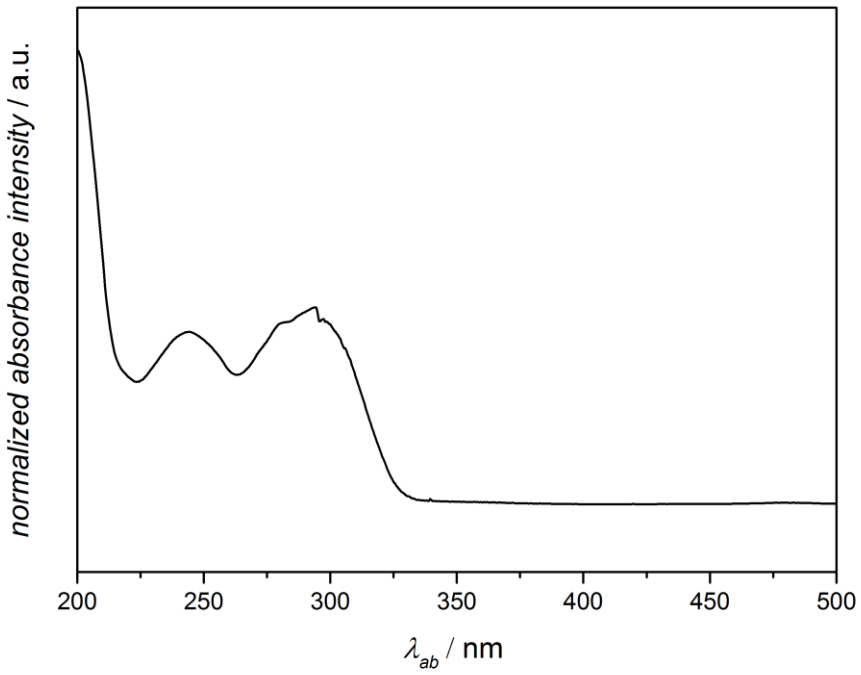

Figure 81 UV/Vis spectrum of *tert*-butyl 4-(5-(2-methoxy-1,1,3,3-tetramethylisoindolin-5-yl)-2H-tetrazol-2-yl)benzoate **18** in MeCN.

tert-Butyl-4-(5-(2-oxyl-1,1,3,3-tetramethylisoindolin-5-yl)-2H-tetrazol-2-yl)benzoate (19)

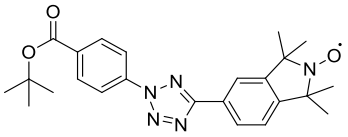

tert-Butyl-4-(5-(2-methoxy-1,1,3,3-tetramethylisoindolin-5-yl)-2H-tetrazol-2-yl)benzoate **18** (380 mg, 0.84 mmol) was dissolved in 5 mL DCM. *m*CPBA (398.1 mg, 2.31 mmol) was added at 0 °C. Reaction mixture was stirred for 3 h at room temperature. Reaction mixture was diluted with DCM and 2 M NaOH (2 × 100 mL). The organic layer was dried over Na_2SO_4 and DCM removed under reduced pressure. The crude product was purified via column chromatography on silica gel using hexane / ethyl acetate (9:1, v / v R_f 0.34) as the eluent. After drying under high vacuum the title compound was obtained as orange oil (350.2 mg, 96 %). HRMS (EI) m / z: calcd. for $[M + Na]^+$ $C_{24}H_{28}N_5NaO_3$ 457.2090 found 457.2080; EPR (THF) *g* 1.9920, a^N 1.4058.

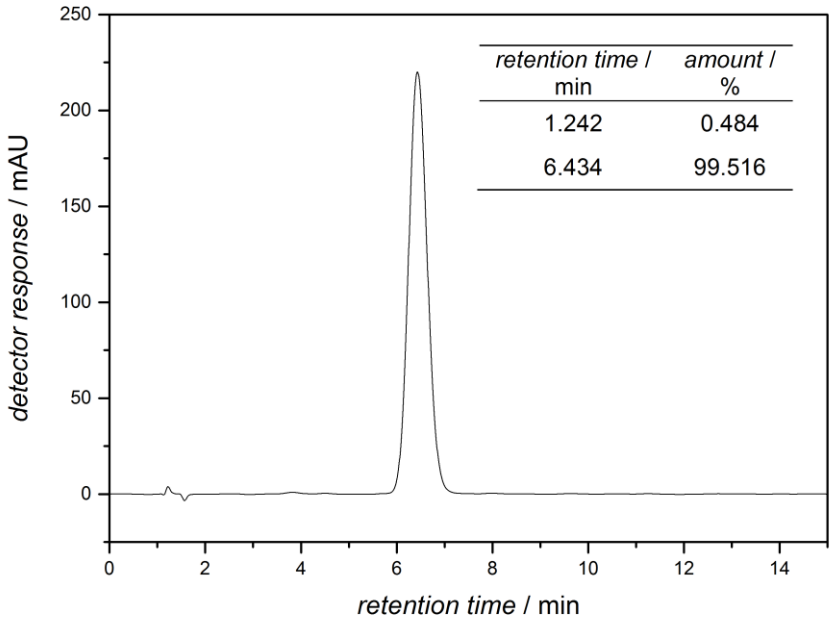

Figure 82 HPLC chromatogram of *tert*-butyl 4-(5-(2-oxyl-1,1,3,3-tetramethylisoindolin-5-yl)-2H-tetrazol-2-yl)benzoate **19** measured in THF / H_2O mixture (55:45, v / v) and detected at 254 nm (absorbance).

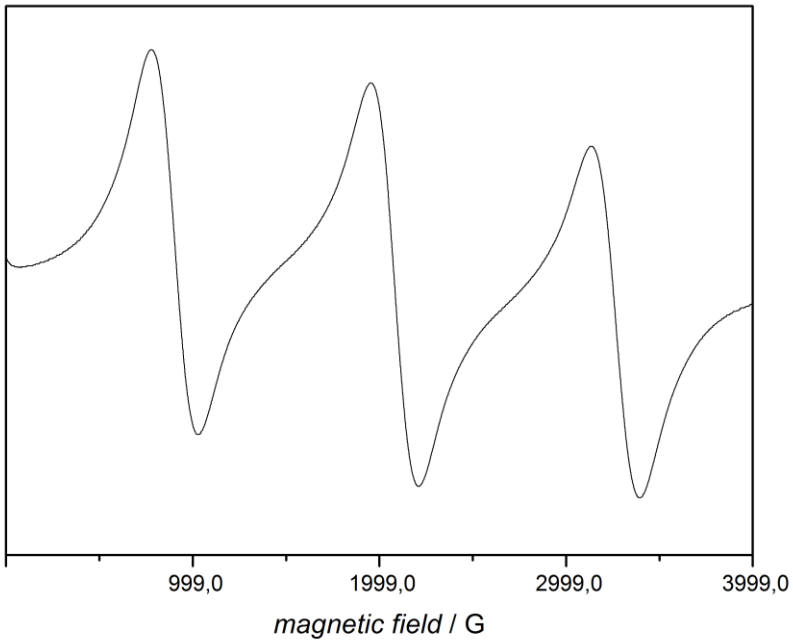

Figure 83 EPR spectrum of *tert*-butyl 4-(5-(2-oxyl-1,1,3,3-tetramethylisoindolin-5-yl)-2H-tetrazol-2-yl)benzoate **19** in THF.

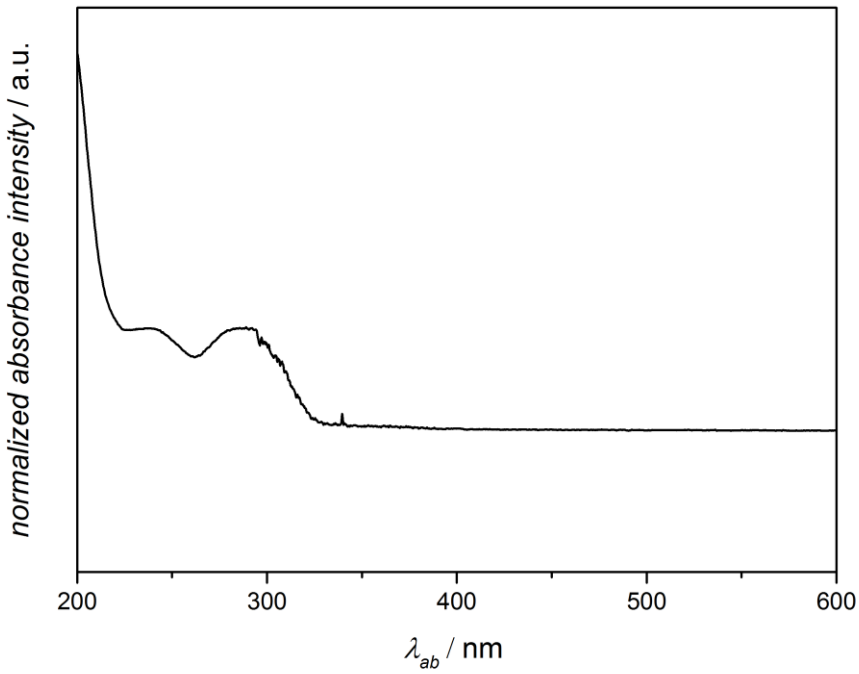

Figure 84 UV/Vis spectrum of *tert*-butyl 4-(5-(2-oxyl-1,1,3,3-tetramethylisoindolin-5-yl)-2H-tetrazol-2-yl)benzoate **19** in MeCN.

8.2 Catalyst Free, Visible Light Induced Polymer Ligation

8.2.1 Materials

1-(2-Hydroxyethyl)-1H-pyrrole 2,5-dione **7** was synthesized according to the literature.[290] 2-(1,3-dioxo-1,3,3a,4,7,7a-hexahydro-2H-4,7-epoxyisoindol-2yl)ethyl 2-(((dodecylthio)carbonothioyl)thio)-2-methyl propanoate **28** was synthesized according to the literature.[291] All other reagents including dipolarophile functional PEGs $\mathbf{E_{1\text{-}4}}$ were purchased from commercial suppliers and used without further purification.

8.2.2 Methods and Analytical Instrumentation

Air-sensitive reactions were carried out under an atmosphere of ultrahigh purity argon.

^{1}H and ^{13}C NMR spectra were recorded on a 400 MHz spectrometer and referenced to the relevant solvent peak stated in the spectrum caption.

High-resolution mass spectra (HRMS) were obtained using a Q Exactive (Orbitrap) mass spectrometer (Thermo Fisher Scientific, San Jose, CA, USA) equipped with a HESI II probe. The instrument calibration was carried out in the m / z range 74 - 1822 using calibration solutions from Thermo Scientific. A constant spray voltage of 4.7 kV and a dimensionless sheath gas of 5 were applied. The capillary temperature and the S-lens RF level were set to 320 °C and 62.0, respectively. The samples were dissolved in a THF / MeOH mixture (3 / 2, v / v) containing 100 µmol of sodium triflate and injected with a flow of 5 $\mu L \cdot min^{-1}$.

Molecular weight determination was performed on a GPC system (PL-GPC 50 Plus, Polymer Laboratories) consisting of an auto injector, a guard column (PL gel Mixed C, 50 × 7.5 mm), three linear columns (PL gel Mixed C, 300 × 7.5 mm, 5 µm bead-size) and a differential refractive index detector using THF as the eluent at 35 °C and a flow rate of 1 $mL \cdot min^{-1}$.

The system was calibrated using narrow PMMA standards (Polymer Standard Service) ranging from 160 to 6 × 106 g·mol^{-1}. Samples were injected from solutions in THF (2 mg·mL^{-1}).

Absorption spectra were recorded using a 300 UV / Vis Spectrometer (Varian Cary) in MeCN ($c_{target\ compound}$ = 20 µmol·L^{-1}).

Fluorescence spectra were recorded using a Fluorescence Spectrometer (Carry Eclipse) in MeCN ($c_{target\ compound}$ = 20 µmol·L-1).

Fluorescence quantum yields were recorded using Hamamatsu Quantaurus QY in MeCN (c = 2.5 µM, λ_{ex} = 365 nm, emission range: 400-800 nm).

Irradiation

All samples were irradiated in a 250 mL round bottom flask with three blue light diodes (Avonec, 410 - 420 nm, 3 W, actinic blue with an emission angle of 120° grafted on cooling elements (Fischer, SK577 - 25SA - 50 mm × 25 mm)) set up triangularly on top of a magnetic stirrer.

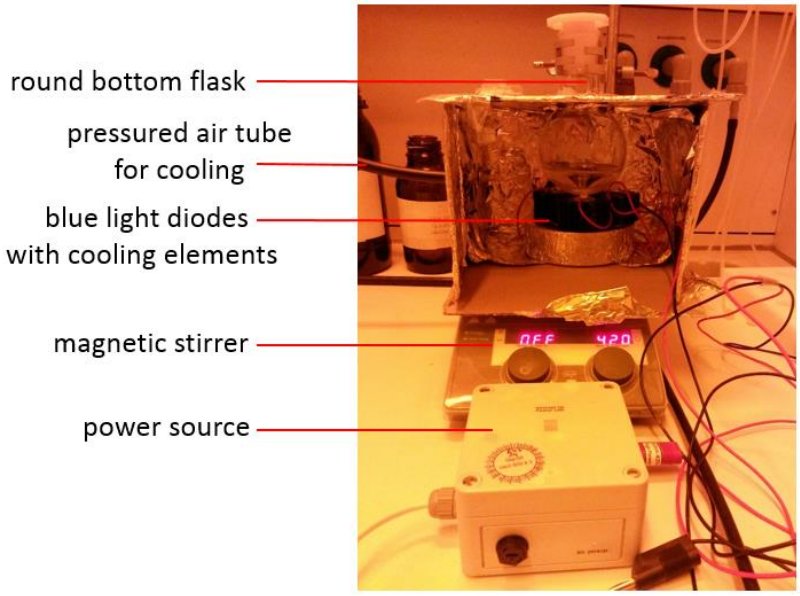

Figure 85 Set up for the photoinduced coupling reactions. A paper box covered with aluminum foil inside was used as reactor.

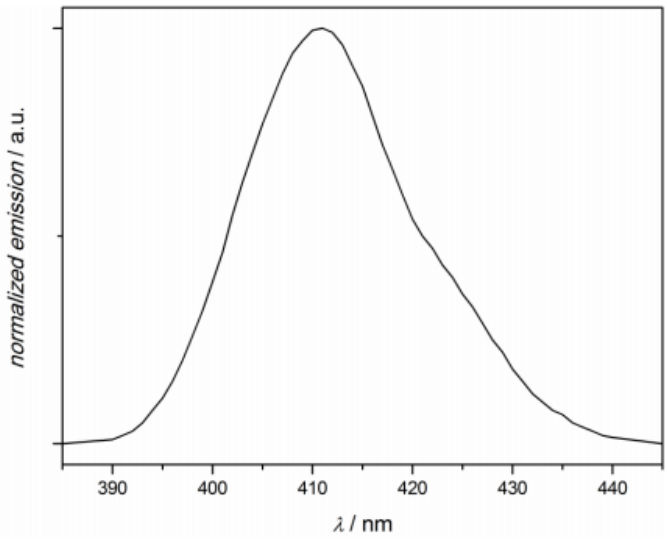

Figure 86 Emission spectrum of Avonec LED, 410 - 420 nm, 3 W, actinic blue.

8.2.3 Synthesis

11-Hydroxyundecyl 4-formylbenzoate (24)

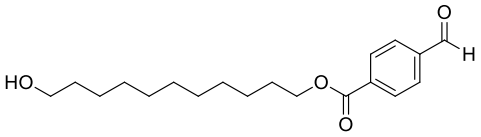

4-formylbenzoic acid (414 mg, 2.76 mmol) and 11-bromoundecan-1-ol (800 mg, 3.20 mmol) were dissolved in 5 mL dry DMF under argon and $NaHCO_3$ (463 mg, 5.51 mmol) was added. The reaction mixture was stirred for 1 h at 125 °C. After cooling down to room temperature the reaction mixture was diluted with 100 mL ethyl acetate washed with 1 M HCl (3 x 100 mL) and dried over $NaSO_4$. Ethyl acetate was removed under reduced pressure. The crude product was purified via column chromatography on silica gel using cyclohexane / ethyl acetate (1:1, v / v R_f 0.62) as the eluent. After drying under high vacuum the title compound **24** was obtained as white solid (781 mg, 88 %). ^{1}H NMR (400 MHz, $CDCl_3$) δ = 10.11 (s, 1 H), 8.23 - 8.18 (m, 2 H), 7.98 - 7.93 (m, 2 H), 4.38 - 4.33 (m, 2 H), 3.66 - 3.63 (m, 2 H), 1.84 - 1.80 (m, 2 H), 1.59 - 1.54 (m, 2 H), 1.40 -1.25 (m, 14 H); ^{13}C NMR (100 MHz, $CDCl_3$) δ = 191.7, 165.7, 139.1, 135.5, 130.2, 129.5, 65.8, 63.1, 32.8, 29.6, 29.5, 29.4, 29.2, 28.6, 26.0, 25.7; HRMS $[M + Na]^+$ m / z: calcd. for $C_{19}H_{28}NaO_4$ 343.1885, found 343.1828.

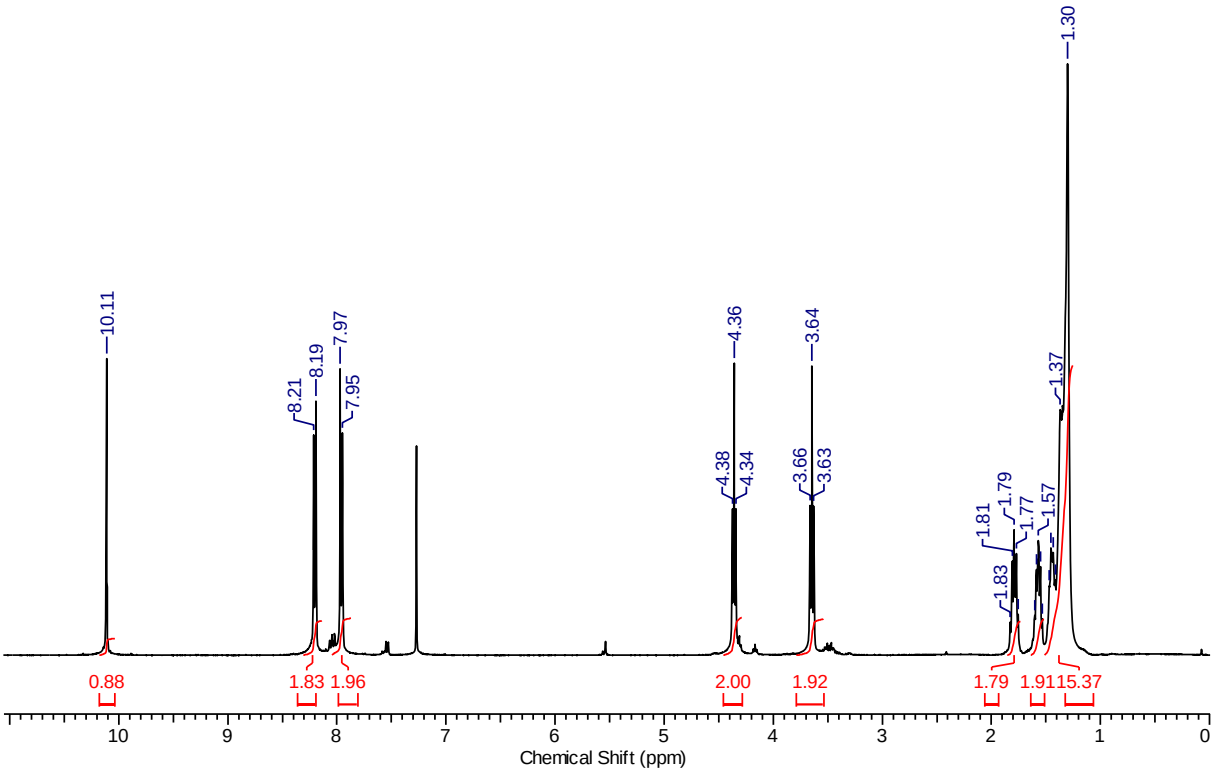

Figure 87 ^{1}H NMR (400 MHz, $CDCl_3$) spectrum of 11-hydroxyundecyl 4-formylbenzoate **24**.

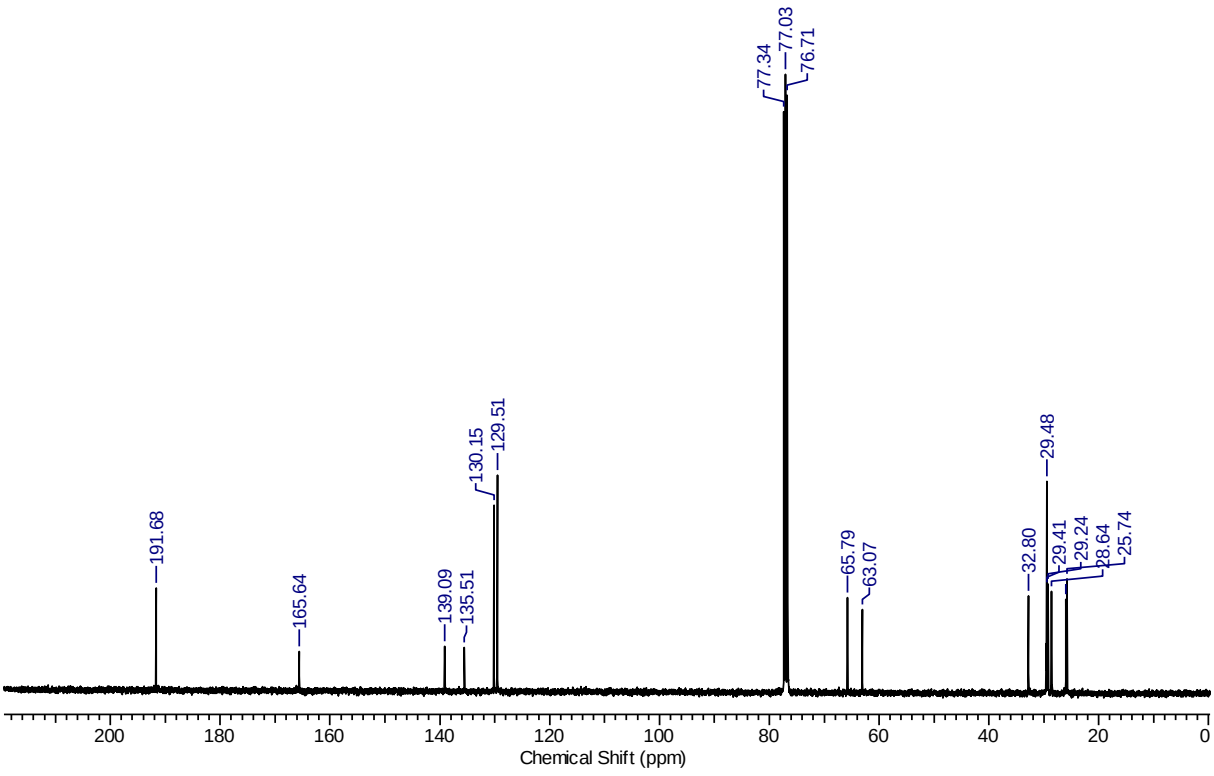

Figure 88 ^{13}C NMR (100 MHz, $CDCl_3$) spectrum of 11-hydroxyundecyl 4-formylbenzoate **24**.

11-Hydroxyundecyl 4-(2-(pyren-1-yl)-2H-tetrazol-5-yl)benzoate (PAT) (22)

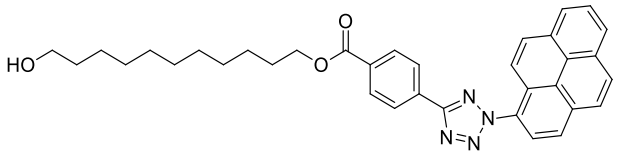

A mixture of 11-hydroxyundecyl 4-formylbenzoate **22** (472.6 mg, 1.48 mmol) and benzenesulfonohydrazide (254.0 mg, 1.48 mmol) in 15 mL EtOH was stirred at ambient temperature for 3 h. The solvent was removed under reduced pressure. The obtained solid was dissolved in 8 mL pyridine (solvent A). In parallel 1-aminopyrene (258.0 mg, 1.19 mmol) was dissolved in 30 mL THF under argon and cooled to -21 °C. A solution of $NaBF_4$ (1050 mg, 9.55 mmol) in 10.5 mL HBF_4 (50%) and 4.5 mL H_2O was added. The reaction mixture was stirred for 20 min at -21 °C. $NaNO_2$ (94.2 mg, 1.37 mmol) in 2 mL H_2O was added. An orange precipitate was formed after stirring at -21 °C for additional 20 min. The solid was collected and added to solution A at 0 °C. The reaction mixture was stirred for 1 h at room temperature, diluted in 80 mL ethyl acetate, extracted with 1 M hydrochloric acid (2 × 100 mL) and dried over $NaSO_4$. Ethyl acetate was removed under reduced pressure. The crude product was purified via recrystallization in EtOH (3 × 30 mL). After drying under high vacuum the title compound was obtained as pink solid (181 mg, 32 %). ^{1}H NMR (400 MHz, $CDCl_3$) δ = 8.40 - 8.06 (m, 13 H), 4.43 - 4.35 (m, 2 H), 3.70 - 3.63 (m, 2 H), 1.79 - 1.70 (m, 2 H), 1.55 - 1.22 (m, 16 H); ^{13}C NMR (100 MHz, $CDCl_3$) δ = 166.1, 164.6, 132.8, 132.3, 131.2, 131.1, 130.5, 130.3, 130.1, 129.4, 127.1, 127.0, 126.9, 126.7, 126.3, 125.1, 125.0, 124.8, 124.1, 122.7, 121.4, 65.5, 63.1, 32.8, 29.6, 29.5, 29.4, 29.3, 28.7, 26.1, 25.8; HRMS $[M + Na]^+$ m / z: calcd for $C_{35}H_{36}N_4NaO_3$ 583.2685 found 583.2685.

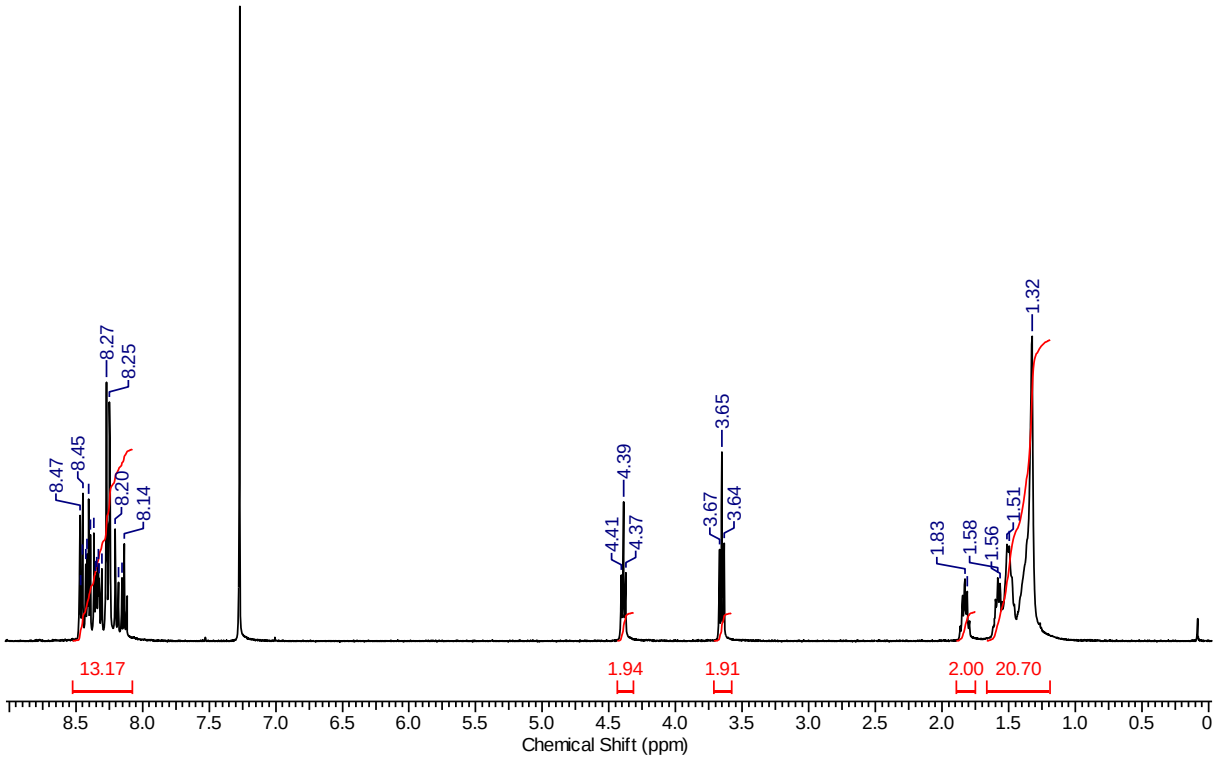

Figure 89 ^{1}H NMR (400 MHz, $CDCl_3$) spectrum of 11-hydroxyundecyl 4-(2-(pyren-1-yl)-2H-tetrazol-5-yl)benzoate **22**.

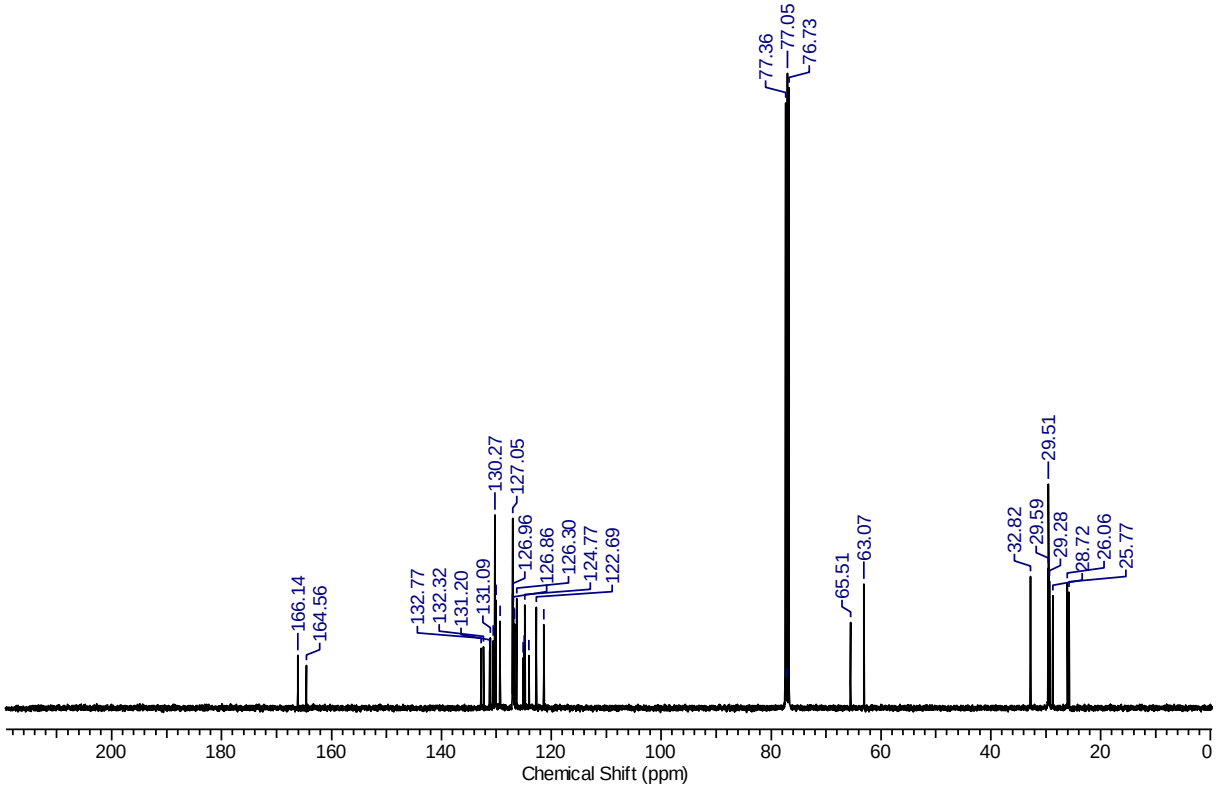

Figure 90 ^{13}C NMR (100 MHz, $CDCl_3$) spectrum of 11-hydroxyundecyl 4-formylbenzoate 11-hydroxyundecyl 4-(2-(pyren-1-yl)-2H-tetrazol-5-yl)benzoate **22**.

PAT end capped PCL (A_1)

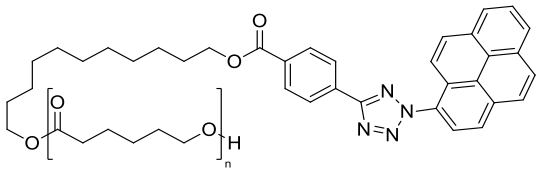

11-hydroxyundecyl 4-(2-(pyren-1-yl)-2H-tetrazol-5-yl)benzoate **22** (98.0 mg, 0.18 mmol) and triazabicyclodecene (TBD) (24.4 mg, 0.18 mmol) were dissolved in 10 mL dry DCM under argon. ε-Caprolacton (500.0 mg, 4.38 mmol) was added. The reaction mixture was stirred at room temperature for 3 h. Benzoic acid (50.0 mg, 0.41 mmol) was added. The solvent was removed under reduced pressure. The crude product was dissolved in ethyl acetate (100 mL) and washed with 1 M HCl (3 × 100 mL) and saturated $NaHCO_3$ (3 × 100 mL). Solvent was removed under reduced pressure and the crude product was precipitated in ice cold cyclohexane. ^{1}H NMR (400 MHz, $CDCl_3$) δ = 8.47-8.12 (m, 13 H), 4.41 - 4.37 (m, 2 H), 4.09 - 4.04 (m, polymer backbone), 3.67 - 3.63 (m, 2 H), 2.33 - 2.28 (m, polymer backbone), 1.86 - 1.79 (m, 2 H), 1.70 - 1.25 (m, 16 H + polymer backbone); M_n = 1.4 kDa (^{1}H NMR), M_n = 2.0 kDa (GPC), $Đ$ = 1.10.

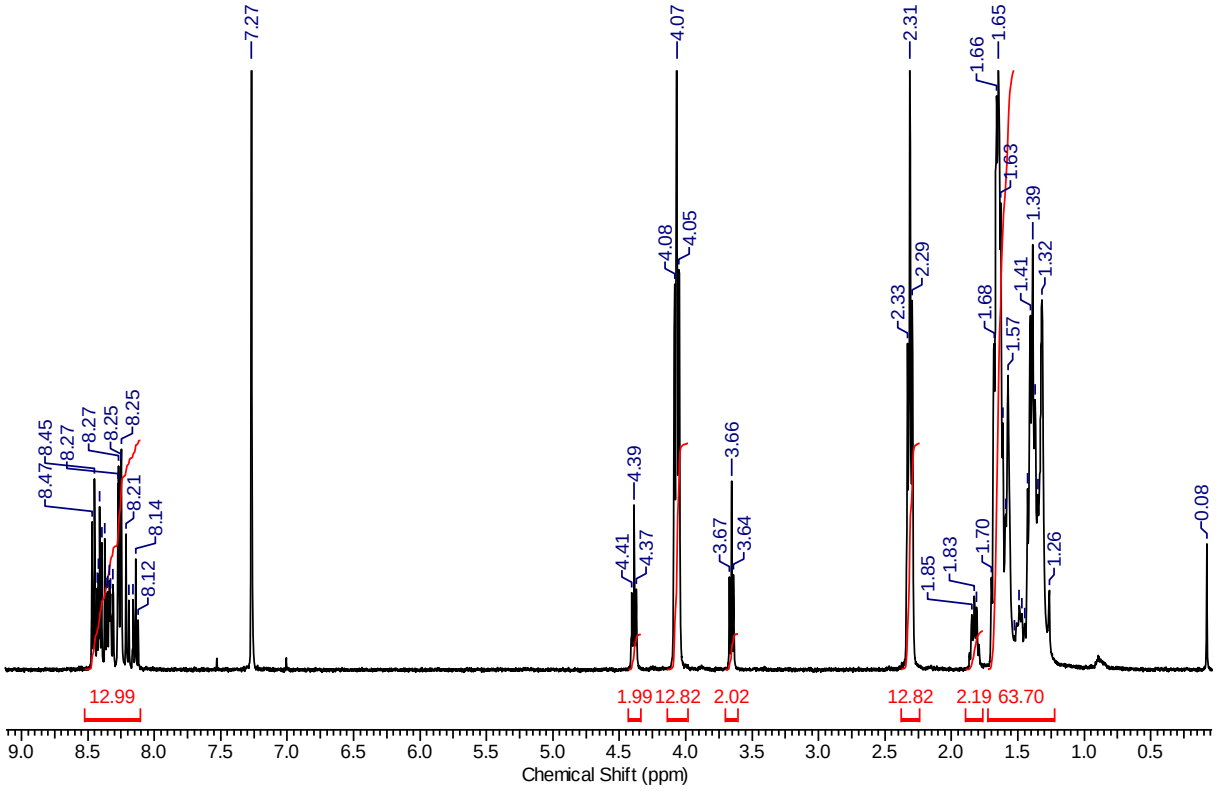

Figure 91 ^{1}H NMR (400 MHz, $CDCl_3$) spectrum of PAT end capped PCL **A₁** synthesized via ROP of hydroxyl functional PAT **22**.

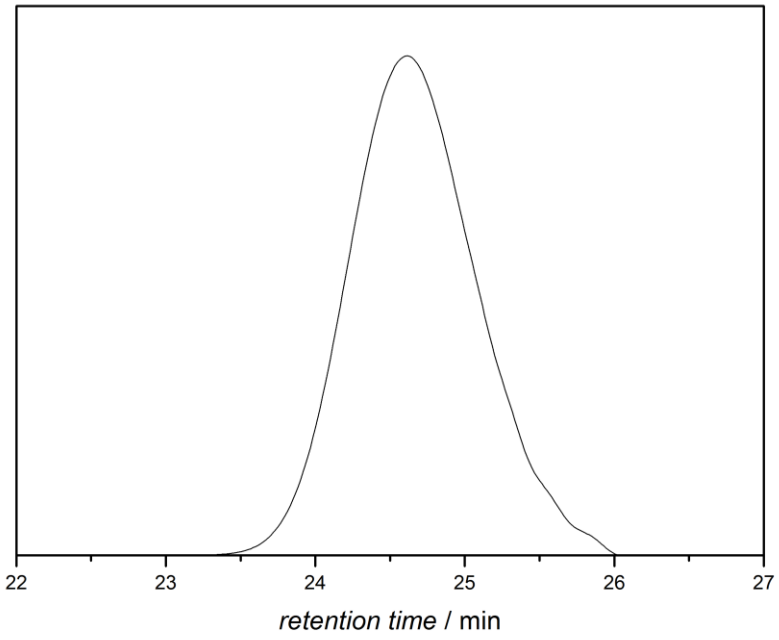

Figure 92 GPC trace of PAT end capped PCL **A₁** obtained in a ROP polymerization employing PAT **22** (M_n = 1.4 kDa (^{1}H NMR), M_n = 2.0 kDa (GPC), $Đ$ = 1.10).

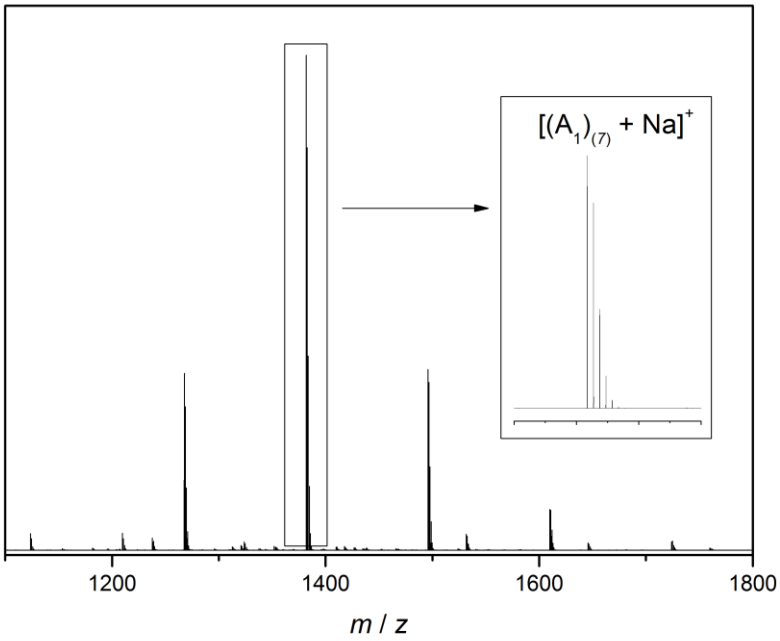

Figure 93 Magnified view into the region of 1100 - 1800 *m* / *z* of a ESI-MS spectrum of PAT end capped PCL **A₁** obtained in ROP polymerization employing PAT **22**. Signals repeat in intervals of 114.14 Dalton. Sodium adduct of PAT end-capped PCL, $[(\mathbf{A_1})_{(7)} + Na]^+$.

PAT end capped PCL (A_2)

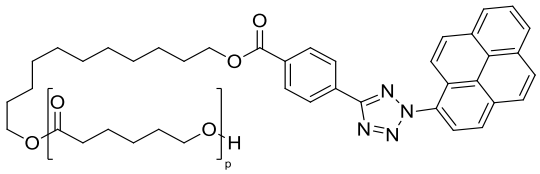

11-hydroxyundecyl 4-(2-(pyren-1-yl)-2H-tetrazol-5-yl)benzoate **22** (98.0 mg, 0.18 mmol) and triazabicyclodecene (TBD) (24.4 mg, 0.18 mmol) were dissolved in 10 mL dry DCM under argon. ε-Caprolacton (700.0 mg, 4.38 mmol) was added. The reaction mixture was stirred at room temperature for 3 h. Benzoic acid (50.0 mg, 0.61 mmol) was added. The solvent was removed under reduced pressure. The crude product was precipitated in cold cyclohexane / EtO_2 mixture (1:1, v / v). ^{1}H NMR (400MHz, $CDCl_3$) δ = 8.47 - 8.12 (m, 13 H), 4.41 - 4.37 (m, 2 H), 4.09 - 4.04 (m, polymer backbone), 3.67 - 3.63 (m, 2 H), 2.33 – 2.28 (m, polymer backbone), 1.86 - 1.79 (m, 2 H), 1.70 - 1.25 (m, 16 H + polymer backbone); M_n = 4.2 kDa (^{1}H NMR), M_n = 5.8 kDa (GPC), $Đ$ = 1.15.

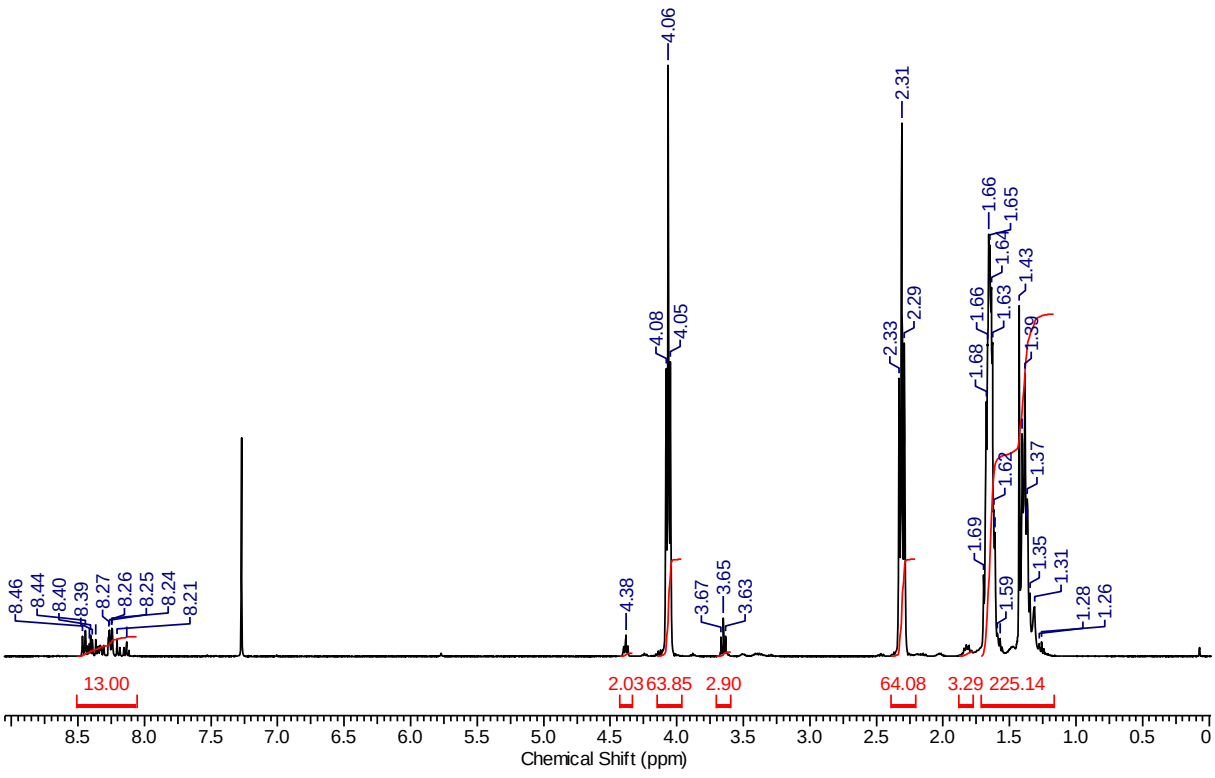

Figure 94 ^{1}H NMR (400 MHz, $CDCl_3$) spectrum of PAT end capped PCL **A_2** synthesized via ROP of hydroxyl functional PAT **22**.

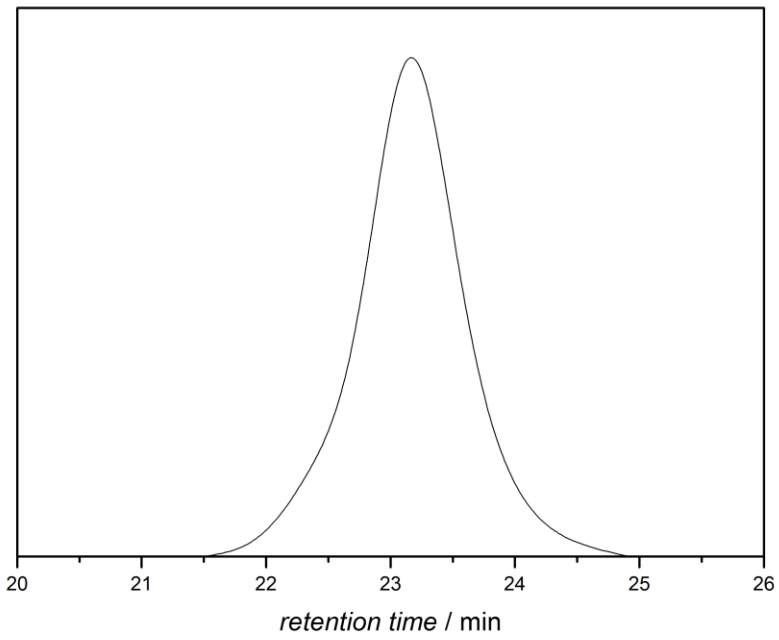

Figure 95 GPC trace of PAT end capped PCL **A_2** obtained in ROP polymerization employing PAT **22** (M_n = 4.2 kDa (^{1}H NMR), M_n = 5.8 kDa (GPC), $Đ$ = 1.15).

11-Hydroxyundecyl 4-(5-(2-hydroxyethyl)-4,6-dioxo-1-(pyren-1-yl)-1,3a,4,5,6,6a-hexahydropyrrolo[3,4-c]pyrazol-3-yl)benzoate (23)

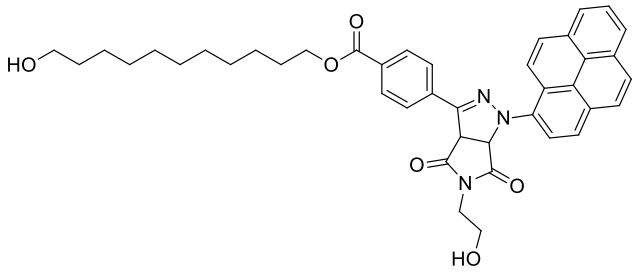

11-hydroxyundecyl 4-(2-(pyren-1-yl)-2H-tetrazol-5-yl)benzoate **22** (10.0 mg, 0.018 mmol) and 1-(2-hydroxyethyl)-1H-pyrrole-2,5-dione **7** (5.0 mg, 0.022 mmol) were dissolved in 40 mL MeCN. The reaction mixture was irradiated at room temperature, at 400 nm for 1 h. The solvent was removed under reduced pressure. The crude product was purified via column chromatography on silica gel using hexane / ethyl acetate (2:1, v / v R_f 0.26) as the eluent. After drying under high vacuum the title compound **23** was obtained as yellow solid (8.0 mg, 71 %). ^{1}H NMR (400MHz, $CDCl_3$) δ = 8.47 - 7.84 (m, 13 H), 5.50 - 5.29 (m, 1H), 4.88 - 4.68 (m, 1 H), 4.29 - 4.16 (m, 2 H), 3.74 - 3.61 (m, 4 H), 3.57 - 3.52 (m, 2 H), 1.80 - 1.68 (m, 2 H), 1.67 -1.21 (m, 16 H); ^{13}C NMR (100 MHz, $CDCl_3$) δ = 172.6, 172.4, 166.2, 143.1, 137.6, 134.5, 131.4, 131.0, 130.7, 129.7, 129.5, 127.6, 127.2, 127.1, 126.7, 126.3, 125.8, 125.3, 125.2, 125.0, 124.7, 123.0, 120.2, 67.7, , 65.3, 63.0, 59.6, 53.2, 42.1, 32.7, 29.5, 29.4, 29.1, 28.6, 26.0, 25.7; HRMS $[M + Na]^+$ m / z: calcd. for $C_{41}H_{43}N_3NaO_6$ 696.3050 found 696.3056.

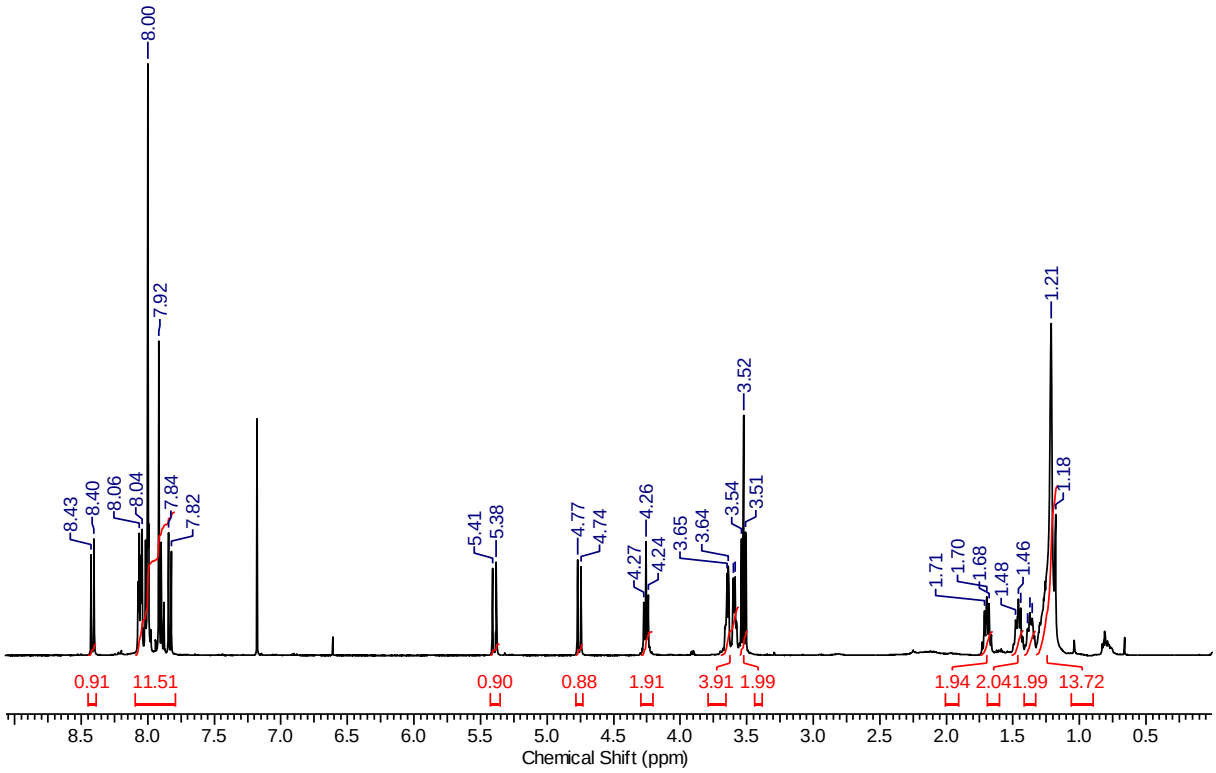

Figure 96 ^{1}H NMR (400 MHz, $CDCl_3$) spectrum of 11-hydroxyundecyl 4-(5-(2-hydroxyethyl)-4,6-dioxo-1-(pyren-1-yl)-1,3a,4,5,6,6a-hexahydropyrrolo[3,4-c]pyrazol-3-yl)benzoate **23**.

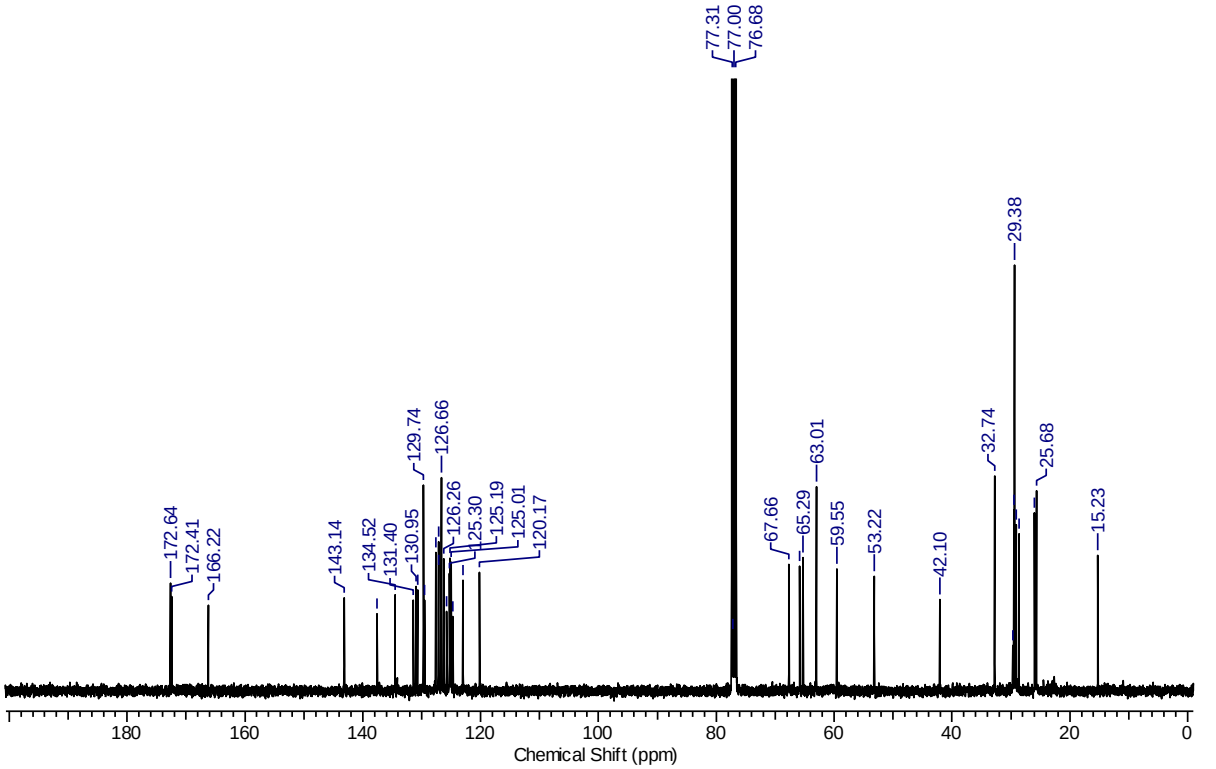

Figure 97 ^{13}C NMR (100 MHz, $CDCl_3$) spectrum of 11-hydroxyundecyl 4-formylbenzoate 11-hydroxyundecyl 4-(2-(pyren-1-yl)-2H-tetrazol-5-yl)benzoate **23**.

General Procedure for Synthesis of Macromolecular Cycloadducts

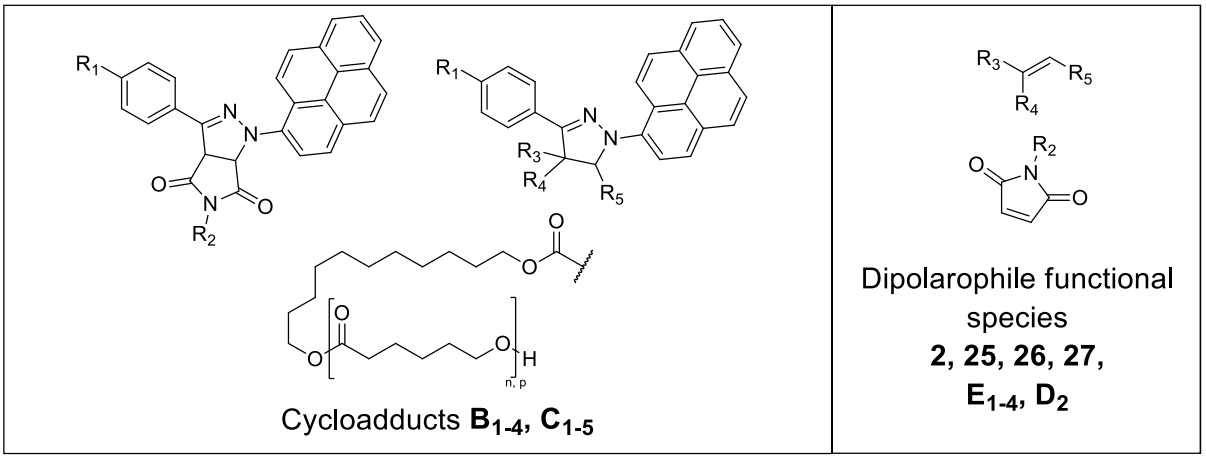

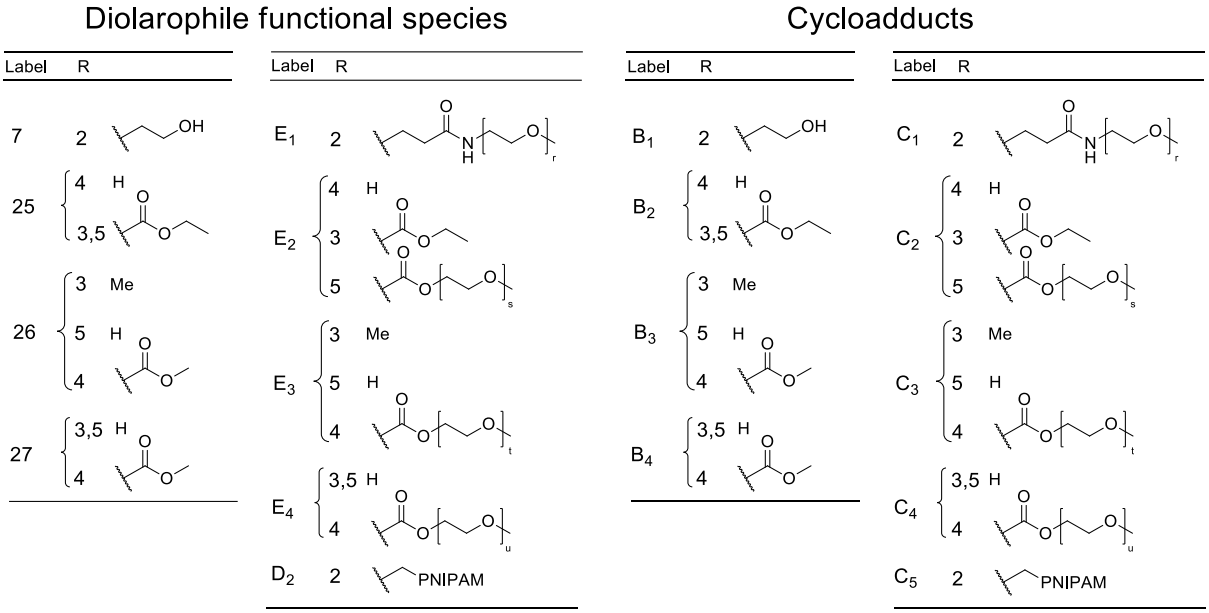

Figure 98 Overview over cycloadducts $\mathbf{B_{1-4}}$ and $\mathbf{C_{1-5}}$ formed *via* NITEC reaction of dipolarophile functional species **2**, **25**, **26**, **27**, $\mathbf{E_{1-4}}$, $\mathbf{D_2}$ and PAT end capped PCL $\mathbf{A_1}$ or $\mathbf{A_2}$. For clarity only one of two possible regioisomers for $\mathbf{B_{3,4}}$ and $\mathbf{C_{2-4}}$ is shown.

PAT end capped PCL and the ene functional species were dissolved in 40 mL solvent. The reaction mixture was irradiated at room temperature, at 410 - 420 nm for 30 min. The solvent was removed under reduced pressure. Refer to Table 1 for further details. ^{1}H NMR (400MHz, $CDCl_3$): $\mathbf{B_1}$ δ = 8.55 - 7.95 (m, 13 H), 5.70 - 5.59 (m, 1 H), 5.12 - 5.04 (m, 1 H), 4.30 - 4.25 (m, 2 H), 4.12 - 4.04 (m, polymer backbone), 3.88 - 3.64 (m, 6 H),

2.37 - 2.31 (m, polymer backbone), 1.86 - 1.21 (m, 18 H + polymer backbone); **B_2** δ = 8.57 - 7.94 (m, 13 H), 5.66 - 5.62 (m, 1 H), 4.88 - 4.84 (m, 1 H), 4.43 - 4.21 (m, 4 H), 4.10 - 4.03 (m, polymer backbone), 3.92 - 3.82 (m, 2 H), 3.68 - 3.62 (m, 2 H), 2.35 - 2.27 (m, polymer backbone), 1.91 - 1.25 (m 24 H + polymer backbone); **B_3** δ = 8.59 - 7.75 (m, 13 H), 4.40 - 4.32 (m, 2 H), 4.12 - 4.00 (m, 4 H + polymer backbone), 3.81 - 3.57 (m, 5 H), 3.42 - 3.36 (m, 1 H), 2.36 - 2.25 (m, polymer back bone), 1.94 - 1.08 (m, 18 H + polymer backbone); **B_4** δ = 8.73 - 7.42 (m, 13 H), 6.99 (s, BHT), 5.67 - 5.14 (m, 1 H), 5.02 (s, BHT), 4.35 - 4.31 (m, 2 H), 4.12 - 4.00 (m, 1 H + polymer backbone), 3.68 - 3.63 (m, 5 H), 3.47 (s, 1 H), 2.41 - 2.24 (m, polymer backbone+ BHT), 1.92 - 1.15 (m, 18 H + polymer backbone + BHT); **C_1** δ = 8.69 - 7.90 (m, 13 H), 5.94 - 5.90 (m, 1 H), 5.34 - 5.29 (m, 1 H), 4.41 - 4.22 (m, 4 H), 4.05 - 3.85 (m, polymer backbone(PCL)), 3.52 - 3.45 (m, 2 H + polymer backbone(PEG)), 3.23 (s, 3 H), 3.12 - 3.05 (m, 2 H), 2.34 - 2.19 (m, polymer backbone(PCL)), 1.82 - 0.95 (m, 18 H + polymer backbone(PCL)); **C_2** δ = 8.58 - 7.73 (m, 13 H), 5.74 - 5.47 (m, 1 H), 4.85 - 4.82 (m, 1 H), 4.41 - 4.17 (m, 4 H), 4.08 - 3.89 (2 H + m, polymer backbone(PCL)), 3.65 - 3.44 (m, 2 H + polymer backbone(PEG), 3.31 (s, 3 H), 2.30 - 2.11 (m, polymer backbone(PCL)), 1.80 - 1.13 (m, 24 H + polymer backbone(PCL)); **C_3** δ = 8.70 - 7.84 (m, 13 H), 6.99 (s, BHT), 4.12 - 4.00 (1 H + m, polymer backbone (PCL)), 3.73 - 3.54 (m, 2 H + polymer backbone(PEG)), 3.55 - 3.43 (m, 3), 3.31 (s, 3 H), 2.40 - 2.16 (m, polymer backbone(PCL + BHT), 1.78 - 1.17 (m, 18 H + polymer backbone(PCL) + BHT); **C_4** δ = 8.54 - 7.54 (m, 13 H), 4.38 - 4.31 (m, 2 H), 4.21 - 3.85 (polymer backbone(PCL)), 3.79 - 3.45 (m, 2 H + polymer backbone(PEG)), 3.39 (s, 3 H), 2.35 - 2.29 (m, polymer backbone(PCL)), 1.88 - 1.14 (m, 18 H + polymer backbone(PCL)); **C_5** refer to Figure 120.

Table 5 Reaction details for the formation of the macromolecular cycloadducts **B_{1-4}** and **C_{1-5}**.

Cyclo adduct	PAT end capped PCL	c_{PCL} / mmol·L^{-1}	$c_{dipolarophile}$ / mmol·L^{-1}	Dipolarophile functional species	solvent	$Đ$[d]	M_n[d] / kDa
B_1[a]	A_1	0.18	2.7	7	MeCN	1.12	2.2
B_2[a]	A_1	0.18	2.7	25	MeCN	1.11	2.1
B_3[a]	A_1	0.18	2.7	26	THF[c]	1.13	2.1
B_4[a]	A_1	0.18	2.7	27	THF[c]	1.14	2.1
C_1[b]	A_2	0.12	0.18	E_1	MeCN	1.12	8.0
C_2[b]	A_2	0.12	0.18	E_2	MeCN	1.15	8.4
C_3[b]	A_2	0.12	0.18	E_3	THF[c]	1.14	8.5
C_4[b]	A_2	0.12	0.18	E_4	THF[c]	1.15	8.7
C_5[b*]	A_2	0.12	0.14	PNIPAM	MeCN	1.24	8.8

[a] Cycloadduct was analysed without any further purification. [b] The crude product was dissolved in ethyl acetate (50 mL) extracted with 1 M hydrochloric acid (4 × 100 mL) and dried over $NaSO_4$. Ethyl acetate was removed under reduced pressure. The residual solid was dissolved in DCM and precipitated in cold hexane / diethyl mixture (1:1). [b*] The crude product was dissolved in ethyl acetate (50 mL) extracted with 1 M hydrochloric acid (1 × 100 mL) and dried over $NaSO_4$. Ethyl acetate was removed under reduced pressure. [c] BHT stabilized THF was used to avoid side products possible formed in radical involving processes (Refer to characterization section of **B_4** for more details). [d] M_n and $Đ$ of cycloadducts were determined by GPC using PMMA calibration standards.

Table 6 Sum formula, the exact masses for experimental results, theoretical values and the deviation of both for PAT end capped PCL **A_1** and cycloadducts **B_{1-4}**.

Label	Sum formula	m / z_{exp}	m / z_{theo}	Δ m / z
A_1	$[C_{83}H_{116}N_4NaO_{19}]^+$	1495.815	1495.813	0.002
B_1	$[C_{83}H_{113}N_3NaO_{20}]^+$	1494.787	1494.782	0.005
B_2	$[C_{83}H_{114}N_2NaO_{21}]^+$	1525.818	1525.812	0.006
B_3	$[C_{82}H_{114}N_2NaO_{19}]^+$	1567.862	1567.859	0.003
B_4	$[C_{87}H_{122}N_2NaO_{21}]^+$	1553.831	1553.844	0.013

Macromolecular Cycloadduct (B_1)

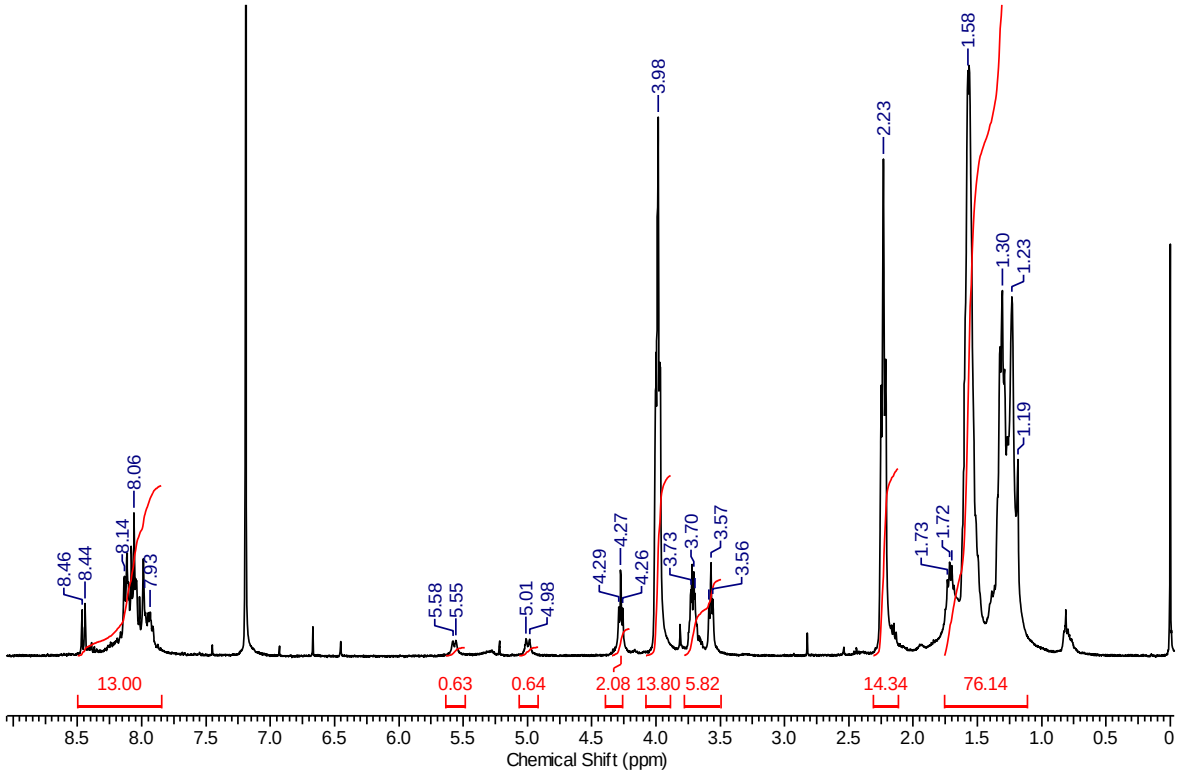

Figure 99 ^{1}H NMR (400 MHz, $CDCl_3$) spectrum of the macromolecular cycloadduct **B_1**

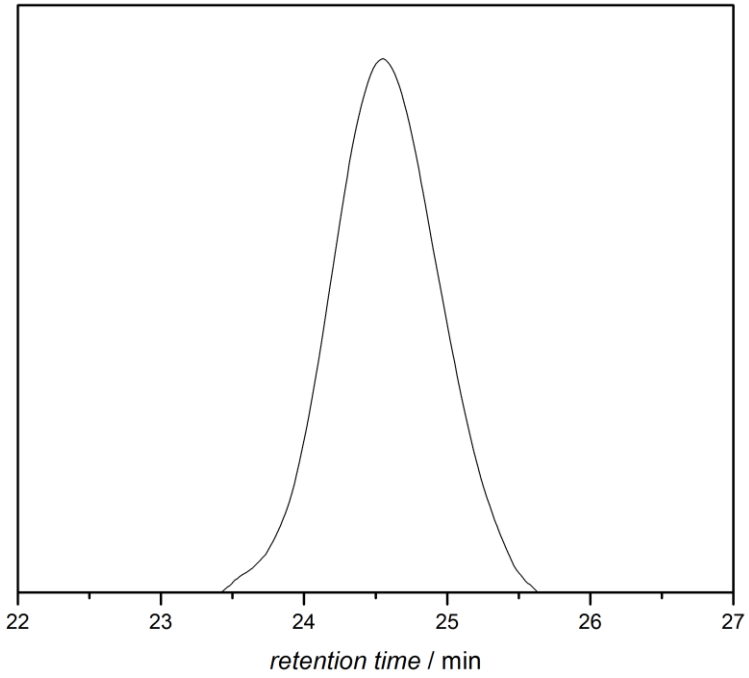

Figure 100 GPC trace of the macromolecular cycloadduct **B_1** in THF.

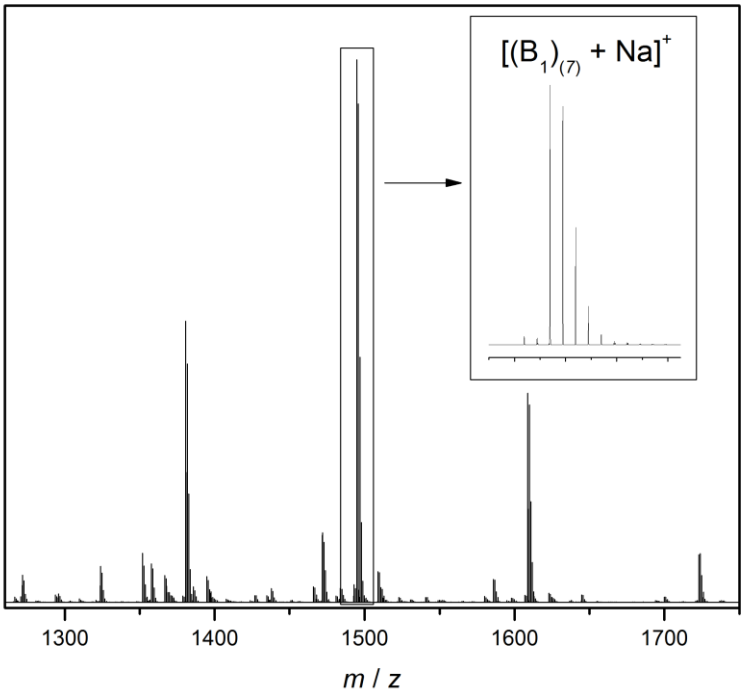

Figure 101 Magnified view into the region of 1260 - 1750 *m* / *z* of a ESI-MS spectrum of macromolecular cycloadduct **B₁**. Signals repeat in intervals of 114.14 Dalton. Sodium adduct of PAT end capped PCL, $[(\mathbf{B_1})_{(n)} + Na]^+$.

Macromolecular Cycloadduct (B_2)

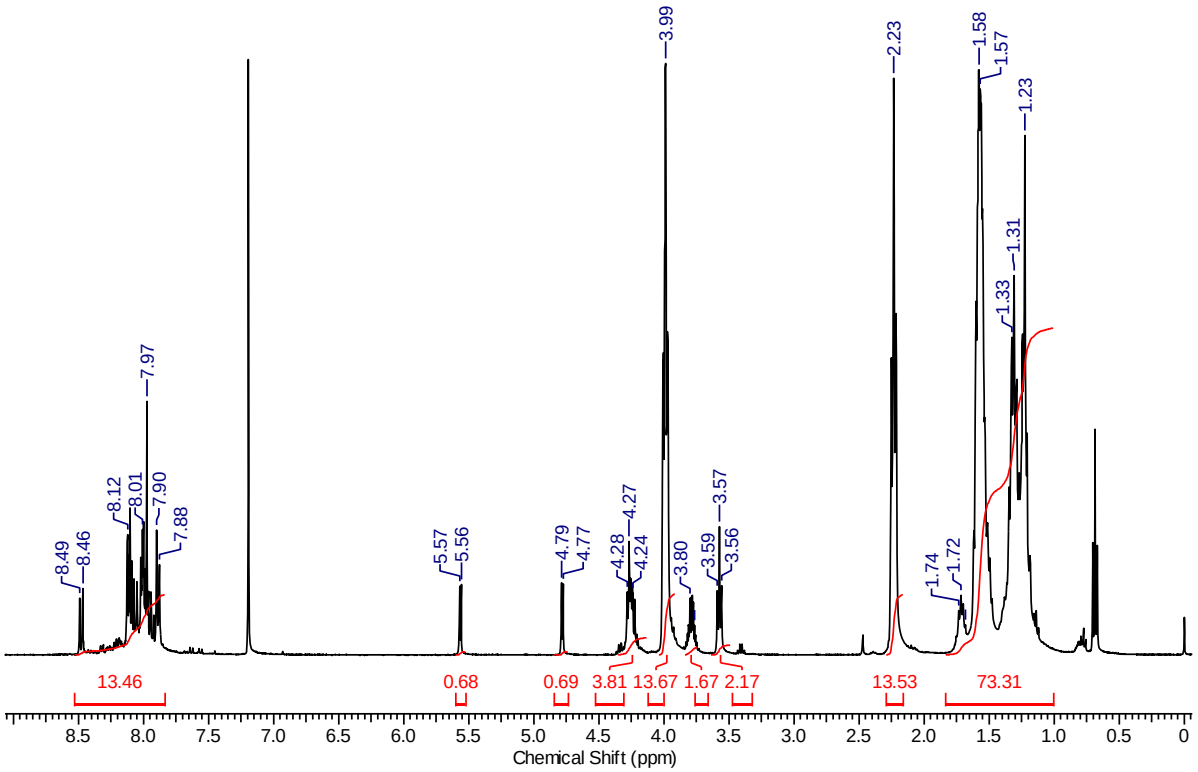

Figure 102 1H NMR (400 MHz, $CDCl_3$) spectrum of macromolecular cycloadduct **B_2**.

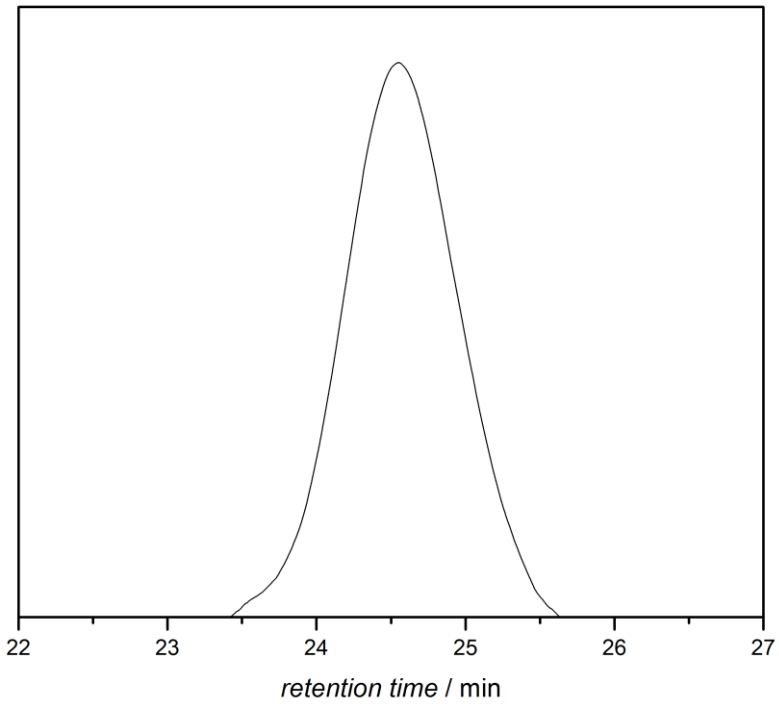

Figure 103 GPC trace of the macromolecular cycloadduct **B_2** in THF.

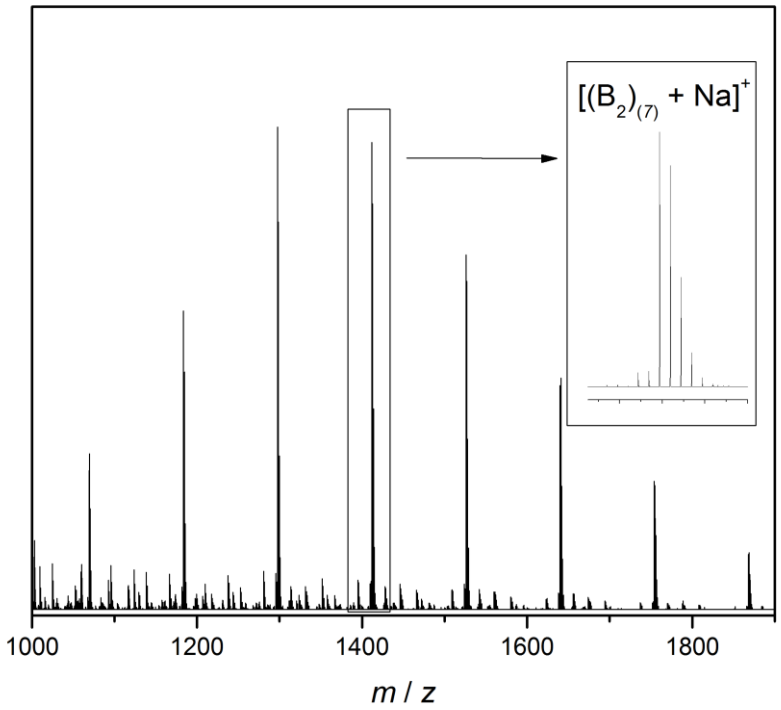

Figure 104 Magnified view into the region of 1000 - 1900 *m* / *z* of ESI-MS spectrum of macromolecular cycloadduct **B₂**. Signals repeat in in tervals of 114.14 Dalton. Sodium adduct of PAT end capped PCL, $[(\mathbf{B_2})_{(7)} + Na]^+$.

Macromolecular Cycloadduct (B_3)

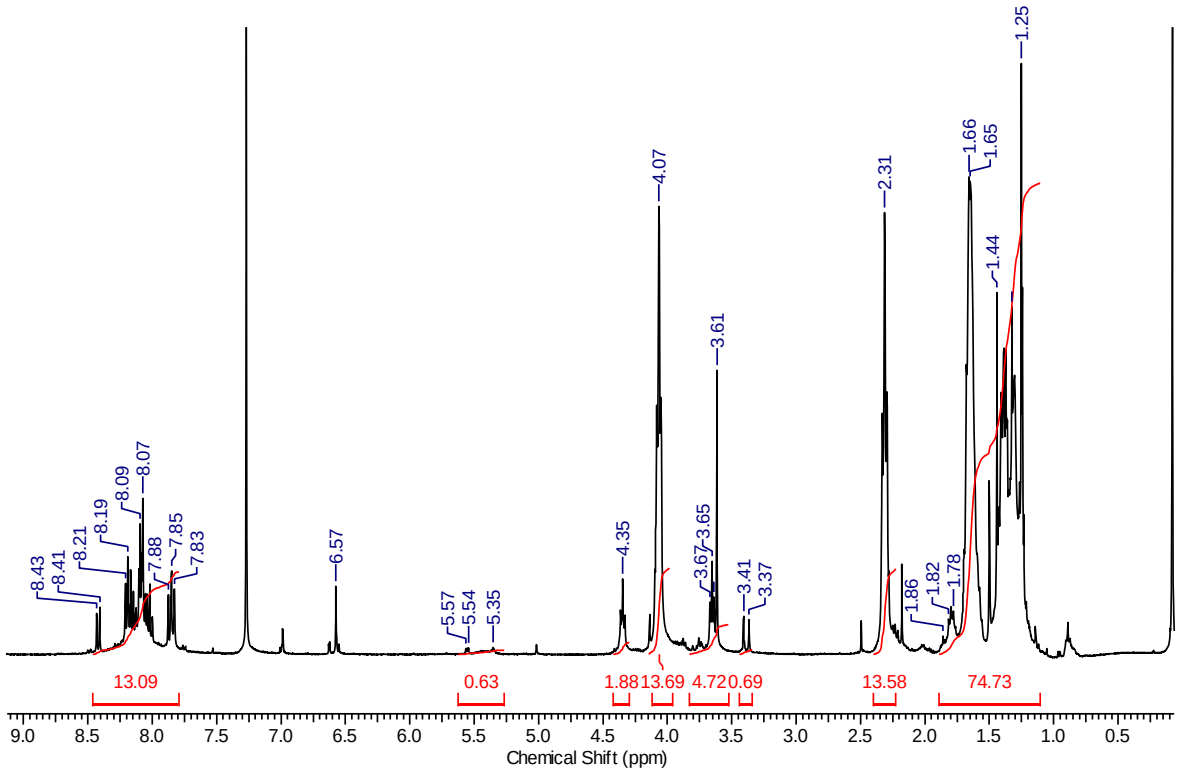

Figure 105 ^{1}H NMR (400 MHz, $CDCl_3$) spectrum of the macromolecular cycloadduct **B_3**. Residual BHT can be observed, used as a radical scavenger during the formation of the **B_3** to avoid side reactions involving radical species.

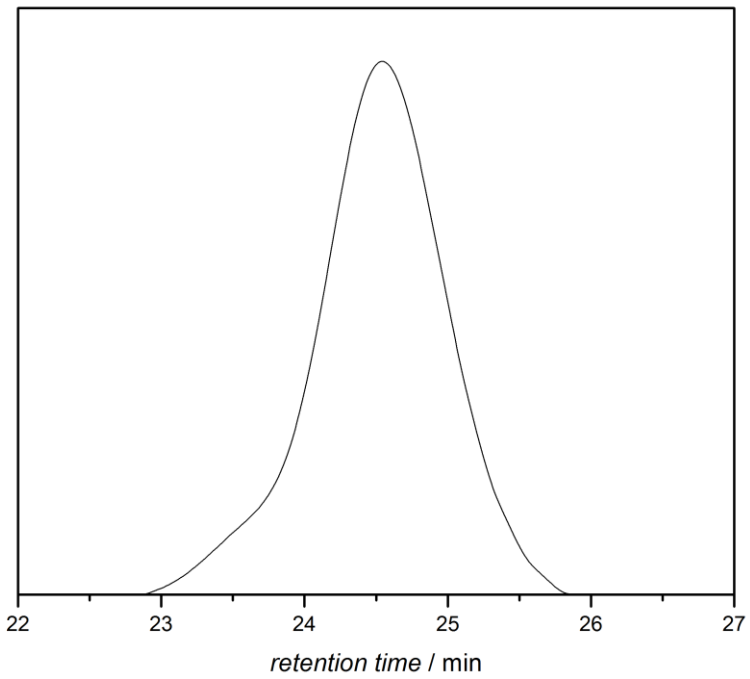

Figure 106 GPC trace of the macromolecular cycloadduct **B₃** in THF.

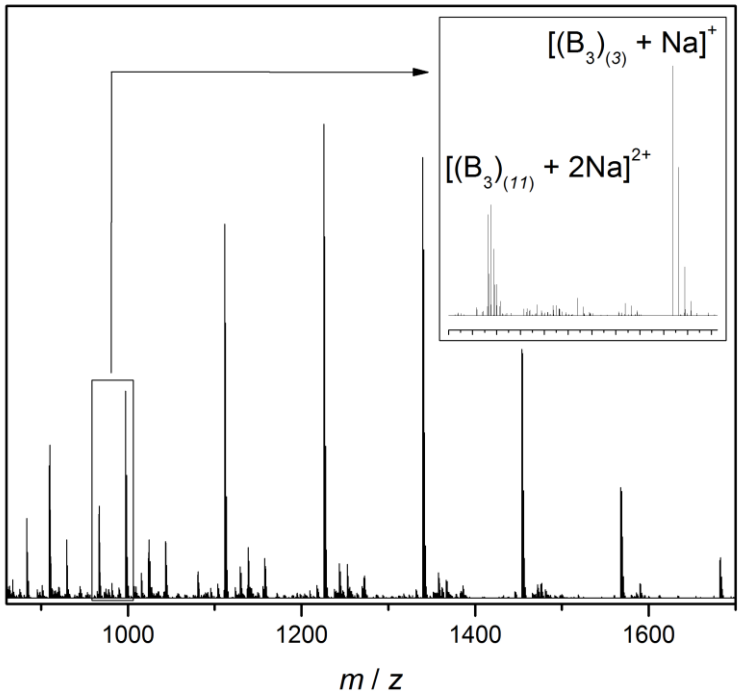

Figure 107 Magnified view into the region of 960 - 1700 *m / z* of ESI-MS spectrum of macromolecular cycloadduct **B₃**. Signals repeat in intervals of 114.14 Dalton. Sodium adduct of PAT end capped PCL, $[(\mathbf{B_3})_{(3)} + Na]^+$ and $[(\mathbf{B_3})_{(11)} + 2Na]^{2+}$.

Macromolecular Cycloadduct (B_4)

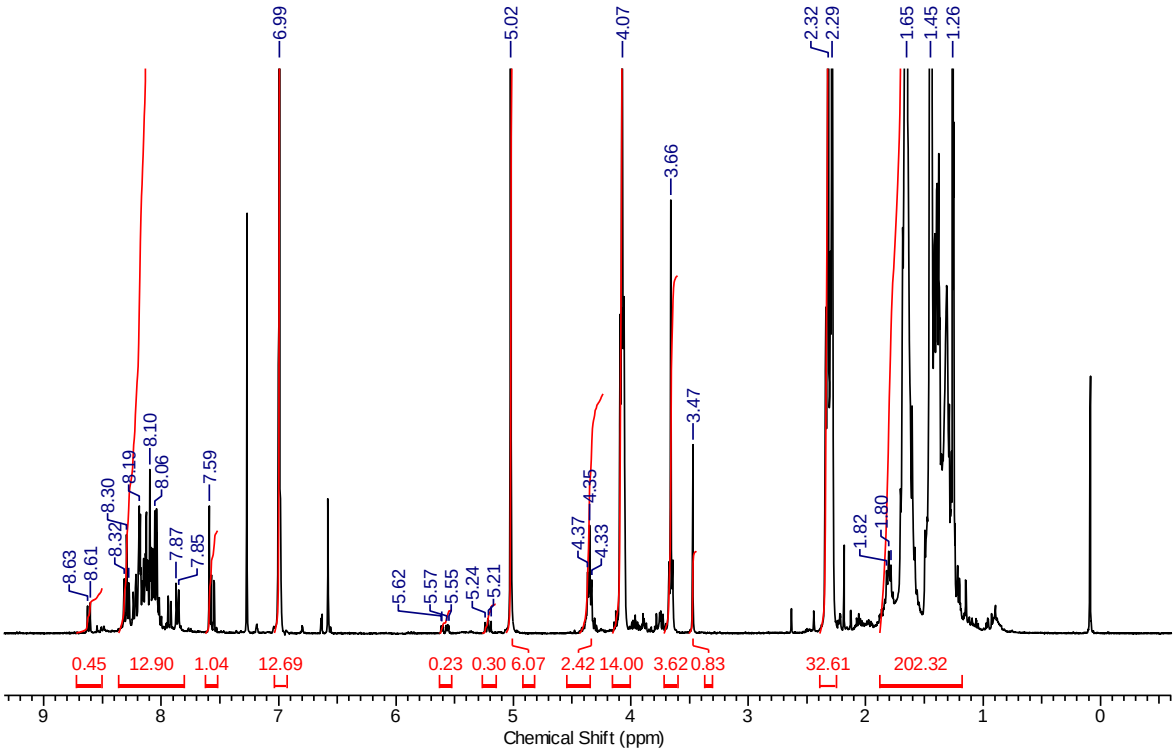

Figure 108 ^{1}H NMR (400 MHz, $CDCl_3$) spectrum of macromolecular cycloadduct **B_4**. Residual BHT can be observed, used as a radical scavenger during the formation of the **B_4** to avoid side reactions involving radical species.

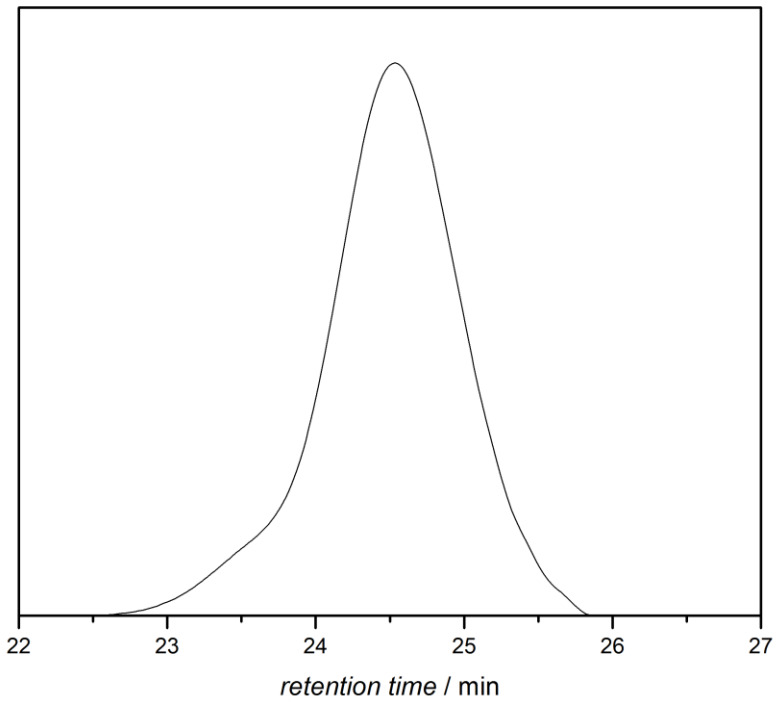

Figure 109 GPC trace of the macromolecular cycloadduct **B_4** in THF.

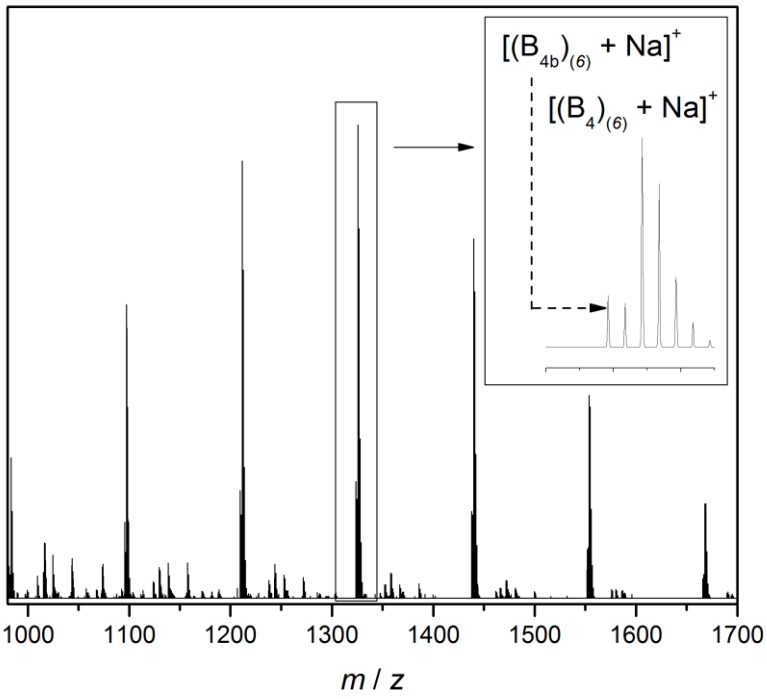

Figure 110 Magnified view into the region of 960 - 1700 *m / z* of ESI-MS spectrum of macromolecular cycloadduct **B4**. Signals repeat in intervals of 114.14 Dalton. Sodium adduct of PAT end capped PCL, $[(\mathbf{B_4})_{(6)} + Na]^+$ and $[(\mathbf{B_{4b}})_{(6)} + Na]^+$. Side product **B4b** assumed to be formed in a radical elimination reaction of **B4**. Refer to Figure 111 for the structure of **B4b**.

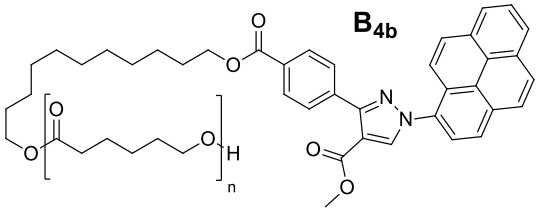

Figure 111 Structure of **B4b** is assumed to be a radical elimination reaction product of the macromolecular cycloadduct **B4**. For clarity only one of two possible regioisomer of **B4b** is shown.

Macromolecular Cycloadduct (C_1)

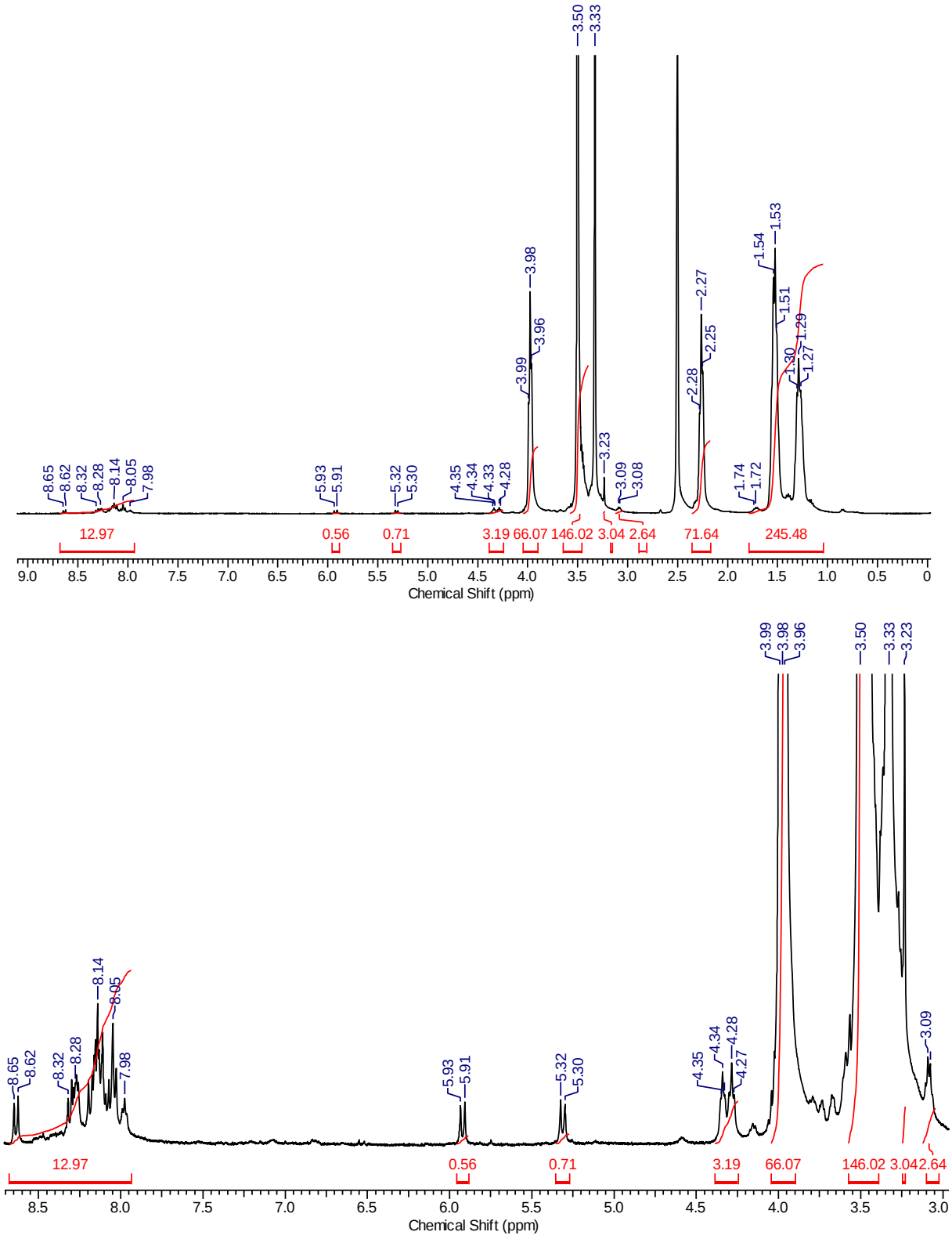

Figure 112 ^{1}H NMR (400 MHz, DMSO) spectrum of the macromolecular cycloadduct **C_1**. Full spectrum of the PCL-*b*-PEG block copolymer (above), magnification of the 8.7 - 2.9 ppm region (below).

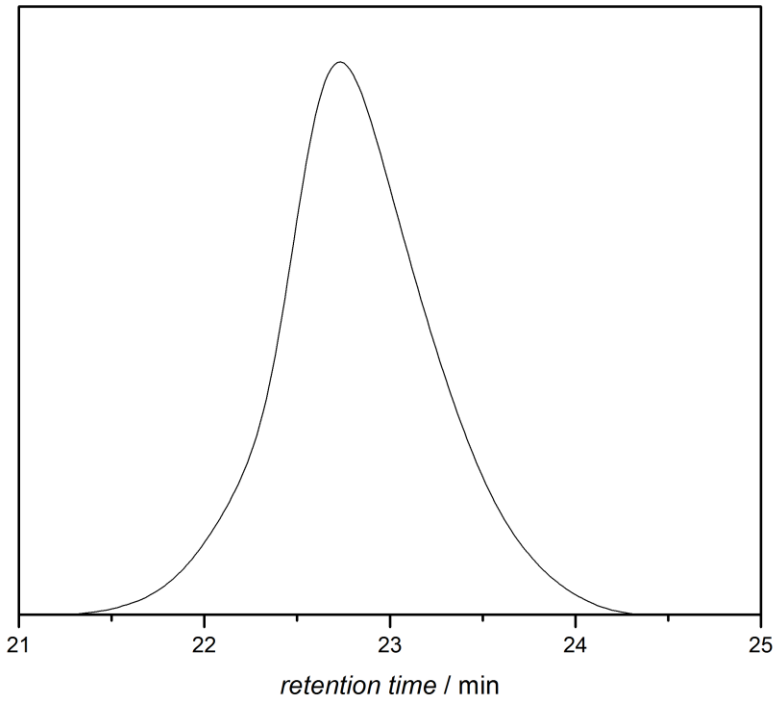

Figure 113 GPC trace of the macromolecular cycloadduct **C_1** in THF.

Macromolecular Cycloadduct (C_2)

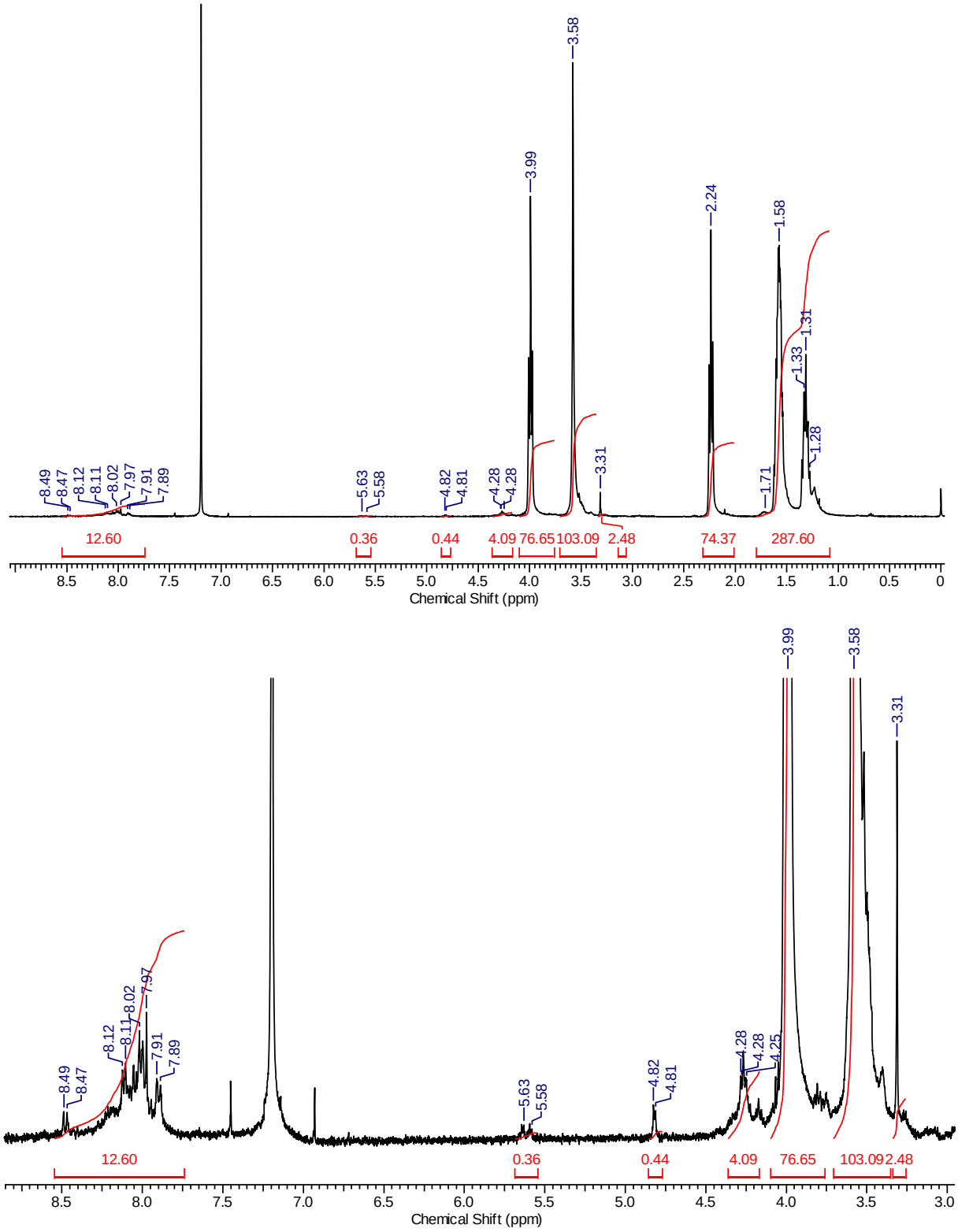

Figure 114 ^{1}H NMR (400 MHz, $CDCl_3$) spectrum of the macromolecular cycloadduct **C_2**. Full spectrum of the PCL-*b*-PEG block copolymer (above), magnification of the 8.7 - 2.9 ppm region (below).

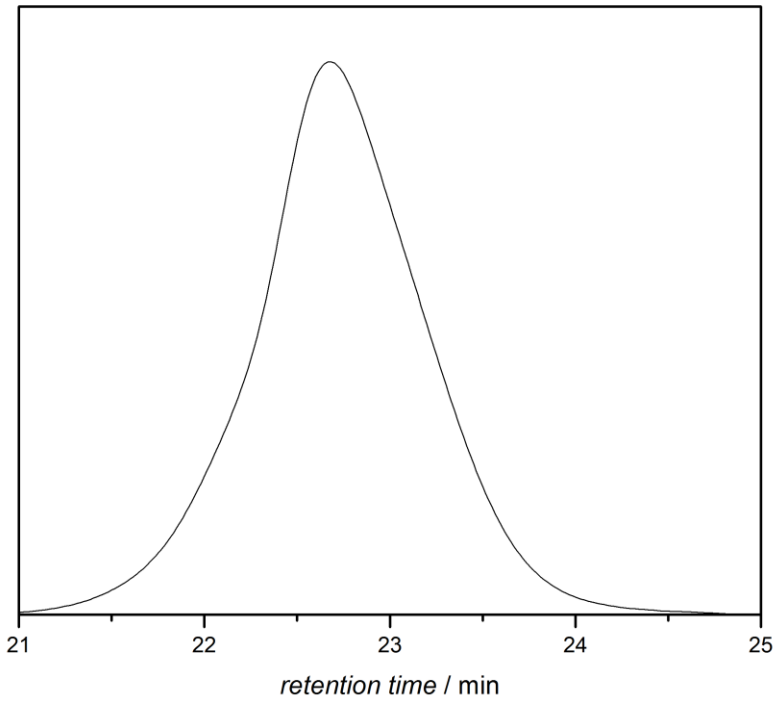

Figure 115 GPC trace of the macromolecular cycloadduct **C_2** in THF.

Macromolecular Cycloadduct (C_3)

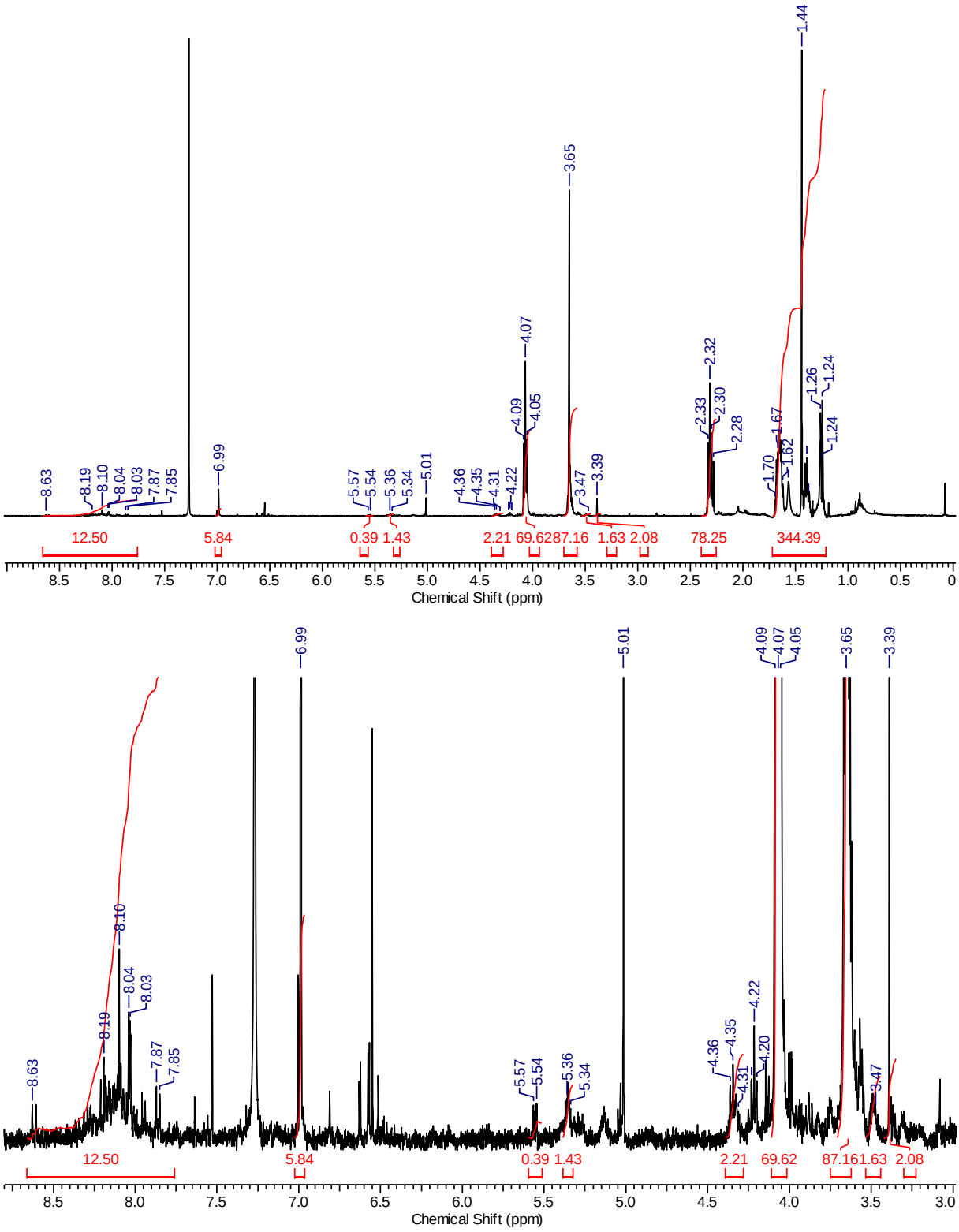

Figure 116 ^{1}H NMR (400 MHz, $CDCl_3$) spectrum of macromolecular cycloadduct **C_3**. Full spectrum of the PCL-*b*-PEG block copolymer (above), magnification of the 8.6 - 3.0 ppm region (below). BHT can be observed, used as a radical scavenger during the formation of **C_3** to avoid side reactions involving radical species.

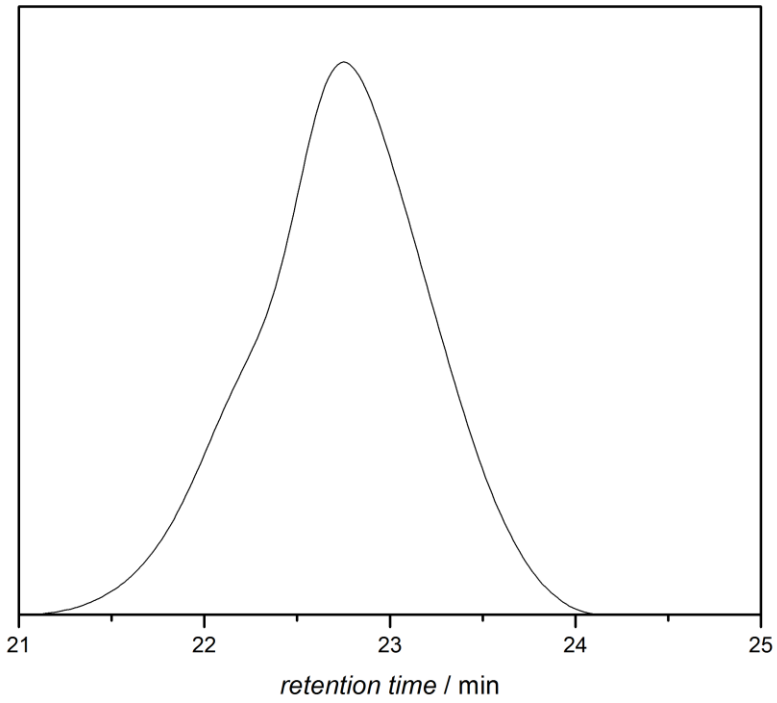

Figure 117 GPC trace of the macromolecular cycloadduct **C_3** in THF.

Macromolecular Cycloadduct (C_4)

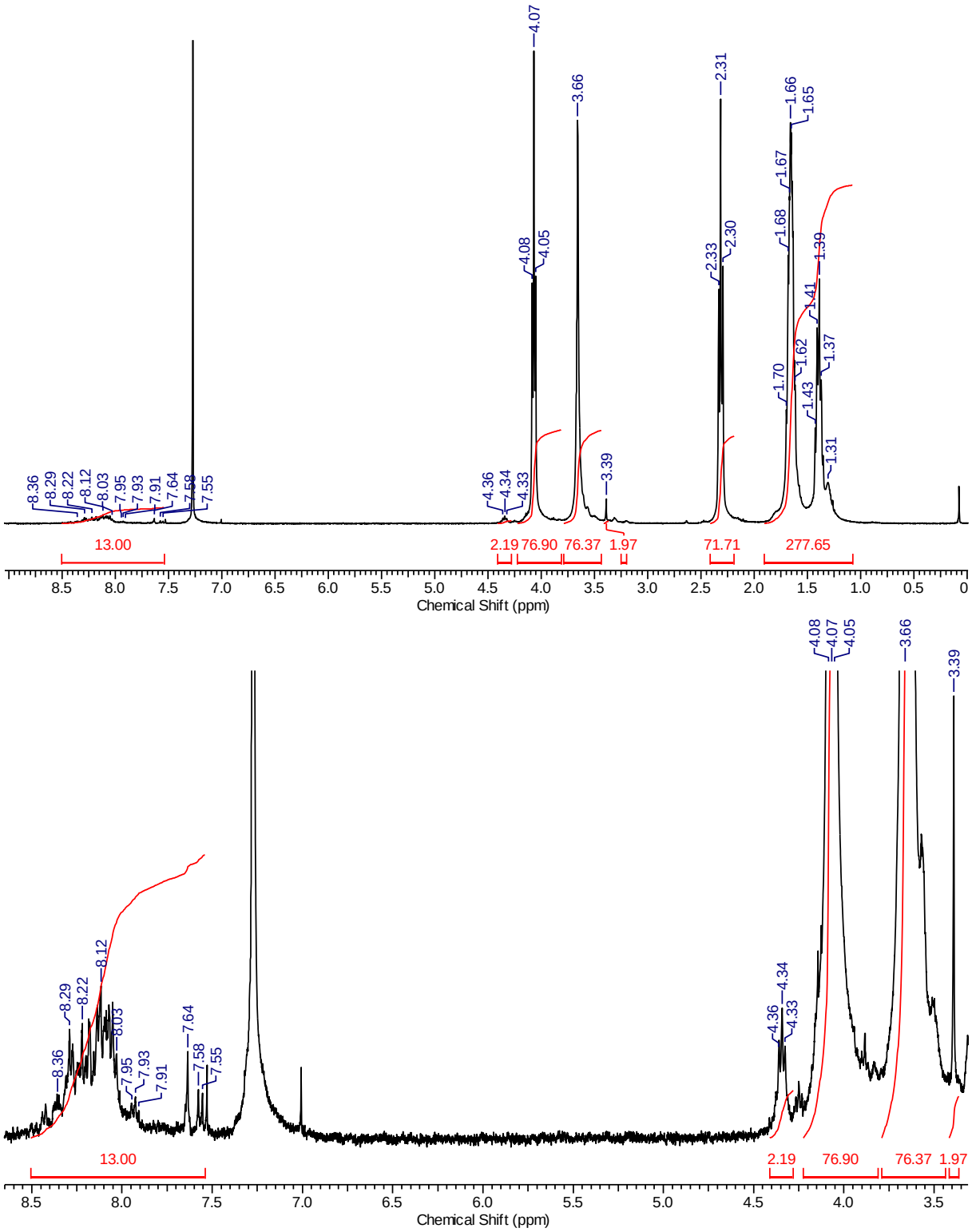

Figure 118 ^{1}H NMR (400 MHz, $CDCl_3$) spectrum of the macromolecular cycloadduct **C_4**. Full spectrum of the PCL-*b*-PEG block copolymer (above), magnification of the 8.6 - 3.4 ppm region (below).

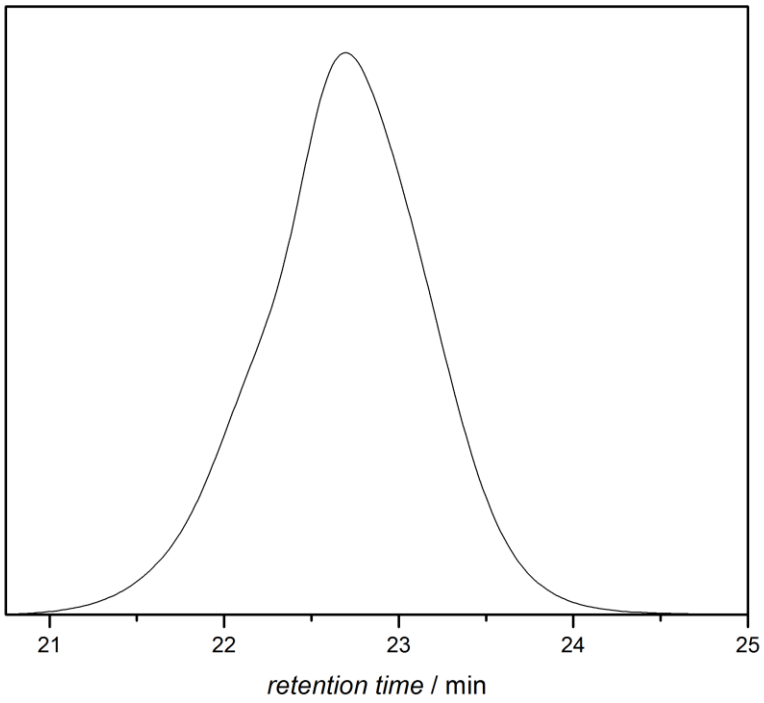

Figure 119 GPC trace of the macromolecular cycloadduct **C_4** in THF.

Macromolecular Cycloadduct (C_5)

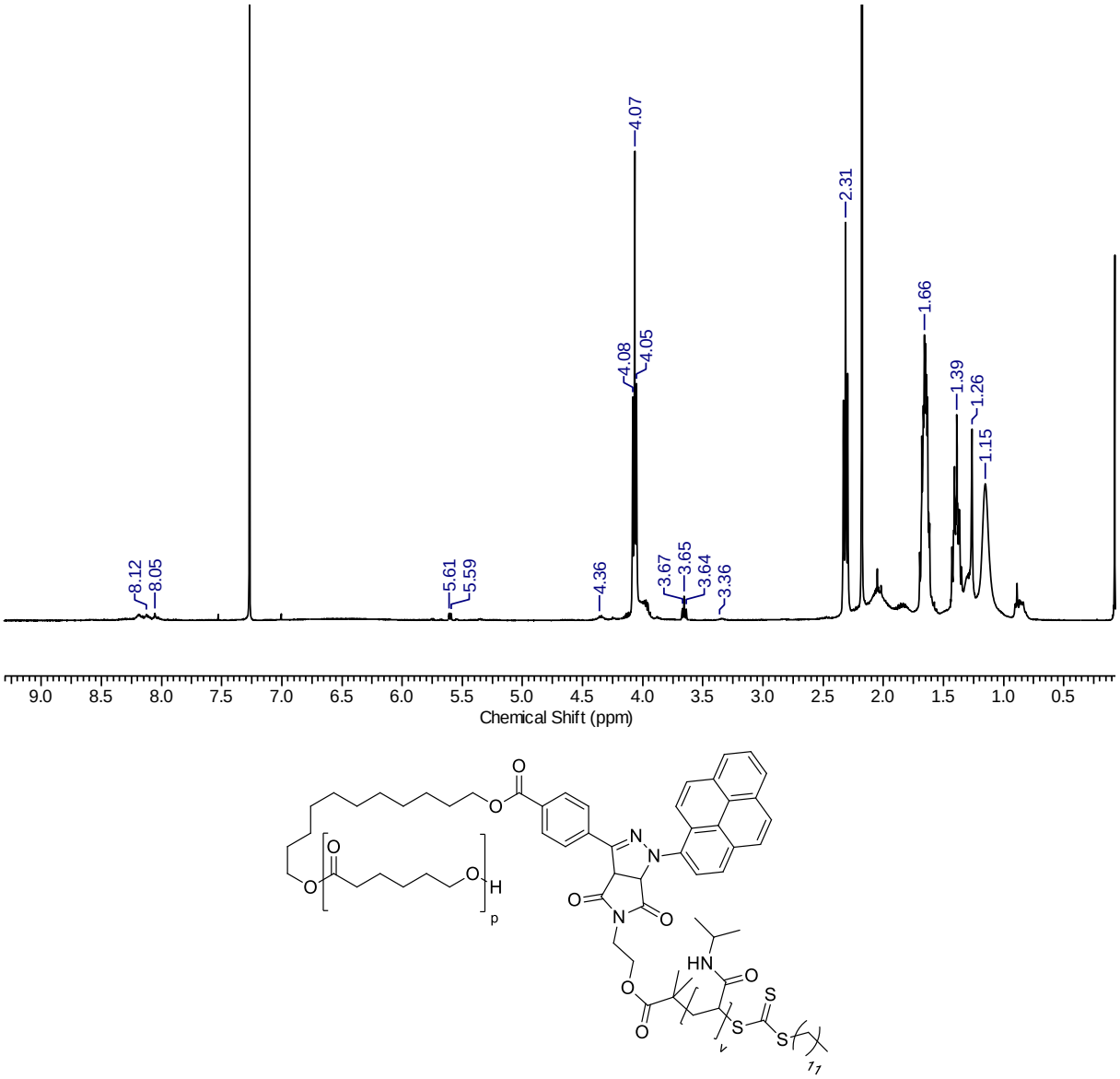

Figure 120 ^{1}H NMR (400 MHz, $CDCl_3$) spectrum of macromolecular cycloadduct **C_5**.

Synthesis of Maleimide End Capped PNIPAM (D_2)

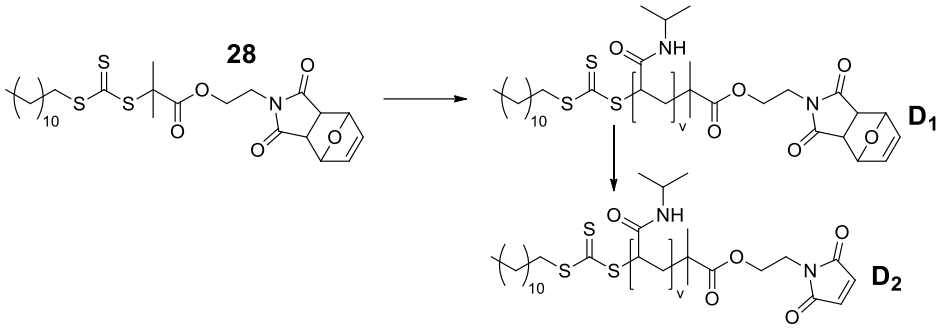

Scheme 33 Synthetic path for the formation of the maleimide functional PNIPAM **D_2**. Refer to the corresponding synthetic procedures of **D_1** and **D_2** for reaction details.

PNIPAM (D_1)

1.00 g NIPAM, **28** and AIBN (molar ratio: 1000:10:1) were dissolved in 5 mL DMF (monomer concentration = 1.77 mol·L^{-1}) and degassed *via* three consecutive freeze-pump-thaw cycles. Subsequently, the polymerization mixture was stirred at 60 °C for 8 h. The polymerization was quenched by cooling with liquid nitrogen and exposing the mixture to oxygen. The polymerization mixture was precipitated twice in diethyl ether. The obtained polymer was dried under reduced pressure to obtain a yellowish solid. ^{1}H NMR (400 MHz, $CDCl_3$): δ = 7.00 - 5.81 (bs, polymer backbone+ 2 H), 5.25 (s, 2 H), 3.99 (s, polymer backbone + 4 H), 3.76 (s, 2 H), 3.34 (s, 2 H), 2.90 (s, 2 H), 2.49 (s, polymer backbone), 2.34 - 0.93 (m, polymer backbone + 24 H), 0.89 – 0.84 (m, 3 H); M_n = 4.7 kDa (^{1}H NMR), M_n = 5.8 kDa (GPC), $Đ$ = 1.20.*

*GPC was measured in DMAC.

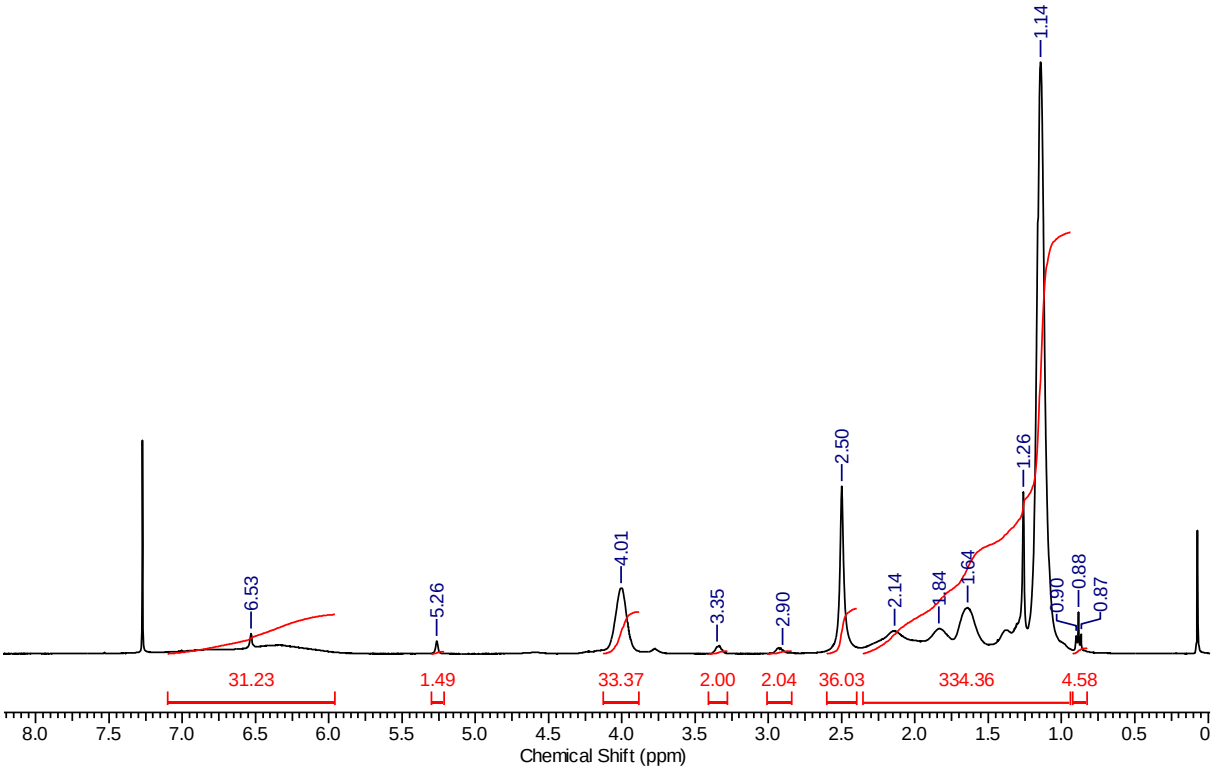

Figure 121 ^{1}H NMR (400 MHz, $CDCl_3$) spectrum of PNIPAM **D_1**.

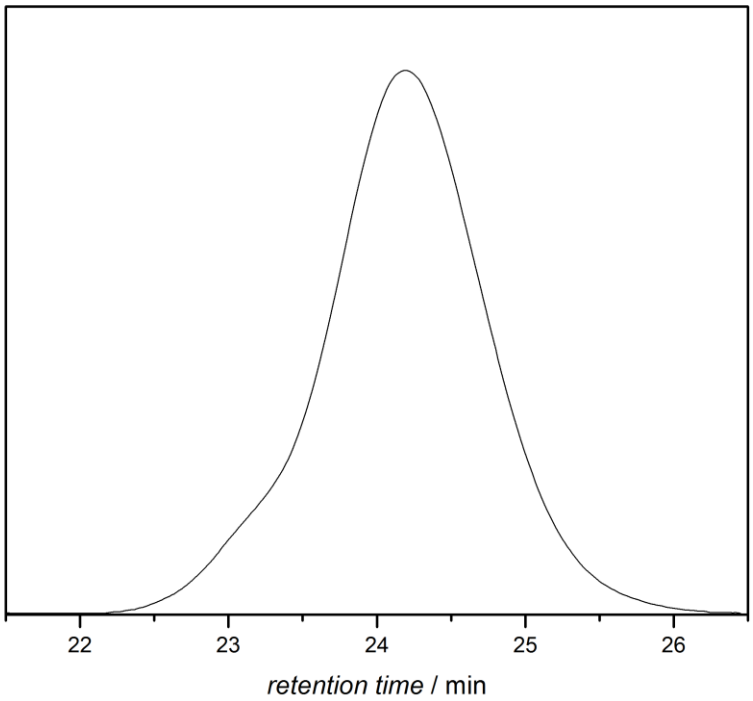

Figure 122 GPC trace of PNIPAM **D_1** in DMAC**.**

PNIPAM (D_2)

The PNIPAM **D_1** was placed in a round bottom flask and heated in bulk under reduced pressure at 95 °C for 10 h. ^{1}H NMR (400 MHz, $CDCl_3$): δ = 7.00 – 5.70 (bs, polymer backbone + 2 H), 3.99 (s, polymer backbone + 4 H), 3.80 (s, 2 H), 3.33 (s, 2 H), 2.51 (s, polymer backbone), 2.34 - 0.93 (m, polymer backbone + 24 H), 0.89 - 0.85 (m 3 H) M_n = 4.7 kDa (^{1}H NMR), M_n = 2.9 kDa (GPC), $Đ$ = 1.08.

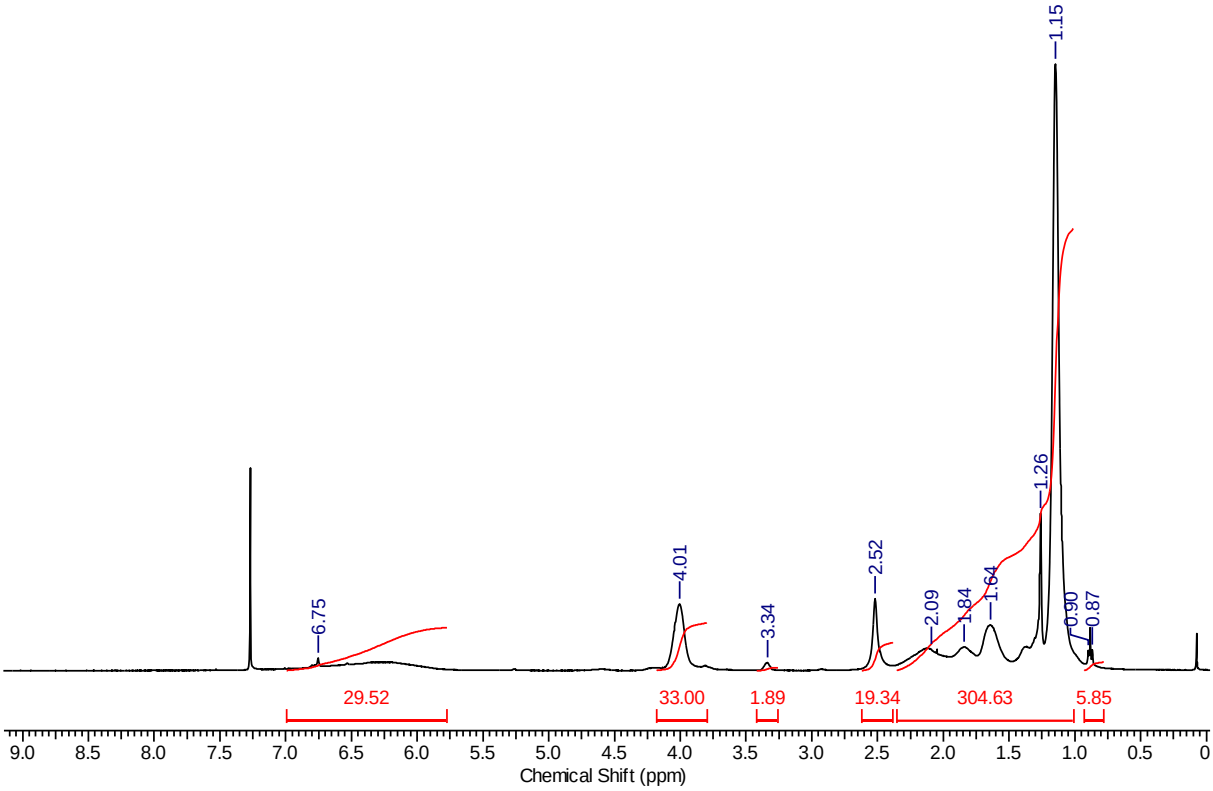

Figure 123 ^{1}H NMR (400 MHz, $CDCl_3$) spectrum of PNIPAM **D_2**.

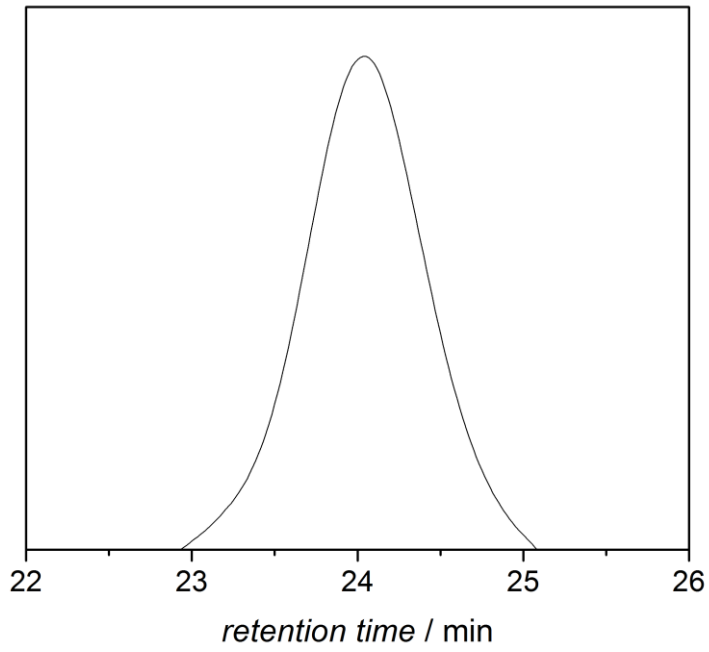

Figure 124 GPC trace of PNIPAM D_2 in THF.

8.2.4 Spectroscopic Data

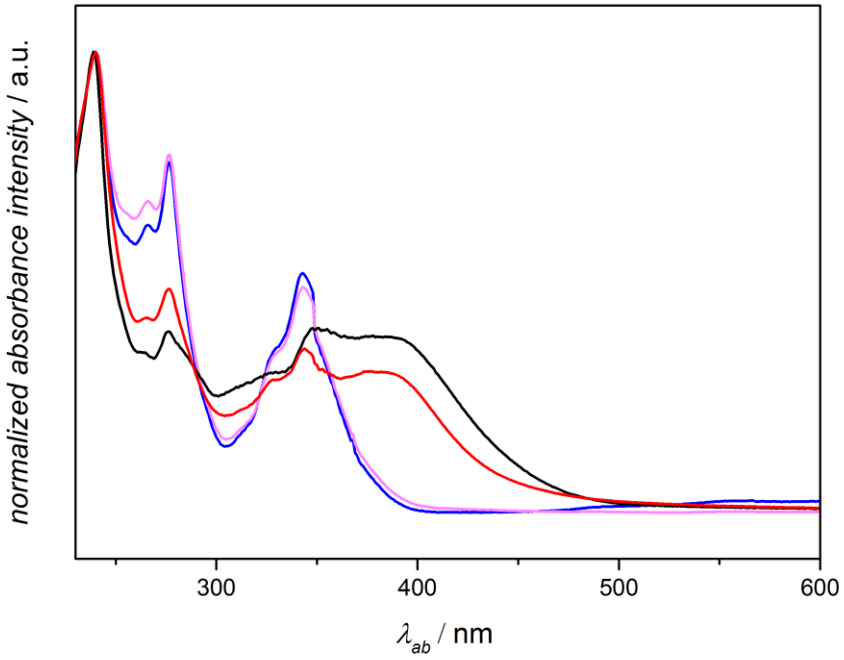

Figure 125 Normalized absorption spectrum of PAT **22** (blue), pyrazoline **23** (black), PAT end capped PCL **A_1** (pink), pyrazoline containing PEG-*b*-PCL block copolymer **C_1** (red) in MeCN.

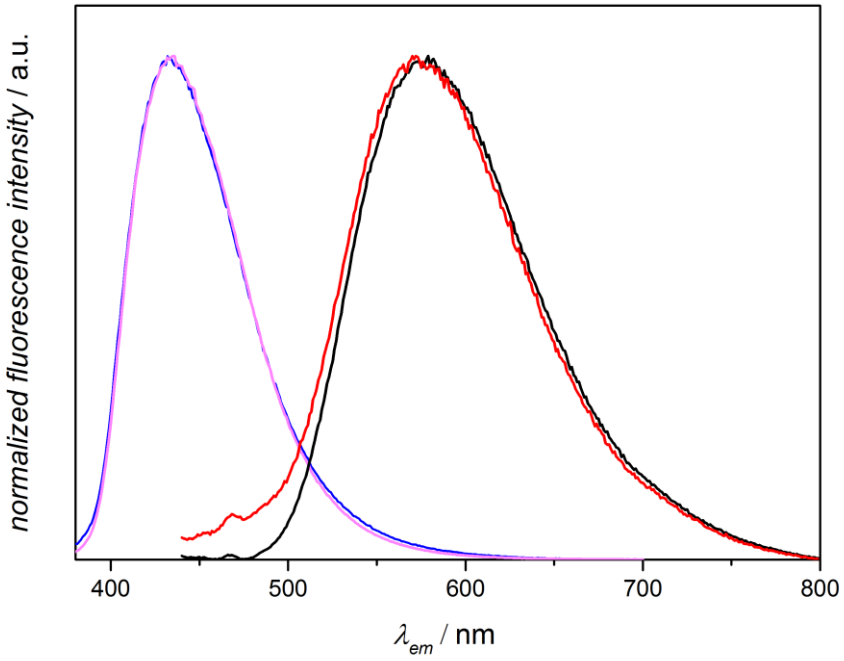

Figure 126 Normalized fluorescence spectrum of PAT **22** (blue), pyrazoline **23** (black), PAT end-capped PCL **A_1** (pink), pyrazoline containing PEG-*b*-PCL block copolymer **C_1** (red) in MeCN.

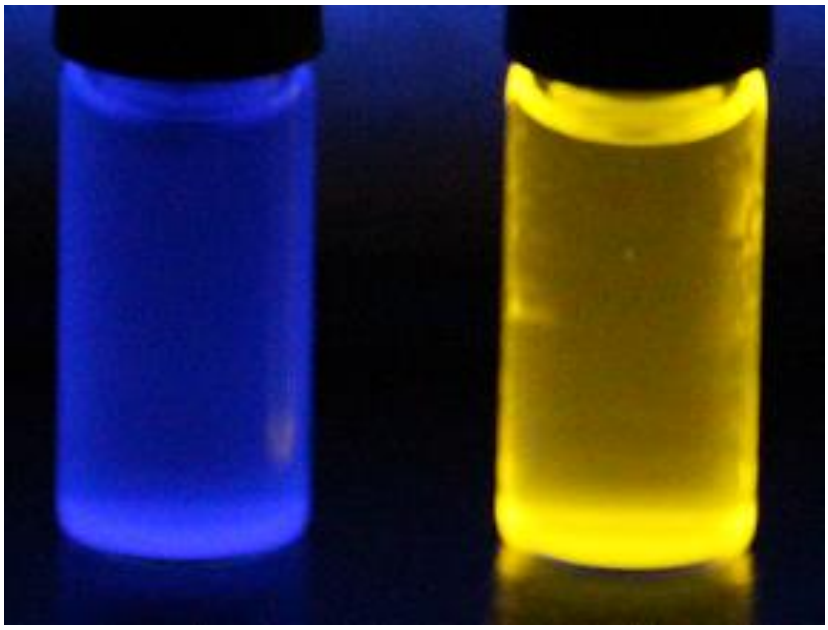

Figure 127 Fluorescence behaviour of PAT **22** (left) and pyrazoline **23** (right) irradiated with a UV hand lamp at 365 nm.

8.3 Near Infrared Photoinduced Coupling Reactions Assisted by Upconversion Nanoparticles

8.3.1 Materials

1-(2-Hydroxyethyl)-1H-pyrrole-2,5-dione **7** was synthesized according to the literature.[290] 11-Hydroxyundecyl 4-(2-(pyren-1-yl)-2H-tetrazol-5-yl)benzoate (PAT) **22** and PAT end capped PCL $\mathbf{A_{1,2}}$ were synthesized according to the literature.[279] Maleimide end capped PEG was purchased from Creative PEGWorks. β-Phase $NaYF_4$:TmYb@$NaYF_4$ UCNPs (core = $NaYF_4$: 0.5 mol % Tm^{3+} : 30 mol % Yb^{3+}; shell = $NaYF_4$) were prepared and fully characterized by TEM, XRD, DLS, and UV-vis as stated in the supporting information of our previous work.[292] The maleimide-PEG-biotin HABA avidin kit was purchased from Thermo Fisher Scientific. All other reagents including the 1 mm thick pork tissue were purchased from commercial suppliers and used without further purification.

8.3.2 Methods and Analytical Instrumentation

^{1}H and ^{13}C NMR spectra were recorded on a 400 MHz spectrometer and referenced to the relevant solvent peak. The employed solvent is listed in the spectrum descriptions.

High-resolution mass spectra (HRMS) were obtained using a Q Exactive (Orbitrap) mass spectrometer (Thermo Fisher Scientific, San Jose, CA, USA) equipped with a HESI II probe. The instrument calibration was carried out in the *m* / *z* range 74 - 1822 using calibration solutions from Thermo Scientific. A constant spray voltage of 4.7 kV and a dimensionless sheath gas of 5 were applied. The capillary temperature and the S-lens RF level were set to 320 °C and 62.0, respectively. The samples were dissolved in a THF:MeOH mixture (volume ratio 3:2) containing 100 µmol of sodium triflate and injected with a flow of 5 $\mu L \cdot min^{-1}$.

Molecular weight determination was performed on a GPC system (PL-GPC 50 Plus, Polymer Laboratories) consisting of an auto injector, a guard column (PLgel Mixed C, 50 × 7.5 mm), three linear columns (PLgel Mixed C, 300 × 7.5 mm, 5 µm bead-size) and a differential refractive index detector using THF as the eluent at 35 °C and a flow rate of 1 $mL \cdot min^{-1}$. The system was calibrated using narrow PS standards (Polymer Standard Service) ranging from 160 to 6×10^{6} $g \cdot mol^{-1}$. Samples were injected from solutions in THF (2 $mg \cdot mL^{-1}$).

Absorption spectra were recorded using a 300 UV / Vis Spectrometer (Varian Cary) in MeCN ($c_{\text{target compound}}$ = 20 $\mu mol \cdot L^{-1}$).

Fluorescence spectra were recorded using a Carry Eclipse fluorescence spectrometer in MeC ($c_{\text{target compound}}$ = 20 $\mu mol \cdot L^{-1}$).

HPLCs were recorded using set-up consisting of a Rheodyne injection valve 7725i with 20 µL loop, an Agilent Technologies Series 1200 degasser, a quarternary gradient pump, a column oven, a photodiode array-detector

(Varian ELSD-Detector 385-LC), a Macherey-Nagel Polactec column (length: 125 mm, diameter: 4 mm, particle size: 5 µm, flow rate: 1 mL·min^{-1}, temperature: 20 °C). Gradient: starting with THF / acetonitrile / H_2O + 0.1 % trifluoroacetic acid 10 / 10 / 95 vol. % ramping within 10 min up to 80 / 20 / 20 vol. %.

Irradiation

The irradiation source was a diode laser with 974 nm emission (device type P976MF, Photon Tec Berlin GmbH). For all irradiation experiments, the employed setup is illustrated in Figure 128. For the tissue shielded irradiation, a piece of tissue was placed between the laser and sample solution. To minimize overheating of the tissue, pulsed mode of the laser was used ('switch on' time = 5 s, 'switch off' time = 3 s).

Details of the laser source: The diode laser was equipped with an adjustable fiber collimator (Changchun New Industries Optoelectronics Technology). The output power of the diode laser for inducing the photoreactions was fixed at 14 W, which was controlled by a tabletop laser driver (device type ds11-la12v08-pa08v16-t9519-254-282, OsTech GmbH i.G.). The output power of the diode laser was measured using an optical power meter (model 407A, Spectra-Physics Corp.).

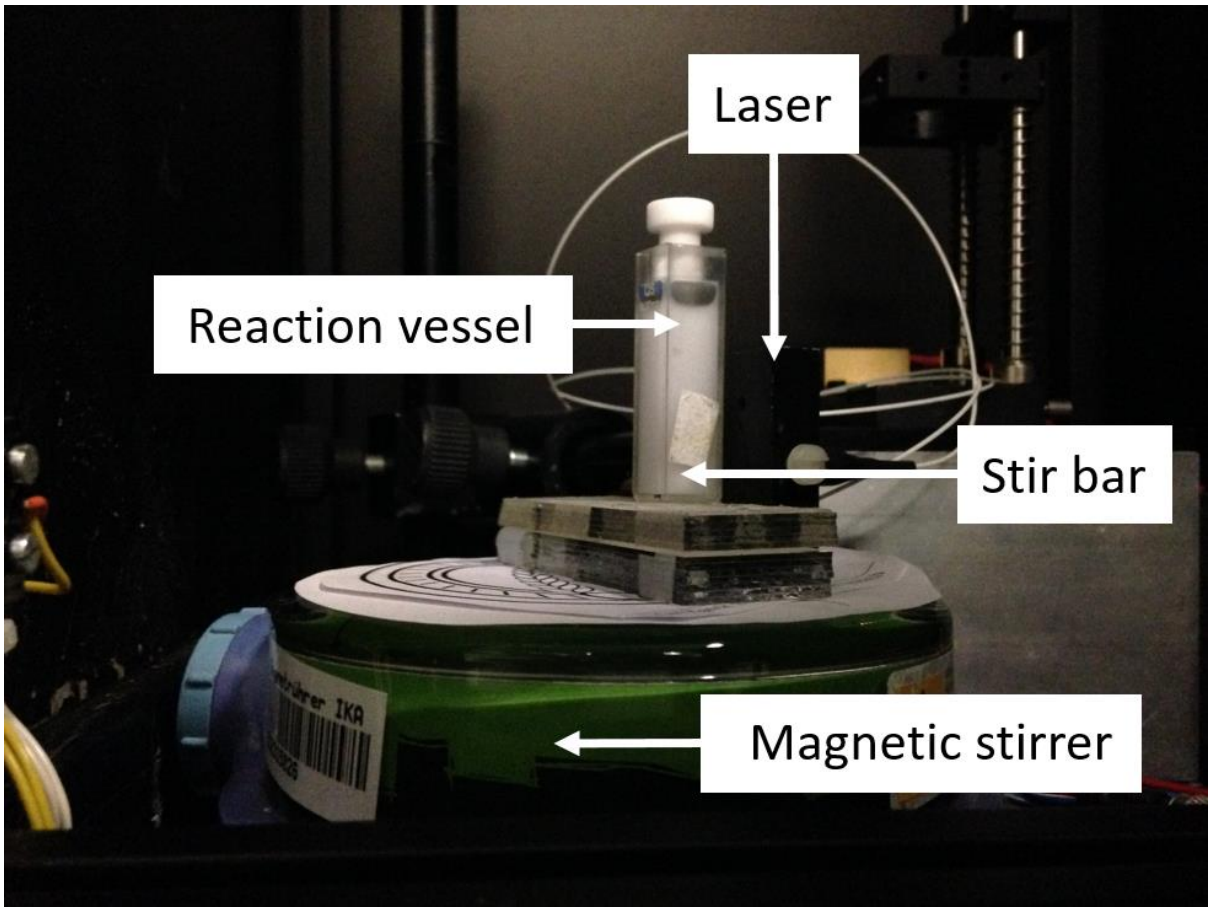

Figure 128 Experimental set up for the upconversion photoinduced coupling chemistry.

8.3.3 Synthesis

11-Hydroxyundecyl 4-(5-(2-hydroxyethyl)-4,6-dioxo-1-(pyren-1-yl)-1,3a,4,5,6,6a-hexahydropyrrolo [3,4-c]pyrazol-3-yl)benzoate (23)

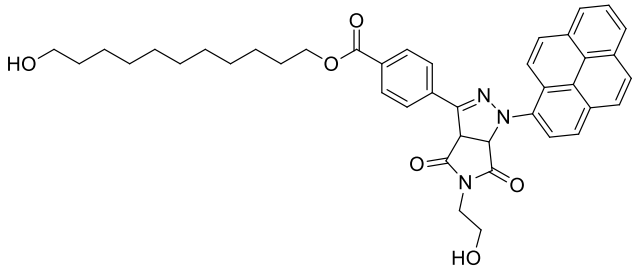

The PAT molecule **22** (0.35 mM, 1 eq.) and hydroxyl funtionalized maleimide **7** (0.38 mM, 1.1 eq.) were mixed in MeCN (3 mL) containing 3.3 $mg \cdot mL^{-1}$ UCNPs. The mixture was magnetically stirred during irradiation by the NIR laser. HRMS $[M + Na]^+$ *m* / *z*: calcd for $C_{41}H_{43}N_3NaO_6$ 696.3050, found 696.3058.

Polymer End Group Modification and Formation of Block Copolymers

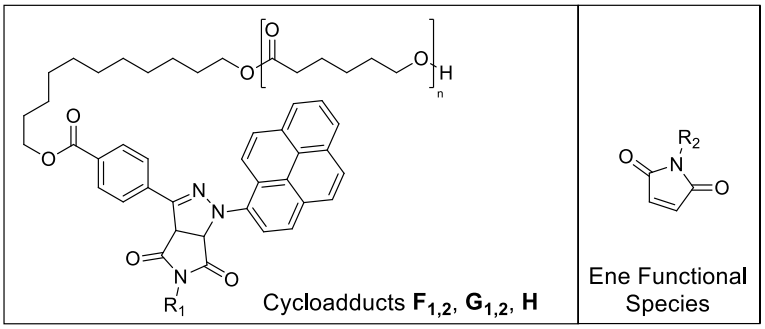

Label	R	
$F_{1,2}$	1	
$G_{1,2}$	1	
E_1	2	
J	2	
H	1	

Figure 129 Overview over the structures of cycloadducts $\mathbf{F_{1,2}}$ and $\mathbf{G_{1,2}}$. Refer to Section 8.3.4) for synthesis of **H**.

The PAT functional PCL was mixed with hydroxyl functionalized maleimide in MeCN (3 mL) containing UCNPs (without tissue, 33 mg·mL^{-1}; with tissue, 50 mg mL^{-1}). Subsequently, the mixture was magnetically stirred during NIR irradiation. For the irradiation experiment with tissue, a pork tissue (1 mm thickness) was placed between the NIR laser and the sample. To avoid overheating, pulsed irradiation was used (5 seconds irradiation time and 3 seconds dark time). For the polymer-polymer coupling experiment, the same procedure was used. ^{1}H NMR ($CDCl_3$) $\mathbf{F_1}$ δ = 8.54 - 7.96 (m, 13 H), 5.68 - 5.61 (m, 1 H), 5.12 - 5.05 (m, 1 H), 4.40 - 4.30 (m, 2 H), 4.12 - 4.04 (m, polymer backbone), 3.85 - 3.60 (m, 6 H), 2.37 - 2.25 (m, polymer backbone), 1.86 - 1.21 (m, 18 H + polymer backbone); $\mathbf{F_2}$ δ = 8.53 - 7.94 (m, 13 H), 5.70 - 5.60 (m, 1 H), 5.14 - 5.05 (m, 1 H), 4.40 - 4.30 (m, 2 H), 4.12 - 4.04 (m, polymer backbone), 3.84 - 3.62 (m, 6 H), 2.39 - 2.25

(m, polymer backbone), 1.86 - 1.19 (m, 18 H + polymer backbone); **G_1** δ = 8.59 - 7.97 (m, 13 H), 5.74 - 5.67 (m, 1 H), 5.15 - 5.09 (m, 1 H), 4.41 - 4.22 (m, 2 H), 4.05 - 3.85 (m, polymer back bone (PCL)), 3.72 - 3.50 (m, 6 H + polymer back bone (PEG)), 3.47 - 3.43 (m, 2 H), 3.39 - 3.31 (m, 5 H), 2.38 - 2.24 (m, polymer backbone (PCL)), 1.92 - 1.20 (m, 18 H + polymer back bone (PCL)); **G_2** δ = 8.60 - 7.95 (m, 13 H), 5.74 - 5.65 (m, 1 H), 5.14 - 5.09 (m, 1 H), 4.41 - 4.21 (m, 2 H), 4.04 - 3.85 (m, polymer backbone (PCL)), 3.74 - 3.50 (m, 6 H + polymer backbone (PEG)), 3.45 - 3.43 (m, 2 H), 3.39 - 3.30 (m, 5 H), 2.38 - 2.21 (m, polymer backbone (PCL)), 1.92 - 1.21 (m, 18 H + polymer backbone (PCL)).

Table 7 M_n and $Đ$ of PAT capped PCL **$A_{1,2}$** before and after coupling with maleimide **7** or maleimide end capped PEG to form **$F_{1,2}$** or **$G_{1,2}$**. All reactions were carried out in MeCN.

Lable	PAT end capped PCL	c_{PCL} / mmol·L^{-1}	c_{ene} / mmol·L^{-1}	Ene capped polymer	$Đ_{ene}$	$M_n^{[c]}{}_{ene}$ / kDa	$Đ_{cyclo\ adduct}$	$M_n^{[c]}{}_{cyclo\ adduct}$ / kDa
F_1[a]	A_1	0.5	0.75	-	-	-	1.09	2.2
F_2[a]	A_1	0.5	0.75	-	-	-	1.09	2.2
G_1[b]	A_2	2.4	3.6	PEG E_1	1.o3	3.3	1.09	7.9
G_2[b]	A_2	2.4	3.6	PEG E_1	1.03	3.3	1.09	8.0

[a] The cycloadduct was analyzed without any further purification. [b] The crude product was dissolved in ethyl acetate (50 mL) extracted with 1 M hydrochloric acid (4 × 100 mL) and dried over $NaSO_4$. Ethyl acetate was removed under reduced pressure. The residual solid was dissolved in 50 mL DCM and extracted with 1 M hydrochloric acid (1 × 100 mL). [c] M_n was determined by GPC using PS calibration standards.

Table 8 Sum formula, the exact masses of the experimentally obtained data, theoretical *m* / *z* values and the deviation of both for PAT end capped PCL **A_1** and cycloadducts **$F_{1,2}$**.

Label	Sum formula	m / z_{exp}	m / z_{theo}	Δ m / z
A_1	$[C_{83}H_{116}N_4NaO_{19}]^+$	1495.815	1495.813	0.002
B_1	$[C_{83}H_{113}N_3NaO_{20}]^+$	1494.787	1494.789	0.002
B_2	$[C_{83}\ H_{113}N_3NaO_{20}]^+$	1494.787	1494.781	0.006

Macromolecular Cycloadduct (F_1)

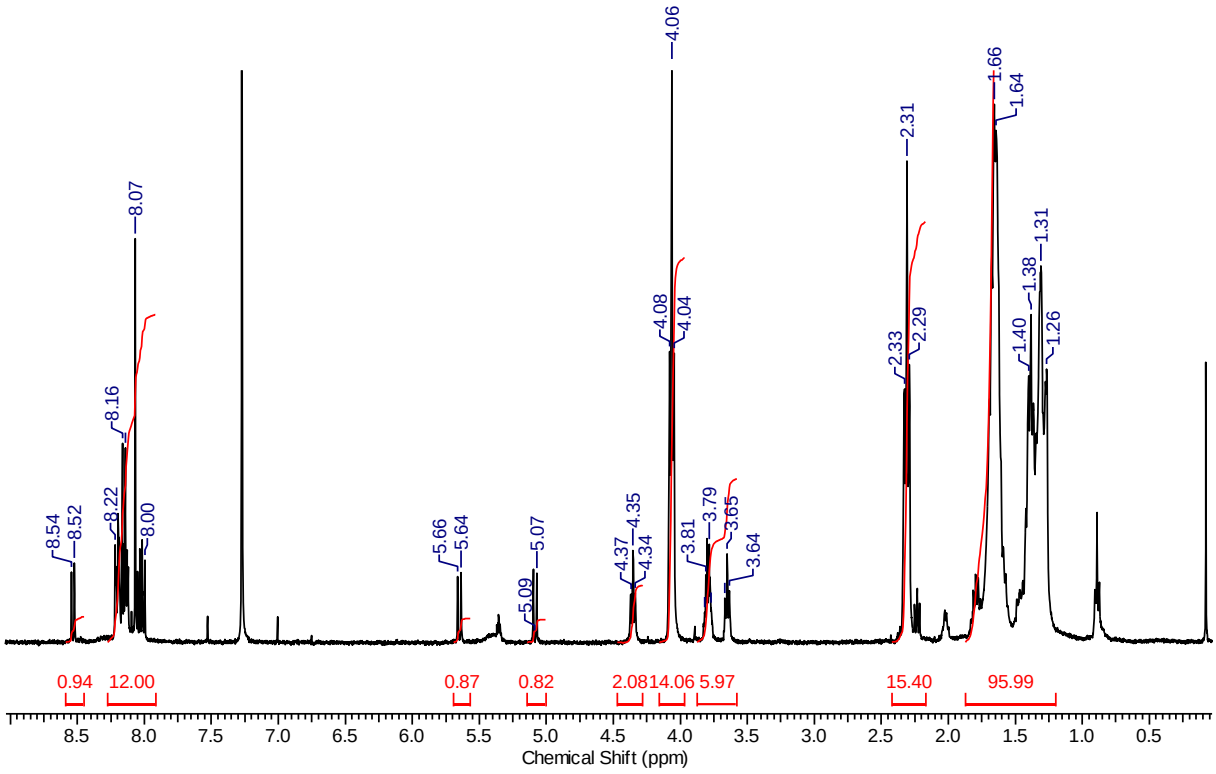

Figure 130 ^{1}H NMR (400 MHz, $CDCl_3$) spectrum of the cycloadduct **F_1**.

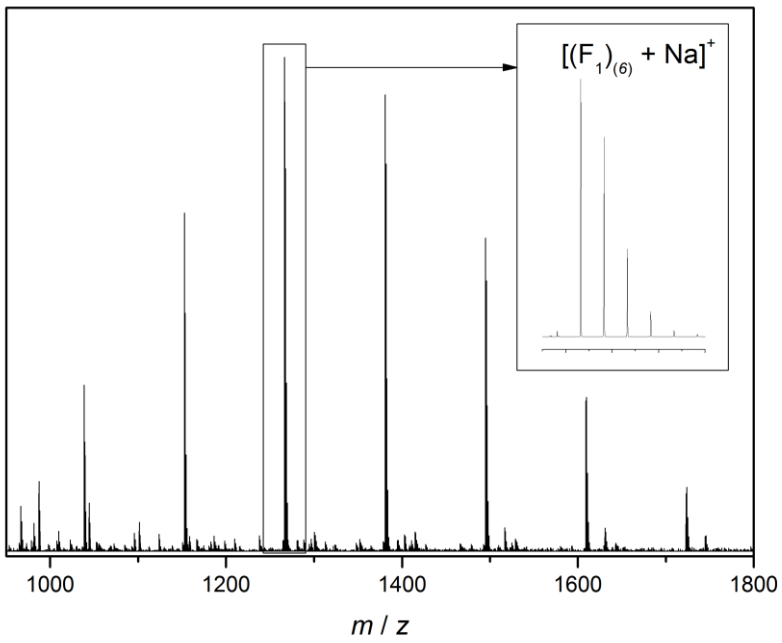

Figure 131 Magnified view into the region of 950 - 1800 *m* / *z* of the ESI-MS spectrum of cycloadduct **F₁**. Signals repeat in intervals of 114.14 Dalton. Sodium adduct of PAT end-capped PCL, $[(F_1)_{(6)} + Na]^+$.

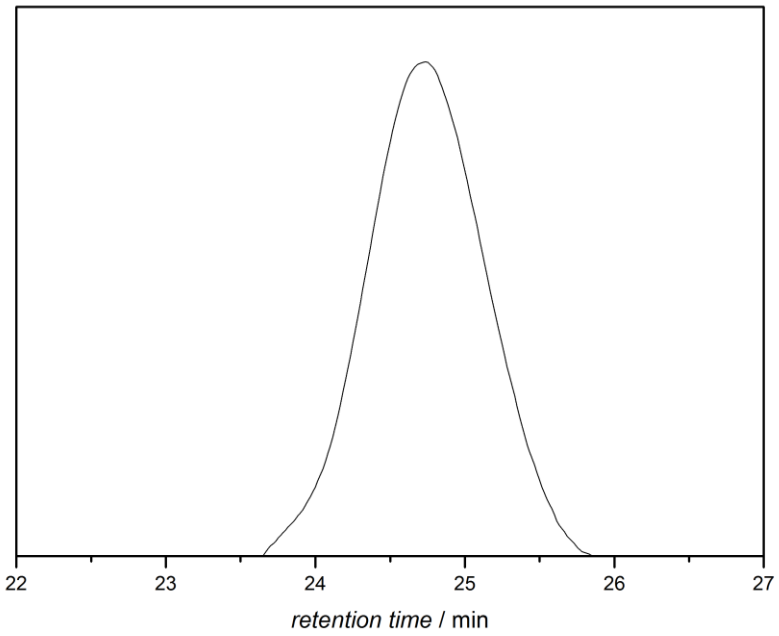

Figure 132 GPC trace of the cycloadduct **F₁** in THF (Refer to Table 7 for corresponding M_n and $Đ$).

Macromolecular Cycloadduct (F_2)

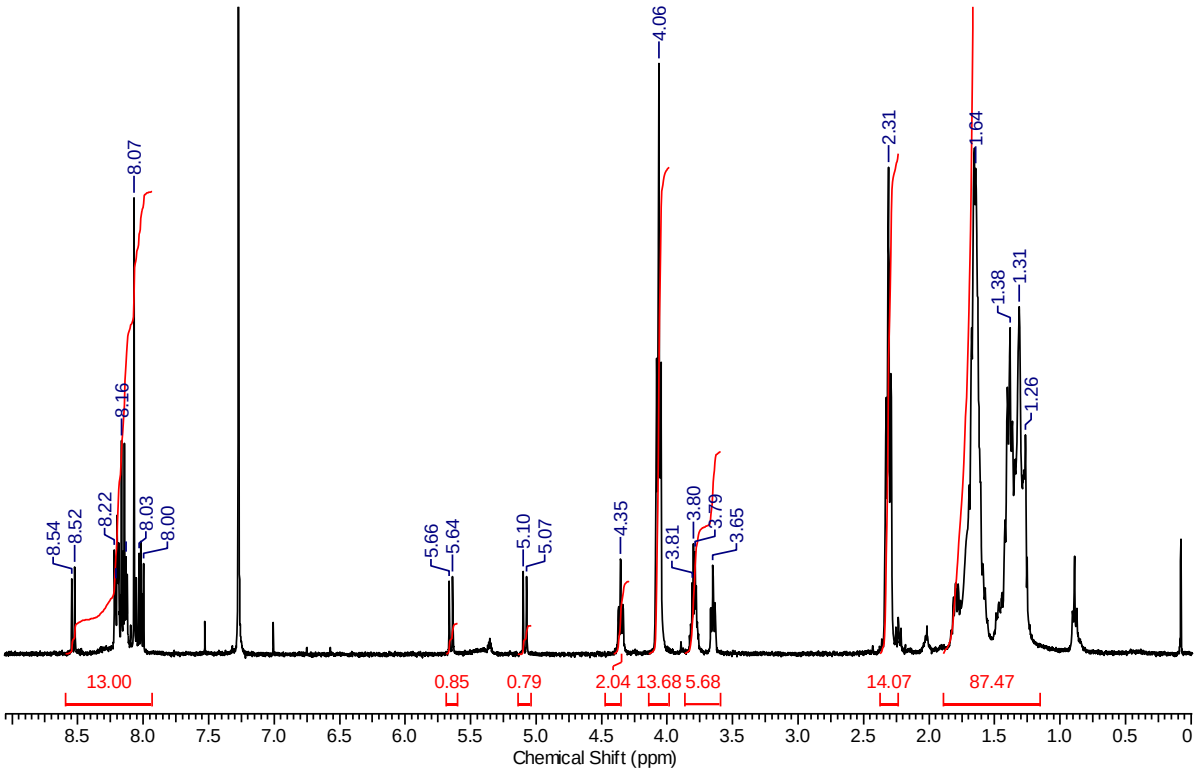

Figure 133 ^{1}H NMR (400 MHz, $CDCl_3$) spectrum of the cycloadduct **F_2**.

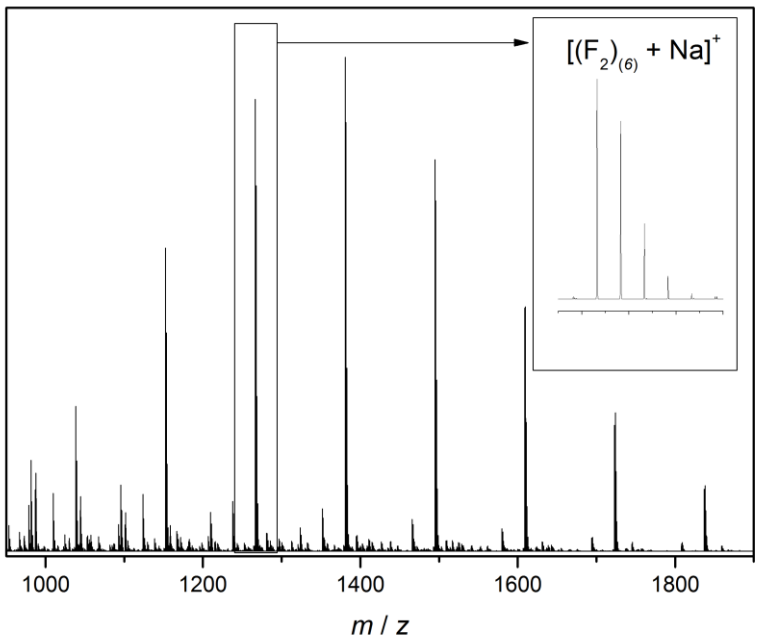

Figure 134 Magnified view into the region of 950 - 1900 *m / z* of the ESI-MS spectrum of cycloadduct **F_2**. Signals repeat in intervals of 114.14 Dalton. Sodium adduct of PAT end-capped PCL, $[(F_2)_{(6)} + Na]^+$.

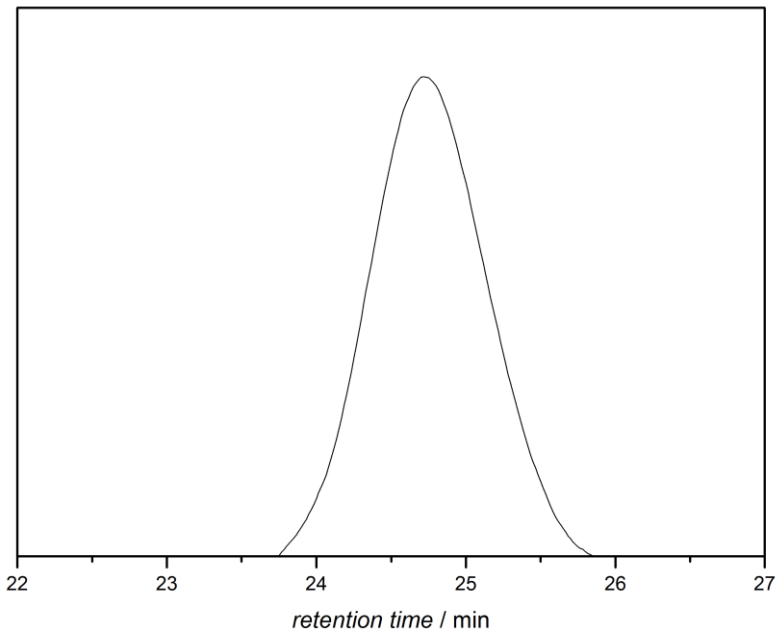

Figure 135 GPC trace of the cycloadduct **F₂** in THF (Refer to Table 7 for corresponding M_n and $Đ$).

Macromolecular Cycloadduct (G_1)

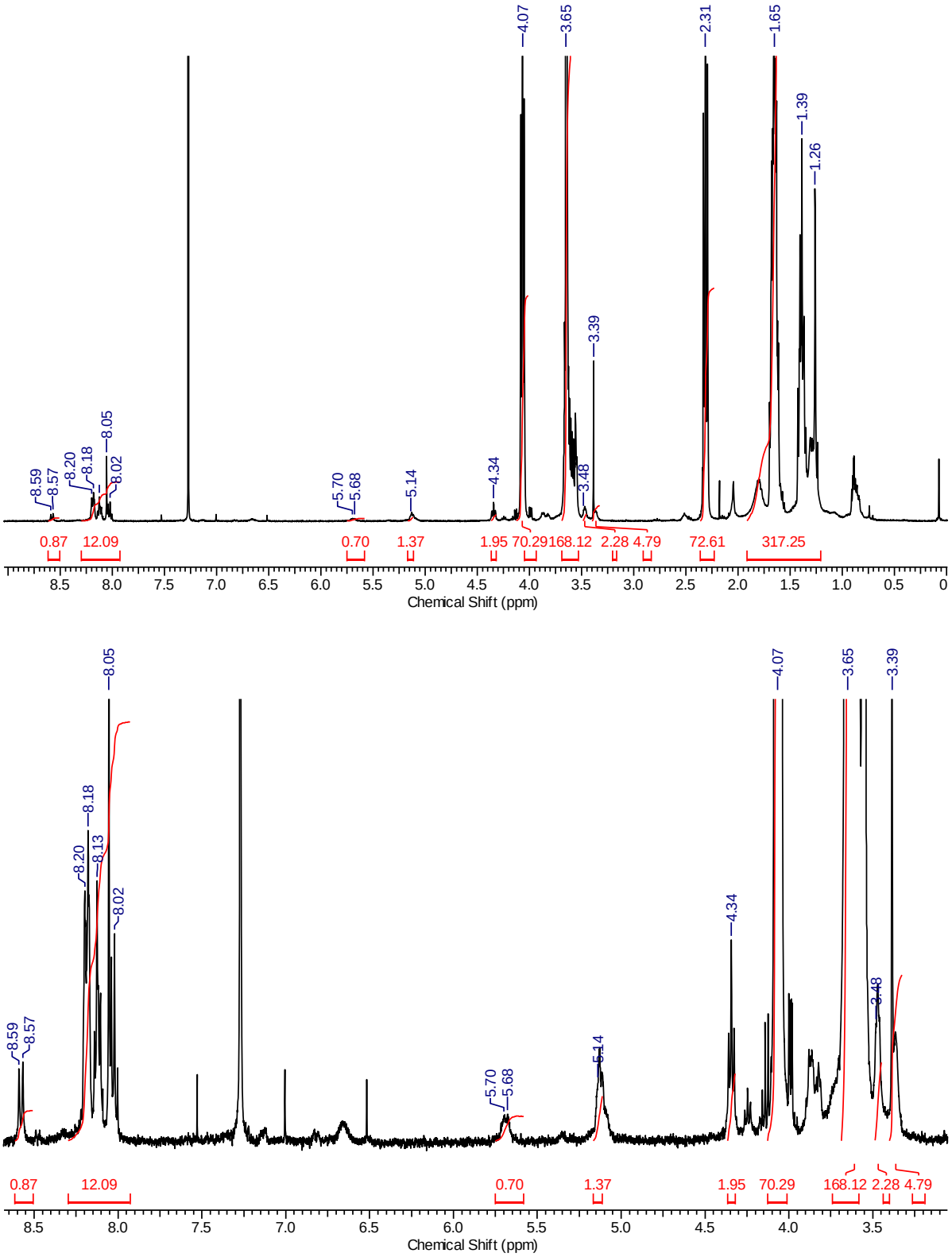

Figure 136 ^{1}H NMR (400 MHz, $CDCl_3$) spectrum of the cycloadduct **G_1**. Full spectrum of the PCL-*b*-PEG block copolymer (top) and magnification of the 8.7 - 2.9 ppm region (bottom).

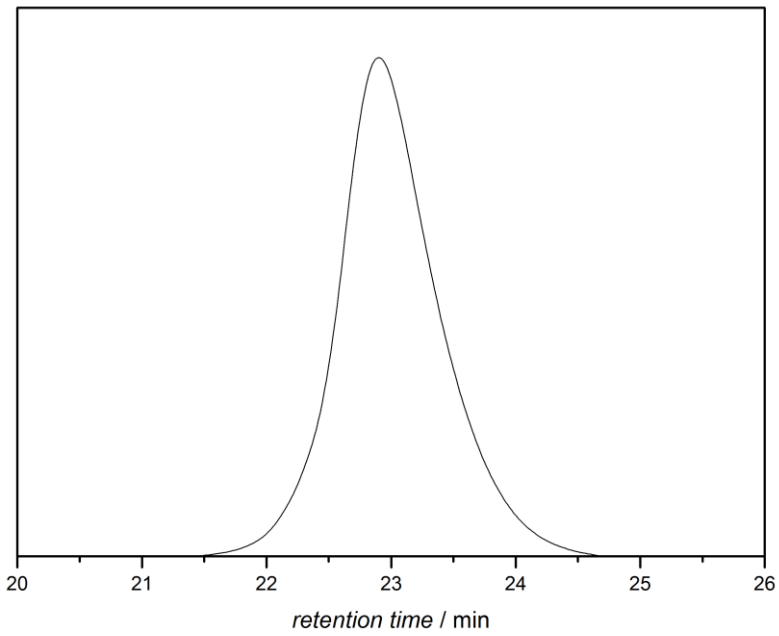

Figure 137 GPC of the cycloadduct **G_1** in THF (Refer to Table 7 for corresponding M_n and $Đ$).

Macromolecular Cycloadduct (G_2)

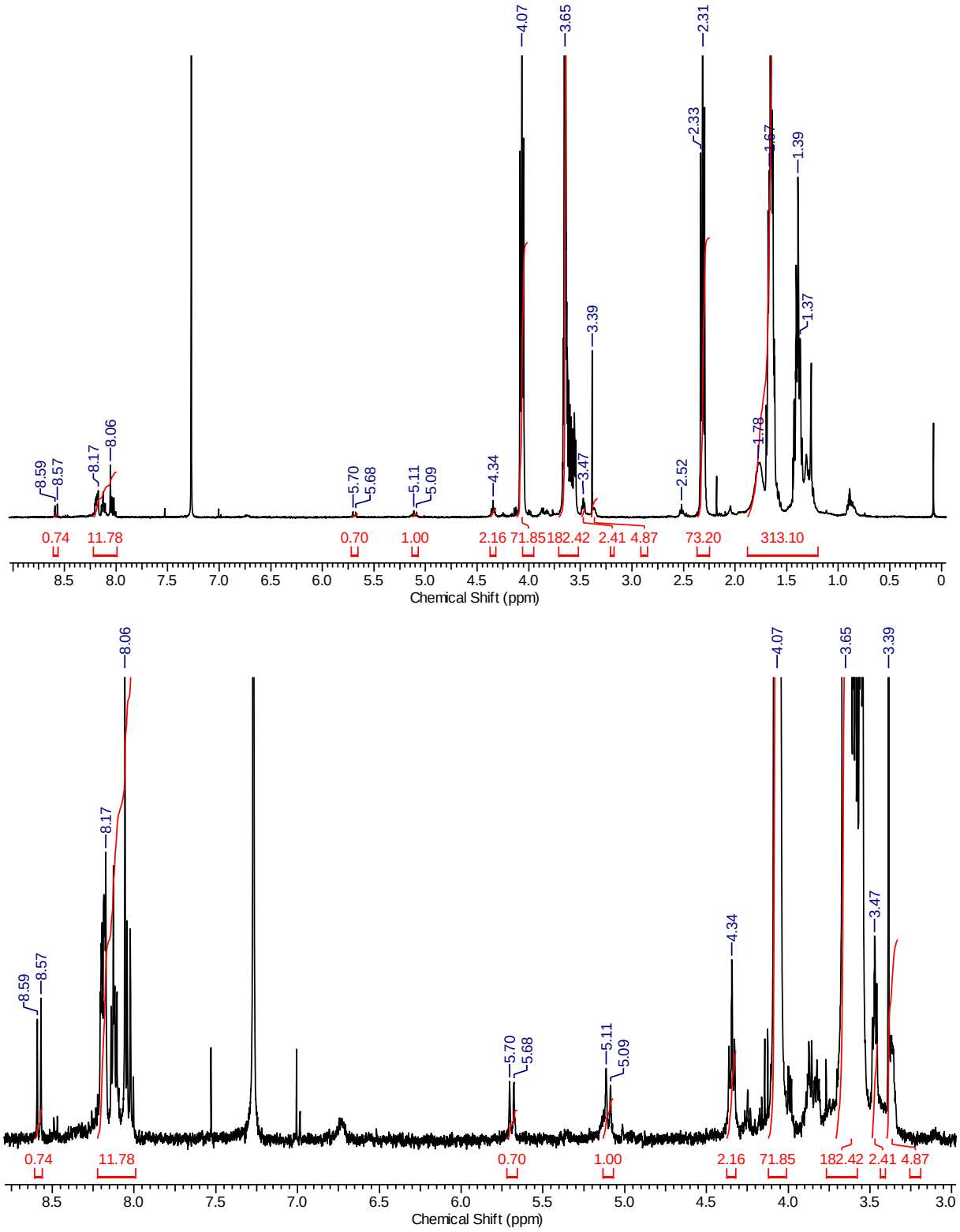

Figure 138 ^{1}H NMR (400 MHz, $CDCl_3$) spectrum of the cycloadduct **G_2**. Full spectrum of the PCL-*b*-PEG block copolymer (top) and magnification of the 8.7 - 2.9 ppm region (bottom).

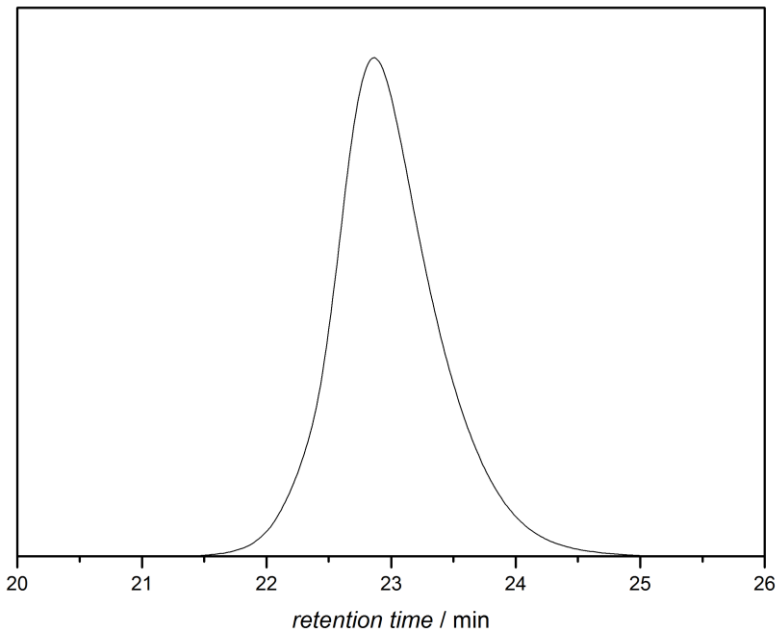

Figure 139 GPC of the cycloadduct **G_2** in THF (see Table 7 for the corresponding M_n and $Đ$).

8.3.4 Spectroscopic Data

Kinetic Studies on Formation of Cycloadduct (23)

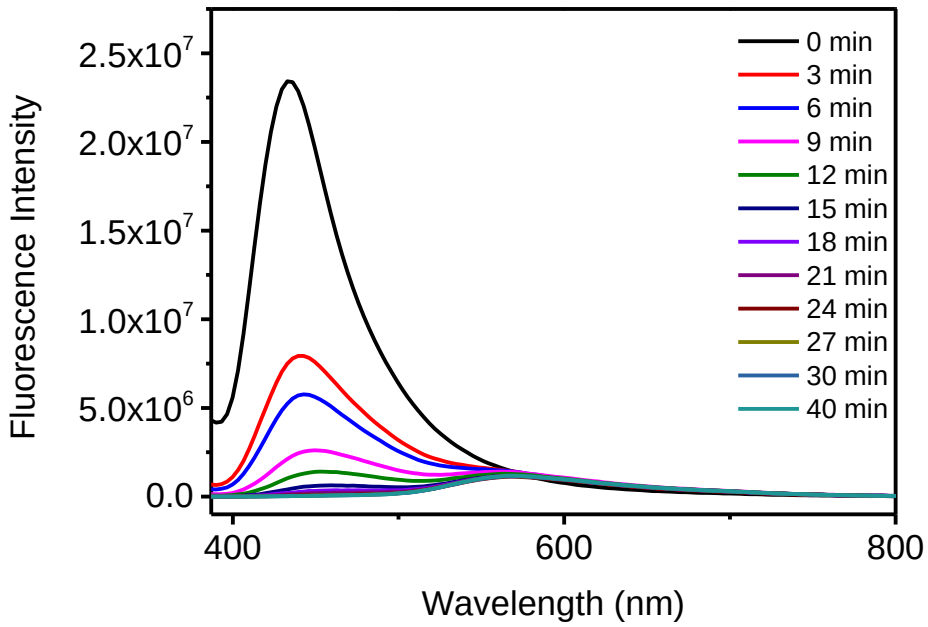

Figure 140 Fluorescence trace of the upconversion assisted coupling reaction of PAT **22** and hydroxy functionalized maleimide **7** (c_{PAT} = 0.35 mM, PAT:HFM = 1:1.1, MeCN, $c_{(UCNPs)}$ = 3.3 mg mL^{-1}, λ_{ex} = 365 nm).

Spectroscopic Data of Tetrazole (22), Pyrazoline (23) and Macromolecular Cycloadducts ($F_{1,2}$) and ($G_{1,2}$).

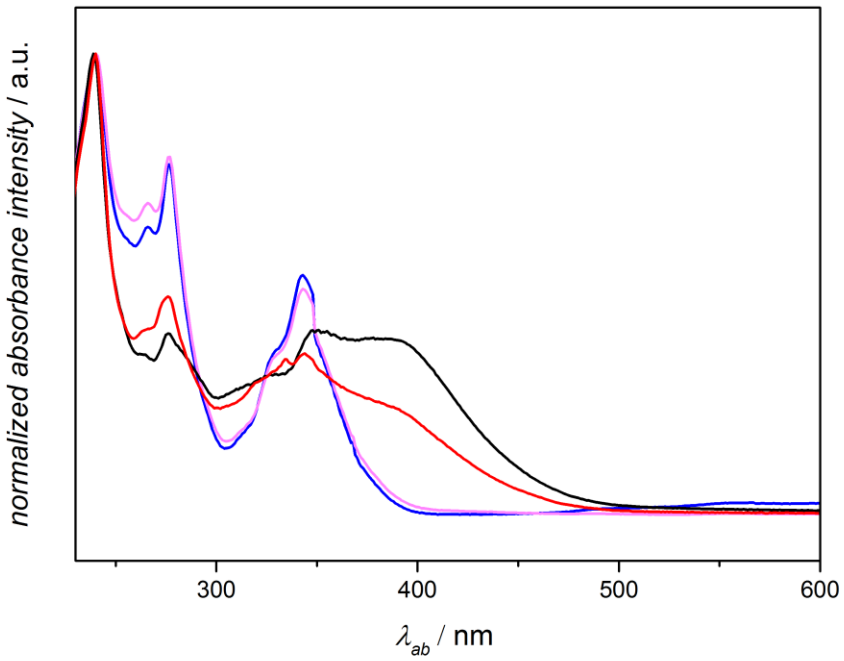

Figure 141 Normalized absorption spectra of PAT **22** (blue), pyrazoline **23** (black), PAT end-capped PCL **A_2** (pink) and pyrazoline containing PCL **F_1** (red) in MeCN.

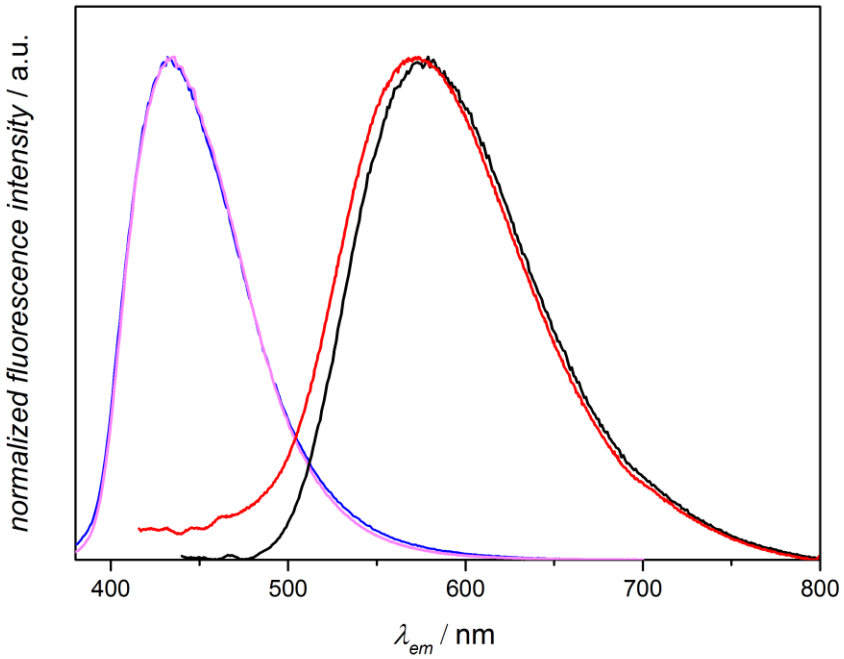

Figure 142 Normalized fluorescence spectra of PAT **22** (blue), pyrazoline **23** (black), PAT end-capped PCL **A_2** (pink), pyrazoline containing PCL **G_1** (red) in MeCN. λ_{ex} = 365 nm for **22** and **23**, λ_{ex} = 400 nm for **A_2** and **G_1**.

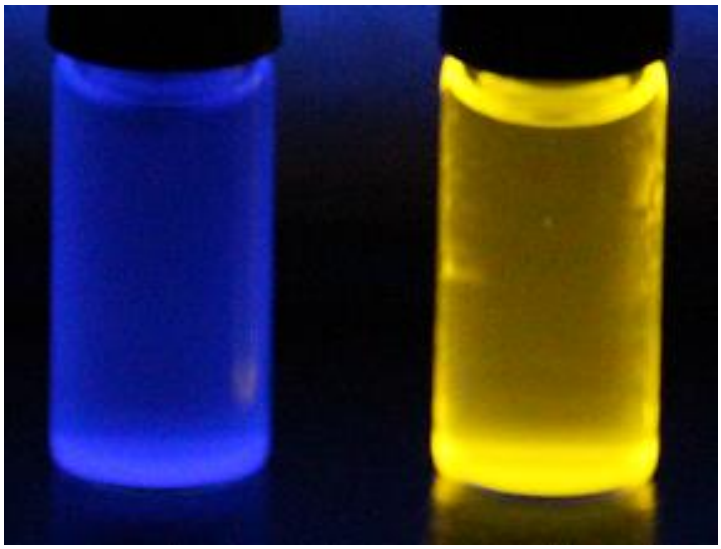

Figure 143 Fluorescence behaviour of PAT **22** (left) and pyrazoline **23** (right) irradiated with a UV hand lamp at 365 nm.

Biotin Related Studies

Preparation of the Biotin End Capped PEG-b-PCL Block F

PAT functional PCL **A_2** (1 mM) was mixed with maleimide end capped, biotin functional PEG (1.5 mM) in MeCN (3 mL) containing UCNPs (50 mg·mL^{-1}). The mixture was magnetically stirred during irradiation with NIR light. A 1 mm thick pork tissue was placed between the NIR source and the sample solution. NIR irradiation was pulsed (with 5 seconds on and 3 seconds off).

Measurement of Biotin Activity

The bio-activity of biotin was measured according to the instructions of the producer (Instructions, Pierce Biotin Quantification Kit, Thermo Scientific).[3] the HABA / Avidin premix was equilibrated at ambient temperature. 100 µL of ultrapure water was added to one microtube (standard kit from Thermo Fisher, catalogue No. 28005) of the HABA / Avidin Premix. 20 µL of the HABA / Avidin Premix solution was added to the PBS (pH = 7.2, V = 2 mL) in a well. The well was placed on an orbital shaker. The absorbance of the solution in the well was detected. 30 µL of biotin end capped PEG **J** or biotin end capped PEG-*b*-PCL block **H** (0.2 mM) were added to the well containing the HABA / avidin reaction mixture. The absorbance of the solution was detected again. The procedure was repeated for 0, 6 and 9 µM solutions of biotin containing compound.

Biotin and avidin (or streptavidin) bind non-covalently with a higher binding affinity than most antigen-antibody interactions. HABA / avidin (4'-hydroxyazobenzene-2- carboxylic acid) complexes show strong absorption at 500 nm. If biotin containing species are added to the HABA / avidin complex, HABA is replaced by biotin, since biotin features a much higher binding affinity towards avidin. Therefore, the HABA absorption efficiency will decrease due to its poor solubility in aqueous solution. Quantification

of the biotin content can be achieved by recording the absorption spectrum change before and after addition of biotin.

Calculation of the number of biotin moiety (activity) after the reaction

Biotin activity = ΔA_{500} (**H**) / ΔA_{500} (**J**) · 100 % = 0.08 / 0.09 · 100 % = 88 %

ΔA_{500} (**J**) = Absorption value (500 nm) of HABA / avidin after addition of **H** - Absorption value (500 nm) of HABA / avidin

ΔA_{500} (**F**) = Absorption value (500 nm) of HABA / avidin after addition of **F** - Absorption value (500 nm) of HABA / avidin

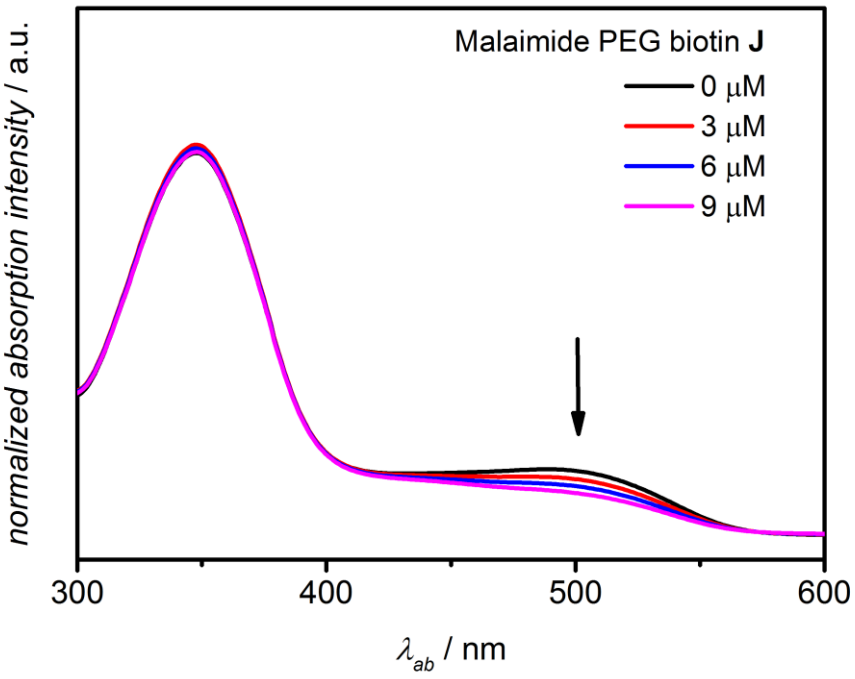

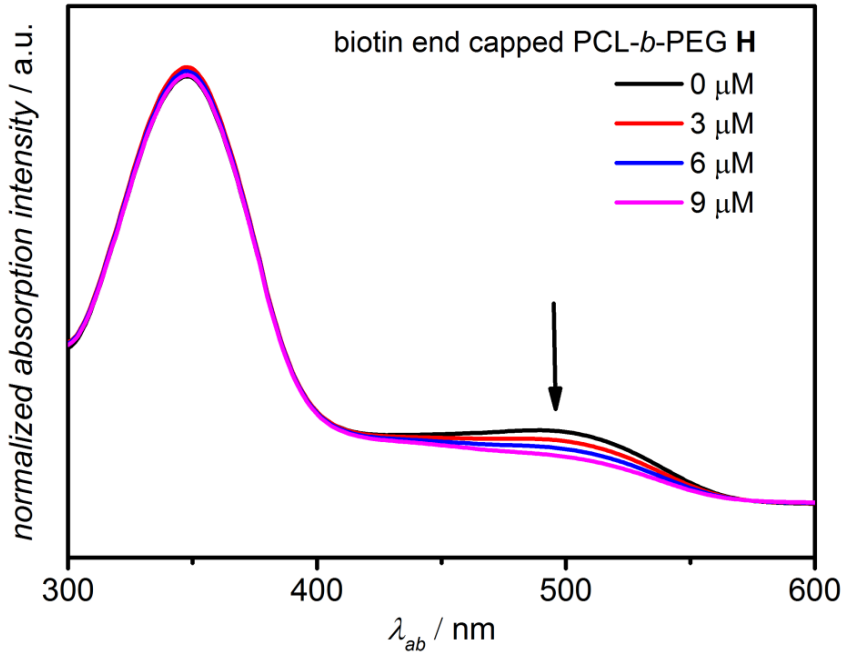

Figure 341 Absorption spectra of HABA / avidin mixtures before and after adding of biotin containing solutions **J** and **H** in concentration range 0 – 9 µM. The arrow illustrates the absorption band used for the biotin activity calculations.

8.4 λ-Orthogonal Photoligations, Novel Avenue for Advanced Surface Patterning

8.4.1 Materials

1-(2-Hydroxyethyl)-1H-pyrrole-2,5-dione was synthesized according to the literature[290] 11-hydroxyundecyl 4-(2-(pyren-1-yl)-2H-tetrazol-5-yl)benzoate PAT **22** was synthesized according to the procedure in the Section 8.2.3. 2-(2,5-dioxo-2,5-dihydro-1H-pyrrol-1-yl)ethyl 2-bromo-2-methylpropanoate **32** was synthesized according to the literature. All other reagents were purchased from commercial suppliers and used without further purification.

8.4.2 Methods and Analytical Results

^{1}H and ^{13}C NMR spectra were recorded on a 400 MHz spectrometer and referenced to the relevant solvent peak. The employed solvent is listed in the spectrum descriptions.

High-resolution mass spectra (HRMS) were obtained using a Q Exactive (Orbitrap) mass spectrometer (Thermo Fisher Scientific, San Jose, CA, USA) equipped with a HESI II probe. The instrument calibration was carried out in the *m* / *z* range 74 - 1822 using calibration solutions from Thermo Scientific. A constant spray voltage of 4.7 kV and a dimensionless sheath gas of 5 were applied. The capillary temperature and the S-lens RF level were set to 320 °C and 62.0, respectively. The samples were dissolved in a THF:MeOH mixture (volume ratio 3:2) containing 100 µmol of sodium triflate and injected with a flow of 5 $\mu L \cdot min^{-1}$.

Absorption spectra were recorded using a 300 UV / Vis Spectrometer (Varian Cary) in MeCN ($c_{\text{target compound}}$ = 20 $\mu mol \cdot L^{-1}$).

ToF-SIMS (Time-of-Flight Secondary Ion Mass Spectrometry) was performed on a TOF.SIMS5 instrument (ION-TOF GmbH, Münster, Germany). This spectrometer is equipped with a bismuth cluster primary ion source and a reflectron type time-of-flight analyzer. UHV base pressure was < 5×10^{-9} mbar. For high mass resolution the Bi source was operated in the "high current bunched" mode providing short Bi_3^+ primary ion pulses at 25 keV energy and a lateral resolution of approx. 4 µm. The short pulse length of 1.3 ns allowed for high mass resolution. For imaging large fields of view the sample stage and the primary beam were scanned. Usually for 5 × 4 mm fields of view 500 × 400 individual data points were recorded with 30 scans and 4 adjacent points were binned to increase the dynamic range. Primary ion doses were kept below 10^{11} ions / cm^2 (static SIMS limit) for all measurements. Spectra were calibrated on the omnipresent C^-, CH^-, CH_2^-, C_2^-, C_3^-; or on the C^+, CH^+, CH_2^+, CH_3^+, and Si^+ peaks. Based on these datasets the chemical assignments for characteristic fragments

were determined. For the depth profiling of patterned samples a dual beam analysis was performed: The primary ion source was again operated in "burst alignment" mode with a scanned area of 50 × 50 μm^2 (256 × 256 data points) and a sputter gun (operated with Cs ions, 500 eV, scanned over a concentric field of 500 × 500 μm^2) was applied to erode the sample. The obtained image stack was split in two separate fields of interest, the first comprising the HDT SAM areas of the sample, the second comprising the MUD areas. From both parts the Au^- signals versus sputter time were extracted. Images larger than the maximum deflection range of the primary ion gun of 500 × 500 μm^2 were obtained using the manipulator stage scan mode.

Irradiation

NITEC reactions at 410-420 nm

NITEC reactions in solution at 410 – 420 nm were performed using the set up described in the Section 8.2.3.

Surface based NITEC reactions at 410 – 420 nm were performed using following set up:

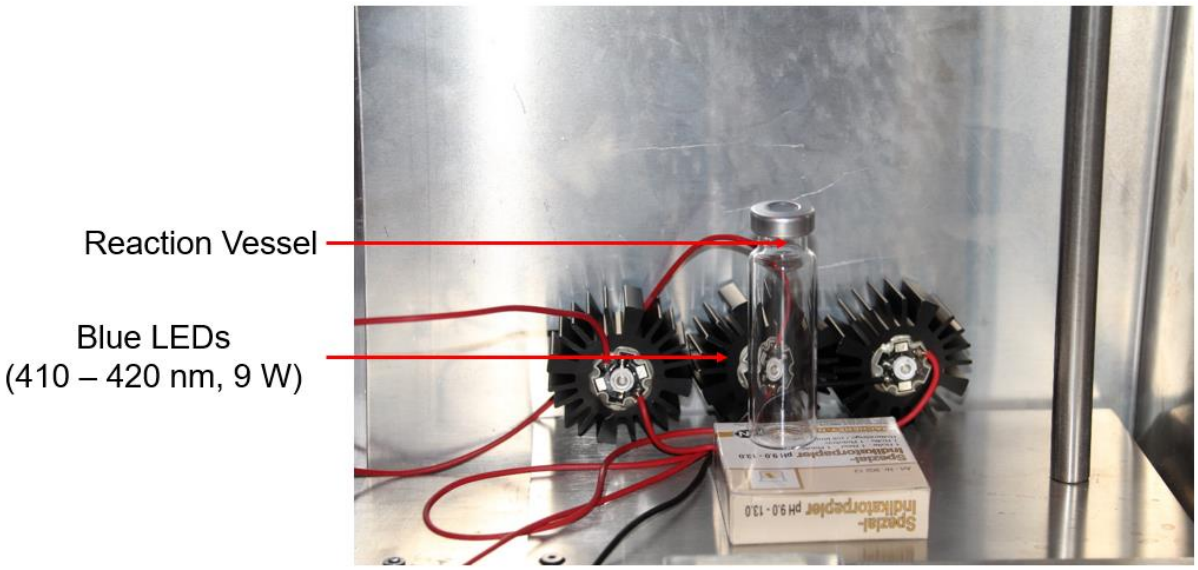

Figure 144 Set up for the surface based NITEC reaction at 410 – 420 nm. The mask holder inclusive the mask was placed into the reaction vessel in the presence of the appropriate dipolarophile containing solvent.

NITEC reactions at 320 nm

NITEC reactions in solution at 320 nm were performed using following set up:

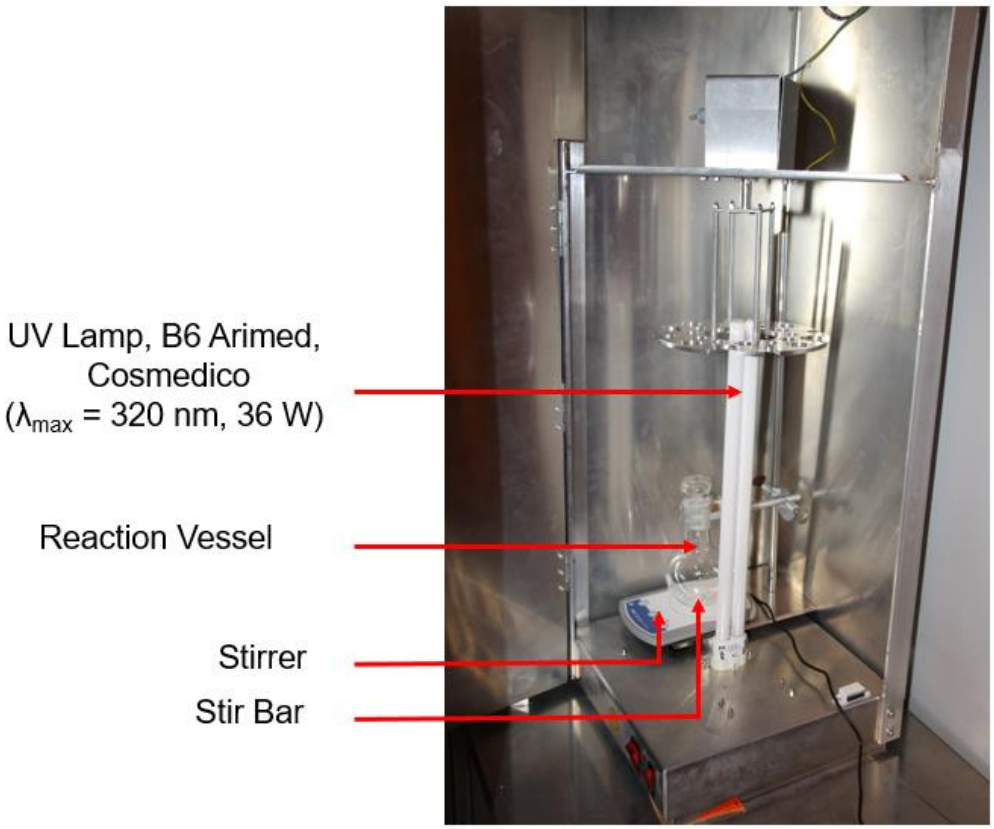

Figure 145 Set up for the solution based NITEC reaction at 320 nm.

NITEC reactions on the surface at 320 nm were performed using following set up:

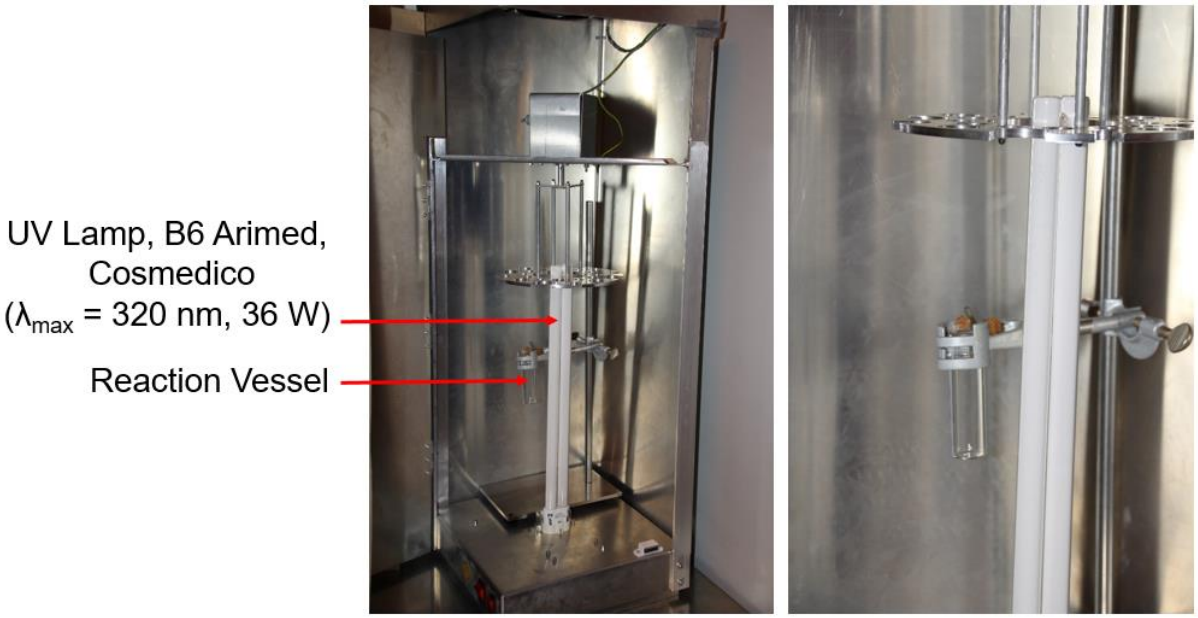

Figure 146 Set up for the surface based NITEC reaction at 320 nm. The mask holder inclusive the mask was placed into the reaction vessel in presence of the appropriate dipolarophile containing solvent.

8.4.3 Synthesis in Solution

11-Hydroxyundecyl 4-(2-(4-methoxyphenyl)-2H-tetrazol-5-yl)-benzoate (37)

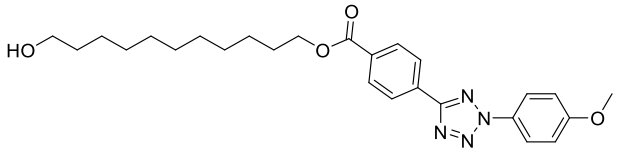

A mixture of 11-hydroxyundecyl 4-formylbenzoate **24** (1725.0 mg, 5.39 mmol) and 4-methylbenzenesulfonohydrazide (1004.2 mg, 5.39 mmol) in 50 mL EtOH were stirred at ambient temperature for 5 h. The solvent was removed under reduced pressure. The obtained solid was dissolved in 30 mL pyridine (solvent A). In parallel p-anisidine (350.0 mg, 2.85 mmol) was dissolved in 14 mL of solvent mixture (HCl / H_2O / EtOH in ratio 1:3:3) under Ar and cooled to 0 °C. A solution of $NaNO_2$ (0.2 mg, 2.85 mmol) in 2 mL H_2O was added. The reaction mixture was stirred for 10 min at 0°C (solvent B). The solvent B was added to solution A at room temperature. The reaction mixture was stirred for 1 h and added to 300 mL 1M HCl. The resulting precipitate was collected washed with cold EtOH and purified via recrystallization in EtOH (80 mL). After drying under high vacuum the title compound was obtained as white solid (611 mg, 1.33 mmol, 46 %). ^{1}H NMR (400MHz ,$CDCl_3$) δ = 8.57 - 6.89 (m, 8 H), 4.40 - 4.32 (m, 2 H), 3.91 (s, 3 H), 3.68 - 3.63 (m, 2 H), 1.93 - 1.75 (m, 2 H), 1.67 - 1.53 (m, 2 H), 1.52 - 1.26 (m, 14 H); ^{13}C NMR (100 MHz ,$CDCl_3$) δ = 166.1, 164.2, 160.7, 132.1, 131.3, 130.3, 130.1, 126.9, 121.5, 114.7, 65.4, 63.1, 55.7, 32.8, 29.6, 29.5, 29.4, 29.2, 28.7, 26.0, 25.7; HRMS $[M + Na]^+$ m / z: calcd for $C_{26}H_{34}N_4NaO_4$ 489.2478, found 489.2479.

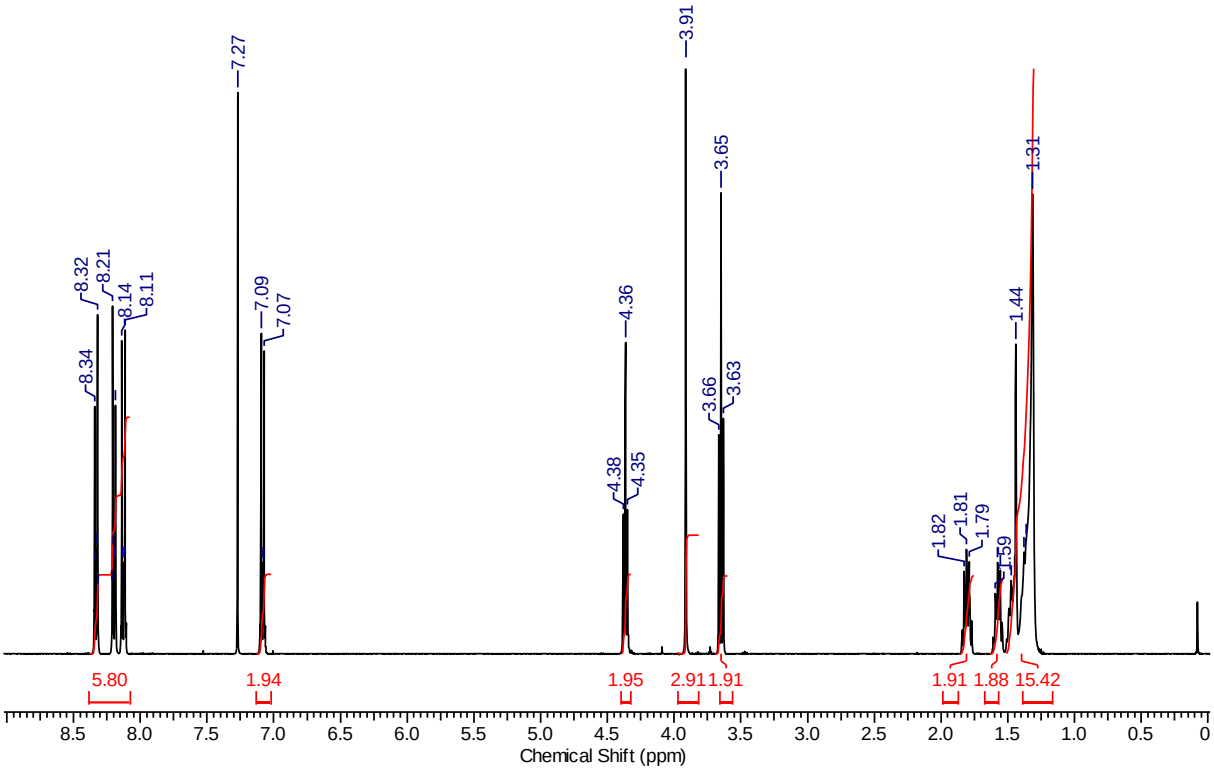

Figure 147 ^{1}H NMR (400 MHz, $CDCl_3$) spectrum of 11-hydroxyundecyl 4-(2-(4-methoxyphenyl)-2H-tetrazol-5-yl)benzoate **37**.

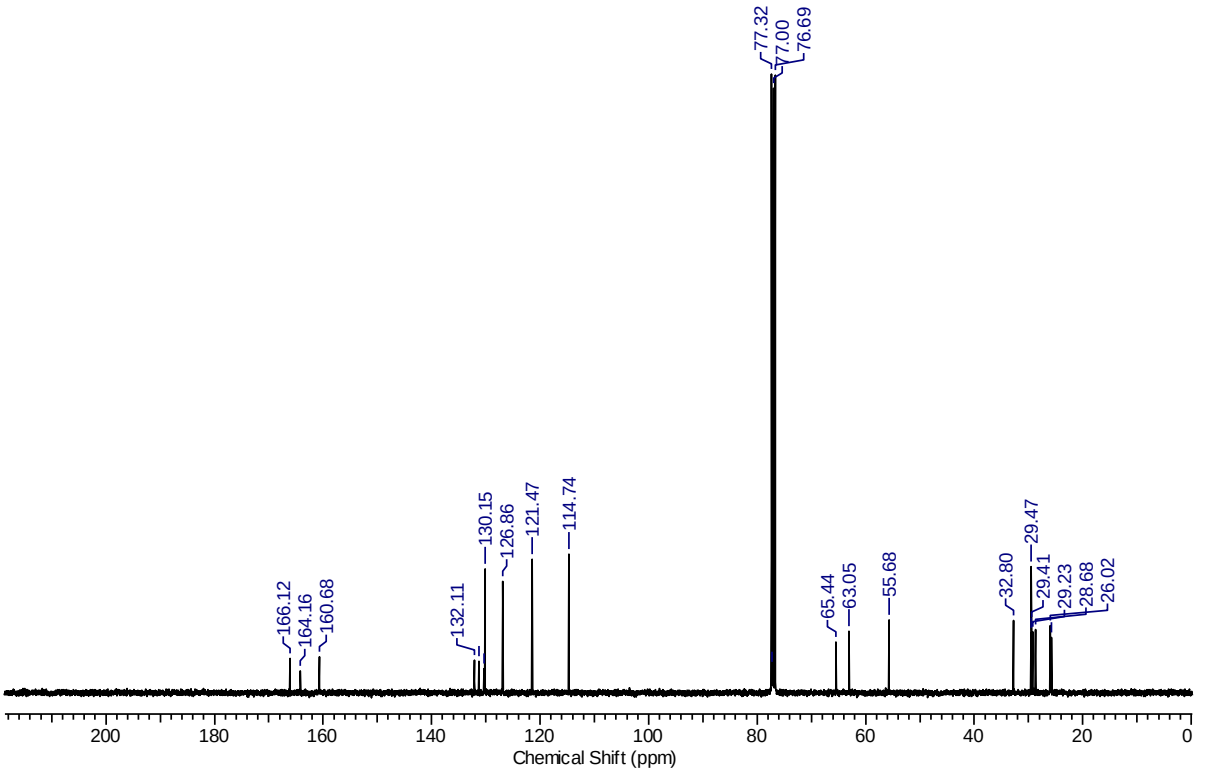

Figure 148 ^{13}C NMR (100 MHz, $CDCl_3$) spectrum of 11-hydroxyundecyl 4-(2-(4-methoxyphenyl)-2H-tetrazol-5-yl)benzoate **37**.

Ethyl (11-((4-(2-(4-methoxyphenyl)-2H-tetrazol-5-yl)benzoyl)-oxy)undecyl) fumarate (30)

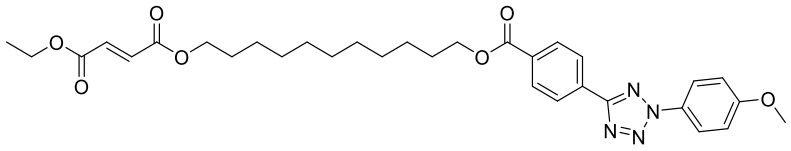

11-Hydroxyundecyl 4-(2-(4-methoxyphenyl)-2H-tetrazol-5-yl)benzoate **37** (200 mg, 0.43 mmol), Et_3N (86.7 mg, 0.86 mmol) were dissolved in 5 ml dry DCM und Ar. Ethyl (E)-4-chloro-4-oxobut-2-enoate (151,07 mg, 0.93 mmol) dissolved in 2 mL dry DCM was added at 0 °C. The reaction mixture was stirred at room temperature for 30 min. After removing the solvent under reduced pressure the crude product was recrystallized in 20 mL EtOH. After drying under high vacuum the title compound was obtained as off white solid (211 mg, 0.36 mmol, 83 %). ^{1}H NMR (400MHz ,$CDCl_3$) δ = 8.47 - 6.97 (m, 8 H), 4.47 - 4.15 (m, 6 H), 3.91 (s, 3 H), 1.90 - 1.74 (m, 2 H), 1.73 - 1.21 (m, 19 H); ^{13}C NMR (100 MHz ,$CDCl_3$) δ = 166.1, 165.1, 164.2, 160.7, 133.7, 133.6, 132.1, 131.3, 130.3, 130.1, 126.9, 121.5, 114.7, 65.5, 65.4, 61.3, 55.7, 29.5, 29.3, 29.2, 28.7, 28.5, 26.0, 25.9, 14.1; HRMS $[M + Na]^+$ m / z: calcd for $C_{32}H_{40}N_4NaO_7$ 615.2795, found 615.2805.

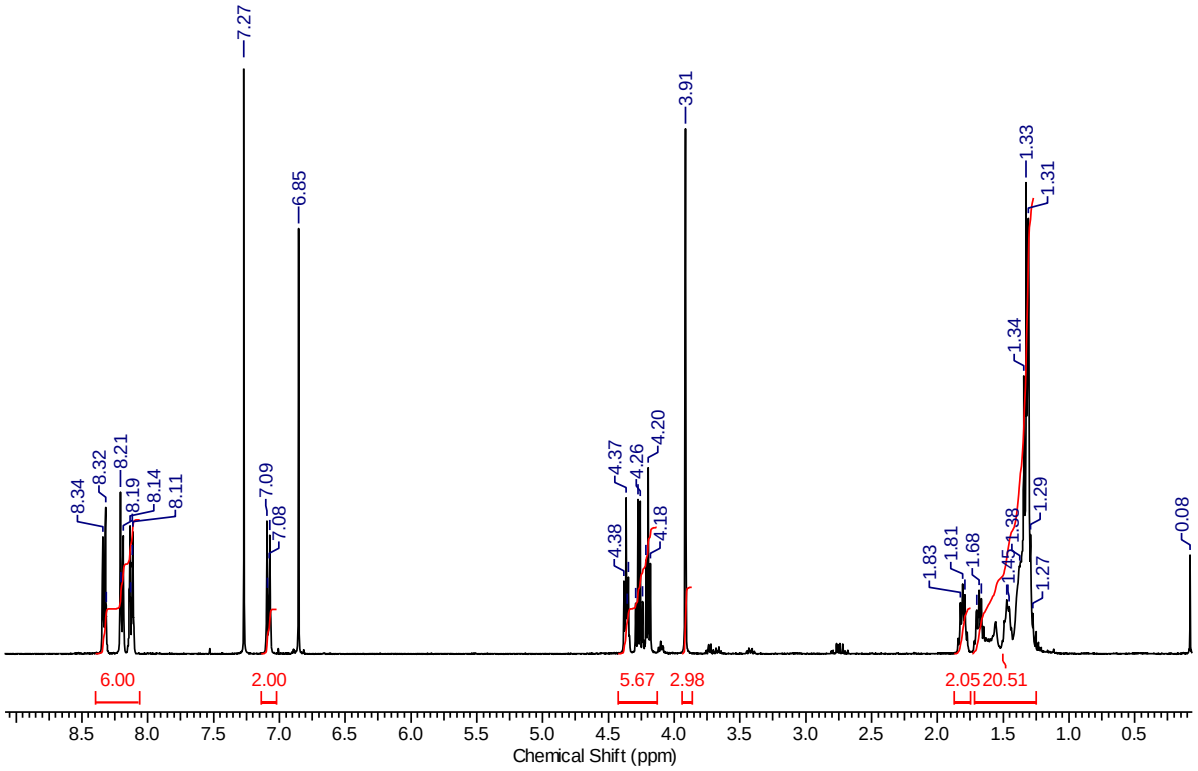

Figure 149 ^{1}H NMR (400 MHz, $CDCl_3$) spectrum of ethyl (11-((4-(2-(4-methoxyphenyl)-2H-tetrazol-5-yl)benzoyl)oxy)undecyl) fumarate **30**.

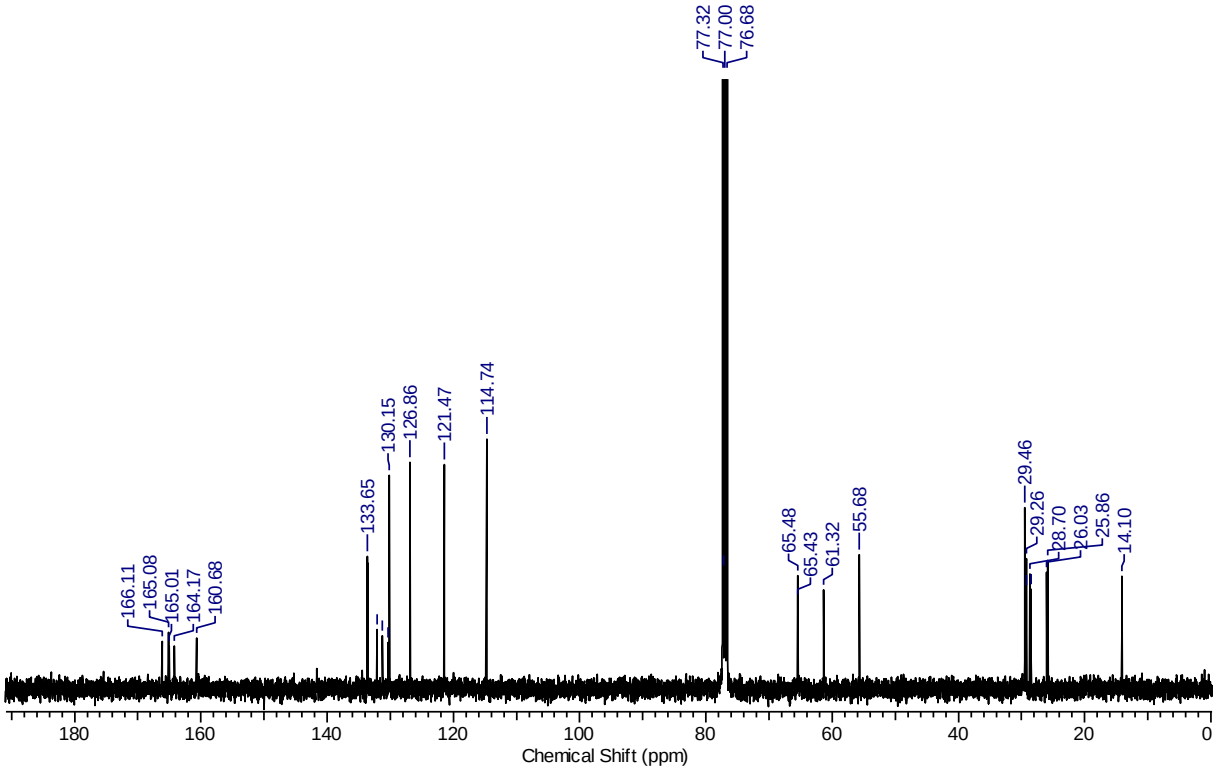

Figure 150 ^{13}C NMR (100 MHz, $CDCl_3$) spectrum of ethyl (11-((4-(2-(4-methoxyphenyl)-2H-tetrazol-5-yl)benzoyl)oxy)undecyl) fumarate **30**.

4-Oxo-4-((11-((4-(2-(pyren-1-yl)-2H-tetrazol-5-yl)benzoyl)-oxy)undecyl)oxy)butanoic acid (34)

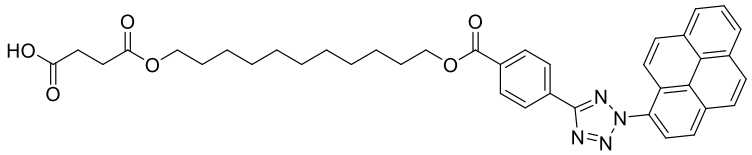

11-Hydroxyundecyl 4-(2-(pyren-1-yl)-2H-tetrazol-5-yl)benzoate **22** (190 mg, 0.33 mmol), succinic anhydride (188 mg, 1.88 mmol), DMAP (128 mg, 1.05 mmol), Et_3N (365 mg, 3.61 mmol) were dissolved in dry 1,4-dioxane under Ar atmosphere. The reaction mixture was stirred for 4 d at 50°C. After removing the solvent under reduced pressure the crude product was recrystallized in EtOH (2 x 40 mL). After drying under high vacuum, the title compound was obtained as a dark red solid (138 mg, 0.21 mmol, 63 %). ^{1}H NMR (400MHz, $CDCl_3$) δ = 8.55 - 8.04 (m, 13 H), 4.42 - 4.35 (m, 2 H), 4.14 - 4.06 (m, 2 H), 2.75 - 2.60 (m, 4 H), 1.88 - 1.77 (m, 2 H), 1.69 - 1.56 (m, 2 H), 1.54 - 1.27 (m, 14 H); ^{13}C NMR (100 MHz ,$CDCl_3$) δ = 176.5, 172.6, 166.1, 164.5, 132.8, 132.3, 131.2, 131.1, 130.5, 130.2, 130.1, 130.0, 129.4, 127.0, 126.9, 126.7, 126.3, 125.1, 125.0, 124.8, 124.1, 122.7, 121.4, 77.3, 65.5, 64.8, 39.6, 29.7, 29.5, 29.4, 29.2, 29.2, 28.7, 28.5, 26.0, 25.9; HRMS $[M + Na]^+$ m / z: calcd for $C_{39}H_{40}N_4NaO_6$ 683.2846, found 683.2840.

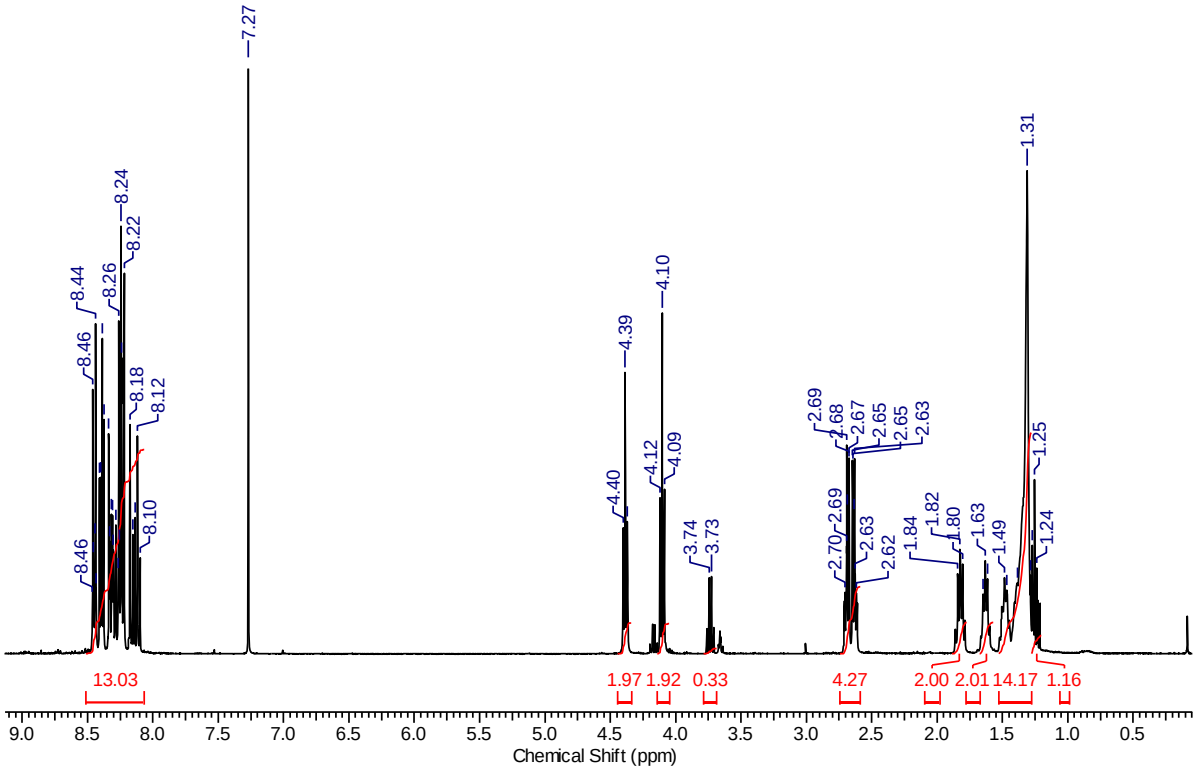

Figure 151 ^{1}H NMR (400 MHz, $CDCl_3$) spectrum of 4-oxo-4-((11-((4-(2-(pyren-1-yl)-2H-tetrazol-5-yl)benzoyl)oxy)undecyl)oxy)butanoic acid **34**.

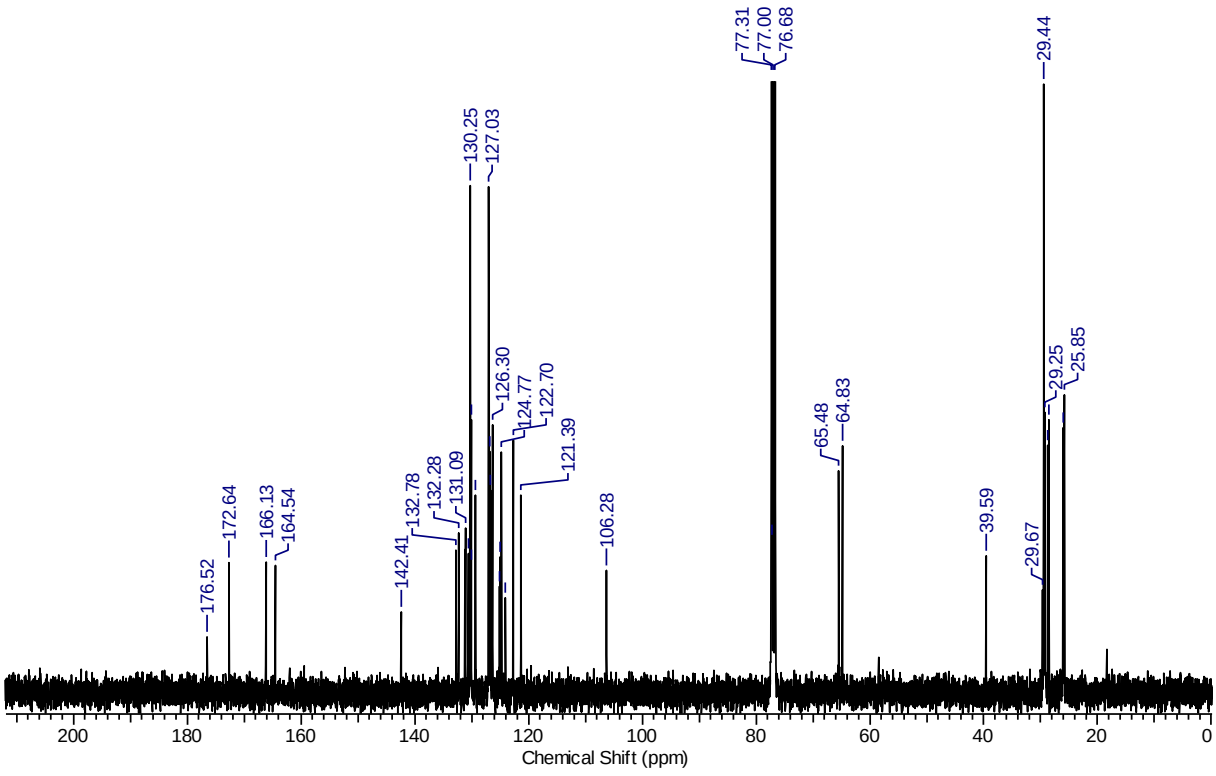

Figure 152 13C NMR (100 MHz, CDCl3) spectrum of 4-oxo-4-((11-((4-(2-(pyren-1-yl)-2H-tetrazol-5-yl)benzoyl)oxy)undecyl)oxy)butanoic acid **34**.

4,4-Diethoxy-9,12-dioxo-3,13-dioxa-8-aza-4-silatetracosan-24-yl 4-(2-(pyren-1-yl)-2H-tetrazol-5-yl)benzoate(35)*

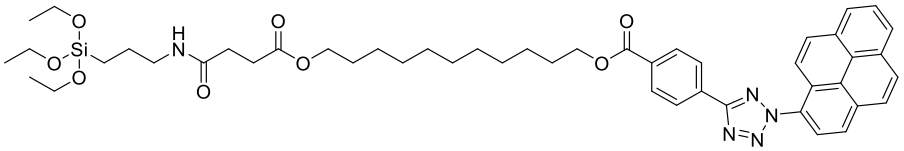

4-Oxo-4-((11-((4-(2-(pyren-1-yl)-2H-tetrazol-5-yl)benzoyl)oxy)undecyl)oxy)butanoic acid **34** (500 mg, 0.77 mmol) was dissolved in 10 mL dry THF under Ar and 1,1'-carbonyldiimidazole (CDI) (128 mg, 0.79 mmol) was added. The reaction mixture was stirred over night at room temperature. APTS (87 mg, 0.79 mmol) was added to the solution. The reaction mixture was stirred for additional 4 h and the solvent was removed under reduced pressure. The crude product was dissolved in small amount of dry DCM an purified via column chromatography on silica gel using cyclohexane / ethyl acetate (1:1, v / v R_f 0.48) as eluent. After drying under high vacuum the title compound was obtained as green solid (260 mg, 0.30 mmol, 39 %). ^{1}H NMR (400MHz ,$CDCl_3$) δ = 8.56 - 8.07 (m, 13 H), 4.45 - 4.32 (m, 2 H), 4.08 (t, J = 6.8 Hz, 2 H), 3.89 - 3.67 (m, 6 H), 3.28-3.24 (m, 2 H), 2.71 - 2.59 (m, 2 H), 2.52 - 2.41 (m, 2 H), 1.88 - 1.74 (m, 2 H), 1.73 - 1.14 (m, 29 H), 0.70 - 0.56 (m, 2 H).

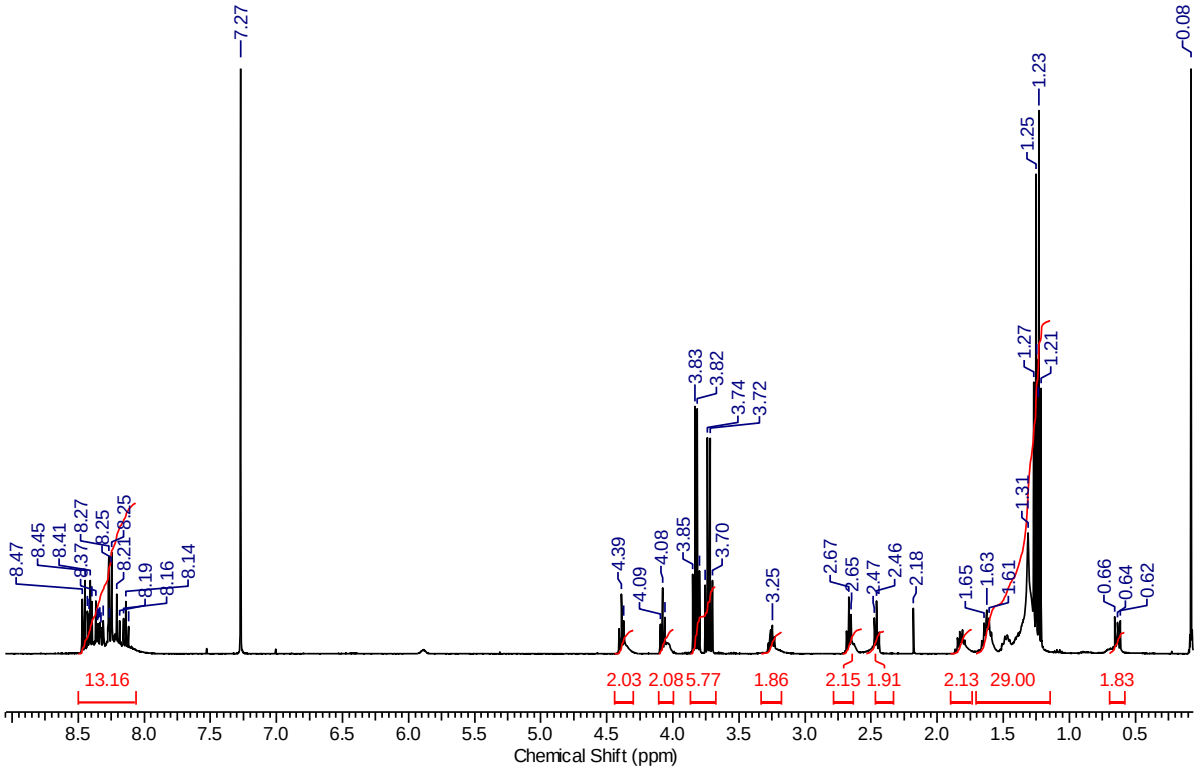

Figure 153 ^{1}H NMR (400 MHz, $CDCl_3$) spectrum of 4,4-diethoxy-9,12-dioxo-3,13-dioxa-8-aza-4-silatetracosan-24-yl 4-(2-(pyren-1-yl)-2H-tetrazol-5-yl)benzoate **35**.

*All used glassware were heated out to avoid H_2O contamination. No ^{13}C NMR or ESI-MS data could be collected, due to high sensitivity of the title compound towards sun light, heat and H_2O.

2-(2,5-Dioxo-2,5-dihydro-1H-pyrrol-1-yl)ethyl 4,4,4-trifluorobutanoate (36)

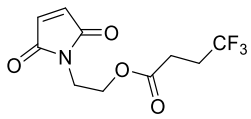

1-(2-Hydroxyethyl)-1H-pyrrole-2,5-dione (100.0 mg, 0.71 mmol) **7**, 4,4,4-trifluorobutanoic acid (184.6 mg, 1.31 mmol), dicyclohexylcarbodiimide (DCC) (190.2 mg, 0.92 mmol), and DMAP (17.3 mg, 0.14 mmol) were dissolved in 5 mL THF and stirred over night at room temperature. The solvent was removed under reduced pressure. The crude product was purified via column chromatography on silica gel using cyclohexane / ethyl acetate (1:1, v / v R_f 0.26) as the eluent. After drying under high vacuum the title compound was obtained as a white solid (89 mg, 0.34 mmol, 47 %). ^{1}H NMR (400MHz ,$CDCl_3$) δ = 6.74 (s, 2 H), 4.33 - 4.23 (m, 2 H), 3.87 - 3.76 (m, 2 H), 2.61 - 2.36 (m, 4 H); ^{13}C NMR (100 MHz ,$CDCl_3$) δ = 170.7, 170.4, 134.3, 62.2, 36.8, 29.3 (m), 27.0 (m); HRMS $[M + Na]^+$ m / z: calcd for $C_{10}H_{10}F_3NNaO_4$ 288.0460, found 289.0493.

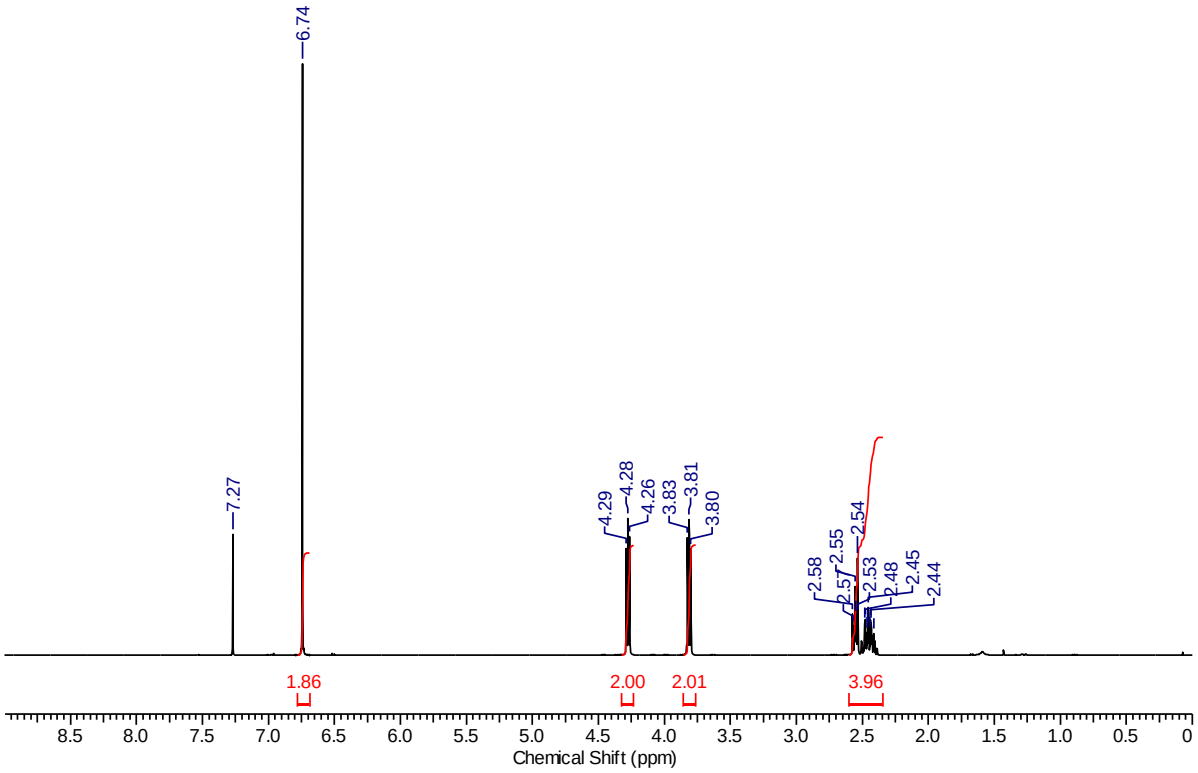

Figure 154 ^{1}H NMR (400 MHz, $CDCl_3$) spectrum of 2-(2,5-dioxo-2,5-dihydro-1H-pyrrol-1-yl)ethyl 4,4,4-trifluorobutanoate **36**.

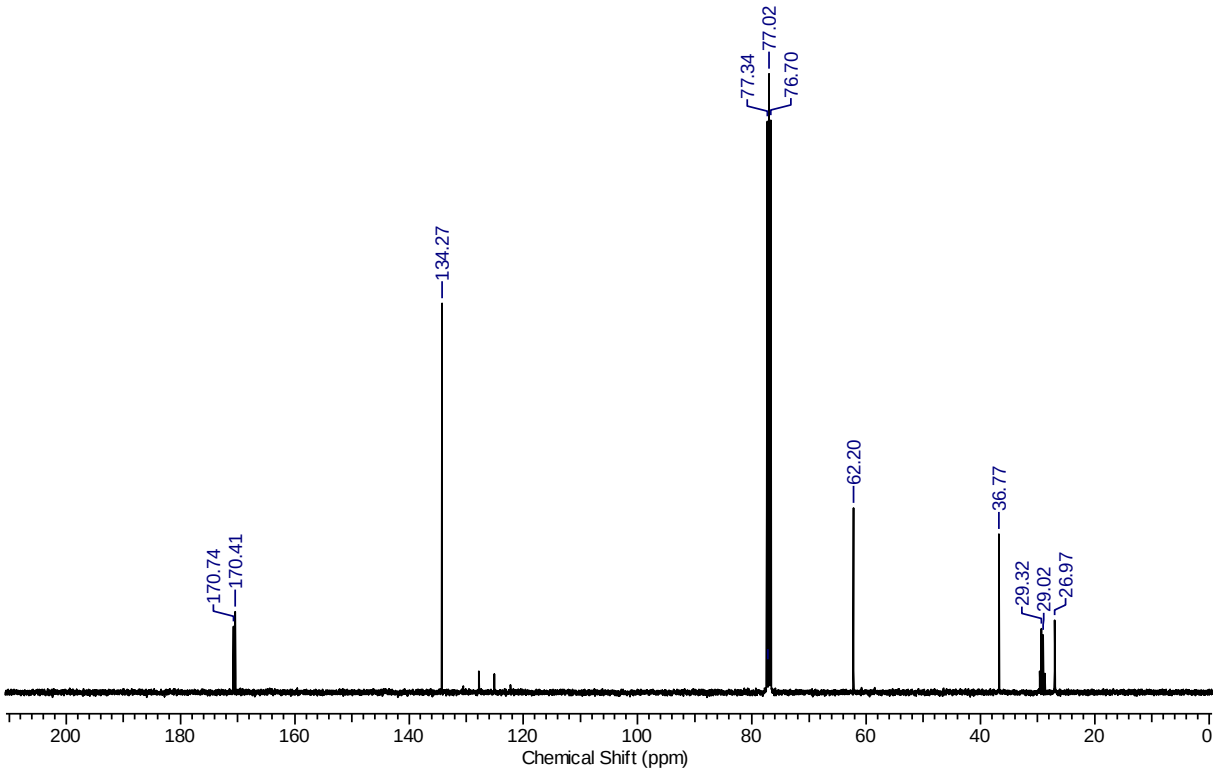

Figure 155 ^{13}C NMR (100 MHz, $CDCl_3$) spectrum of 2-(2,5-dioxo-2,5-dihydro-1H-pyrrol-1-yl)ethyl 4,4,4-trifluorobutanoate **37**.

5-Ethyl 4-(11-((4-(2-(4-methoxyphenyl)-2H-tetrazol-5-yl)benzoyl)oxy)undecyl) 3-(4-(((11-hydroxyundecyl)oxy)carbonyl)phenyl)-1-(pyren-1-yl)-4,5-dihydro-1H-pyrazole-4,5-dicarboxylate (31)

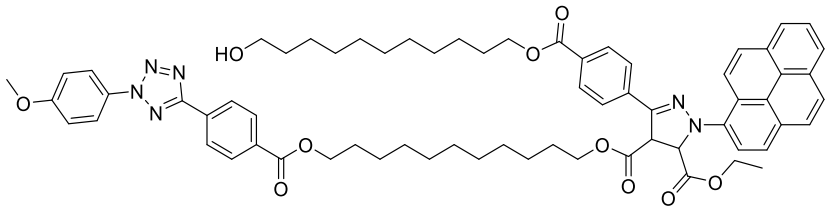

PAT **22** (10 mg, 17.9 μmol) and ethyl (11-((4-(2-(4-methoxyphenyl)-2H-tetrazol-5-yl)benzoyl)oxy)undecyl) fumarate **30** (10.6 mg, 17.9 μmol) were dissolved in MeCN and irradiated for 1 h at 410-420 nm, room temperature. The solvent was removed under reduced pressure. The crude product was purified via column chromatography on silica gel using cyclohexane / ethyl acetate (1:1, v / v R_f 0.46) as the eluent. After drying under high vacuum the title compound was obtained as yellow solid (13.0 mg, 10.3 μmol, 73%). ^{1}H NMR (400MHz ,$CDCl_3$) δ = 8.51 - 7.83 (m, 21 H), 5.69 – 5.65 (m, 1 H), 4.90 – 4.85 (m, 1 H), 4.36 - 4.11 (m, 6 H), 3.86 - 3.63 (m, 5 H), 3.69 – 3.60 (m, 2 H), 1.79 - 1.63 (m, 4 H), 1.61 - 1.09 (m, 35 H); ^{13}C NMR (100 MHz ,$CDCl_3$) δ = 169.0, 166.3, 164.1, 160.7, 145.2, 138.4, 135.5, 132.1, 131.4, 131.3, 131.1, 130.4, 130.3, 130.1, 129.7, 129.5, 129.3, 127.5, 127.2, 126.9, 126.8, 126.3, 126.1, 125.5, 125.1, 125.1, 124.9, 124.8, 122.9, 121.7, 121.5, 71.0, 66.6, 65.9, 65.4, 65.3, 63.0, 62.4, 61.7, 55.7, 55.4, 55.3, 32.8, 29.5, 29.5, 29.4, 29.3, 29.2, 29.1, 29.0, 28.8, 28.7, 28.5, 28.0, 26.0, 25.8, 25.7, 25.3, 14.1, 13.5;HRMS [M + Na]$^+$ m / z: calcd for $C_{67}H_{74}N_6NaO_{10}$ 1145.5364, found 1145.5392.*

*A rearomatisation product of the title compound was detected *via* ESI-MS exclusively (Refer to the Figure 156).

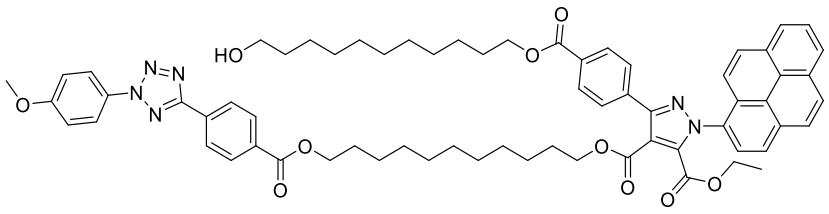

Figure 156 Rearomatisation product of **31**.

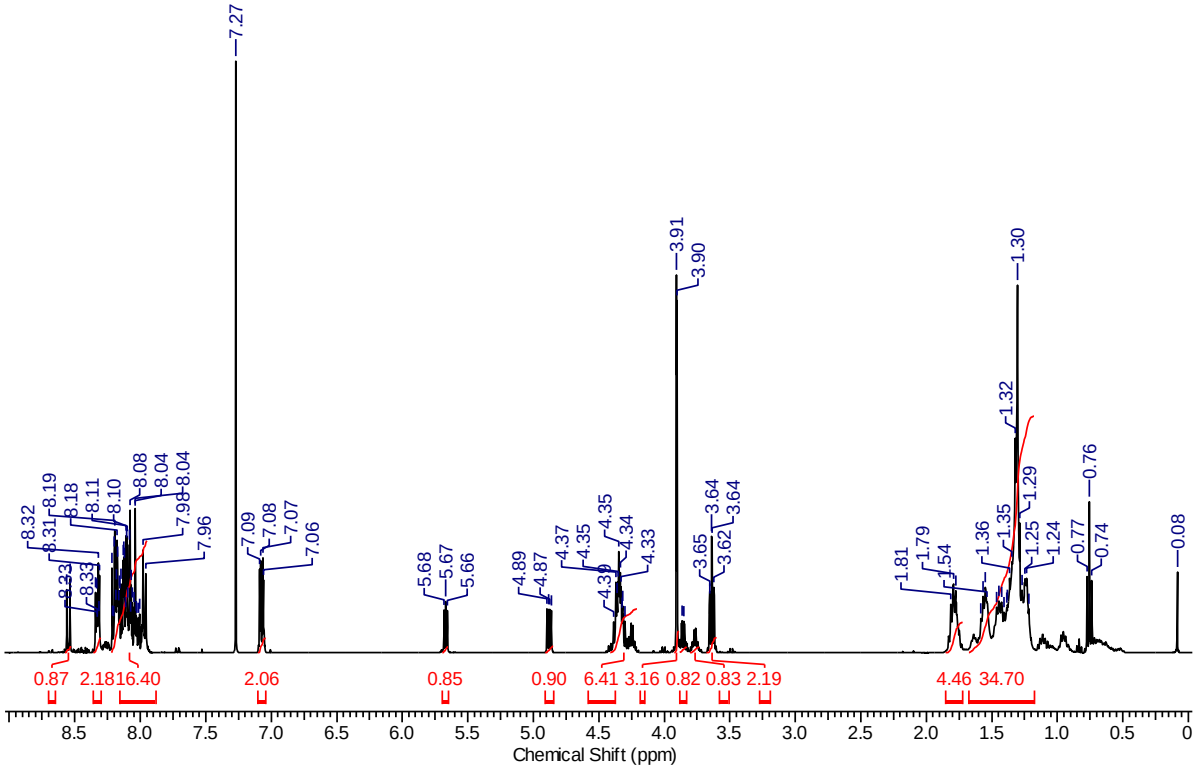

Figure 157 ^{1}H NMR (400 MHz, $CDCl_3$) spectrum of 5-ethyl 4-(11-((4-(2-(4-methoxyphenyl)-2H-tetrazol-5-yl)benzoyl)oxy)undecyl) 3-(4-(((11-hydroxyundecyl)oxy)-carbonyl)phenyl)-1-(pyren-1-yl)-4,5-dihydro-1H-pyrazole-4,5-dicarboxylate **31**.

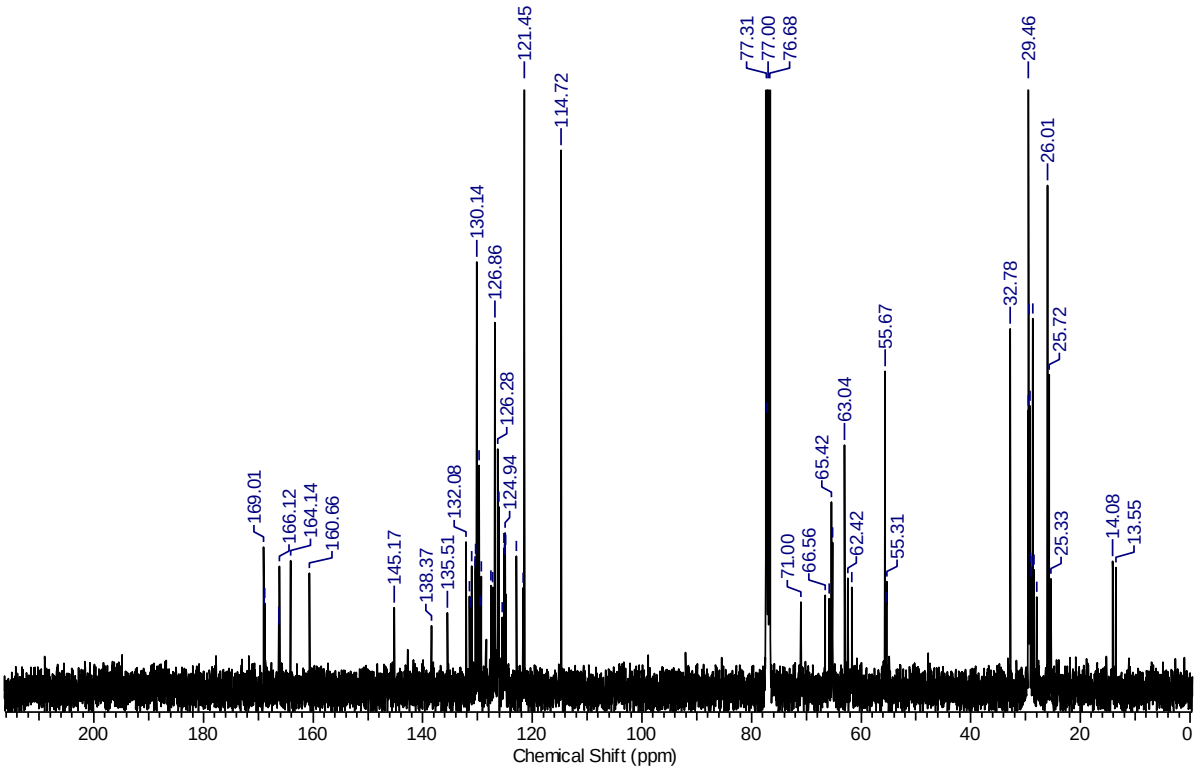

Figure 158 ^{13}C NMR (100 MHz, $CDCl_3$) spectrum of 5-ethyl 4-(11-((4-(2-(4-methoxyphenyl)-2H-tetrazol-5-yl)benzoyl)oxy)undecyl) 3-(4-(((11-hydroxyundecyl)-oxy)carbonyl)phenyl)-1-(pyren-1-yl)-4,5-dihydro-1H-pyrazole-4,5-dicarboxylate **31**.

4-(11-((4-(5-(2-((2-Bromo-2-methylpropanoyl)oxy)ethyl)-1-(4-methoxyphenyl)-4,6-dioxo-1,3a,4,5,6,6a-hexahydropyrrolo[3,4-c]pyrazol-3-yl)benzoyl)oxy)undecyl) 5-ethyl 3-(4-(((11-hydroxyundecyl)oxy)carbonyl)phenyl)-1-(pyren-1-yl)-4,5-dihydro-1H-pyrazole-4,5-dicarboxylate (33)

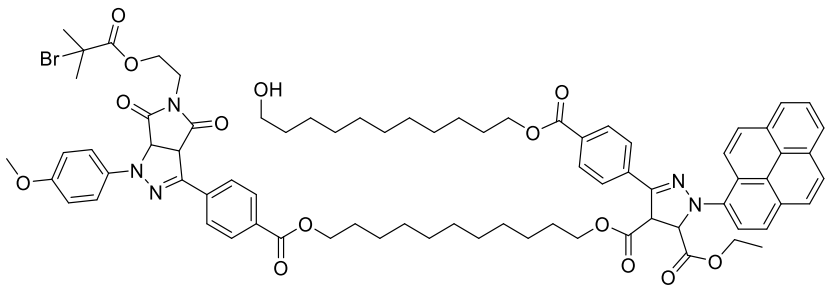

5-Ethyl 4-(11-((4-(2-(4-methoxyphenyl)-2H-tetrazol-5-yl)benzoyl)oxy)undecyl) 3-(4-(((11-hydroxyundecyl)oxy)carbonyl)phenyl)-1-(pyren-1-yl)-4,5-dihydro-1H-pyrazole-4,5-dicarboxylate **31** (10.0 mg, 8.9 μmol) and 2-(2,5-dioxo-2,5-dihydro-1H-pyrrol-1-yl)ethyl 2-bromo-2-methylpropanoate **32** (2.6 mg, 8.9 μmol) were dissolved in MeCN and irradiated for 1 h at 320 nm, room temperature. The solvent was removed under reduced pressure. The crude product was purified via column chromatography on silica gel using cyclohexane / ethyl acetate (1:1, v / v R_f 0.38) as the eluent. After drying under high vacuum the title compound was obtained as yellow solid (7.0 mg, 5.1 μmol, 57 %). ^{1}H NMR (400MHz ,$CDCl_3$) δ = 8.58 - 7.88 (m, 17 H), 7.55 - 7.47 (m, 2 H), 6.97 - 6.88 (m, 2 H), 5.71 - 5.63 (m, 1 H), 5.19 - 5.08 (m, 1 H), 4.93 - 4.80 (m, 2 H), 4.44 - 3.70 (m, 16 H), 3.68 - 3.58 (m, 2 H), 1.84 - 1.71 (m, 10 H), 1.67 - 1.51 (m, 2 H), 1.50 - 1.17 (m, 35 H); HRMS $[M + Na]^+$ m / z: calcd for $C_{77}H_{86}BrN_5NaO_{14}$ 1406.5252, found 1406.5138.

*A rearomatisation product of the title compound was detected *via* ESI-MS (refer to the Figure 159).

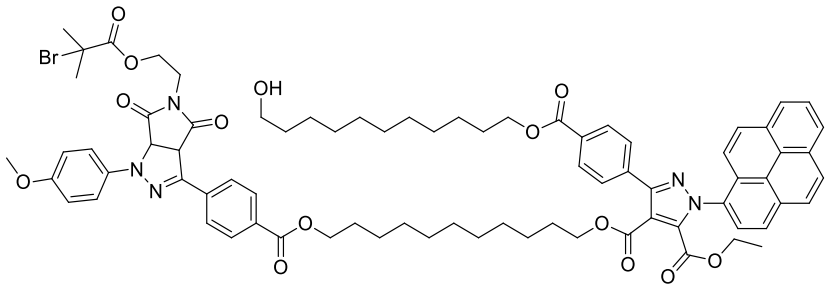

Figure 159 Rearomatisation product of **33**.

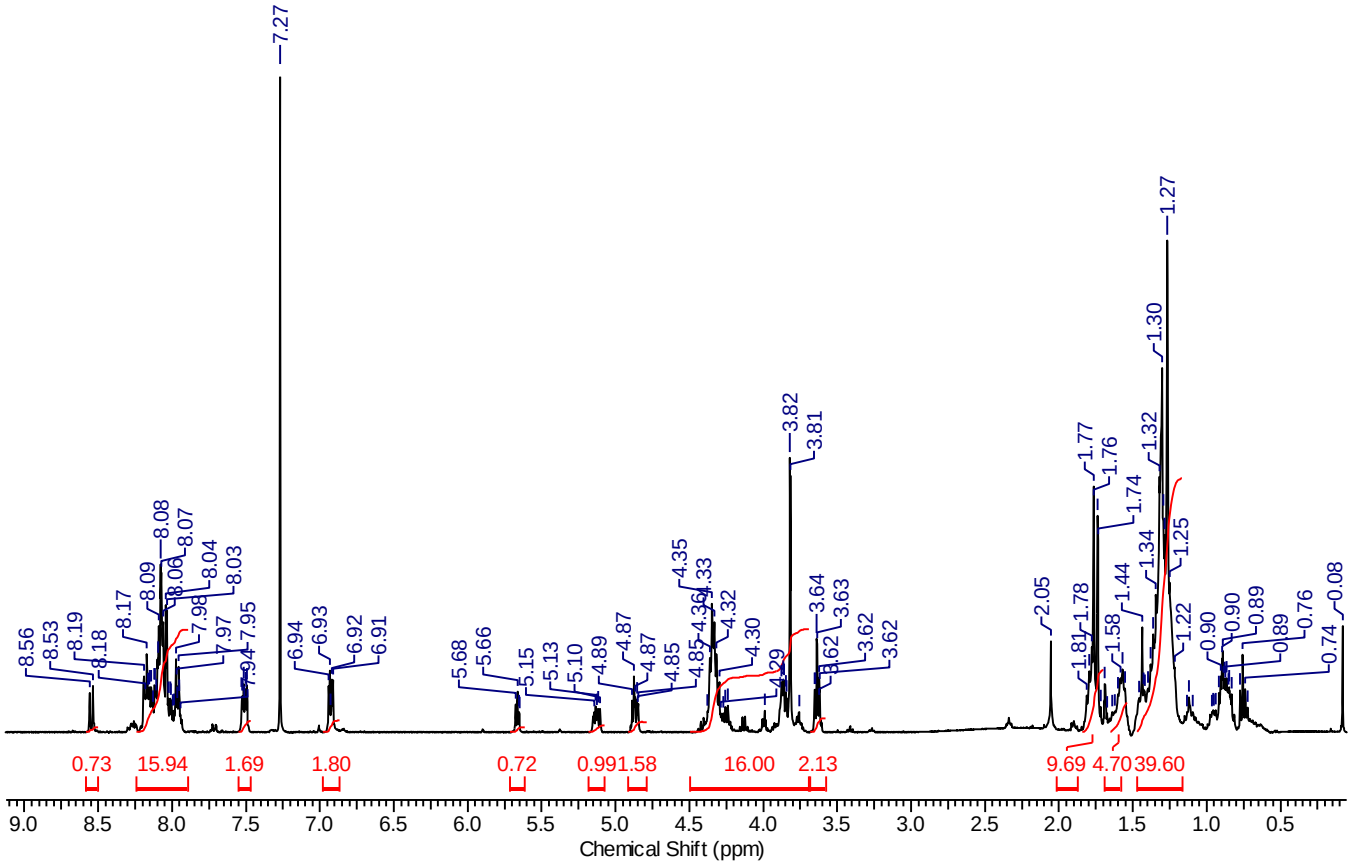

Figure 160 ^{1}H NMR (400 MHz, $CDCl_3$) spectrum of 4-(11-((4-(5-(2-((2-bromo-2-methylpropanoyl)oxy)ethyl)-1-(4-methoxyphenyl)-4,6-dioxo-1,3a,4,5,6,6a-hexahydro-pyrrolo[3,4-c]pyrazol-3-yl)benzoyl)oxy)undecyl) 5-ethyl 3-(4-(((11-hydroxyundecyl)-oxy)carbonyl)phenyl)-1-(pyren-1-yl)-4,5-dihydro-1H-pyrazole-4,5-dicarboxylate **33**.

8.4.4 Surface Modifications

General remarks:

All processes on the surface were performed in silica and grease free fume hood in a "red light" lab.

Ultrapure Ar was used.

Ceramic tweezers were used for all processes involving piranha solution.

HPLC grade solvents were used for all rinsing steps.

Dry solvents and Ar atmosphere were applied for all photo-induced reactions.

Silicon wafer activation

The silicon wafer was placed in freshly prepared piranha solution (conc. H_2SO_4/H_2O_2, ratio 2:1) in a vial. The sample was heated in a shaker at 80 ºC for 1 h. The silica wafer was taken out of the piranha solution and rinsed with Milli-Q water dried under Ar flow and used for the silanization immediately.

Silanization of the silicon wafer with PAT (I)

The activated silicon wafer was placed into a vial. 4,4-Diethoxy-9,12-dioxo-3,13-dioxa-8-aza-4-silatetracosan-24-yl 4-(2-(pyren-1-yl)-2H-tetrazol-5-yl)benzoate (2 mg, 2.3 µmol) was dissolved in 2 mL dry toluene and added to the vial. The vial was placed in an oven at 50 ºC for 5 h and overnight at room temperature. The silicon wafer was taken out of the solution and rinsed with dichloromethane and dried under Ar flow.

Grafting of ethyl (11-((4-(2-(4-methoxyphenyl)-2H-tetrazol-5-yl)benzoyl)oxy)undecyl) fumarate onto the silicon wafer via NITEC at 410 – 420 nm (II)

The silicon wafer **I** was placed into a mask holder with a shadow mask. The resulting set up was placed into a vial. 4 mL of MeCN containing ethyl-(11-((4-(2-(4-methoxyphenyl)-2H-tetrazol-5-yl)benzoyl)oxy)undecyl) fumarate **31** (5.8 mg, 9.8 µmol) were purged with Ar for 5 min and added to the vial. The set up was irradiated at 410 – 420 nm for 3 h. The silicon wafer was taken out of the mask holder, rinsed with dichloromethane and dried under Ar flow.

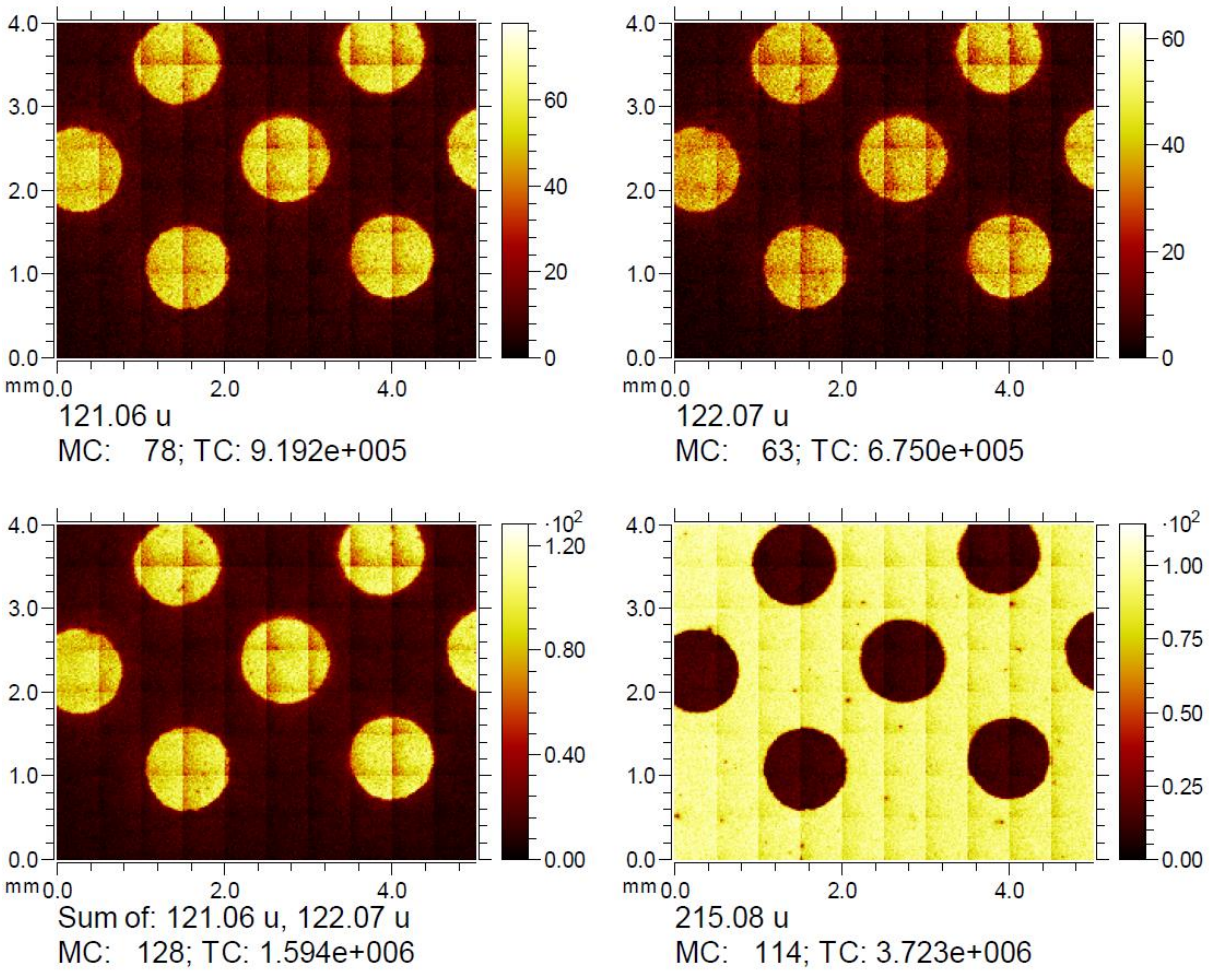

Figure 161 ToF-SIMS image of surface **II** (positive mode).

Blank experiment: The silicon wafer **I** was placed into a mask holder with a shadow mask. The resulting set up was placed into a vial. 4 mL MeCN containing ethyl (11-((4-(2-(4-methoxyphenyl)-2H-tetrazol-5-yl)benzoyl)oxy)undecyl) fumarate **31** (5.8 mg, 9.8 µmol) were purged with Ar and added to the vial. The set up was placed in the dark for 3 h. The silicon wafer was taken out of the mask holder, rinsed with dichloromethane and dried under Ar flow.

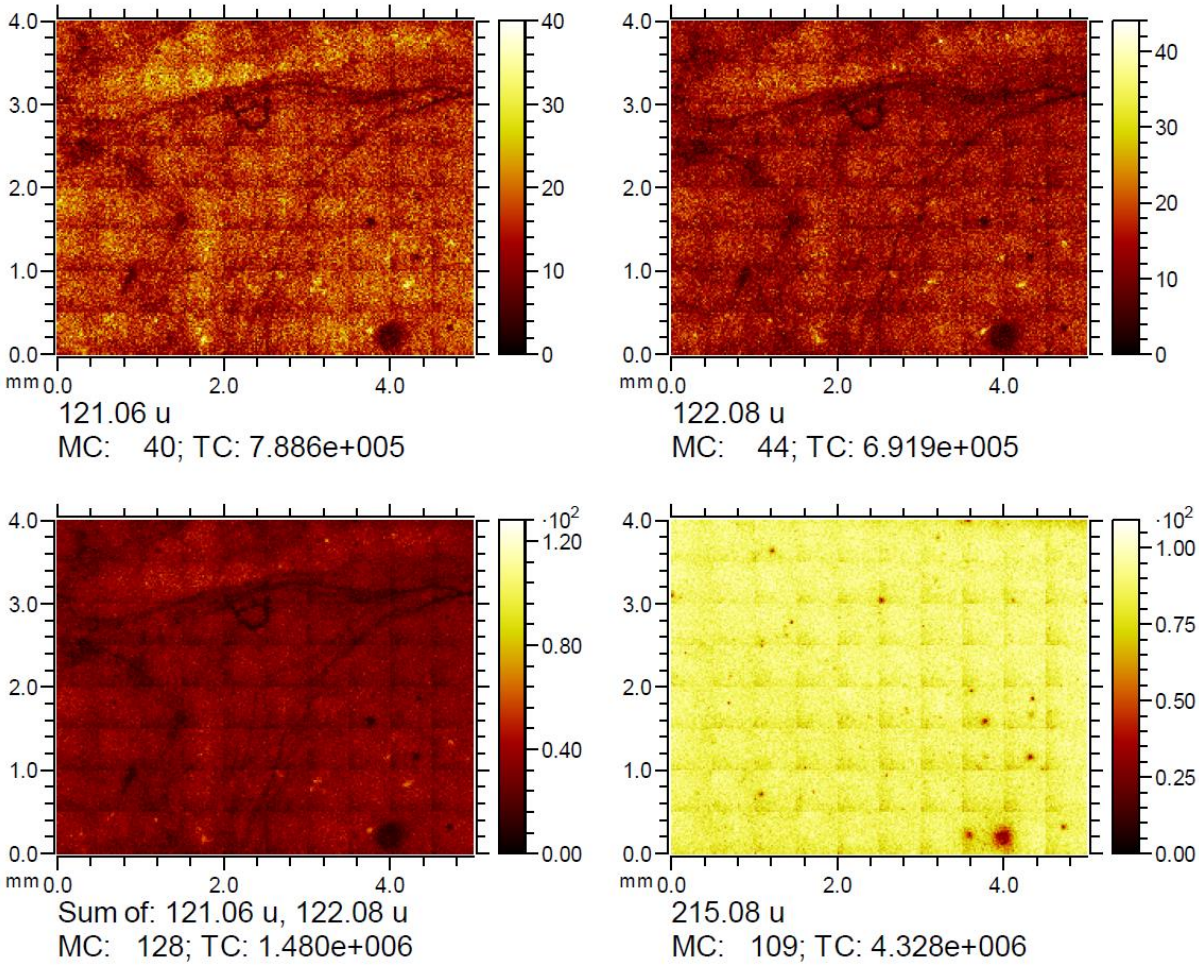

Figure 162 ToF-SIMS image of blank sample of surface **II** (positive mode).

Grafting of 2-(2,5-dioxo-2,5-dihydro-1H-pyrrol-1-yl)ethyl 2-bromo-2-methylpropanoate onto the silicon wafer via NITEC at 410 -420 nm (III)

The silicon wafer **II** was placed into a mask holder without a shadow mask. The resulting set up was placed into a vial. 4.5 mL of MeCN containing 2-(2,5-dioxo-2,5-dihydro-1H-pyrrol-1-yl)ethyl 2-bromo-2-methylpropanoate **32** (3.6 mg, 12.5 µmol) were purged with Ar for 5 min and added to the vial. The set up was irradiated at 410 – 420 nm for 3 h. The silicon wafer was taken out of the mask holder, rinsed with dichloromethane and dried under Ar flow.

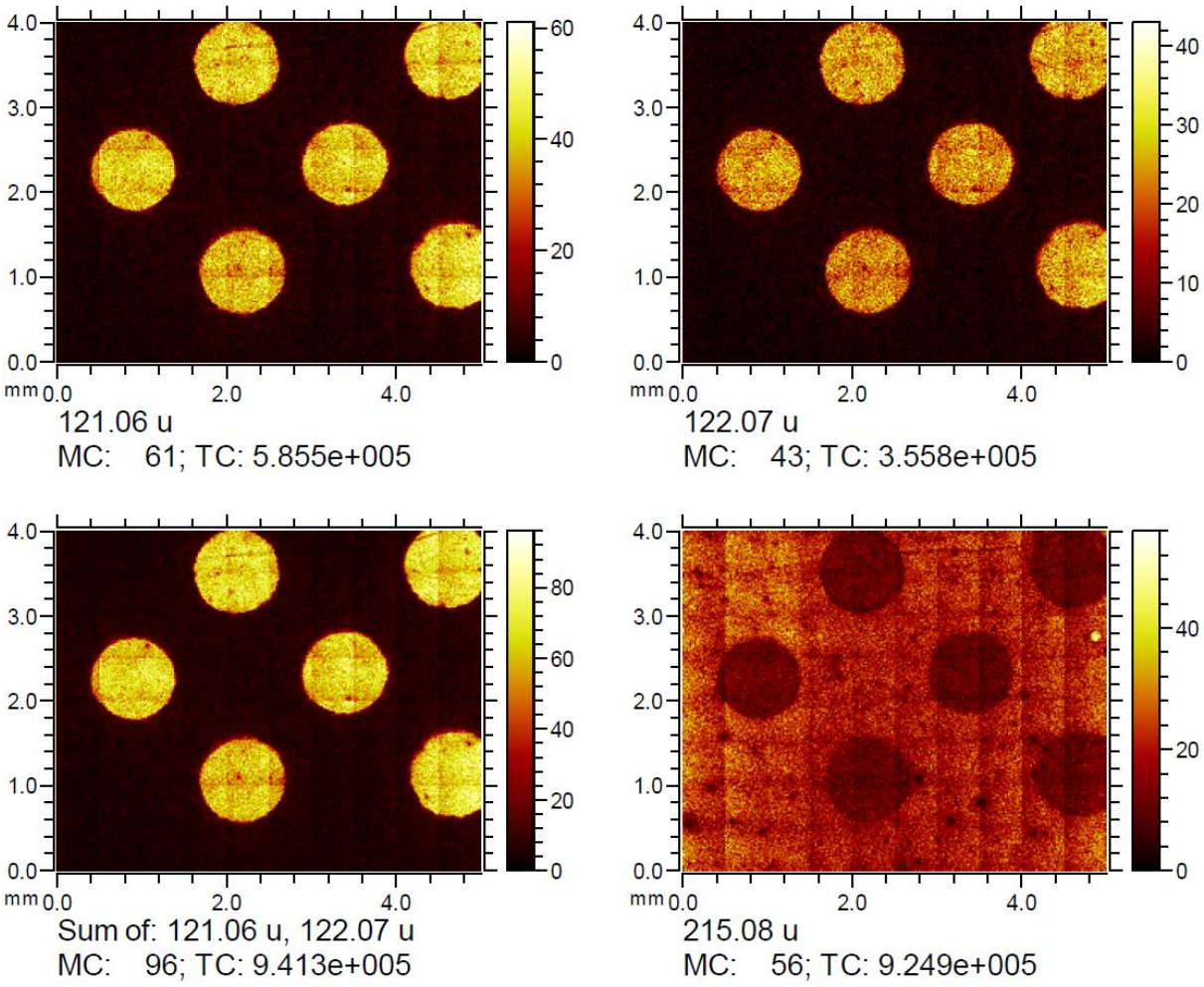

Figure 163 ToF-SIMS image of surface **III** (positive mode).

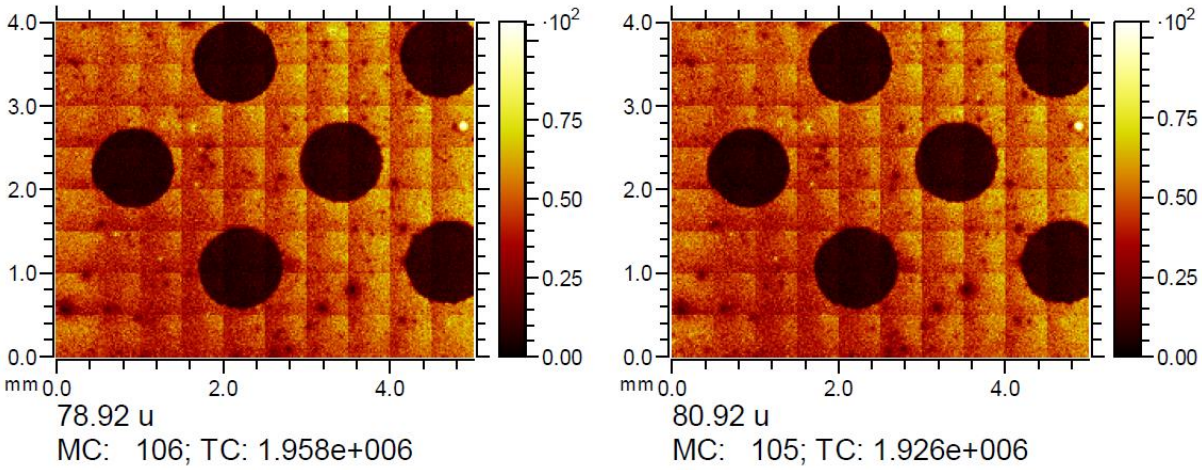

Figure 164 ToF-SIMS image of surface **III** (negative mode).

Grafting of 2-(2,5-dioxo-2,5-dihydro-1H-pyrrol-1-yl)ethyl 4,4,4-trifluorobutanoate onto the silicon wafer via NITEC at 320 nm (IV)

The silicon wafer **III** was placed into a mask holder without a shadow mask. The resulting set up was placed into a vial. 4.2 mL of dichloromethane containing 2-(2,5-dioxo-2,5-dihydro-1H-pyrrol-1-yl)ethyl 4,4,4-trifluorobutanoate **36** (2.9 mg, 11.0 µmol) were purged with Ar for 5 min and added to the vial. The set up was irradiated at 320 nm for 1 h. The silicon wafer was taken out of the mask holder, rinsed with dichloromethane and dried under Ar flow.

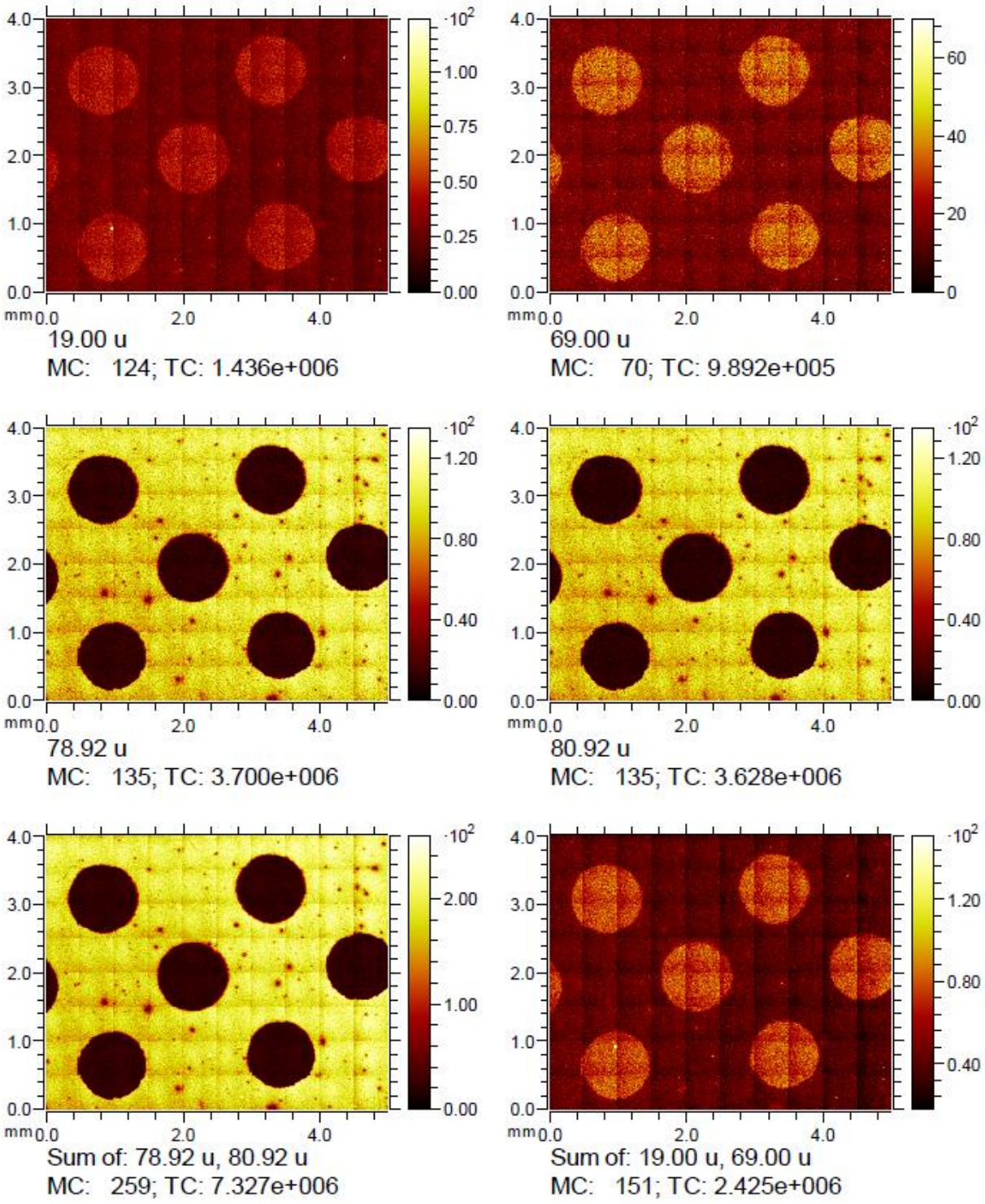

Figure 165 ToF-SIMS image of surface **IV** (negative mode).

Blank experiment: The silicon wafer **III** was placed into a mask holder without a shadow mask. The resulting set up was placed into a vial. 4.2 mL dichloromethane containing 2-(2,5-dioxo-2,5-dihydro-1H-pyrrol-1-yl)ethyl 4,4,4-trifluorobutanoate **36** (2.9 mg, 11.0 µmol) were purged with Ar for 5 min and added to the vial. The set up was placed in the dark for 1 h. The silicon wafer was taken out of the mask holder, rinsed with dichloromethane and dried under Ar flow.

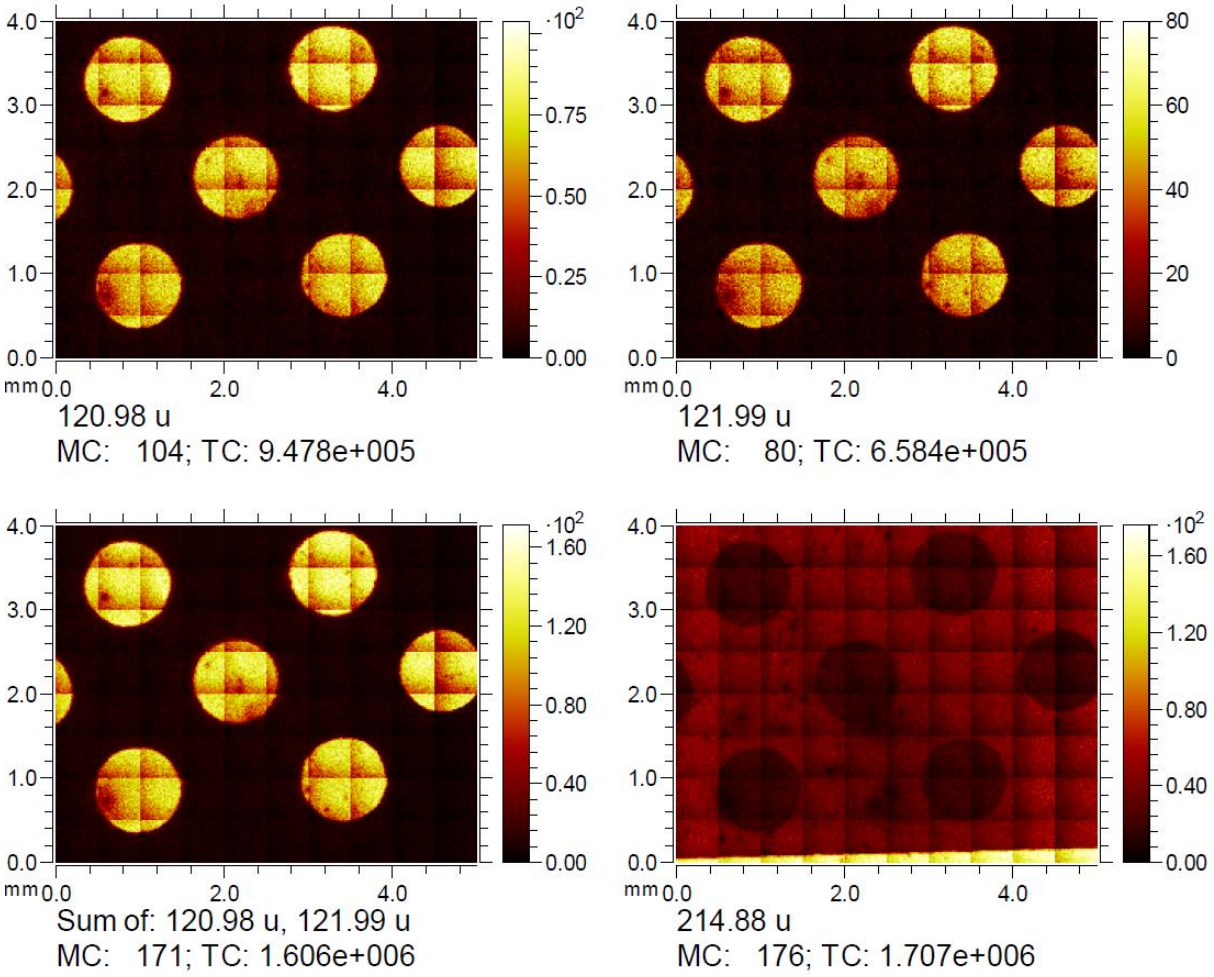

Figure 166 ToF-SIMS image of blank sample of surface **IV** (positive mode).

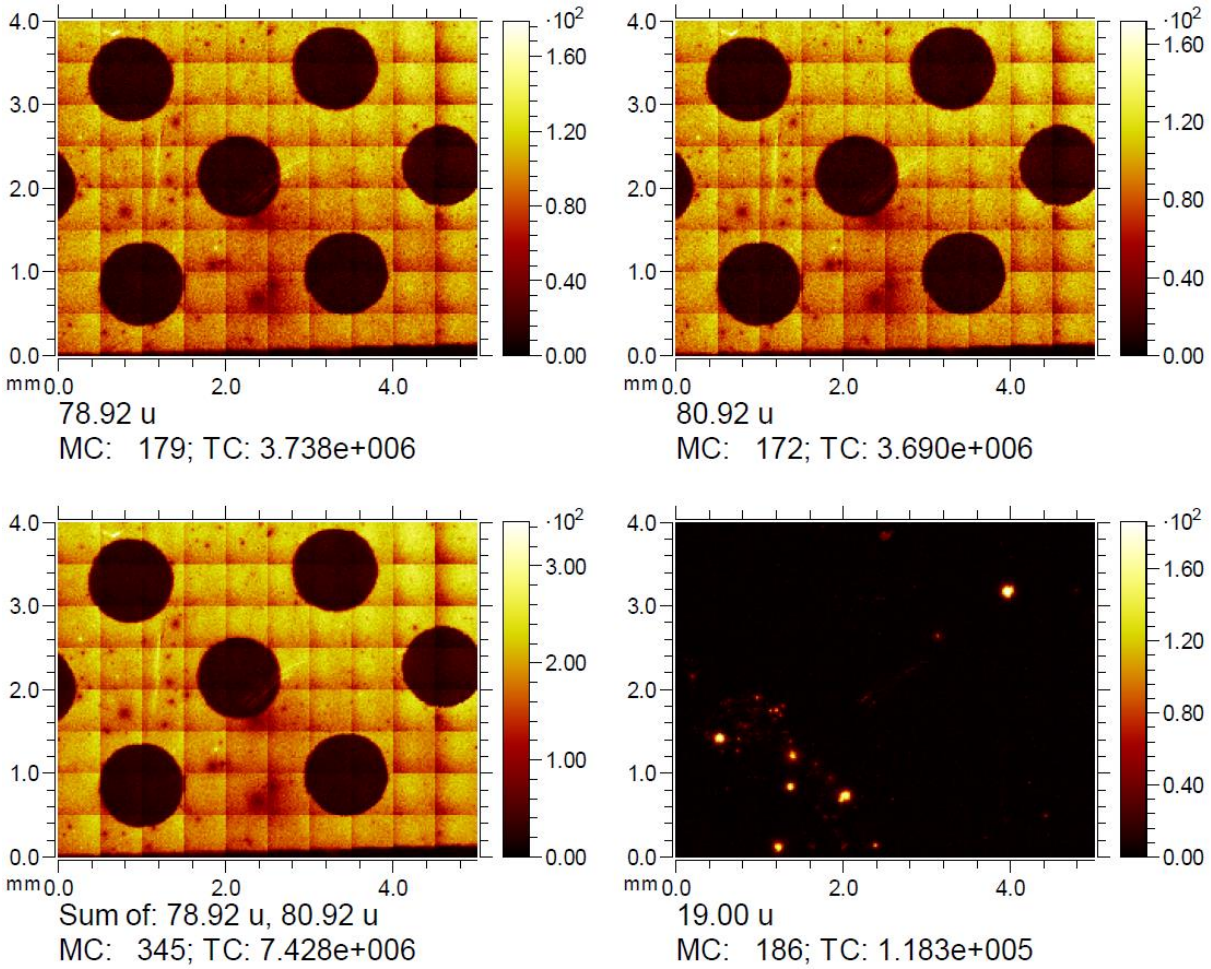

Figure 167 ToF-SIMS image of blank sample of surface **IV** (negative mode).

List of Figures and Schemes

Figures

Schemes

Tables

Abbreviations

3D	Three dimensional
A	Absorbance
APTS	3-Aminopropyltriethoxysilan
AIBN	Azobisisobutyronitrile
Ar	Argon
c	Concentration
CDI	1,1'-Carbonyldiimidazole
CHO	Chinese hamster ovary
cm	centimetre
Da	Dolten
$D_{0,1,n}$	Doublet states
DCC	N N’-Dicyclohexylcarbodiimide
Δ*E*	Stabilization Energy
eq.	equivalent(s)
ESA	Excited state absorption
ESI-MS	Electrospray ionization mass spectrometry
ETU	Energy transfer upconversion
EPR	Electron paramagnetic resonance
FRP	Free radical polymerization
g	Gram
GPC	Gel permeation chromatography
h	Hour
h	Planck's constant
HABA	4’-Hydroxyazobenzene-2- carboxylic acid
HOMO	Highest occupied molecular orbital
HPLC	High performance liquid chromatography
HRMS	High-Resolution-Mass Spectrometry
I	Light intensity
ISC	Intersystem crossing

J	Joule
L	Litre
l	Length of the absorption path
LED	Light-emitting diode
MeCN	Acetonitrile
MA	Methyl acrylate
MMA	Methyl methacrylate
mol	Mole
LUMO	Lowest occupied molecular orbital
NaAsc	Sodium ascorbate
NIR	Near infrared
NITEC	Nitrile imine-mediated tetrazole-ene cycloaddition
nm	Nanometre
NMR	Nuclear magnetic resonance spectroscopy
O	Oxidation agent
PA	Photon avalanche
PAT	Pyrene aryl tetrazole
PCL	Poly-ε-caprolactone
PEG	Polyethylene glycol
PFN	Profluorescent nitroxide
PMMA	Polymethylmethacrylate
PNIPAM	Poly(N-isopropylacrylamide)
ppm	Parts per million
PS	Polystyrene
PROXYL	2,2,5,5-Tetramethylpyrrolidine-1-yloxyl
RDRP	Reversible deactivation radical polymerization
R	Reduction agent
R_f	Retarding-front
ROS	Reactive oxygen species
rt	Room temperature
S_0	Single ground state
S_1	Lowest excited state

SEM	Scanning electron microscope
SOMO	Singly occupied molecular orbital
t	time
T_1	Triplet state
TEMPO	2,2,6,6-Tetramethylpiperidin-1-yloxyl
TMIO	1,1,3,3-Tetramethylisoindoline-2-yloxyl
TLC	Thin layer chromatography
ToF-SIMS	Time-of-Flight Secondary Ion Mass Spectrometry
TPA	Two photon absorption
UCNP	Upconversion nanoparticle
W	Watt
UV-Vis	Ultraviolet–visible spectroscopy
V	Volume
VLPC	Visible light photoredox catalysis
ε	molar extinction coefficient
ν	Frequency
λ	Wavelength
Å	Angstrom
$Đ$	Polydispersity
Φ	Quantum yield

References

(1) Balzani, V.; Credi, A.; Venturi, M. *ChemSusChem* **2008**, *1*, 26.
(2) Wang, W.; Nossoni, Z.; Berbasova, T.; Watson, C. T.; Yapici, I.; Lee, K. S. S.; Vasileiou, C.; Geiger, J. H.; Borhan, B. *Science* **2012**, *338*, 1340.
(3) Sekharan, S.; Katayama, K.; Kandori, H.; Morokuma, K. *Journal of the American Chemical Society* **2012**, *134*, 10706.
(4) Ciamician, G. *Science* **1912**, *36*, 385.
(5) Ehrlich, P. R.; Ehrlich, A. H. *Proceedings of the Royal Society B: Biological Sciences* **2013**, *280*.
(6) V. Balzani, N. A. *Energy for a Sustainable World: From the Oil Age to a Sun-Powered Future*; Wiley-VCH Verlag GmbH: Weinheim, 2010.
(7) Wylie, R. G.; Ahsan, S.; Aizawa, Y.; Maxwell, K. L.; Morshead, C. M.; Shoichet, M. S. *Nat Mater* **2011**, *10*, 799.
(8) Adzima, B. J.; Tao, Y.; Kloxin, C. J.; DeForest, C. A.; Anseth, K. S.; Bowman, C. N. *Nat Chem* **2011**, *3*, 256.
(9) Hiltebrandt, K.; Pauloehrl, T.; Blinco, J. P.; Linkert, K.; Börner, H. G.; Barner-Kowollik, C. *Angewandte Chemie* **2015**, *127*, 2880.
(10) V. Balzani, P. C., A. Juris *Photochemistry and Photophysics. Concepts, Research, Applications.*; Wiley-VCH Verlag GmbH & Co. KGaA, 2014.
(11) Dadashi-Silab, S.; Doran, S.; Yagci, Y. *Chemical Reviews* **2016**.
(12) Quick, A. S.; Rothfuss, H.; Welle, A.; Richter, B.; Fischer, J.; Wegener, M.; Barner-Kowollik, C. *Advanced Functional Materials* **2014**, *24*, 3571.
(13) Song, W.; Wang, Y.; Qu, J.; Madden, M. M.; Lin, Q. *Angewandte Chemie International Edition* **2008**, *47*, 2832.
(14) Song, W.; Wang, Y.; Qu, J.; Lin, Q. *Journal of the American Chemical Society* **2008**, *130*, 9654.
(15) Arndt, S.; Wagenknecht, H.-A. *Angewandte Chemie International Edition* **2014**, *53*, 14580.
(16) Merkel, M.; Peewasan, K.; Arndt, S.; Ploschik, D.; Wagenknecht, H.-A. *ChemBioChem* **2015**, *16*, 1541.
(17) Barner-Kowollik, C.; Du Prez, F. E.; Espeel, P.; Hawker, C. J.; Junkers, T.; Schlaad, H.; Van Camp, W. *Angewandte Chemie International Edition* **2011**, *50*, 60.
(18) Tasdelen, M. A.; Yagci, Y. *Angewandte Chemie International Edition* **2013**, *52*, 5930.
(19) Yoon, T. P.; Ischay, M. A.; Du, J. *Nat Chem* **2010**, *2*, 527.
(20) Szwarc, M. *Nature* **1956**, *178*, 1168.
(21) Stenzel, M. H.; Barner-Kowollik, C. *Materials Horizons* **2016**.
(22) Hirao, A.; Goseki, R.; Ishizone, T. *Macromolecules* **2014**, *47*, 1883.
(23) Mori, H.; Masuda, S.; Endo, T. *Macromolecules* **2006**, *39*, 5976.
(24) Penczek, S. *Journal of Polymer Science Part A: Polymer Chemistry* **2000**, *38*, 1919.
(25) Szwarc, M.; Levy, M.; Milkovich, R. *Journal of the American Chemical Society* **1956**, *78*, 2656.
(26) Nuyken, O.; Pask, S. *Polymers* **2013**, *5*, 361.

(27) Ledwith, A. In *Ions and Ion Pairs and their Role in Chemical Reactions*; Pergamon: 1979, p 159.
(28) Litvinenko, G.; Müller, A. H. E. *Macromolecules* **1997**, *30*, 1253.
(29) Pratt, R. C.; Lohmeijer, B. G. G.; Long, D. A.; Waymouth, R. M.; Hedrick, J. L. *Journal of the American Chemical Society* **2006**, *128*, 4556.
(30) Hsieh, Y. N.; Yu, T. L. *Journal of Applied Polymer Science* **1999**, *73*, 2413.
(31) Knani, D.; Gutman, A. L.; Kohn, D. H. *Journal of Polymer Science Part A: Polymer Chemistry* **1993**, *31*, 1221.
(32) Braunecker, W. A.; Matyjaszewski, K. *Progress in Polymer Science* **2007**, *32*, 93.
(33) Miljevic, B.; Fairfull-Smith, K. E.; Bottle, S. E.; Ristovski, Z. D. *Atmospheric Environment* **2010**, *44*, 2224.
(34) Barner-Kowollik, C. *Handbook of RAFT Polymerization*; Wiley-VCH: Weinheim, 2008.
(35) Moad, G.; Rizzardo, E.; Thang, S. H. *Australian Journal of Chemistry* **2005**, *58*, 379.
(36) Chiefari, J.; Chong, Y. K.; Ercole, F.; Krstina, J.; Jeffery, J.; Le, T. P. T.; Mayadunne, R. T. A.; Meijs, G. F.; Moad, C. L.; Moad, G.; Rizzardo, E.; Thang, S. H. *Macromolecules* **1998**, *31*, 5559.
(37) Moad, G.; Rizzardo, E.; Thang, S. H. *Polymer* **2008**, *49*, 1079.
(38) Geelen, P.; Klumperman, B. *Macromolecules* **2007**, *40*, 3914.
(39) Ladavière, C.; Lacroix-Desmazes, P.; Delolme, F. *Macromolecules* **2009**, *42*, 70.
(40) Liu, J.; Liu, H.; Boyer, C.; Bulmus, V.; Davis, T. P. *Journal of Polymer Science Part A: Polymer Chemistry* **2009**, *47*, 899.
(41) Zhang, L.; Chen, Y. *Polymer* **2006**, *47*, 5259.
(42) Chong, Y. K.; Moad, G.; Rizzardo, E.; Thang, S. H. *Macromolecules* **2007**, *40*, 4446.
(43) Pound, G.; Aguesse, F.; McLeary, J. B.; Lange, R. F. M.; Klumperman, B. *Macromolecules* **2007**, *40*, 8861.
(44) Bernard, J.; Lortie, F.; Fenet, B. *Macromolecular Rapid Communications* **2009**, *30*, 83.
(45) Fleet, R.; McLeary, J. B.; Grumel, V.; Weber, W. G.; Matahwa, H.; Sanderson, R. D. *Macromolecular Symposia* **2007**, *255*, 8.
(46) Merican, Z.; Schiller, T. L.; Hawker, C. J.; Fredericks, P. M.; Blakey, I. *Langmuir* **2007**, *23*, 10539.
(47) Xue, X.; Zhang, W.; Cheng, Z.; Zhu, J.; Zhu, X. *Journal of Polymer Science Part A: Polymer Chemistry* **2008**, *46*, 5626.
(48) Benaglia, M.; Chiefari, J.; Chong, Y. K.; Moad, G.; Rizzardo, E.; Thang, S. H. *Journal of the American Chemical Society* **2009**, *131*, 6914.
(49) Keddie, D. J.; Moad, G.; Rizzardo, E.; Thang, S. H. *Macromolecules* **2012**, *45*, 5321.
(50) Wang, Z.; He, J.; Tao, Y.; Yang, L.; Jiang, H.; Yang, Y. *Macromolecules* **2003**, *36*, 7446.
(51) Scales, C. W.; Convertine, A. J.; McCormick, C. L. *Biomacromolecules* **2006**, *7*, 1389.
(52) Yang, M.; Mao, J.; Nie, W.; Dong, Z.; Wang, D.; Zhao, Z.; Ji, X. *Journal of Polymer Science Part A: Polymer Chemistry* **2012**, *50*, 2075.
(53) Postma, A.; Davis, T. P.; Moad, G.; O'Shea, M. S. *Macromolecules* **2005**, *38*, 5371.

(54) Kaupp, M.; Vogt, A. P.; Natterodt, J. C.; Trouillet, V.; Gruendling, T.; Hofe, T.; Barner, L.; Barner-Kowollik, C. *Polymer Chemistry* **2012**, *3*, 2605.
(55) Xu, J.; He, J.; Fan, D.; Wang, X.; Yang, Y. *Macromolecules* **2006**, *39*, 8616.
(56) Thomas, D. B.; Convertine, A. J.; Hester, R. D.; Lowe, A. B.; McCormick, C. L. *Macromolecules* **2004**, *37*, 1735.
(57) Gruendling, T.; Pickford, R.; Guilhaus, M.; Barner-Kowollik, C. *Journal of Polymer Science Part A: Polymer Chemistry* **2008**, *46*, 7447.
(58) Gregory, A.; Stenzel, M. H. *Progress in Polymer Science* **2012**, *37*, 38.
(59) Adelsberger, J.; Kulkarni, A.; Jain, A.; Wang, W.; Bivigou-Koumba, A. M.; Busch, P.; Pipich, V.; Holderer, O.; Hellweg, T.; Laschewsky, A.; Müller-Buschbaum, P.; Papadakis, C. M. *Macromolecules* **2010**, *43*, 2490.
(60) Xu, X.; Smith, A. E.; Kirkland, S. E.; McCormick, C. L. *Macromolecules* **2008**, *41*, 8429.
(61) Liu, Z.; Hu, J.; Sun, J.; He, G.; Li, Y.; Zhang, G. *Journal of Polymer Science Part A: Polymer Chemistry* **2010**, *48*, 3573.
(62) Inglis, A. J.; Sinnwell, S.; Stenzel, M. H.; Barner-Kowollik, C. *Angewandte Chemie International Edition* **2009**, *48*, 2411.
(63) Li, Y.-G.; Shi, P.-J.; Zhou, Y.; Pan, C.-Y. *Polymer International* **2004**, *53*, 349.
(64) Quinn, J. F.; Chaplin, R. P.; Davis, T. P. *Journal of Polymer Science Part A: Polymer Chemistry* **2002**, *40*, 2956.
(65) Stenzel-Rosenbaum, M.; Davis, T. P.; Chen, V.; Fane, A. G. *Journal of Polymer Science Part A: Polymer Chemistry* **2001**, *39*, 2777.
(66) Stenzel, M. H.; Davis, T. P. *Journal of Polymer Science Part A: Polymer Chemistry* **2002**, *40*, 4498.
(67) Chapman, R.; Jolliffe, K. A.; Perrier, S. *Australian Journal of Chemistry* **2010**, *63*, 1169.
(68) Fischer, H. *Chemical Reviews* **2001**, *101*, 3581.
(69) Wang, Y.; Kwak, Y.; Buback, J.; Buback, M.; Matyjaszewski, K. *ACS Macro Letters* **2012**, *1*, 1367.
(70) Maria, S.; Stoffelbach, F.; Mata, J.; Daran, J.-C.; Richard, P.; Poli, R. *Journal of the American Chemical Society* **2005**, *127*, 5946.
(71) Teodorescu, M.; Gaynor, S. G.; Matyjaszewski, K. *Macromolecules* **2000**, *33*, 2335.
(72) Uegaki, H.; Kotani, Y.; Kamigaito, M.; Sawamoto, M. *Macromolecules* **1997**, *30*, 2249.
(73) Matyjaszewski, K.; Xia, J. *Chemical Reviews* **2001**, *101*, 2921.
(74) Tang, W.; Matyjaszewski, K. *Macromolecules* **2006**, *39*, 4953.
(75) Tang, C.; Kowalewski, T.; Matyjaszewski, K. *Macromolecules* **2003**, *36*, 8587.
(76) Tang, C.; Kowalewski, T.; Matyjaszewski, K. *Macromolecules* **2003**, *36*, 1465.
(77) Matyjaszewski, K. *Macromolecular Symposia* **2003**, *195*, 25.
(78) Matyjaszewski, K.; Shipp, D. A.; Wang, J.-L.; Grimaud, T.; Patten, T. E. *Macromolecules* **1998**, *31*, 6836.
(79) Matyjaszewski, K.; Shipp, D. A.; McMurtry, G. P.; Gaynor, S. G.; Pakula, T. *Journal of Polymer Science Part A: Polymer Chemistry* **2000**, *38*, 2023.
(80) Kowalewski, T.; Tsarevsky, N. V.; Matyjaszewski, K. *Journal of the American Chemical Society* **2002**, *124*, 10632.
(81) Shipp, D. A.; Wang, J.-L.; Matyjaszewski, K. *Macromolecules* **1998**, *31*, 8005.

(82) Matyjaszewski, K.; Jakubowski, W.; Min, K.; Tang, W.; Huang, J.; Braunecker, W. A.; Tsarevsky, N. V. *Proceedings of the National Academy of Sciences* **2006**, *103*, 15309.
(83) Jakubowski, W.; Min, K.; Matyjaszewski, K. *Macromolecules* **2006**, *39*, 39.
(84) Kwak, Y.; Magenau, A. J. D.; Matyjaszewski, K. *Macromolecules* **2011**, *44*, 811.
(85) Kwak, Y.; Matyjaszewski, K. *Polymer International* **2009**, *58*, 242.
(86) Li, X.; Wang, W.-J.; Li, B.-G.; Zhu, S. *Macromolecular Reaction Engineering* **2011**, *5*, 467.
(87) Li, J.; Chen, H.; Mu, G.; Sun, J.; Sun, Y.; Wang, C.; Ren, Q.; Ji, J. *Reactive and Functional Polymers* **2013**, *73*, 1517.
(88) Qian, T.; Wang, J.; Cheng, T.; Zhan, X.; Zhang, Q.; Chen, F. *Journal of Polymer Science Part A: Polymer Chemistry* **2016**, *54*, 2040.
(89) Matyjaszewski, K.; Tsarevsky, N. V. *Journal of the American Chemical Society* **2014**, *136*, 6513.
(90) Inglis, A. J.; Paulöhrl, T.; Barner-Kowollik, C. *Macromolecules* **2010**, *43*, 33.
(91) Jasinski, N.; Lauer, A.; Stals, P. J. M.; Behrens, S.; Essig, S.; Walther, A.; Goldmann, A. S.; Barner-Kowollik, C. *ACS Macro Letters* **2015**, *4*, 298.
(92) Matyjaszewski, K.; Pintauer, T.; Gaynor, S. *Macromolecules* **2000**, *33*, 1476.
(93) Petton, L.; Mes, E. P. C.; Van Der Wal, H.; Claessens, S.; Van Damme, F.; Verbrugghe, S.; Du Prez, F. E. *Polymer Chemistry* **2013**, *4*, 4697.
(94) Morris, J.; Telitel, S.; Fairfull-Smith, K. E.; Bottle, S. E.; Lalevee, J.; Clement, J.-L.; Guillaneuf, Y.; Gigmes, D. *Polymer Chemistry* **2015**, *6*, 754.
(95) Goto, A.; Fukuda, T. *Progress in Polymer Science* **2004**, *29*, 329.
(96) Studer, A.; Harms, K.; Knoop, C.; Müller, C.; Schulte, T. *Macromolecules* **2004**, *37*, 27.
(97) Studer, A.; Schulte, T. *The Chemical Record* **2005**, *5*, 27.
(98) Hawker, C. J.; Bosman, A. W.; Harth, E. *Chemical Reviews* **2001**, *101*, 3661.
(99) Bertin, D.; Chauvin, F.; Marque, S.; Tordo, P. *Macromolecules* **2002**, *35*, 3790.
(100) Benoit, D.; Grimaldi, S.; Robin, S.; Finet, J.-P.; Tordo, P.; Gnanou, Y. *Journal of the American Chemical Society* **2000**, *122*, 5929.
(101) Steenbock M, K. M., Muellen K. *Macromol Chem Phys* **1998**, *199*.
(102) Chung, T. C.; Janvikul, W.; Lu, H. L. *Journal of the American Chemical Society* **1996**, *118*, 705.
(103) Druliner, J. D. *Macromolecules* **1991**, *24*, 6079.
(104) Le Grognec, E.; Claverie, J.; Poli, R. *Journal of the American Chemical Society* **2001**, *123*, 9513.
(105) Braunecker, W. A.; Itami, Y.; Matyjaszewski, K. *Macromolecules* **2005**, *38*, 9402.
(106) Tebben, L.; Studer, A. *Angewandte Chemie International Edition* **2011**, *50*, 5034.
(107) Piloty, O.; Schwerin, B. G. *Berichte der deutschen chemischen Gesellschaft* **1901**, *34*, 1863.
(108) H. Wieland, M. O. *Ber. Dtsch. Chem. Ges.* **1914**, *47*.
(109) O. L. Lebedev, S. N. K. *Khim. Khim. Tekhnol.* **1959**, *3*, 649.
(110) O. L. Lebedev, S. N. K. *Chem. Abstr.* **1962**, *56*, 15479.
(111) Forrester, A. R.; Thomson, R. H. *Nature* **1964**, *203*, 74.

(112) Ovcharenko, L. B. V. V. A. R. V. I. *Synthetic chemistry of stable nitroxide*; CRC Pres: New York, 1994.
(113) Eli Breuer, H. G. A., Arnold Nielsen *Nitrones, Nitronates and Nitroxides*; John Wiley & Sons, 1989.
(114) Nickolai Kocherginsky, H. M. S. *Nitroxide Spin Labels: Reactions in Biology and Chemistry*; CRC Press 1995.
(115) Griffiths, P.; Moad, G.; Rizzardo, E. *Australian Journal of Chemistry* **1983**, *36*, 397.
(116) E., B. S.; Ugesh, C.; S., M. A. *Chemistry Letters* **1997**, *26*, 857.
(117) Likhtenstein, G. I.; Ishii, K.; Nakatsuji, S. i. *Photochemistry and Photobiology* **2007**, *83*, 871.
(118) Blinco, J. P.; Fairfull-Smith, K. E.; Morrow, B. J.; Bottle, S. E. *Australian Journal of Chemistry* **2011**, *64*, 373.
(119) L. Stryer, H. O. G. *Proc. Natl. Acad. Sci. USA* **1965**, *54*.
(120) I. M. Bystryak, G. I. L., A. I. Kotelnikov, O. H.; Hankovsky, K. H. *Russ. J. Phys. Chem.* **1986**, *60*.
(121) Gerlock, J. L.; Zacmanidis, P. J.; Bauer, D. R.; Simpson, D. J.; Blough, N. V.; Salmeen, I. T. *Free Radical Research Communications* **1990**, *10*, 119.
(122) Green, S. A.; Simpson, D. J.; Zhou, G.; Ho, P. S.; Blough, N. V. *Journal of the American Chemical Society* **1990**, *112*, 7337.
(123) Blough, N. V.; Simpson, D. J. *Journal of the American Chemical Society* **1988**, *110*, 1915.
(124) Abrams, F. S.; London, E. *Biochemistry* **1993**, *32*, 10826.
(125) Asuncion-Punzalan, E.; London, E. *Biochemistry* **1995**, *34*, 11460.
(126) Kaiser, R. D.; London, E. *Biochemistry* **1998**, *37*, 8180.
(127) K. Kachel, E. A.-P., E. London *Biochemistry* **1995**, *34*.
(128) Micallef, A. S.; Blinco, J. P.; George, G. A.; Reid, D. A.; Rizzardo, E.; Thang, S. H.; Bottle, S. E. *Polymer Degradation and Stability* **2005**, *89*, 427.
(129) Coenjarts, C.; García, O.; Llauger, L.; Palfreyman, J.; Vinette, A. L.; Scaiano, J. C. *Journal of the American Chemical Society* **2002**, *125*, 620.
(130) Ballesteros, O. G.; Maretti, L.; Sastre, R.; Scaiano, J. C. *Macromolecules* **2001**, *34*, 6184.
(131) Yang, X.-F.; Guo, X.-Q. *Analyst* **2001**, *126*, 1800.
(132) Jockusch, S.; Dedola, G.; Lem, G.; Turro, N. J. *The Journal of Physical Chemistry B* **1999**, *103*, 9126.
(133) Sato, S.; Suzuki, M.; Soma, T.; Tsunoda, M. *Spectrochim Acta A Mol Biomol Spectrosc* **2008**, *70*, 799.
(134) Bueno, C.; Mikelsons, L.; Maretti, L.; Scaiano, J. C.; Aspée, A. *Photochemistry and Photobiology* **2008**, *84*, 1535.
(135) Toniolo, C.; Crisma, M.; Formaggio, F. *Peptide Science* **1998**, *47*, 153.
(136) Pispisa, B.; Mazzuca, C.; Palleschi, A.; Stella, L.; Venanzi, M.; Wakselman, M.; Mazaleyrat, J.-P.; Rainaldi, M.; Formaggio, F.; Toniolo, C. *Chemistry – A European Journal* **2003**, *9*, 4084.
(137) Bognár, B.; Øz, E.; Hideg, K.; Kálai, T. *Journal of Heterocyclic Chemistry* **2006**, *43*, 81.
(138) Kálai, T.; Hideg, É.; Vass, I.; Hideg, K. *Free Radical Biology and Medicine* **1998**, *24*, 649.
(139) Hideg, É.; Kálai, T.; Hideg, K.; Vass, I. *Biochemistry* **1998**, *37*, 11405.
(140) Lozinsky, E.; Martin, V. V.; Berezina, T. A.; Shames, A. I.; Weis, A. L.; Likhtenshtein, G. I. *Journal of Biochemical and Biophysical Methods* **1999**, *38*, 29.

(141) Keddie, D. J.; Johnson, T. E.; Arnold, D. P.; Bottle, S. E. *Organic & Biomolecular Chemistry* **2005**, *3*, 2593.
(142) Kálai, T.; Balog, M.; Jekő, J.; Hubbell, W. L.; Hideg, K. *Synthesis* **2002**, *2002*, 2365.
(143) Keddie, D. J.; Fairfull-Smith, K. E.; Bottle, S. E. *Organic & Biomolecular Chemistry* **2008**, *6*, 3135.
(144) Fairfull-Smith, K. E.; Blinco, J. P.; Keddie, D. J.; George, G. A.; Bottle, S. E. *Macromolecules* **2008**, *41*, 1577.
(145) Fairfull-Smith, K. E.; Bottle, S. E. *European Journal of Organic Chemistry* **2008**, *2008*, 5391.
(146) Stroh, C.; Mayor, M.; von Hänisch, C. *European Journal of Organic Chemistry* **2005**, *2005*, 3697.
(147) Morris, J. C.; McMurtrie, J. C.; Bottle, S. E.; Fairfull-Smith, K. E. *The Journal of Organic Chemistry* **2011**, *76*, 4964.
(148) Martins, C. D. M. G.; Barcarolli, I. F.; de Menezes, E. J.; Giacomin, M. M.; Wood, C. M.; Bianchini, A. *Aquatic Toxicology* **2011**, *101*, 88.
(149) Lozinsky, E.; Martin, V. V.; Berezina, T. A.; Shames, A. I.; Weis, A. L.; Likhtenshtein, G. I. *Journal of biochemical and biophysical methods* **1999**, *38*, 29.
(150) Ahn, H.-Y.; Fairfull-Smith, K. E.; Morrow, B. J.; Lussini, V.; Kim, B.; Bondar, M. V.; Bottle, S. E.; Belfield, K. D. *Journal of the American Chemical Society* **2012**, *134*, 4721.
(151) Lozinsky, E.; Novoselsky, A.; Shames, A. I.; Saphier, O.; Likhtenshtein, G. I.; Meyerstein, D. *Biochimica et Biophysica Acta (BBA) - General Subjects* **2001**, *1526*, 53.
(152) Saphier, O.; Silberstein, T.; Shames, A. I.; Likhtenshtein, G. I.; Maimon, E.; Mankuta, D.; Mazor, M.; Katz, M.; Meyerstein, D.; Meyerstein, N. *Free Radical Research* **2003**, *37*, 301.
(153) Sylvester, P. D.; Ryan, H. E.; Smith, C. D.; Micallef, A. S.; Schiesser, C. H.; Wille, U. *Polymer Degradation and Stability* **2013**, *98*, 2054.
(154) Blinco, J. P.; Keddie, D. J.; Wade, T.; Barker, P. J.; George, G. A.; Bottle, S. E. *Polymer Degradation and Stability* **2008**, *93*, 1613.
(155) Moghaddam, L.; Blinco, J. P.; Colwell, J. M.; Halley, P. J.; Bottle, S. E.; Fredericks, P. M.; George, G. A. *Polymer Degradation and Stability* **2011**, *96*, 455.
(156) Colwell, J. M.; Walker, J. R.; Blinco, J. P.; Micallef, A. S.; George, G. A.; Bottle, S. E. *Polymer Degradation and Stability* **2010**, *95*, 2101.
(157) Braslau, R.; Rivera, F.; Lilie, E.; Cottman, M. *The Journal of Organic Chemistry* **2013**, *78*, 238.
(158) Lussini, V. C.; Blinco, J. P.; Fairfull-Smith, K. E.; Bottle, S. E. *Chemistry – A European Journal* **2015**, *21*, 18258.
(159) Aspée, A.; García, O.; Maretti, L.; Sastre, R.; Scaiano, J. C. *Macromolecules* **2003**, *36*, 3550.
(160) Stevanovic, S.; Miljevic, B.; Surawski, N. C.; Fairfull-Smith, K. E.; Bottle, S. E.; Brown, R.; Ristovski, Z. D. *Environmental Science & Technology* **2013**, *47*, 7655.
(161) Miljevic, B.; Heringa, M. F.; Keller, A.; Meyer, N. K.; Good, J.; Lauber, A.; DeCarlo, P. F.; Fairfull-Smith, K. E.; Nussbaumer, T.; Burtscher, H.; Prevot, A. S. H.; Baltensperger, U.; Bottle, S. E.; Ristovski, Z. D. *Environmental Science & Technology* **2010**, *44*, 6601.

(162) Alaghmand, M.; Blough, N. V. *Environmental Science & Technology* **2007**, *41*, 2364.
(163) Wedler, G. *Lehrbuch der Physicalischen Chemie*; Wiley-VCH, 1997.
(164) Becker, H. G. O. *Einführung in die Photochemie*; Georg Thieme Verlag 1983.
(165) Rückamp, R.; Benckiser, E.; Haverkort, M. W.; Roth, H.; Lorenz, T.; Freimuth, A.; Jongen, L.; Möller, A.; Meyer, G.; Reutler, P.; Büchner, B.; Revcolevschi, A.; Cheong, S. W.; Sekar, C.; Krabbes, G.; Grüninger, M. *New Journal of Physics* **2005**, *7*, 144.
(166) Porter, G.; Tchir, M. F. *Journal of the Chemical Society D: Chemical Communications* **1970**, 1372.
(167) Porter, G.; Tchir, M. F. *Journal of the Chemical Society A: Inorganic, Physical, Theoretical* **1971**, 3772.
(168) Pauloehrl, T.; Delaittre, G.; Winkler, V.; Welle, A.; Bruns, M.; Börner, H. G.; Greiner, A. M.; Bastmeyer, M.; Barner-Kowollik, C. *Angewandte Chemie International Edition* **2012**, *51*, 1071.
(169) Tischer, T.; Claus, T. K.; Bruns, M.; Trouillet, V.; Linkert, K.; Rodriguez-Emmenegger, C.; Goldmann, A. S.; Perrier, S.; Börner, H. G.; Barner-Kowollik, C. *Biomacromolecules* **2013**, *14*, 4340.
(170) Preuss, C. M.; Tischer, T.; Rodriguez-Emmenegger, C.; Zieger, M. M.; Bruns, M.; Goldmann, A. S.; Barner-Kowollik, C. *Journal of Materials Chemistry B* **2014**, *2*, 36.
(171) Stolzer, L.; Quick, A. S.; Abt, D.; Welle, A.; Naumenko, D.; Lazzarino, M.; Wegener, M.; Barner-Kowollik, C.; Fruk, L. *Chemical Communications* **2015**, *51*, 3363.
(172) Winkler, M.; Mueller, J. O.; Oehlenschlaeger, K. K.; Montero de Espinosa, L.; Meier, M. A. R.; Barner-Kowollik, C. *Macromolecules* **2012**, *45*, 5012.
(173) Tyson, D. S.; Ilhan, F.; Meador, M. A. B.; Smith, D. D.; Scheiman, D. A.; Meador, M. A. *Macromolecules* **2005**, *38*, 3638.
(174) Grosch, B.; Orlebar, C. N.; Herdtweck, E.; Massa, W.; Bach, T. *Angewandte Chemie International Edition* **2003**, *42*, 3693.
(175) Oehlenschlaeger, K. K.; Mueller, J. O.; Heine, N. B.; Glassner, M.; Guimard, N. K.; Delaittre, G.; Schmidt, F. G.; Barner-Kowollik, C. *Angewandte Chemie International Edition* **2013**, *52*, 762.
(176) Hiltebrandt, K.; Elies, K.; D'hooge, D. R.; Blinco, J. P.; Barner-Kowollik, C. *Journal of the American Chemical Society* **2016**, *138*, 7048.
(177) Mukhina, O. A.; Kuznetsov, D. M.; Cowger, T. M.; Kutateladze, A. G. *Angewandte Chemie International Edition* **2015**, *54*, 11516.
(178) Clovis, J. S.; Eckell, A.; Huisgen, R.; Sustmann, R. *Chemische Berichte* **1967**, *100*, 60.
(179) Mueller, J. O.; Guimard, N. K.; Oehlenschlaeger, K. K.; Schmidt, F. G.; Barner-Kowollik, C. *Polymer Chemistry* **2014**, *5*, 1447.
(180) Mueller, J. O.; Voll, D.; Schmidt, F. G.; Delaittre, G.; Barner-Kowollik, C. *Chemical Communications* **2014**, *50*, 15681.
(181) Dürr, C. J.; Lederhose, P.; Hlalele, L.; Abt, D.; Kaiser, A.; Brandau, S.; Barner-Kowollik, C. *Macromolecules* **2013**, *46*, 5915.
(182) Wang, Y.; Hu, W. J.; Song, W.; Lim, R. K. V.; Lin, Q. *Organic Letters* **2008**, *10*, 3725.
(183) Blasco, E.; Piñol, M.; Oriol, L.; Schmidt, B. V. K. J.; Welle, A.; Trouillet, V.; Bruns, M.; Barner-Kowollik, C. *Advanced Functional Materials* **2013**, *23*, 4011.

(184) Tischer, T.; Rodriguez-Emmenegger, C.; Trouillet, V.; Welle, A.; Schueler, V.; Mueller, J. O.; Goldmann, A. S.; Brynda, E.; Barner-Kowollik, C. *Advanced Materials* **2014**, *26*, 4087.
(185) Mrowczynski, R.; Magerusan, L.; Turcu, R.; Liebscher, J. *Polymer Chemistry* **2014**, *5*, 6593.
(186) Rodriguez-Emmenegger, C.; Preuss, C. M.; Yameen, B.; Pop-Georgievski, O.; Bachmann, M.; Mueller, J. O.; Bruns, M.; Goldmann, A. S.; Bastmeyer, M.; Barner-Kowollik, C. *Advanced Materials* **2013**, *25*, 6123.
(187) Wang, Y.; Rivera Vera, C. I.; Lin, Q. *Organic Letters* **2007**, *9*, 4155.
(188) Vollhardt, K. P. C. *Organische Chemie*, 2011.
(189) Wang, Y.; Song, W.; Hu, W. J.; Lin, Q. *Angewandte Chemie International Edition* **2009**, *48*, 5330.
(190) Li, Z.; Qian, L.; Li, L.; Bernhammer, J. C.; Huynh, H. V.; Lee, J.-S.; Yao, S. Q. *Angewandte Chemie International Edition* **2016**, *55*, 2002.
(191) Feng, W.; Li, L.; Yang, C.; Welle, A.; Trapp, O.; Levkin, P. A. *Angewandte Chemie International Edition* **2015**, *54*, 8732.
(192) Zhang, Y.; Liu, W.; Zhao, Z. *Molecules* **2014**, *19*, 306.
(193) Zheng, S.-L.; Wang, Y.; Yu, Z.; Lin, Q.; Coppens, P. *Journal of the American Chemical Society* **2009**, *131*, 18036.
(194) Willenbacher, J.; Wuest, K. N. R.; Mueller, J. O.; Kaupp, M.; Wagenknecht, H.-A.; Barner-Kowollik, C. *ACS Macro Letters* **2014**, *3*, 574.
(195) San Miguel, V.; Bochet, C. G.; del Campo, A. *Journal of the American Chemical Society* **2011**, *133*, 5380.
(196) Franklin, J. M.; Surampudi, L. N.; Ashbaugh, H. S.; Pozzo, D. C. *Langmuir* **2012**, *28*, 12593.
(197) Inui, H.; Murata, S. *Journal of the American Chemical Society* **2005**, *127*, 2628.
(198) Hiltebrandt, K.; Kaupp, M.; Molle, E.; Menzel, J. P.; Blinco, J. P.; Barner-Kowollik, C. *Chemical Communications* **2016**, *52*, 9426.
(199) Padwa, A.; Smolanoff, J. *Journal of the American Chemical Society* **1971**, *93*, 548.
(200) Albrecht, E.; Mattay, J.; Steenken, S. *Journal of the American Chemical Society* **1997**, *119*, 11605.
(201) Padwa, A. *Accounts of Chemical Research* **1976**, *9*, 371.
(202) Lim, R. K. V.; Lin, Q. *Chemical Communications* **2010**, *46*, 7993.
(203) Wagenknecht, H.-A. *ChemPhysChem* **2013**, *14*, 3197.
(204) Mueller, J. O.; Schmidt, F. G.; Blinco, J. P.; Barner-Kowollik, C. *Angewandte Chemie International Edition* **2015**, *54*, 10375.
(205) An, P.; Yu, Z.; Lin, Q. *Chemical Communications* **2013**, *49*, 9920.
(206) An, P.; Yu, Z.; Lin, Q. *Organic Letters* **2013**, *15*, 5496.
(207) Yu, Z.; Ho, L. Y.; Wang, Z.; Lin, Q. *Bioorganic & Medicinal Chemistry Letters* **2011**, *21*, 5033.
(208) Lauer, A.; Fast, D. E.; Kelterer, A.-M.; Frick, E.; Neshchadin, D.; Voll, D.; Gescheidt, G.; Barner-Kowollik, C. *Macromolecules* **2015**, *48*, 8451.
(209) P. W. Atkins, J. d. P. *Pydikalische Chemie*, 2010.
(210) Ried, W.; Hillenbrand, H. *Justus Liebigs Annalen der Chemie* **1954**, *590*, 128.
(211) Nicewicz, D. A.; MacMillan, D. W. C. *Science* **2008**, *322*, 77.
(212) Ischay, M. A.; Anzovino, M. E.; Du, J.; Yoon, T. P. *Journal of the American Chemical Society* **2008**, *130*, 12886.

(213) Narayanam, J. M. R.; Tucker, J. W.; Stephenson, C. R. J. *Journal of the American Chemical Society* **2009**, *131*, 8756.
(214) Ma, Z.; Wang, X.; Wang, X.; Rodriguez, R. A.; Moore, C. E.; Gao, S.; Tan, X.; Ma, Y.; Rheingold, A. L.; Baran, P. S.; Chen, C. *Science* **2014**, *346*, 219.
(215) Ghosh, I.; Ghosh, T.; Bardagi, J. I.; König, B. *Science* **2014**, *346*, 725.
(216) Pirnot, M. T.; Rankic, D. A.; Martin, D. B. C.; MacMillan, D. W. C. *Science* **2013**, *339*, 1593.
(217) Fidaly, K.; Ceballos, C.; Falguieres, A.; Veitia, M. S.-I.; Guy, A.; Ferroud, C. *Green Chemistry* **2012**, *14*, 1293.
(218) Angnes, R. A.; Li, Z.; Correia, C. R. D.; Hammond, G. B. *Organic & Biomolecular Chemistry* **2015**, *13*, 9152.
(219) Romero, N. A.; Nicewicz, D. A. *Chemical Reviews* **2016**.
(220) Shen, T.; Zhao, Z.-G.; Yu, Q.; Xu, H.-J. *Journal of Photochemistry and Photobiology A: Chemistry* **1989**, *47*, 203.
(221) Discekici, E. H.; Treat, N. J.; Poelma, S. O.; Mattson, K. M.; Hudson, Z. M.; Luo, Y.; Hawker, C. J.; de Alaniz, J. R. *Chemical Communications* **2015**, *51*, 11705.
(222) Eisenhart, T. T.; Dempsey, J. L. *Journal of the American Chemical Society* **2014**, *136*, 12221.
(223) Prier, C. K.; Rankic, D. A.; MacMillan, D. W. C. *Chemical Reviews* **2013**, *113*, 5322.
(224) Göppert-Mayer, M. *Naturwissenschaften* **1929**, *17*, 932.
(225) Göppert-Mayer, M. *Ann. Phys.* **1931**, *9*.
(226) Hughes, V. G., L. *Phys. Rev.* **1950**, *79*.
(227) Kaiser, W.; Garrett, C. G. B. *Physical Review Letters* **1961**, *7*, 229.
(228) Peticolas, W. L.; Goldsborough, J. P.; Rieckhoff, K. E. *Physical Review Letters* **1963**, *10*, 43.
(229) Zipfel, W. R.; Williams, R. M.; Webb, W. W. *Nat Biotech* **2003**, *21*, 1369.
(230) Pawlicki, M.; Collins, H. A.; Denning, R. G.; Anderson, H. L. *Angewandte Chemie International Edition* **2009**, *48*, 3244.
(231) Birge, R. R.; Pierce, B. M. *International Journal of Quantum Chemistry* **1986**, *29*, 639.
(232) He, G. S.; Tan, L.-S.; Zheng, Q.; Prasad, P. N. *Chemical Reviews* **2008**, *108*, 1245.
(233) Birch, D. J. S. *Spectrochimica Acta Part A: Molecular and Biomolecular Spectroscopy* **2001**, *57*, 2313.
(234) Harvey, C. D.; Svoboda, K. *Nature* **2007**, *450*, 1195.
(235) Gug, S.; Charon, S.; Specht, A.; Alarcon, K.; Ogden, D.; Zietz, B.; Léonard, J.; Haacke, S.; Bolze, F.; Nicoud, J.-F.; Goeldner, M. *ChemBioChem* **2008**, *9*, 1303.
(236) Wecksler, S.; Mikhailovsky, A.; Ford, P. C. *Journal of the American Chemical Society* **2004**, *126*, 13566.
(237) LaFratta, C. N.; Fourkas, J. T.; Baldacchini, T.; Farrer, R. A. *Angewandte Chemie International Edition* **2007**, *46*, 6238.
(238) Scrimgeour, J.; Sharp, D. N.; Blanford, C. F.; Roche, O. M.; Denning, R. G.; Turberfield, A. J. *Advanced Materials* **2006**, *18*, 1557.
(239) Tétreault, N.; von Freymann, G.; Deubel, M.; Hermatschweiler, M.; Pérez-Willard, F.; John, S.; Wegener, M.; Ozin, G. A. *Advanced Materials* **2006**, *18*, 457.
(240) Walker, E.; Rentzepis, P. M. *Nat Photon* **2008**, *2*, 406.

(241) Dy, J. T.; Maeda, R.; Nagatsuka, Y.; Ogawa, K.; Kamada, K.; Ohta, K.; Kobuke, Y. *Chemical Communications* **2007**, 5170.
(242) Yu, Z.; Ohulchanskyy, T. Y.; An, P.; Prasad, P. N.; Lin, Q. *Journal of the American Chemical Society* **2013**, *135*, 16766.
(243) Urdabayev, N. K.; Poloukhtine, A.; Popik, V. V. *Chemical Communications* **2006**, 454.
(244) Belfield, K. D.; Bondar, M. V.; Liu, Y.; Przhonska, O. V. *Journal of Physical Organic Chemistry* **2003**, *16*, 69.
(245) Parthenopoulos, D. A.; Rentzepis, P. M. *Science* **1989**, *245*, 843.
(246) Belfield, K. D.; Liu, Y.; Negres, R. A.; Fan, M.; Pan, G.; Hagan, D. J.; Hernandez, F. E. *Chemistry of Materials* **2002**, *14*, 3663.
(247) Sekkat, Z.; Ishitobi, H.; Kawata, S. *Optics Communications* **2003**, *222*, 269.
(248) Cumpston, B. H.; Ananthavel, S. P.; Barlow, S.; Dyer, D. L.; Ehrlich, J. E.; Erskine, L. L.; Heikal, A. A.; Kuebler, S. M.; Lee, I. Y. S.; McCord-Maughon, D.; Jinqui, Q.; Röckel, H.; Rumi, M.; Xiang-Li, W.; Marder, S. R.; Perry, J. W. *Nature* **1999**, *398*, 51.
(249) Carling, C.-J.; Boyer, J.-C.; Branda, N. R. *Journal of the American Chemical Society* **2009**, *131*, 10838.
(250) Chivian, J. S.; Case, W. E.; Eden, D. D. *Applied Physics Letters* **1979**, *35*, 124.
(251) Auzel, F. *Chemical Reviews* **2004**, *104*, 139.
(252) Wang, F.; Liu, X. *Chemical Society Reviews* **2009**, *38*, 976.
(253) Heer, S.; Kömpe, K.; Güdel, H. U.; Haase, M. *Advanced Materials* **2004**, *16*, 2102.
(254) Haase, M.; Schäfer, H. *Angewandte Chemie International Edition* **2011**, *50*, 5808.
(255) Han, S.; Deng, R.; Xie, X.; Liu, X. *Angewandte Chemie International Edition* **2014**, *53*, 11702.
(256) Jayakumar, M. K. G.; Idris, N. M.; Zhang, Y. *Proceedings of the National Academy of Sciences* **2012**, *109*, 8483.
(257) Yang, Y.; Shao, Q.; Deng, R.; Wang, C.; Teng, X.; Cheng, K.; Cheng, Z.; Huang, L.; Liu, Z.; Liu, X.; Xing, B. *Angewandte Chemie International Edition* **2012**, *51*, 3125.
(258) Chien, Y.-H.; Chou, Y.-L.; Wang, S.-W.; Hung, S.-T.; Liau, M.-C.; Chao, Y.-J.; Su, C.-H.; Yeh, C.-S. *ACS Nano* **2013**, *7*, 8516.
(259) Zhao, L.; Peng, J.; Huang, Q.; Li, C.; Chen, M.; Sun, Y.; Lin, Q.; Zhu, L.; Li, F. *Advanced Functional Materials* **2014**, *24*, 363.
(260) Ruggiero, E.; Habtemariam, A.; Yate, L.; Mareque-Rivas, J. C.; Salassa, L. *Chemical Communications* **2014**, *50*, 1715.
(261) Chen, Z.; Sun, W.; Butt, H.-J.; Wu, S. *Chemistry – A European Journal* **2015**, *21*, 9165.
(262) Wu, S.; Butt, H.-J. *Advanced Materials* **2016**, *28*, 1208.
(263) Abdul Jalil, R.; Zhang, Y. *Biomaterials* **2008**, *29*, 4122.
(264) Chatterjee, D. K.; Rufaihah, A. J.; Zhang, Y. *Biomaterials* **2008**, *29*, 937.
(265) Nyk, M.; Kumar, R.; Ohulchanskyy, T. Y.; Bergey, E. J.; Prasad, P. N. *Nano Letters* **2008**, *8*, 3834.
(266) Shan, J.; Chen, J.; Meng, J.; Collins, J.; Soboyejo, W.; Friedberg, J. S.; Ju, Y. *Journal of Applied Physics* **2008**, *104*, 094308.
(267) Liu, G.; Zhou, L.; Su, Y.; Dong, C.-M. *Chemical Communications* **2014**, *50*, 12538.

(268) Stepuk, A.; Mohn, D.; Grass, R. N.; Zehnder, M.; Krämer, K. W.; Pellé, F.; Ferrier, A.; Stark, W. J. *Dental Materials* **2012**, *28*, 304.
(269) Scheps, R. *Progress in Quantum Electronics* **1996**, *20*, 271.
(270) Armstrong, J. A.; Bloembergen, N.; Ducuing, J.; Pershan, P. S. *Physical Review* **1962**, *127*, 1918.
(271) Dalton, L. R.; Harper, A. W.; Ghosn, R.; Steier, W. H.; Ziari, M.; Fetterman, H.; Shi, Y.; Mustacich, R. V.; Jen, A. K. Y.; Shea, K. J. *Chemistry of Materials* **1995**, *7*, 1060.
(272) Zipfel, W. R.; Williams, R. M.; Christie, R.; Nikitin, A. Y.; Hyman, B. T.; Webb, W. W. *Proceedings of the National Academy of Sciences* **2003**, *100*, 7075.
(273) Lederhose, P.; Haworth, N. L.; Thomas, K.; Bottle, S. E.; Coote, M. L.; Barner-Kowollik, C.; Blinco, J. P. *The Journal of Organic Chemistry* **2015**, *80*, 8009.
(274) Weiss, D. S. *Journal of Photochemistry* **1976**, *6*, 301.
(275) Watkins, A. R. *Chemical Physics Letters* **1974**, *29*, 526.
(276) Chattopadhyay, S. K.; Das, P. K.; Hug, G. L. *Journal of the American Chemical Society* **1983**, *105*, 6205.
(277) Fenton, H. J. H. *Journal of the Chemical Society, Transactions* **1894**, *65*, 899.
(278) Gerlock, J. L.; Zacmanidis, P. J.; Bauer, D. R.; Simpson, D. J.; Blough, N. V.; Salmeen, I. T. *Free Radical Research* **1990**, *10*, 119.
(279) Lederhose, P.; Wust, K. N. R.; Barner-Kowollik, C.; Blinco, J. P. *Chemical Communications* **2016**, *52*, 5928.
(280) Hsiao, J. S.; Webber, S. E. *The Journal of Physical Chemistry* **1992**, *96*, 2892.
(281) Tanaka, E.; Choi, H.; Fujii, H.; Bawendi, M.; Frangioni, J. *Ann Surg Oncol* **2006**, *13*, 1671.
(282) Choi, H. S.; Nasr, K.; Alyabyev, S.; Feith, D.; Lee, J. H.; Kim, S. H.; Ashitate, Y.; Hyun, H.; Patonay, G.; Strekowski, L.; Henary, M.; Frangioni, J. V. *Angewandte Chemie International Edition* **2011**, *50*, 6258.
(283) Choi, H. S.; Gibbs, S. L.; Lee, J. H.; Kim, S. H.; Ashitate, Y.; Liu, F.; Hyun, H.; Park, G.; Xie, Y.; Bae, S.; Henary, M.; Frangioni, J. V. *Nat Biotech* **2013**, *31*, 148.
(284) Lederhose, P.; Chen, Z.; Müller, R.; Blinco, J. P.; Wu, S.; Barner-Kowollik, C. *Angewandte Chemie International Edition* **2016**, n/a.
(285) Ulbricht, J.; Jordan, R.; Luxenhofer, R. *Biomaterials* **2014**, *35*, 4848.
(286) Kolb, H. C.; Finn, M. G.; Sharpless, K. B. *Angewandte Chemie International Edition* **2001**, *40*, 2004.
(287) Thomas, K.; Chalmers, B. A.; Fairfull-Smith, K. E.; Bottle, S. E. *European Journal of Organic Chemistry* **2013**, *2013*, 853.
(288) Zhao, Y.; Truhlar, D. G. *The Journal of Chemical Physics* **2006**, *125*, 194101.
(289) Frisch, M. J.; Trucks, G. W.; Schlegel, H. B.; Scuseria, G. E.; Robb, M. A.; Cheeseman, J. R.; Scalmani, G.; Barone, V.; Mennucci, B.; Petersson, G. A.; Nakatsuji, H.; Caricato, M.; Li, X.; Hratchian, H. P.; Izmaylov, A. F.; Bloino, J.; Zheng, G.; Sonnenberg, J. L.; Hada, M.; Ehara, M.; Toyota, K.; Fukuda, R.; Hasegawa, J.; Ishida, M.; Nakajima, T.; Honda, Y.; Kitao, O.; Nakai, H.; Vreven, T.; Montgomery, J. A., Jr.; Peralta, J. E.; Ogliaro, F.; Bearpark, M.; Heyd, J. J.; Brothers, E.; Kudin, K. N.; Staroverov, V. N.; Kobayashi, R.; Normand, J.; Raghavachari, K.; Rendell, A.; Burant, J. C.;

Iyengar, S. S.; Tomasi, J.; Cossi, M.; Rega, N.; Millam, J. M.; Klene, M.; Knox, J. E.; Cross, J. B.; Bakken, V.; Adamo, C.; Jaramillo, J.; Gomperts, R.; Stratmann, R. E.; Yazyev, O.; Austin, A. J.; Cammi, R.; Pomelli, C.; Ochterski, J. W.; Martin, R. L.; Morokuma, K.; Zakrzewski, V. G.; Voth, G. A.; Salvador, P.; Dannenberg, J. J.; Dapprich, S.; Daniels, A. D.; Farkas, O.; Foresman, J. B.; Ortiz, J. V.; Cioslowski, J.; Fox, D. J. *Gaussian 09* **2009**, Gaussian, Inc.: Wallingford, CT.

(290) Heath, W. H.; Palmieri, F.; Adams, J. R.; Long, B. K.; Chute, J.; Holcombe, T. W.; Zieren, S.; Truitt, M. J.; White, J. L.; Willson, C. G. *Macromolecules* **2008**, *41*, 719.

(291) Wuest, K. N. R.; Trouillet, V.; Goldmann, A. S.; Stenzel, M. H.; Barner-Kowollik, C. *Macromolecules* **2016**.

(292) He, S.; Krippes, K.; Ritz, S.; Chen, Z.; Best, A.; Butt, H.-J.; Mailander, V.; Wu, S. *Chemical Communications* **2015**, *51*, 431.

Acknowledgemts

It would take another 300 pages to acknowledge everyone who has contributed to my accomplishments as a scientist in an appropriate way. However, I will try to express my deep gratitude to everyone, who has supported me through the last couple years in a few sentences. Firstly, I would like to thank my supervisors Dr. James P. Blinco (QUT) and Prof. Christopher Barner-Kowollik (KIT) for their support and trust in me. Thank you for inspiring me, for guiding me through several challenges and providing me with the best possible conditions to accomplish my PhD thesis. I also would like to acknowledge Prof. Steven Bottle, who is my associate supervisor at QUT. Many thanks to Dr. Christoph Dürr and Dr. Sebastian Emmerling who taught me the basics of scientific research.

I would like to say thanks to the people from the M6 lab in Brisbane. A special thank you goes to Kai Anders Hansen, Komba Thomas, Jason Morris, Kye Masters and Anthony Verderosa. Thanks for making my stay in Brisbane a big highlight, and contributing to the success of my projects. I enjoyed every minute we spent together over the last couple of years including the late sessions in the lab, the time we spent in our share house, the long stays in the pubs (combined with pool), the house parties, the surfing sessions, hours of free court basketball and the sparring.

I also would like to thank the macroarc members for providing a nice and productive working environment and being great colleagues. Special thanks go to the 'Westy-Team', with special thanks in particular to Carolin Heiler, Rouven Müller and Kai Pahnke for their support and help.

Ich danke auch meinen Freunden, Mitbewohnern und Leuten aus der MACH 1 Kampsportschule.

Obwohl Sie am Ende meiner Liste stehen, sind es diejenigen den ich am meisten zu verdanken habe. Es sind Menschen auf dich ich in jeder

Lebenslage zählen konnte und kann und vor denen ich den tiefsten Respekt verspüre. Ich danke meiner Frau, meinen Eltern und meinem Bruder für deren bedingungslose Unterstützung und die viele Geduld und Verständnis mit mir. Ich wäre ohne sie nie da angekommen wo ich gerade stehe.

List of Publications and Presentations

Journal articles

(6_b) Near infrared photoinduced coupling reactions assisted by upconversion nanoparticles

Paul Lederhose, Zhijun Chen, Rouven Müller, James P. Blinco, Si Wu, Christopher Barner-Kowollik, *Angewandte Chemie International Edition* 2016, DOI: 10.1002/anie.201606425.

(6_a) Lichtgesteuerte Kupplungsreaktionen im nahen Infrarot mittels Aufkonvertierungs-Nanopartikeln

Paul Lederhose, Zhijun Chen, Rouven Müller, James P. Blinco, Si Wu, Christopher Barner-Kowollik, *Angewandte Chemie* 2016, DOI: 10.1002/ange.201606425.

(5) Catalyst free visible light induced cycloaddition as an avenue for polymer ligation

Paul Lederhose, Kilian N. R. Wüst, Christopher Barner-Kowollik, James P. Blinco, *Chemical Communications* 2016, 52, 5928 - 5931.

(4) Design of redox/radical sensing molecules via nitrile imine-mediated tetrazole-ene cycloaddition (NITEC)

Paul Lederhose, Naomi L. Haworth, Komba Thomas, Steven E. Bottle, Michelle L. Coote, Christopher Barner-Kowollik, James P. Blinco, *Journal of Organic Chemistry* 2015, 80, 8009 - 8017.

(3) Photo-induced ligation of acrylonitrile-butadiene rubber: selective tetrazole-ene coupling of chain-end functionalized copolymers of 1,3-butadiene

Christoph J. Dürr, Paul Lederhose, Lebohang Hlalele, Doris Abt, Andreas Kaiser, Sven Brandau, Christopher Barner-Kowollik, *Macromolecules* 2013, 46, 5915 - 5923.

(2) Mechanistic insights into the UV-induced radical copolymerization of 1,3-butadiene with acrylonitrile

Lebohang Hlalele, Christoph J. Dürr, Paul Lederhose, Andreas Kaiser, Stefan Hüsgen, Sven Brandau, Christopher Barner-Kowollik, *Macromolecules* 2013, 46, 2109 - 2117.

(1) High molecular weight acrylonitrile-butadiene architectures via a combination of RAFT polymerization and orthogonal copper mediated azide-alkyne cycloaddition

Christoph J. Dürr, Sebastian G. J. Emmerling, Paul Lederhose, Andreas Kaiser, Sven Brandau, Michael Klimpel and Christopher Barner-Kowollik, *Polym. Chem*. 2012, 1048 – 1060.

Patents

(1) Nitrile rubbers coupled via bisdihydropyrazole groups, production of modified nitrile rubbers and their use

Brandau, Sven; Kaiser, Andreas; Westeppe, Uwe; Barner-Kowollik, Christopher; Duerr, Christoph; Lederhose, Paul, US 20140357801.

Presentations

(2) Design of redox/radical sensing materials via nitrile imine-mediated tetrazole-ene cycloaddition (NITEC)

Royal Australian Chemical Institute National Congress, Adelaide, Australia, 2014.

(1) Design of nano-structured, reactive polymer films

Queensland University of Technology, Brisbane, Australia, 2013.